Mass transfer of solutes in turbulent wall bounded flows reacting with the conduit surface

A thesis submitted in partial fulfilment of the requirements for the degree of Doctor of Philosophy and the Diploma of Imperial College London

by

Kaveh Sookhak Lari

Sections of

Environmental and Water Resources Engineering

& Fluid Mechanics

Department of Civil and Environmental Engineering

Imperial College London

London, July 2011

To *Maman* and *Baba*, for their infinite kindness, help and encouragement ...

and to the other me, *Venus*.

Although I was working on “turbulence”, she kept everything “laminar”.

I hereby certify that this submission is my own work. Any quotation from, or description of the works of, others is acknowledged herein by reference to the source.

Kaveh Sookhak Lari

Abstract

This thesis focuses on the decay of chlorine in pipes of drinking water distribution networks due to wall and bulk demand. Accurate prediction of chlorine decay is important, as both chlorine concentrations which are too low and too high pose serious health risks, the former due to pathogen formation and the latter due to the formation of disinfection by-products. Water quality models used for the prediction of chlorine decay make use of parameterisations for the wall demand in the form of Sherwood number *Sh* correlations, which couple the wall mass flux to a Reynolds number *Re*, Schmidt number *Sc* and wall roughness. These correlations are subject to significant uncertainty, particularly for turbulent flows. A combined analytical and numerical approach is taken to study in detail the interaction between flow, turbulence and mass transport, with the aim of improving the understanding and accuracy of wall demand parameterisations for chlorine.

Simulations of the chlorine decay in an axisymmetric pipe with hydraulically smooth walls were performed for $Re = 10^4$ to 10^6 and $Sc = 1000$ using Reynolds averaged conservation equations. These values are typical for chlorine transport in distribution networks. The simulations confirmed that the assumptions made in water quality models for chlorine wall demand are valid. Asymptotic solutions for high *Sc* solutes were developed which are applicable both to linear and nonlinear wall reactions. Results showed that the *Sh* correlation is independent of the reaction type.

For rough walls, the two main wall demand parameterisations are mutually inconsistent: one is valid for low and the other for high wall demand coefficients only. Numerical simulation of flow and high *Sc* mass transport over a d-type rough surface at $Re = 2.5 \times 10^5$ showed that the inconsistency between the two parameterisations was caused by the geometry. For low wall demand coefficients, the existence of roughness elements causes higher wall demand than for a smooth wall. However, at high wall demand coefficients the maximum wall demand achievable in the cavities was much smaller than for the crests. Hence, the effective surface area and therefore the wall demand became lower than for a smooth wall. A parameterisation was developed which reproduced the solute mass decay over the entire range of wall demand coefficients.

Most of the solutions and parameterisations developed in this thesis are on the same level of description as water quality models. The findings of this thesis can be used as supportive evidence for the validity of assumptions made for water quality models, and to inform how processes should be modelled when these assumptions are violated.

Acknowledgements

This is a great opportunity to express my respect to my supervisor Dr Maarten van Reeuwijk for his infinite patience and many hours, days and months spent guiding me during the research period. I am thankful for his continuous support, involvement, fruitful advice, expertise and encouragement.

I also want to thank Prof. Čedo Maksimović for the opportunity to undertake this research, as well as his moral support. Thanks are due to all the colleagues and staff members at the Department of Civil Engineering of Imperial College London who made this place a peaceful environment for research.

Finally, I want to thank my parents and my wife for their infinite support, without which this work would have never been completed.

Nomenclature

A summary of the notation used in the thesis (except the appendices) is presented here. Numbers in parentheses refer to the sections in which the notation appears for the first time. Dimensions, including mass M, length L, time T and dimensionless, are represented in brackets. For the case of italic subscripts, a maximum two levels of subscript (such as $\mathbf{Symbol}_{subscript_{subscript}}$) are used throughout the thesis.

Symbols

A_{h}	Hydraulic cross-section area	$[L^2]$	(2.4.1)
$\widetilde{A}$	Integration constant	$[-]$	(7.1)
A^+	Empirical constant (=26)	$[-]$	(4.2)
$\mathbf{A}_{\mathrm{u}}$	Matrix of coefficients for u in RANS equation	$[-]$	(4.3)
a_1	Empirical coefficient	$[-]$	(2.5.3)
a_1	Taylor expansion series coefficient	$[-]$	(3.3)
a_2	Empirical coefficient	$[-]$	(2.5.3)
a_2	Taylor expansion series coefficient	$[-]$	(3.3)
a_3	Empirical coefficient	$[-]$	(2.5.3)
a_3	Taylor expansion series coefficient	$[-]$	(3.3)
$\widetilde{B}$	Variable ($= \widetilde{\lambda}_0 + \ln\widetilde{\lambda}_0$)	$[-]$	(7.4)
B^+	Empirical constant (=4)	$[-]$	(4.2)

$\mathbf{B}_{\mathsf{k}}$	Matrix of coefficients for k in k equation	$[-]$	(4.3)
$\mathbf{B}_{\mathrm{u}}$	Matrix of coefficients for u in k equation	$[-]$	(4.3)
b	Empirical constant (=9.5×10^{-4})	$[-]$	(4.2)
b_1	Taylor expansion series coefficient	$[-]$	(3.3)
b_2	Taylor expansion series coefficient	$[-]$	(3.3)
b_3	Taylor expansion series coefficient	$[-]$	(3.3)
C	Typical concentration variation in streamwise direction	$[ML^{-3}]$	(7.1)
C_1	Empirical coefficient (=1.44)	$[-]$	(4.3)
C_2	Empirical coefficient (=1.92)	$[-]$	(4.3)
$\mathrm{C_f}$	Normalized local drag by friction	$[-]$	(8.3)
$C_{\mathrm{k_w}}$	Empirical coefficient	$[-]$	(2.5.3)
$\mathrm{C_p}$	Normalized local drag by pressure	$[-]$	(8.3)
C_μ	Empirical coefficient (=0.09)	$[-]$	(4.3)
$\mathbf{C}_{\mathrm{u}}$	Matrix of coefficients for u in ε equation	$[-]$	(4.3)
$\mathbf{C}_{\varepsilon}$	Matrix of coefficients for ε in ε equation	$[-]$	(4.3)
c	Concentration (also RA concentration)	$[ML^{-3}]$	(3.2)
c_0	c_{x} at $x = 0$	$[ML^{-3}]$	(2.4.3)
c_{r}	Radial concentration scaling function	$[-]$	(5.1)
c_{x}	Crosswise mean concentration	$[ML^{-3}]$	(2.4.3)
$\widetilde{c}$	Normalized RA concentration (= c/c_0)	$[-]$	(7.1)
$\widetilde{c}_{\mathrm{x}}$	Normalized crosswise mean concentration (= c_{x}/c_0)	$[-]$	(7.1)
D	Diffusion coefficient	$[L^2T^{-1}]$	(2.5.2)
d	Depth of the cavity	$[L]$	(2.5.2)
$\check{d}$	Averaged height of roughness elements	$[L]$	(2.5)
E	Relative residual	$[-]$	(4.3)
E	Empirical function	$[L^2T^{-4}]$	(8.1)
$\widetilde{E}$	Variable	$[-]$	(7.3)
e	Relative error	$[-]$	(5.4)
F	Velocity similarity function	$[-]$	(3.3)

$\widetilde{F}$	Variable	$[-]$	(7.3)
f	Fanning friction factor	$[-]$	(2.4.2)
f	Function	$[-]$	(7.1)
f_1	Empirical function	$[-]$	(8.1)
f_2	Empirical function	$[-]$	(8.1)
f_μ	Damping function	$[-]$	(8.1)
g	Gravitational acceleration	$[LT^{-2}]$	(2.4.2)
g	Function	$[-]$	(7.2)
gr	Gram	$[M]$	(2.2.1)
J	Mass flux	$[ML^{-2}T^{-1}]$	(2.4.3)
K_1	Growth parameter	$[LT^{-1}]$	(10.4)
K_2	Growth parameter	$[-]$	(10.4)
K_3	Growth parameter	$[M^{-1}L^3]$	(10.4)
k	Decay coefficient (also the eigenvalue)	$[L^{-1}]$	(2.4.3)
k	Turbulent kinetic energy	$[L^2T^{-2}]$	(4.3)
k	Matrix of unknown k values	$[L^2T^{-2}]$	(4.3)
k_t	Decay rate	$[T^{-1}]$	(2.4.3)
k_b	Bulk demand coefficient	$[T^{-1}]$	(2.4.3)
k_f	Mass transfer coefficient	$[LT^{-1}]$	(2.4.3)
k_w	Wall demand coefficient	$[LT^{-1}]$	(2.4.3)
$\widetilde{k}$	Dimensionless decay coefficient	$[-]$	(7.3)
kg	Kilogram	$[M]$	(2.2.1)
L	Pipe length	$[L]$	(2.4.2)
L	Typical length scale for concentration variation	$[L]$	(7.1)
L_E	Entrance length	$[L]$	(2.4.2)
L_e	*e* folding length	$[L]$	(5.1)
l_m	Mixing length	$[L]$	(4.2)
lit	Litre	$[L^3]$	(1.1)
m	Metre	$[L]$	(2.2.3)

mg	Milligram	$[M]$	(1.1)
mlit	Millilitre	$[L^3]$	(2.2.3)
mm	Millimetre	$[L]$	(2.2.3)
N	Number of cells	$[-]$	(4.3)
n	Surface normal direction	$[L]$	(8.3)
$\mathbf{n}$	Node in the network	$[-]$	(2.4.2)
$\vec{n}$	Unit vector for surface normal direction	$[L]$	(8.3)
P	Crosswise mean p	$[ML^{-1}T^{-2}]$	(2.4.2)
P	Turbulent kinetic energy production	$[L^2T^{-3}]$	(4.3)
P_h	Hydraulic perimeter	$[L]$	(2.4.2)
p	Pressure (also RA pressure)	$[ML^{-1}T^{-2}]$	(3.1)
p	Kinematic pressure (also RA kinematic pressure)	$[L^2T^{-2}]$	(3.5)
Q	Mean volumetric flow rate	$[L^3T^{-1}]$	(2.4.1)
R	Pipe radius	$[L]$	(2.4.1)
$\dot{\mathrm{R}}$	Crosswise mean bulk reaction rate	$[ML^{-3}T^{-1}]$	(2.4.3)
r	Radial coordinate	$[L]$	(3.5)
$\dot{\mathrm{r}}$	Bulk reaction rate (also RA bulk reaction rate)	$[ML^{-3}T^{-1}]$	(3.1)
r_h	Hydraulic radius	$[L]$	(2.4.2)
$\mathbf{r}_\mathrm{u}$	Right hand side matrix for u in RANS equation	$[-]$	(4.3)
S	Shift in the log law	$[-]$	(8.3)
s	Surface tangential coordinate	$[L]$	(8.3)
$\vec{s}$	Unit vector for surface tangential coordinate	$[L]$	(8.3)
sec	Second	$[T]$	(2.4.1)
T_m	Timescale for mass depletion in MTBL	$[T]$	(7.4)
t	Time	$[T]$	(2.4.3)
U	Crosswise mean u	$[LT^{-1}]$	(2.4.1)
u	Velocity (also RA streamwise velocity)	$[LT^{-1}]$	(3.2)
$\mathbf{u}$	Matrix of unknown u values	$[LT^{-1}]$	(4.3)
u_τ	Friction velocity	$[LT^{-1}]$	(2.5)

urf	Under relaxation factor	$[-]$	(4.3)
v	Wall normal velocity (also RA wall normal velocity)	$[LT^{-1}]$	(3.3)
$\vec{v}$	Velocity vector	$[LT^{-1}]$	(8.3)
w	Width of the cavity	$[L]$	(2.5.2)
X	Dummy variable	$[-]$	(3.1)
x	Streamwise coordinate	$[L]$	(2.4.2)
$\widetilde{x}$	Non dimensional streamwise coordinate ($= x/\mathrm{L}$)	$[-]$	(7.1)
$\vec{x}$	Unit vector for x coordinate	$[L]$	(8.3)
y	Wall distance (also wall normal coordinate)	$[L]$	(3.3)
$\widetilde{y}$	Wall normal coordinate in mass transfer unit ($= y/\delta_\mathrm{m}$)	$[-]$	(7.1)
Z	Elevation head	$[L]$	(2.4.2)
α	Variable ($= \sqrt[3]{bSc}$)	$[-]$	(5.4)
$\widetilde{\alpha}$	Dimensionless second-order wall demand coefficient	$[-]$	(7.4)
α_d	Ratio of the MTBL thickness inside the cavity to d	$[-]$	(9.4)
β	Variable ($= \mathrm{k_w} Sc/u_\tau$)	$[-]$	(5.4)
$\widetilde{\beta}$	Coefficient in generic linear boundary condition	$[-]$	(7.3)
Γ	Numerical diffusion	$[L^2T^{-1}]$	(9.2)
$\widetilde{\gamma}$	Coefficient in generic linear boundary condition	$[-]$	(7.3)
δ	Half channel width	$[L]$	(8.2)
δ_L	Infinitesimal length in x direction	$[L]$	(2.4.3)
δ_m	Thickness of the MTBL	$[L]$	(7.1)
δ_v	Viscous length scale (unit) ($= \nu/u_\tau$)	$[L]$	(2.5)
ε	Turbulent kinetic energy dissipation rate	$[L^2T^{-3}]$	(4.3)
$\widetilde{\varepsilon}$	Modified turbulent kinetic energy dissipation rate	$[L^2T^{-3}]$	(8.1)
$\boldsymbol{\varepsilon}$	Matrix of unknown ε values	$[L^2T^{-3}]$	(4.3)
$\widetilde{\eta}$	Variable ($= 4\pi\sqrt{3}\widetilde{\alpha}/9$)	$[-]$	(7.4)
$\theta_{\mathrm{k_f}}$	Adjusting coefficient for $\mathrm{k_f}$	$[-]$	(2.5.3)
$\theta_{\mathrm{k_w}}$	Adjusting coefficient for $\mathrm{k_w}$	$[-]$	(2.5.3)
ι	Constant (=0.83)	$[-]$	(7.2)

κ	von Karman constant (=0.41)	$[-]$	(3.3)
Λ	Ratio of first-order wall to bulk decay coefficient	$[-]$	(6.2)
λ	Periodic length	$[L]$	(2.5.2)
$\widetilde{\lambda}$	Parameter for change of variables	$[-]$	(7.4)
$\widetilde{\lambda}_0$	$\widetilde{\lambda}$ at $\widetilde{x}$=0	$[-]$	(7.4)
μ	Dynamic viscosity	$[ML^{-1}T^{-1}]$	(2.4.1)
ν	Kinematic viscosity	$[L^2T^{-1}]$	(2.4.1)
ρ	Density	$[ML^{-3}]$	(2.4.1)
σ_k	Empirical coefficient (=1)	$[-]$	(4.3)
σ_ε	Empirical coefficient (=1.3)	$[-]$	(4.3)
$\widetilde{\sigma}$	Coefficient in generic linear boundary condition	$[-]$	(7.3)
τ	Stress (also shear stress)	$[ML^{-1}T^{-2}]$	(2.4.2)
Ψ	Stream function	$[L^2T^{-1}]$	(8.3)

Dimensionless numbers

Da	Damköhler number	$[-]$	(6.2)
Re	Reynolds number	$[-]$	(2.4.1)
Re_d	Roughness *Re*	$[-]$	(2.5.3)
Re_t	Local *Re*	$[-]$	(8.1)
Re_τ	Shear *Re*	$[-]$	(4.2)
Sc	Schmidt number	$[-]$	(2.5.2)
Sh	Sherwood number	$[-]$	(2.5.2)

Superscripts

$X^{(n+1)}$	New iteration	(4.3)
$X^{(n)}$	Old iteration	(4.3)
X^T	Transpose	(4.3)

X'	Fluctuation	(3.2)
$\hat{X}$	Instantaneous	(3.2)
X^+	Plus units	(3.3)

Italic subscripts

X_a	Analytical	(5.4)
X_{ca}	Cavity	(9.3)
X_{cr}	Crest	(9.3)
X_D	Diffusive	(5.4)
X_{far}	Far field	(7.4)
X_i	Node *i* in the network	(2.4.2)
	In *i* direction	(3.1)
	Associated with the *i*th cell(s) in streamwise direction	(5.1)
X_{in}	Entering the node in the network	(2.4.2)
X_j	Node j in the network	(2.4.2)
	In j direction	(3.1)
	Associated with the jth cell(s) in wall normal direction	(4.3)
X_{LS}	Launder Sharma model	(9.1)
X_n	Associated with the *n*th eigenvalue	(2.4.2)
X_{out}	Leaving the node in the network	(2.4.2)
X_R	Rough surfaces	(2.5.3)
X_r	In *r* direction	(4.3)
X_T	Turbulence	(3.4)
X_{tot}	Total	(5.4)
X_w	Wall	(2.4.3)
X_x	In *x* direction	(7.4)

Mathematical operators

$\arctan(X)$	Arc tangent	(5.4)
$d(X)$	Differential	(2.4.3)
$\exp(X)$	Exponential	(4.2)
$\ln(X)$	Natural logarithm	(3.3)
$\log(X)$	Logarithm to base 10	(2.5.1)
$W_0(X)$	Lambert W function	(7.4)
$\Delta(X)$	Differences (of two X values)	(2.4.2)
$\Sigma(X)$	Summation (of several X values)	(2.4.2)
$\partial(X)$	Partial differential	(3.1)

Averaging operators

$\langle X \rangle$	Crosswise averaging operator	(5.1)
$\overline{X}$	Reynolds averaging operator	(3.2)

Numbers

e	Euler's (also known as Napier's) number	(2.4.3)
π	Ratio of Euclidean circle's circumference to its diameter	(2.4.1)

Acronyms

1D	One-dimensional	(5)
2D	Two-dimensional	(5)
2D	Three-dimensional	(6.2.2)
AWWA	American Water Works Association	(2.4.3)
am	Ante meridian	(2.2.2)

C	Centigrade	(2.2.1)
DBP	Disinfection by-product	(1.1)
DNS	Direct numerical simulation	(1.4)
DO	Dissolved oxygen	(2.2.1)
EU	European Union	(2.2.1)
EVM	Eddy viscosity model	(3.4)
HAA	Haloacetic acid	(2.2.1)
HRN	High Reynolds number	(4.1)
LES	Large eddy simulation	(2.5.2)
LRN	Low Reynolds number	(4.1)
LS	Launder Sharma	(8)
MCL	Maximum contaminant level	(2.2.1)
MPN	Most probable number	(2.2.1)
MTBL	Mass transfer boundary layer	(5.3.1)
NOM	Natural organic matter	(2.2.1)
NS	Navier Stokes	(3.1)
NTU	Nephelometric turbidity unit	(2.2.1)
ODE	Ordinary differential equation	(5.1)
PC	Personal computer	(2.4.2)
PE	Polyethylene	(2.2.3)
PVC	Polyvinyl chloride	(2.2.3)
pm	Post meridian	(2.2.2)
RA	Reynolds averaged	(3.1)
RANS	Reynolds averaged Navier Stokes	(2.5.2)
SDWA	Safe Drinking Water Act	(2.1)
THM	Trihalomethane	(2.2.1)
UK	United Kingdom	(2.2.3)
UNICEF	United Nations Children’s Fund	(2.2.1)
USA	United States of America	(2.1)

US EPA	United States Environmental Protection Agency	(1.2)
WHO	World Health Organization	(1.1)

Chemical symbols

Cl_2	Chlorine	(2.2.1)
CN^-	Cyanide	(2.5.2)
Fe^{2+}	Ferrous	(2.3)
Fe^{3+}	Ferric	(2.3)
H_2O	Water	(2.3)
HCl	Chloridric acid	(2.3)
$HOCl$	Hypochlorite acid	(2.3)

Registered marks

EPANET	(1.2)
InfoWater	(1.2)
MATLAB	(4.2)
OpenFOAM	(8.2)
WaterGEMS	(1.2)

Contents

List of Figures

List of Tables

CHAPTER 1

Introduction

Fresh water[1] is a scarce resource. Of all the water on Earth, only 3% is fresh, and most of this water is inaccessible for use because it is stored in glaciers and ice caps. Only 1% of the total amount of fresh water resource is accessible in the form of groundwater and surface water, and most communities rely on these resources for survival and welfare[2] (Petersen *et al.*, 2010).

The quality of fresh water resources is continuously under threat, often from human activities. Major sources for water contamination include industrial and urban wastewater streams, agricultural pesticides and fertilizers, and leachate from landfills. It is estimated that nearly two thirds of nations worldwide will face fresh water stress by the year 2025 (UN Environment Programme, 2008). Among different water contaminations, pathogens (disease causing microorganisms) have the most fatal effects. Each year, millions of people die because of infectious diarrheal disease caused by waterborne pathogens (WHO, 2010). Tragically, many of these deaths could have been easily prevented with basic procedures for water disinfection and sanitation[3].

In urban areas, the solution to ensure safe access to drinking water is to install a modern water supply system, as schematically shown in figure 1.1. The preliminary component of a typical water supply system comprises infrastructure for water intake from a water resource. The water then enters a water treatment plant, where it is disinfected and impurities are removed using various chemical and physical processes. After treatment, the water is temporarily stored in storage tanks until it is delivered to the consumer by means of a drinking water distribution network (Twort *et al.*, 2000). The wastewater produced is then

[1] Water with less than 500 parts per million of dissolved solids (Crittenden *et al.*, 2005).

[2] Some of the countries in arid and semi arid regions also use desalinated sea water for their domestic consumption (Abderrahman, 2000).

[3] One of the Millennium Goals of The United Nations (UN) is to "halve, by 2015, the proportion of the population without sustainable access to safe drinking water and basic sanitation". In addition, the UN has declared the period 2005-2015 the Decade of Water for Life (UN Millennium Project, 2005).

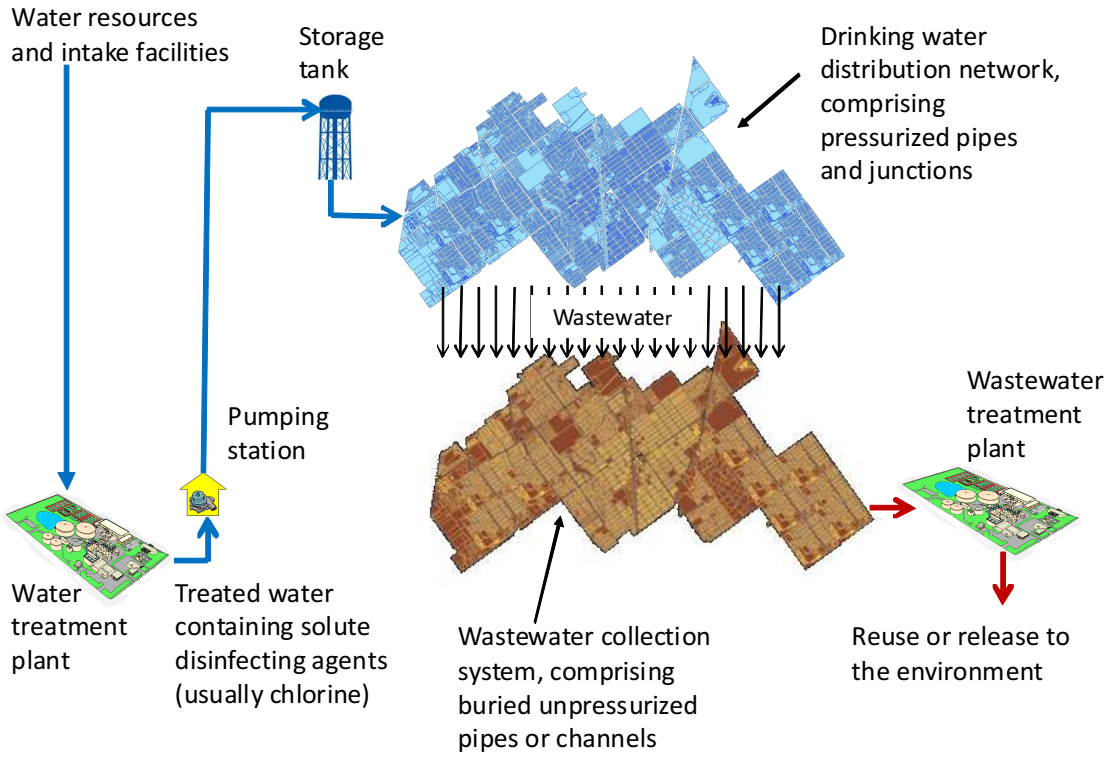

FIGURE 1.1. Schematic of a water supply system which usually includes a water treatment plant, storage tanks and a water distribution network. A water supply system is usually accompanied by a wastewater collection network, wastewater treatment plant and disposal facilities. Figure is not to scale.

collected and transported via a separate network to a wastewater treatment plant, where the wastewater is treated for agricultural reuse or safe release to the environment (Tchobanoglous *et al.*, 2003).

1.1. The chlorine deficit problem

To avoid degradation of the water quality during the transit time from the water treatment plant to the consumer, a disinfecting agent, usually chlorine, is injected into the water to protect it against growth of pathogens. The World Health Organization (WHO) water quality guideline indicates that the minimum chlorine residual (the amount of measurable chlorine remaining after disinfecting the water with chlorine)

anywhere in the drinking water distribution network should not be less than 0.2 milligrams per litre (mg/lit) (WHO, 2010). However, it is far from trivial to enforce this guideline.

A drinking water distribution network generally consists of thousands of pipes of different size, material and age arranged in a complex network structure. In addition, there is large spatial and temporal variability in the water demand, as thousands of households consume water independently and intermittently. Consequently, the residence time of the water in the network is highly variable. During this time, the chlorine residual is depleted due to reactions with other solutes in the water, or with the network's pipe surfaces (Rossman *et al.*, 1994). Chlorine depletion due to reactions with the pipe wall is generally referred to as *wall demand*; depletion due to reactions inside the water is called *bulk demand*. When the chlorine residual falls below the minimum threshold, it is referred to as the chlorine deficit problem (figure 1.2).

When a chlorine deficit problem occurs in a water distribution network, it can create critical health risks. For instance, Agard *et al.* (2002) performed a study in the distribution network of Trinidad, and observed that 96% of the chlorine residual was depleted during the transport and delivery process, which resulted in increased levels of diarrheal pathogens. This is not an isolated incident; these problems resurface regularly worldwide. Recent examples include incidents in Europe (Egorov *et al.*, 2002), America (LeChevallier *et al.*, 1996), Asia (Semenza *et al.*, 1998) and Africa (Bailey & Thompson, 1995).

A seemingly straightforward solution to avoid the chlorine deficit problem is to dramatically increase the concentration of chlorine residual in the water. However, apart from having an adverse effect on the taste of water, high chlorine concentrations lead to unacceptable levels of disinfection by-products (DBPs), which are known to be carcinogenic. Consequently, the standards also state a maximum concentration of chlorine residual; the WHO guidelines recommend an upper threshold of 5.0 mg/lit (WHO, 2010).

Clearly, it is a formidable challenge to design and operate a drinking water distribution network for which the water quality and quantity is according to specification at every point in the network, at every point in time. Crucial tools for meeting this challenge are mathematical models for prediction of flow and water quality in the distribution network.

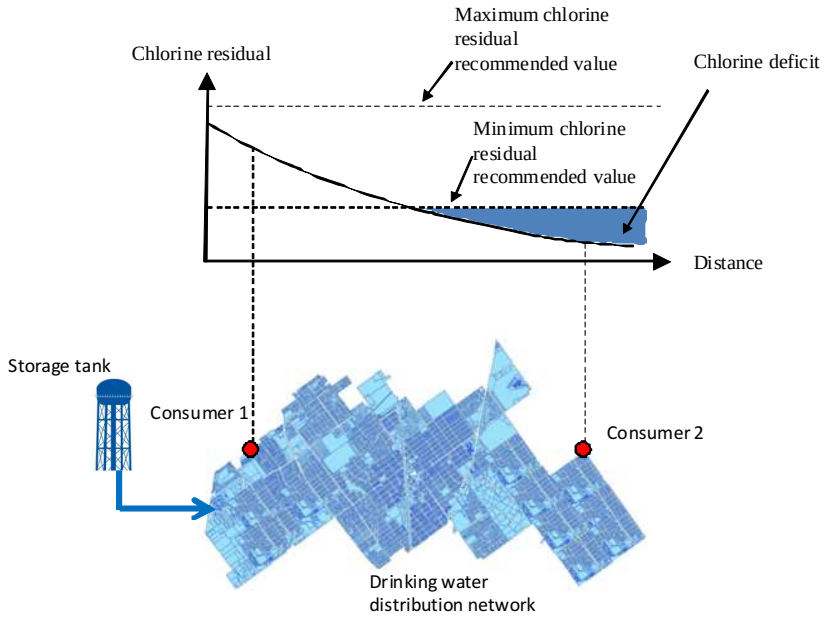

FIGURE 1.2. Chlorine deficit problems occur when the chlorine residual falls below the minimum threshold due to wall and bulk demands in the network. Figure is not to scale.

1.2. Water quality models and parameterisations

Several water quality models have been developed over the years. One of the most widely used models is EPANET, which is open source and has been developed by the United States Environmental Protection Agency (US EPA) (Rossman, 2000). This model serves as the basis for several other (commercial) water quality models such as WaterGEMS and InfoWater (Walski *et al.*, 2003).

The first step in creating predictions for water quality in distribution networks is to obtain accurate estimations for the flow rate in each of the network pipes. EPANET simplifies the distribution network to a level on which pipes are represented simply as links between junctions (nodes) that have a certain volume flow rate. This integral approach requires a parameterisation of the head losses incurred in the pipes, i.e. explicit correlations which link frictional and other losses to the mean velocity inside the pipe. Once the flow is determined, a water quality model can be executed. Current EPANET-based water quality models

use the transport equations for solute mass, taking into account the solute mass decay (due to wall and bulk demands) to predict solute concentration in all pipes in the network. Here, the integral approach requires parameterisations for the wall demand. Similar to the case of the flow field, such parameterisations correlate a solute mass flux due to wall demand to the mean concentration inside the pipe.

Parameterisations are extremely useful as they capture the essentials of complex processes in simple algebraic relations. They allow models to be formulated on a high level, without having to include, in the context of water distribution networks, details of the flow and the solute mass transport in each single pipe, which would be computationally prohibitively expensive. However, as the solute mass decay is directly dependant on the parameterisations, any uncertainties / inaccuracies in the parameterisation will immediately translate into inaccurate predictions. Currently, there are large uncertainties in parameterisations for wall demand, in particular, in turbulent flows. As turbulent flow is the norm in water distribution networks (Ho, 2008), it is important to identify the source of uncertainties and create better parameterisations. The work presented in this thesis is a step in this direction.

1.3. Aims and objectives

The primary aim of this thesis is to increase the understanding of the effects of flow and turbulence on wall demand and to use it to improve existing parameterisations. The thesis then explores whether and to what extent detailed numerical simulations and analytical methods can be used to decrease the uncertainties in the wall demand parameterisations.

In order to study the complex interaction between the flow, solute mass transport and wall demand in detail, the mass transport in a single network pipe will be considered. As will be discussed in chapter 2, this type of modelling is representative for modelling water distribution networks, because the residence time of the fluid in junctions is very small compared to the residence time in the pipe.

The flow is assumed to be fully turbulent and in a statistically steady-state. The solute mass is assumed not to cause any density differences in the fluid, and only single species reactions will be considered. Numerical models will be used to perform simulations for various scenarios involving rough and smooth pipe walls. The models provide detailed information of both flow and solute mass transport inside the pipe and

across the pipe cross-section.

The objectives of the thesis are to:

(1) review the methods by which the wall friction and wall demand are parameterised in pipes and identify the uncertainties and open research questions in the parameterisations;
(2) select appropriate numerical and analytical models which accurately predict the flow and turbulence levels in pipes;
(3) perform detailed simulations for the mass transport and analyse the results in order to understand the dominant physics governing the wall demand;
(4) use the understanding developed with simulations to develop simple analytical models that capture the physics and can be used as parameterisations;
(5) provide bounds for the applicability of parameterisations currently used in water quality models for distribution networks.

1.4. Outline

The overall structure of the thesis, as well as the contribution of each chapter, is described in this section. The thesis comprises ten chapters and three appendices. Chapter 2 provides a broad background of the problem. It contains a detailed review of water supply systems, water quality indicators and models and parameterisations for wall friction and wall demand. The current gaps in knowledge are identified which lead to four research questions (section 2.6) that will be addressed in the remainder of the thesis.

Flow and mass transport in single pipes are discussed in chapter 3. The chapter includes the governing equations, a discussion on turbulent flows and Reynolds averaging, and concludes with a focused study on axisymmetric pipes with smooth walls, which will form the focus of chapters 4 to 7.

Mass transport requires detailed information on the flow and turbulence inside the pipe. In chapter 4, flow and turbulence models are discussed as well as their implementation. The models are validated using data from direct numerical simulation (DNS).

Chapters 5 to 9 contain the main results of the thesis. The studies in chapters 5 to 7 are associated with

hydraulically smooth pipes. Hydraulically rough pipes are studied in chapters 8 and 9. The contents of the main chapters are briefly introduced below.

Chapters 5 to 7 study the criteria under which the current wall demand parameterisations hold and present appropriate parameterisations for the cases where the current parameterisations are subject to uncertainties. Chapter 5 includes a study on first-order wall demands. In chapter 6, the effect of simultaneous first-order wall and bulk demands is discussed. Nonlinear wall demands are studied in chapter 7.

The studies in chapters 8 and 9 address flow and mass transport in rough pipes. The flow over a particular rough surface is studied in chapter 8. A detailed comparison of flow simulations with DNS data in the literature is made. Results of this chapter are then used in chapter 9 to simulate first-order wall demands in turbulent rough pipe flows.

Chapter 10 includes the conclusions and recommendations. In addition, appendix A discusses effects of pipe wall curvature on wall demand. Computational codes developed for this thesis are presented in appendix B. Appendix C includes a list of publications.

CHAPTER 2

Background

Meeting the objectives posed in the introduction requires background knowledge of water quality, treatment and transport, as provided in the current chapter. The chapter starts with a brief introduction of the history of water supply systems (section 2.1). A discussion on the components of water supply systems is presented in section 2.2. One of the components being discussed in that section is the drinking water distribution network. Chlorine wall and bulk demand in networks are discussed in section 2.3, and mathematical models for networks are introduced in section 2.4. The latter section introduces the most important operational indicators for the purpose of network design, history of water quality modelling and the key assumptions made in water quality models. The methods by which wall friction and demand are parameterised are introduced in section 2.5. Discussions on the open research questions in such parameterisations and the position of the current study in addressing them is presented in section 2.6. The chapter ends with a summary (section 2.7).

2.1. History of water supply systems

Civilizations have historically flourished around water resources. Initial communities were gathered around wells, rivers or lakes, which gave them direct access to water (Mays, 2008). Due to growing populations and migration from rural areas, some residential areas had to be built further away from water resources. In such cases, the only alternative was (and still is) to transport water from resources to the consumers. Consequently, ingenious solutions were developed to solve the water transport problem.

Ancient water transport techniques were mostly open channels which transported surface or ground water. Qanats were networks of underground channels used in ancient Iran, which were able to transport

groundwater hundreds of kilometres away from the aquifer (Motiee *et al.*, 2006). Another example is aqueducts, which were open channels constructed to transport surface water in ancient Rome (Coates-Stephens, 1998). However, these techniques were limited to situations where the water resource was located at a higher elevation than the settlement, which was often not the case.

To overcome this limitation, pressurized water transport was developed. One of the first forms of pressurised water transport occurred in ancient China, where water was transported through a system of stone pipes (Needham, 1985). The method allowed transport of water from lower altitudes to higher altitudes. However, a source of energy was needed to overcome the effect of gravity. Early civilisations relied on wind, surface water streams and muscular energy by animals and men. However, such sources could only provide sufficient energy to support small communities and, therefore, were replaced by mechanical pumps after the steam engine was invented in the eighteenth century (Dickinson, 2010).

Steam engines could provide sufficient energy to transport water in urban area through extended pressurized pipe systems and therefore, application of such systems became more popular in the nineteenth century. For example, London saw its first systematic pressurised water transport system in the middle of the nineteenth century (Hardy, 1984). In the United States of America (USA), pressurised transport of water was used in the late nineteenth century (Mulholland, 2002).

Parallel to the advancements in water transport techniques, an increased awareness of the importance of water quality for public health led to the development of water treatment processes. One of the main advancements was made when research in the nineteenth century showed that microorganisms can cause infectious disease (O'Brien & Goedert, 1996). With microorganisms identified as a source of disease, attention moved towards finding disinfecting agents, which soon led to the discovery of chlorine as a disinfectant (Crittenden *et al.*, 2005). Disinfection of drinking water then became an important task. The first large scale use of chlorine as a water disinfecting agent occurred in 1850, when this compound was used to purify the water supply in London after an outbreak of cholera (Ashbolt, 2004).

In the 1890s, centralized water treatment plants were constructed in the USA. The aim of such plants was to apply various chemical and physical processes to purify drinking water. From the mid-twentieth century, drinking water standards were developed for the municipal drinking water (Crittenden *et al.*, 2005).

For instance, the Safe Drinking Water Act (SDWA) was approved in the US Congress in 1974, which allowed the US EPA to establish regulations and methods for control and monitoring of drinking water quality (Panguluri *et al.*, 2005).

The combination of water treatment plants and pressurized water transport facilities are usually referred to as water supply systems (Twort *et al.*, 2000). The extent to which these systems are in use is one of the indicators for the level of a country's development (WHO, 2010).

2.2. Components of water supply systems

A brief discussion on the main components of a water supply system, namely the water treatment plant, storage tanks and the distribution network, is presented below. These components are also schematically shown in figure 2.1. Water treatment plants are initially introduced after which water storage tanks and distribution networks are discussed.

2.2.1. Water treatment plants.

Water treatment plants receive the water from water resources (via water intake facilities) and treat it for municipal consumption. Various physical and chemical processes are used in different units of a water treatment plant to adjust the level of water impurities so that the treated water meets local water quality standards (Crittenden *et al.*, 2005). The water impurities are classified into two groups: particulate matter and solutes. Each group and its associated treatment processes are discussed separately in this section. In addition, a brief discussion on the use of chlorine for water disinfection and controlling the finished water quality based on local standards is presented (detailed discussions of the subjects covered here can be found in many water treatment textbooks, see e.g. Crittenden *et al.* (2005)).

Particulate matter and associated treatment processes

Particulate matter is characterized as impurities with such large size that they cannot be considered as a part of the fluid[1]. Particulate matter can reduce water quality since it causes an increase in water turbidity. Indeed, the light passing through the water is reflected by the suspended particles and therefore,

[1]This means that mean fluid molecular free path is much less than the size of the particulate matter. The ratio of these two values represents the Knudsen number (Bird *et al.*, 2002).

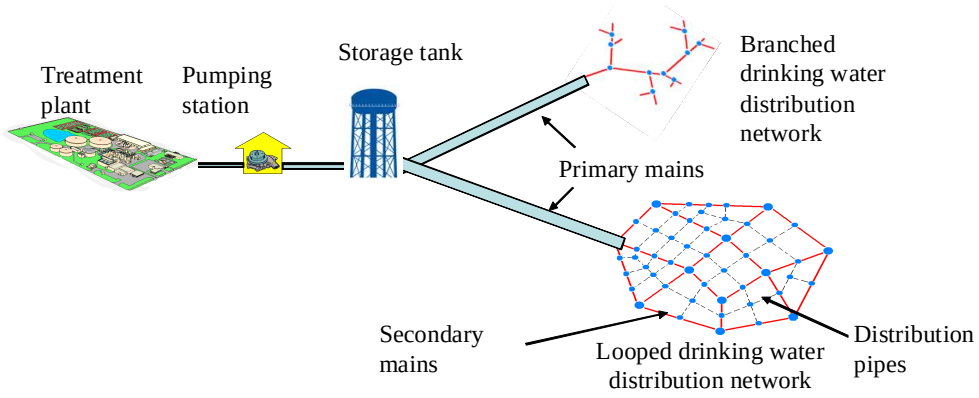

FIGURE 2.1. Components of a water supply system usually include a water treatment plant, pumps, storage tanks and (looped or branched) drinking water distribution networks. Figure is not to scale.

the water loses its transparency. In practice, the lack of transparency in water can be quantified in terms of nephelometric turbidity units (NTU)[2] (Crittenden *et al.*, 2005).

The main natural sources of particulate matter in water are sand and clay. Sand is gravitationally settleable and therefore, it can be removed in a presettling pond in treatment plants. However, clay particles are not gravitationally settleable since they contain repulsive electrical charges on their surfaces. Consequently, a flocculation / coagulation unit is used in which chemical coagulants (such as chloroferric and aluminium chloride) are added to the water to neutralize the electrical charge of clay particles which then form large flocs. The flocs are removed by filtering the water in a filtration unit (Tchobanoglous *et al.*, 2003).

Solutes and associated treatment processes

The second group of water impurities are solutes. In contrast with particulate matter, the size of solutes is of the order of the distance between the water molecules. Consequently, these impurities do not cause water turbidity, although they can decolour the water. Solute compounds in water are categorized into four major groups: metallic ions, non-metallic ions, organic molecules and solute gases (Crittenden *et al.*, 2005).

Some of the most important metallic ions in water are iron, magnesium and manganese which lead to

[2] To have a scale on the magnitude of NTU, well-treated drinking water should have a NTU of less than 5, while in muddy water this value is beyond 10^3 (Crittenden *et al.*, 2005).

odour, taste and colour formation. From a health perspective, nitrate is one of the most important non-metallic ions in water since it has a fatal effect on infants, known as "Blue Baby" syndrome (Tchobanoglous *et al.*, 2003).

Organic molecules, which are usually referred to as natural organic matter (NOM), are mostly end products of various biological activities such as the growth and death of microorganisms. Aside from their effects on the taste and odour of water, the main concern with NOMs is their reaction with chlorine which produces carcinogenic compounds, as discussed in more detail later in this section. One of the most important gases in water is dissolved oxygen (DO) since it prevents the formation of odour in water due to biological activity[3] (Tchobanoglous *et al.*, 2003).

Several processes are used in treatment plants to adjust the level of solute materials. These processes usually include aeration of water, oxidation of solute molecules (in an ozonation unit), adsorption of solute molecules (in an activated carbon unit) and filtration and replacement of solute molecules with other molecules (in reverse osmosis and ion exchange units) (Rossman, 2006). The level of DO is usually adjusted in an aeration unit, metallic ions are removed in oxidation units, NOMs are removed by adsorption processes and non-metallic ions are removed by filtration and replacement processes (Crittenden *et al.*, 2005).

Disinfection of the treated water by chlorine

Once the level of different impurities is adjusted, the water is ready for disinfection. Various forms of microorganisms may exist in water[4], each of which can have serious health risks. For instance, cyanobacteria (also known as blue green algae) produce a very irritative toxin in water. However, the most dangerous microorganisms in terms of human health are coliforms (such as Escherichia coli) which can cause serious diarrheal diseases like cholera[5]. The amount of coliforms in drinking water (which is expressed as the most probable number (MPN) in 100 millilitres (mlit) of water) should be strictly controlled. Consequently, disinfection is vital to eliminate microorganisms and to protect the water from their regrowth (Crittenden *et al.*, 2005).

[3]Biological processes are either aerobic (which need oxygen), anaerobic (which stop if oxygen is present) or anoxic (which are insensitive to the presence of oxygen). Formation of anaerobic activities has a very adverse effect on water quality in terms of odour production (Tchobanoglous *et al.*, 2003).

[4]Algae, viruses, bacteria, fungi, protozoa and helminths are among the living species that may exist in water resources (Crittenden *et al.*, 2005).

[5]The WHO and United Nations Children's Fund (UNICEF) joint project reports that, in 2009, waterborne diarrheal was estimated to have caused 1.1 million deaths in people aged 5 and over and 1.5 million deaths in children under the age of 5 (UNICEF and WHO, 2009).

The most common and reliable method for water disinfection is the injection of chlorine (or its compounds, such as chloramines). Chlorine (Cl_2) is a yellow diatomic gas with a very irritative smell. The disinfecting property of chlorine is discussed in more detail in section 2.3. The main reason for using chlorine as the disinfecting agent is its low cost and high disinfection capability. Chlorine is soluble in water and therefore, it can be used to keep drinking water free of microorganisms during its time in the distribution network[6]. The chlorine concentration in water is referred to as the chlorine residual. Due to the critical property of chlorine in protecting water from the growth of pathogens, the chlorine residual is subject to strict regulations. For instance, WHO suggests 0.2 mg/lit as the lower threshold of chlorine residual in drinking water (WHO, 2008).

The maximum chlorine residual must also be bounded due to the risk of formation of disinfection by-products (DBPs). DBPs are formed by the chemical reaction of chlorine with NOMs (especially humic acids), and the main two groups of DBPs are trihalomethanes (THMs) (such as chloroform) and haloacetic acids (HAAs). Both of the groups are believed to have serious carcinogenic effects, as well as adverse reproductive effects following exposure during pregnancy (WHO, 2008; Porter *et al.*, 2005). Consequently, WHO suggests 5 mg/lit as the upper threshold of chlorine residual in drinking water (WHO, 2008) .

Controlling treated water quality based on water quality standards

The last step before treated water leaves the treatment plant is to check the water quality and compare with the maximum contaminant level (MCL) of the impurities allowed by local standards. A typical list of MCLs in the standards for Canada, USA, European Union (EU) and WHO is presented in table 2.1.

2.2.2. Storage tanks.

Urban water consumption per unit time, also known as water demand, varies substantially through the day. The diurnal variation curves in figure 2.2 show hourly water demand for two typical cities, A and B, where city B has a higher population (and therefore, a higher average daily water demand) than city A. Regardless of the population size, the hourly water demand in an urban area usually includes two peak demands between 6-9 am and 4-7 pm. These two peaks are associated with the working population leaving their homes in the morning and returning in the evening (Swamee & Sharma, 2008). The ratio between the peak in water

[6] At 20^o C and atmospheric pressure, one kilogram (kg) of water dissolves a maximum of 8 grams (gr) of gaseous chlorine (Schmittinger, 2000).

TABLE 2.1. Water quality standards in Canada (Health Canada, 2010), the USA (US EPA, 2009), EU (EU, 1998) and WHO water quality guideline (WHO, 2008). The missing values are not included in the standards.

Impurity	MCL Unit	Canada	USA	EU	WHO
Coliform	MPN	<1	<1	<1	<1
HAA	mg/lit	0.08	0.06	0.03	-
Iron	mg/lit	0.3	0.3	0.4	0.2
Manganese	mg/lit	0.05	0.05	-	0.05
Nitrate	mg/lit	45	10	50	50
THM	mg/lit	0.1	0.1	0.2	0.1
Turbidity	NTU	0.1-1	0.5-1	-	-

demand and the average daily water demand is called the peak flow factor and usually decreases with an increase in the population (figure 2.2) (Twort *et al.*, 2000). One of the reasons for a decrease in the peak flow factor with growing population is that larger cities will have more industrial activity and, therefore, a more uniform water consumption regime is expected.

Managing water treatment processes for a large population is non-trivial. The treatment process usually takes several hours to complete. Consequently, treatment plants base their water production rate on the average daily water demand. To handle the difference between constant water production and time-dependant water consumption, water storage tanks are required.

Storage tanks are reservoirs which store water during the night (when the water demand is lower than the average daily demand) and provide the stored water during peak hours. The required volume of storage tanks is then defined as the water volume which should be stored during the night for further day time consumption[7]. The tanks are also responsible for providing sufficient pressure during water transport and consequently, they must be located at higher elevations that the consumption area.

2.2.3. Drinking water distribution networks.

Water transport from the storage tanks to the consumption area and its further distribution to the consumers is done by an integrated network of buried pipes (which usually includes valves and fire hydrants). The reason that the pipes are buried is to protect the pipe from possible accidents, and to keep the water temperature in a certain range (WHO guidelines suggest 15^oC as a desired water temperature in networks (WHO, 2008)).

[7]In addition, a certain volume of water is reserved to be able to deal with massive fire incidents (Ratnayaka *et al.*, 2009).

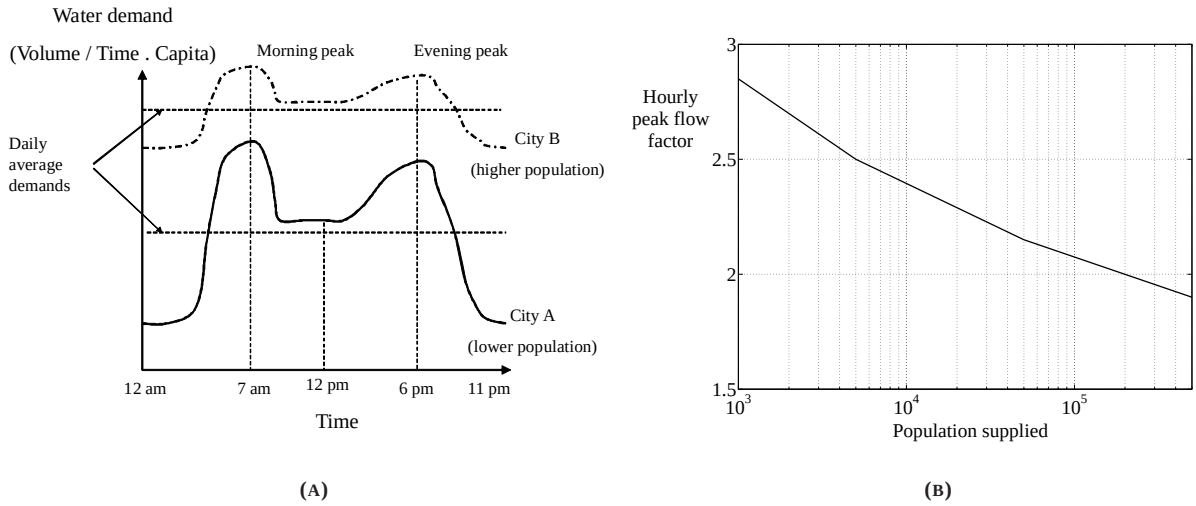

FIGURE 2.2. (A) Hourly water demand for two typical cities, A and B, where city B has a higher population than city A (Swamee & Sharma, 2008). Figure is not to scale. (B) Hourly peak flow factor (Twort *et al.*, 2000).

The layout of a distribution network depends on how consumers are distributed. There are two widely used layouts for networks: branched and looped (figure 2.1). Branched networks are usually implemented for small and decentralized communities, while the looped network is used for centralized communities like a city[8]. Regardless of the layout of the network, various pipes, with different diameters, lengths and materials, are used to transport and deliver the treated water in the network.

Typical pipe materials and their percentage of occurrence in distribution networks in the United Kingdom (UK) and Canada are reported in table 2.2. Each of the materials has its own advantages and disadvantages. For instance, plastic pipes (polyvinyl chloride (PVC) and polyethylene (PE) pipes) are more desirable in terms of reducing pressure drop (as will be discussed later in this chapter). However, manufacturing such pipes in larger diameters is usually more difficult than for metallic and asbestos cement pipes. However, metallic pipes are susceptible to corrosion and asbestos cement pipes are believed to have carcinogenic properties (Ratnayaka *et al.*, 2009). The pipe material also has a significant effect on chlorine depletion due to wall demand, which is discussed in the next section.

[8]The main advantage of a looped network versus a branched one is that in the case of pipe failure, the consumer will have alternative water access routes (Swamee & Sharma, 2008).

The length and diameter of a network pipe depends on its primary duty. Pipes in distribution networks are categorized into three groups: primary mains, secondary mains and distribution pipes. These groups are schematically shown in figure 2.1 and their typical properties are presented in table 2.3.

TABLE 2.2. Percentage of various pipe materials used in drinking water distribution networks in the UK and Canada (Ratnayaka *et al.*, 2009)

Material	Cast iron	Ductile iron	Steel	PE	PVC	Asbestos cement
Percentage in the UK	64	10	4	8	1	13
Percentage in Canada	51	23	0	0	11	15

Primary pipes have the duty of transporting treated water from the water treatment plant to the storage tanks, and then to the consumption area. The length of primary pipes is usually of the order of several kilometres. The minimum diameter of these pipes is recommended to be 350 millimetres (mm) (which may differ slightly between different standards) (Ratnayaka *et al.*, 2009).

Once the treated water is transported to the consumption area, secondary mains deliver water to different districts. The typical length of the secondary mains is of the order of hundreds of metres (m) to a few kilometres, and their standard diameter is 250-300 mm. Distribution pipes are the last stage in the water path from the water resource to the consumer. They serve water demand in streets and alleys. Generally, their length is of the order of tens to hundreds of metres and their standard diameter range is usually 100-200 mm (Ratnayaka *et al.*, 2009).

TABLE 2.3. Typical pipe properties in a drinking water distribution network (Ratnayaka *et al.*, 2009)

Pipe	Diameter	Length	Duty	% in large cities	% in small cities
Primary mains	> 350 mm	Several kilometres	Treatment plant to the city	5	10
Secondary mains	250 – 300 mm	Hundreds of metres to a few kilometres	Water distribution in districts	15	15
Distribution pipes	100 – 200 mm	Tens to hundreds of metres	Delivery of water to households	80	75

2.3. Chlorine wall and bulk demand in networks

The disinfecting property of chlorine comes from the fact that its ions have a high capability to oxidize a large number of other elements. This oxidizing mechanism involves the solution of chlorine in water,

formation of chloridric acid (HCl) and hypochlorite acid ($HOCl$), and reaction between hypochlorite acid and other materials. These steps are introduced in the equations below, where chlorine oxidizes ferrous (Fe^{2+}) to ferric (Fe^{3+}) (Frateur *et al.*, 1999):

$$Cl_2 + H_2O \rightarrow HCl + HOCl$$

$$HCl + HOCl + 2Fe^{2+} \rightarrow 2Fe^{3+} + 2Cl^{-} + H_2O.$$

The same mechanism occurs when chlorine oxidizes constituent materials of a microorganism. Unfortunately, chlorine reacts with a large number of elements, not only microorganisms.

The reaction of chlorine with elements in the bulk of the flow is called bulk demand. NOMs are the main cause for bulk demand, and the most effective way to limit chlorine decay due to bulk demand is to control NOM formation in the network. Indeed, if treatment processes for the removal of solute materials are performed in the treatment plant, the essential materials for the growth of microorganisms in networks are significantly removed and therefore, NOM formation and bulk demand are reduced (Rossman, 2006). Reactants such as metallic ions also cause bulk demand but are less of a problem because they are unlikely to reform in large quantities in the network, unlike NOMs which are continuously formed by biofilms (colonies of microorganisms attached to the pipe surface (Noguera & Morgenroth, 2004)) (Kiéné *et al.*, 1993, 1998; Rossman, 2006).

The reaction of chlorine with the pipe surface is called wall demand, which is mainly caused by corrosion. Consequently, wall demand is higher in metallic pipes (such as cast iron and ductile iron pipes) than in non-metallic pipes (such as PVC and asbestos cement pipes) and therefore, non-metallic pipes are more desirable in terms of chlorine conservation in distribution networks (Frateur *et al.*, 1999; Hallam *et al.*, 2002). Biofilms are also known to cause wall demand, but to a lesser extent (Lu *et al.*, 1999).

The reaction kinetics of chlorine is a complex function of ambient conditions (such as temperature), as well as the concentration of chlorine and other reactants (AWWA, 1996). It is therefore not trivial to define deterministic functions for the effect of each of the affecting parameters on chlorine demand. It is

standard practice to lump the effect of all these parameters into a single reaction rate coefficient called the demand coefficient. Several studies have shown that both wall and bulk reactions for chlorine decay are best captured by first-order reactions in which the rate of chlorine consumption is a first-order function of chlorine concentration (see e.g. Clark & Haught (2005); Mutoti *et al.* (2007)). However, the scatter in the experiments on wall demand is significant and some studies (e.g. Kiéné *et al.* (1998); Jones (2001); Rossman (2006)) indicate that wall demand may be better captured by nonlinear (mostly second-order) wall reactions. A quantitative discussion on the effect of pipe materials and treatment processes on wall and bulk demand is presented in section 2.4.3.

The method by which wall and bulk demand coefficients are measured is briefly introduced here. Bulk demand is usually quantified first. In this case, a volume of water with a known chlorine concentration is left in a non-reactive container for a certain amount of time. From the difference in concentration, a bulk demand coefficient can be inferred. To measure the wall demand coefficient, water is pumped through a pipe at a certain flow velocity. The chlorine concentration at the pipe entrance and exit are measured. By subtracting the contribution of the bulk demand to the chlorine decay, a wall demand coefficient can be calculated. More details can be found in e.g. Mutoti *et al.* (2007).

2.4. Mathematical models for water distribution networks

The main duty of a drinking water distribution network is to provide consumers with drinking water of suitable quantity and quality. Given the complexity of distribution networks, it is crucial to have a good prediction tool to ensure proper network performance.

Network performance indicators will be discussed in section 2.4.1. The indicators discussed include water velocity, pressure and chlorine residual in network pipes[9]. Determination of these indicators requires mathematical modelling of the flow and chlorine transport in networks. Flow and chlorine transport models for distribution networks are introduced in sections 2.4.2 and 2.4.3, respectively. These two sections

[9]Other indicators are also used to evaluate network performance. For instance, water age is an indicator for the time that treated water spends reaching the consumer. However, discussions on such indicators are out of the scope of this study and the reader is referred to water supply textbooks (e.g. Ratnayaka *et al.* (2009)) for more details.

include discussions on the history and evolution of the modelling techniques, the fundamental modelling assumptions and the state-of-the-art in distribution network models.

2.4.1. Main network performance indicators of a distribution network.

Water supply standards indicate that the water velocity in all of the pipes in a network should remain within a certain range, usually from 0.3 metres per second (m / sec) to 1.5 m / sec (Brière, 2007). The lower bound of the velocity is to prevent settling of sediments[10] and the upper bound is to protect pipes from mechanical failure. The velocity range maintains turbulent flow in each of the network pipes[11].

The indicator for determination of the flow regime in a pipe is the Reynolds number (*Re*):

$$Re = \frac{2\rho RU}{\mu} = \frac{2RU}{\nu} \tag{2.1}$$

where R is the pipe radius $[L]$, $U = Q/A_{\mathrm{h}}$ $[LT^{-1}]$ is the crosswise mean velocity (see chapter 3 for more details) in which Q is the mean volumetric flow rate $[L^3T^{-1}]$ and A_{h} is the hydraulic cross-sectional area $[L^2]$ ($= \pi R^2$ for pipes), ρ is the fluid density $[ML^{-3}]$, μ is the dynamic viscosity $[ML^{-1}T^{-1}]$ and $\nu = \mu/\rho$ $[L^2T^{-1}]$ is the kinematic viscosity. The values of ρ, μ and ν for water are shown in figure 2.3 as a function of temperature. It is noted here that $\nu = 10^{-6}$ m^2 / sec is a close approximation for water at 15^{o}C (desired drinking water temperature (WHO, 2008)).

If $Re > 2100$ for pipe flows, the flow is regarded as turbulent and otherwise, the flow is either laminar or in a transition-state (Bird *et al.*, 2002). For the standard water velocity range and pipe diameters introduced in table 2.3, the range of *Re* in a network is typically $10^4 - 10^6$ (Ho, 2008).

The second network indicator, which is again related to the flow, is water pressure, usually expressed in terms of the pressure head $[L]$. The pressure head in each location of the network must fall within a lower and an upper bound. The lower bound (which ensures a minimum water pressure at the consumer's tap

[10] The presence of sediments in the network may have several causes, such as poor treatment, accidents such as pipe burst and release of the pipe surface materials due to corrosion (Ratnayaka *et al.*, 2009).

[11] However, it is sometimes difficult to maintain turbulence in all pipes, for example due to insufficient water demand during the first years of a network's operational life (Merna & Njiru, 2002).

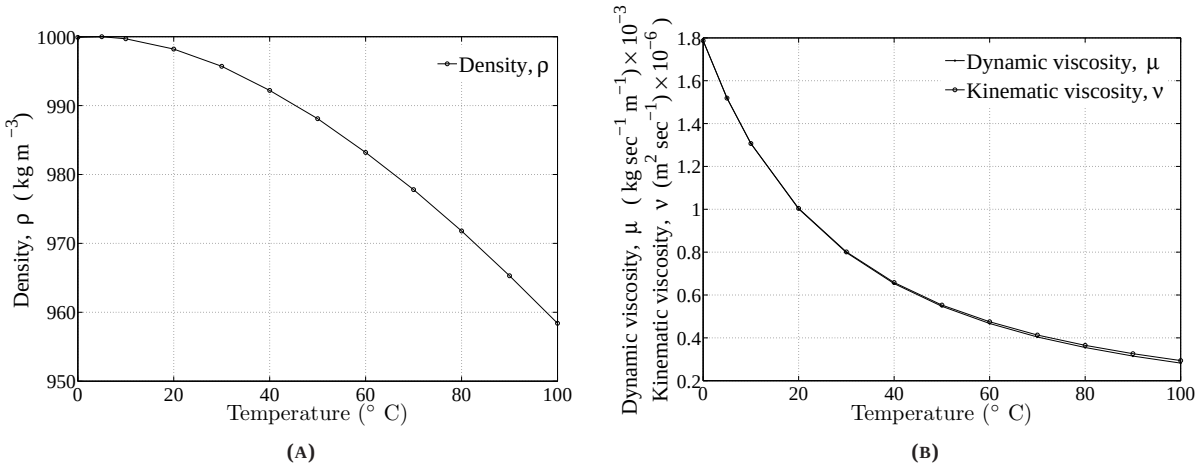

FIGURE 2.3. Water properties as a function of temperature. (A) water density, (B) water dynamic and kinematic viscosity (Crittenden *et al.*, 2005).

during peak water demand) is typically indicated to be 15 m[12]. The upper bound for pressure head (which protects pipes from bursting) is usually 30 m. High pressure heads occur during low water demand, i.e. at night-time (Ratnayaka *et al.*, 2009).

The third network performance indicator is the chlorine residual. The upper and lower bounds for chlorine in water were discussed in section 2.2.1. The maximum chlorine residual in a network occurs immediately after chlorine injection (for example, in a treatment plant or in designated locations in the network) and is therefore, easy to determine. However, due to the size and complexity of the network, the minimum chlorine residual is much harder to control. Chlorine reaction with bulk and pipe wall materials was discussed in section 2.3. It suffices here to remember that if bulk and wall demand are very high, it may cause the chlorine residual to fall below the minimum threshold. This situation (which was schematically shown in figure 1.2) is called the chlorine deficit problem, which may cause critical health problems by increasing the risk of waterborne disease (Lee & Schwab, 2005).

2.4.2. Flow models.

The primary aim of flow models is to determine water velocity and pressure as a function of time in each

[12]This pressure is needed to serve buildings up to three floors. High rise buildings usually need to have their own boosted supply (Twort *et al.*, 2000).

pipe of the network. Because of the large number of pipes in a network, this is a non-trivial task[13]. To keep the flow calculations tractable, the network should be modelled as simply as possible. The simplification with respect to the pipe entrance effect is discussed first. The problem of flow modelling in networks is then introduced using an example. Evolution of the approaches for solving this problem is discussed afterwards.

The first simplification applied in network flow models is to neglect pipe entrance effects. The entrance length, which is the length required to reach fully developed flow, has been studied extensively (see e.g. Schetz & Fuhs (1999)) and the main findings are summarised below.

Figure 2.4 illustrates two pipes which take fluid from a quiescent ambient. The length of the pipe from the inlet to the point where the flow reaches the fully developed velocity profile is referred to as the entrance length L_E [L]. Introducing x as the streamwise direction (with the origin at the pipe inlet), a fully developed flow is reached when the velocity profile no longer changes in the x direction. For the case of laminar and turbulent flows, the entrance length is approximately 220 R and 30 R, respectively[14] (Schetz & Fuhs, 1999). Consequently, the fully developed flow assumption will be appropriate for sufficiently long pipes. As an example, a primary water main with a diameter equal to 350 mm has an entrance length equal to 38.5 m and 5.25 m for laminar and turbulent flows, respectively. This length is negligible in comparison to several kilometres, which is a typical length of such pipes. On the other hand, for a distribution pipe with a diameter equal to 100 mm, $L_E = 1.5$ m -11 m, which can be a considerable fraction of the total pipe length, particularly for short distribution pipes.

By neglecting the entrance length with respect to the pipe length, it is possible to assume a fully developed velocity profile throughout the pipe. Consequently, it is possible to use well-established equations for modelling the pressure drop for fully developed flows in each of the network pipes (as will be shown later in this section). As a result, the flow in a network can be simplified by representing the flow in each network pipe by a volumetric flow rate only. This is demonstrated in the example below.

[13] For instance, the number of pipes in the distribution network of Copenhagen (with an approximate population of 1,200,000) is reported to be approximately 6000 (Babovic *et al.*, 2002).

[14] Determination of L_E for the case of turbulent flows is more challenging than for laminar flows and therefore, L_E for turbulent flows is defined in different ways. The aforementioned value for turbulent flows is reported for the case where the pressure gradient reaches an equilibrium (Schetz & Fuhs, 1999).

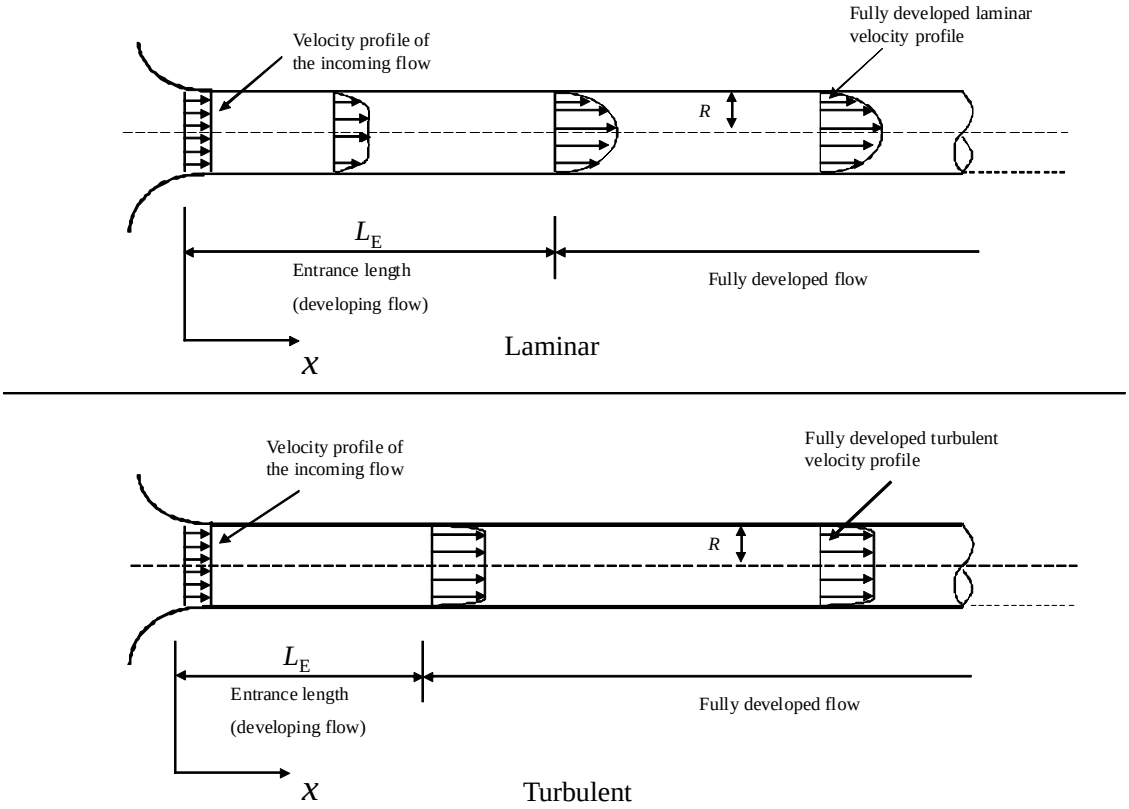

FIGURE 2.4. Entrance length and development of velocity profiles in laminar and turbulent pipe flows (Turbulent profiles represent time averaged values which are discussed in more detail in chapter 3). L_E for turbulent flows is shorter than the counterpart length in laminar flows. Figure is not to scale.

Simple example on flow modelling in a distribution network

Consider a simple network as shown in figure 2.5, comprising two loops, eight pipes with known length (L), diameter and material, one storage tank containing water with a known elevation and seven junctions, which will be referred to as nodes (denoted by **n**). In each of the nodes, there is a known water demand Q_i $[L^3T^{-1}]$, where the subscript i refers to the node index. The water demand Q_i is assumed to be constant for the sake of simplicity. The purpose of flow modelling is to determine water velocity in each pipe and water pressure in each node. The unknowns in this problem then comprise eight velocities in eight pipes and seven

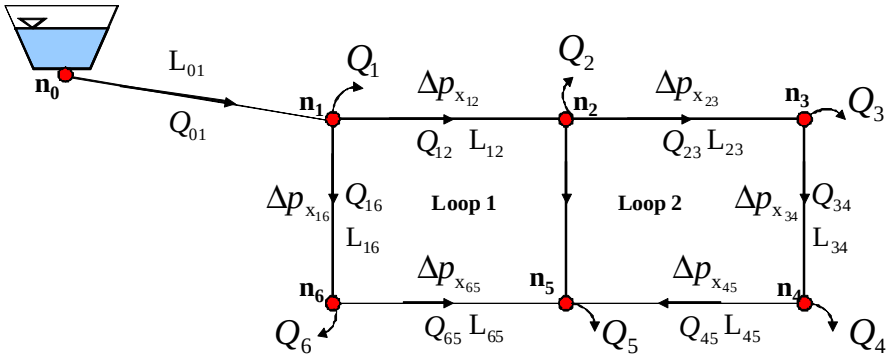

FIGURE 2.5. A typical representative example for modelling flow in looped networks. Figure is not to scale.

values for pressure in seven nodes (15 total unknowns). The same number of equations must exist as well.

Determination of the volumetric flow rate and pressure in the network requires the simultaneous solution of continuity equations for nodes and energy equations for pipes. These equations are briefly discussed here. More discussion is also provided in chapter 3. For the nodes $\mathbf{n}_1$ to $\mathbf{n}_6$, conservation of volume requires that

$$\Sigma Q_{in} = \Sigma Q_{out} \tag{2.2}$$

where the subscripts *in* and *out* represent the flows entering and leaving the node, respectively. Note that the flow rate entering node $\mathbf{n}_0$ is equal to the sum of water demands in the other nodes, which is actually the seventh (global) continuity equation.

The local energy density of the flow is usually expressed in the form of the energy head H $[L]$:

$$H = Z + \frac{\mathrm{P}}{\rho g} + \frac{U^2}{2g} \tag{2.3}$$

where Z is the elevation head $[L]$, P is the pressure $[ML^{-1}T^{-2}]$ and g is the gravitational acceleration $[LT^{-2}]$.

The terms $\mathrm{P}/\rho g$ and $U^2/2g$ are the pressure and velocity head, respectively. An energy balance[15] from the pipe entrance (node $\mathbf{n}_i$) to the pipe exit (node $\mathbf{n}_j$) is then expressed as:

$$H_j = H_i + \Sigma \text{ Head losses.} \tag{2.4}$$

Head losses occur for a variety of reasons. Losses due to valves, pipe bends, contractions and expansions are called minor losses. Losses due to skin friction are referred to as major losses. For simplicity, it is assumed that all pipes are level, straight and of constant diameter. Consequently, only major losses occur. A momentum balance for a pipe of length L_{ij} between nodes $\mathbf{n}_i$ and $\mathbf{n}_j$ results in:

$$\Delta \mathrm{P}_{ij} A_\mathrm{h} = \tau_w \mathrm{L}_{ij} P_\mathrm{h} \tag{2.5}$$

where P_h is the hydraulic perimeter [L] ($2\pi R$ for pipes), τ_w is the wall shear stress [$ML^{-1}T^{-2}$] and $\Delta \mathrm{P}_{ij}$ is the pressure difference between the two nodes [$ML^{-1}T^{-2}$]. Equation 2.5 is usually expressed as:

$$\frac{\Delta \mathrm{P}_{ij}}{\rho g} = f \frac{\mathrm{L}_{ij}}{r_\mathrm{h}} \frac{U_{ij}^2}{2g} \tag{2.6}$$

where

$$f = \frac{2\tau_w}{\rho U^2} \tag{2.7}$$

is the (dimensionless) Fanning friction factor (Bird *et al.*, 2002) and $r_\mathrm{h} = A_\mathrm{h}/P_\mathrm{h}$ is the hydraulic radius [L] (=$R/2$ for pipes). Equation 2.7 relates the wall shear stress to the mean water velocity and therefore, comprises a parameterisation. The Fanning friction factor is a function of *Re* and the pipe surface structure.

[15] Obtained by applying the Bernoulli equation along a streamline and taking into account energy losses (Bird *et al.*, 2002).

Details about the Fanning friction factor are discussed in section 2.5.1.

In the context of the example, equation 2.6 provides eight additional equations[16], thereby creating the same number of equations as unknowns. Equation 2.6 is nonlinear and therefore, iterative solution methods are required to solve the system of equations. Several methods have been developed over the last century, the evolution of which is schematically shown in figure 2.6 and is discussed below.

Evolution of solution methods for flow modelling

The first method for solving a system of nonlinear equations with a network structure originates from structural engineering. Hardy Cross was a structural engineer who developed a novel iterative method for solving moment distribution in frames of a structure in 1932 (Volokh, 2002). Later in 1936, he discovered that there is an analogy between the moment distribution in a structure and the pressure distribution in a looped drinking water distribution network. Consequently, he adapted his method to the determination of pressure and velocity in networks (Cross, 1936). The Hardy Cross method is an iterative algorithm which exploits the fact that the sum of the pressure drops in each loop in the network is zero. This method includes the following steps (Swamee & Sharma, 2008):

(1) Make an initial guess for U for each pipe;
(2) Select the first loop of the network;
(3) Determine pressure drops in the loop (equation 2.6);
(4) Modify the velocities of each of the pipes in the loop so that the net pressure drop becomes zero;
(5) Proceed to the next loop using steps 3 and 4 until all the loops in the network are processed;
(6) Repeat steps 2 to 5 until all the velocities in two sequential iterations are converged.

The main advantage of the Hardy Cross algorithm is that it calculates the flow rate and pressure drop separately. In the early years, the algorithm was used in hand calculations, but it was implemented in computer programs in the 1960s (Liu, 1969). Although the convergence of the method is very slow, it was widely used for 40 years. However, the Hardy Cross method was superseded in the 1980s by more advanced

[16] Since equation 2.6 determines the pressure drops (rather that the absolute pressure), a reference pressure is needed. This reference pressure is usually taken to be the hydrostatic pressure in node $\mathbf{n}_0$ (the storage tank).

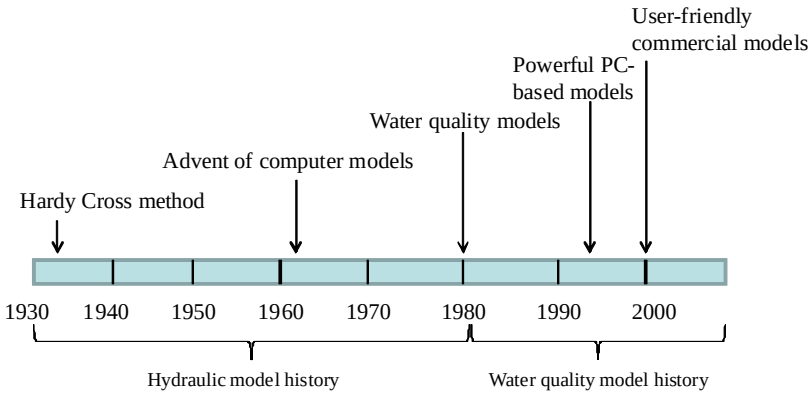

FIGURE 2.6. History of modelling in drinking water distribution networks (Panguluri *et al.*, 2005).

algorithms once personal computers (PCs) became sufficiently powerful to provide direct simultaneous solutions for pressure and velocity (Panguluri *et al.*, 2005; Wood & Rayes, 1981). These algorithms typically linearize the quadratic relationship between the pressure drop and velocity, which allows for the simultaneous solution of pressure and velocity using standard matrix inversion methods. The updated velocities are then used for a new linearization of pressure drop, and this procedure is repeated until the solution is converged.

The main limitation of the Hardy Cross method and later developments in the 1980s was that they were only applicable to steady-state conditions, i.e. they could not handle time-dependent water demand. As typical variations of the water demand in a network will have a timescale from the order of an hour[17] (see figure 2.2), the methods must be modified to consider temporal variations in the water demand. This issue was first considered in the mid 1980s and led to the development of the dynamic demand modelling concept (Grayman *et al.*, 1988).

In a dynamic demand model, the diurnal graph (figure 2.2) is divided into several segments, as shown in figure 2.7. The number of the segments depends on the water demand gradient in each time interval and the more segments are defined, the more accurate the solution will become. In each segment the demand is considered to be steady. This approach is widely used to solve for dynamic demands in distribution networks (Panguluri *et al.*, 2005).

[17] Other variations in a network which are important with respect to modelling are variations in water temperature and initial water quality. However, the timescales for these variations are from the order of several months to several years (DiBona *et al.*, 1992; Bedient *et al.*, 1999).

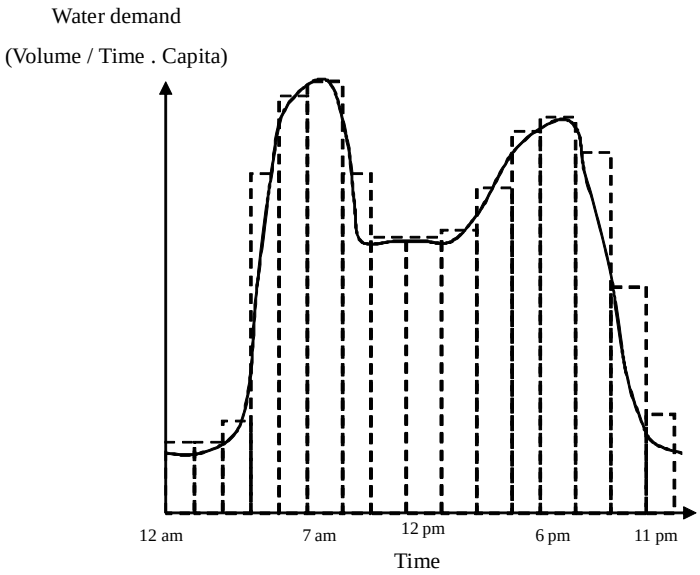

FIGURE 2.7. Dynamic demand modelling relies on dividing the time-dependant demand curve into steady-state segments (Panguluri *et al.*, 2005).

2.4.3. Chlorine residual modelling.

The development of chlorine transport and decay models started after the Safe Drinking Water Act (SDWA) was approved in the US Congress in 1974 (Panguluri *et al.*, 2005). This act allowed the US EPA to establish regulations and methods for controlling and monitoring drinking water quality. The first model for predicting the transport of solute compounds in networks was presented in 1980 (Wood, 1980). The model was able to predict the steady-state concentration of a non-reactive (conservative) solute material in distribution networks. In 1985, the model was upgraded to handle dynamic water demand conditions (figure 2.7) (Clark *et al.*, 1986). However, the main problem with the model was that it was not able to consider depletion of solute compounds due to wall and bulk reactions.

Several waterborne disease outbreaks due to chlorine depletion in networks occurred during the 1980s, which accelerated improvements in modelling of the chlorine decay problem[18] (Hrudey *et al.*, 2003). These

[18]Some of these major waterborne disease outbreaks were in Bramham, England (1980, with 3000 cases of illness) and Pittsfield MA, USA (1985, with 3800 cases of illness) (Hrudey *et al.*, 2003).

improvements were presented in the Water Quality Modelling in Distribution Systems Conference in 1991, where the US EPA and the American Water Works Association (AWWA) Research Foundation brought together researchers from the world for a two-day meeting in Cincinnati, USA (AWWA & US EPA, 1991). This meeting was a milestone in the establishment of chlorine decay modelling as a recognized tool for water quality prediction (Walski *et al.*, 2003).

In 1993, water quality modelling came of age with the development of EPANET by the US EPA (Rossman, 2000). EPANET was the first well-established model with a physical-based methodology for modelling chlorine decay in drinking water distribution networks. EPANET provided the basis for several commercial models, such as WaterGEMS and InfoWater, which are more user-friendly than EPANET (Walski *et al.*, 2003).

EPANET is an open source computer program that models dynamic water demand and decay of a single solute material (such as chlorine) in distribution networks[19]. It is able to consider the performance of valves, pumps and multiple storage tanks. In addition to the determination of velocities and pressures in different points of the network, EPANET is able to determine water age (the time that water spends in the network) and the transport of reactive solute mass (like chlorine). Therefore, it is widely used as a design and research tool to improve understanding of the movement and fate of drinking water constituents in a network (Walski *et al.*, 2003; Rossman, 2000).

Calculations of chlorine transport and decay in EPANET consist of the following steps:

- Provide the network structure, water demands, storage tanks, pipes materials and sizes and the surface topology as input parameters;
- Calculate the flow in the network using the dynamic demand approach;
- Calculate transport and decay of chlorine in the network based on the flow calculations.

As with flow modelling, some key assumptions are made to model chlorine transport in the network. It is assumed that the time that water spends in a network junction is negligible in comparison with the time that water spends in network pipes. Consequently, the effect of wall and bulk reactions in the junctions on

[19] Due to the recent awareness on carcinogenic effects of DBPs, a multi species modelling extension to the EPANET is under development by the US EPA to incorporate simultaneous modelling of chlorine decay and DBP formation (Shang *et al.*, 2008).

chlorine concentration can be neglected. Furthermore, it is assumed that full mixing occurs in the junctions and therefore, the concentration of a species in flows leaving a junction is the volumetric average of the concentrations in flows entering the junction[20]:

$$c_{\mathrm{x}_{out}} = \frac{\Sigma Q_{in} c_{\mathrm{x}_{in}}}{\Sigma Q_{in}} \tag{2.8}$$

where c_{x} represents the crosswise mean concentration of the solute mass (see chapter 5 for more details). These two assumptions allow chlorine transport and decay in the entire network to be modelled as the mass transport in a large number of individual pipes.

Consider a small pipe segment with a length δ_{L} $[L]$ which moves along with the mean velocity U as sketched in figure 2.8. EPANET-based models assume that, except in a very thin layer adjacent to the pipe wall, the concentration throughout the cross-section is equal to c_{x} (due to turbulent mixing). The chlorine is consumed by reactions in the bulk of the fluid with a (crosswise mean) reaction rate $\dot{\mathrm{R}}$ $[ML^{-3}T^{-1}]$ and by reactions with the wall which cause a wall mass flux J_w $[ML^{-2}T^{-1}]$. As the segment moves at velocity U, it is assumed that there is no exchange of mass with the adjacent fluid. Mass conservation for the chlorine residual results in:

$$\frac{d}{dt}\left(A_{\mathrm{h}} \delta_{\mathrm{L}} c_{\mathrm{x}}\right) = -\dot{\mathrm{R}} A_{\mathrm{h}} \delta_{\mathrm{L}} - J_w P_{\mathrm{h}} \delta_{\mathrm{L}}. \tag{2.9}$$

As with flow modelling (where f was used to relate the wall shear stress to the mean velocity), a mass transfer coefficient $\mathrm{k_f}$ $[LT^{-1}]$ is used in EPANET-based models to relate the wall mass flux to the mean concentration (Rossman, 2000):

$$J_w = \mathrm{k_f}\left(c_{\mathrm{x}} - c_w\right) \tag{2.10}$$

[20] In a typical network, two types of junctions can be distinguished: T and cross junctions, which account for 20% and 80% of the total, respectively (Ho, 2008). Recent studies of van Bloemen Waanders *et al.* (2005), Romero-Gomez *et al.* (2006) and Ho (2008) have shown that the assumption of full mixing is not always valid for cross junctions.

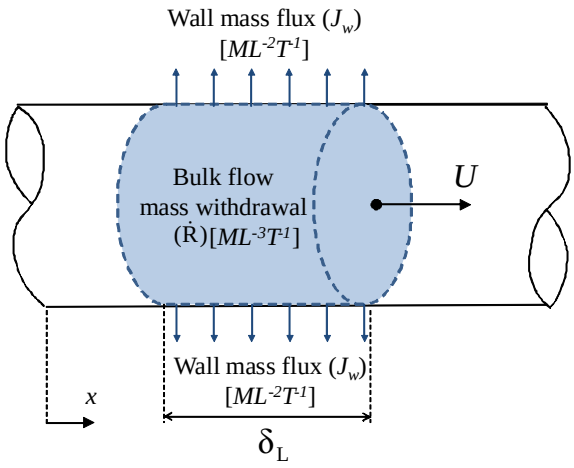

FIGURE 2.8. Chlorine mass conservation for an infinitesimal pipe segment moving along with the mean flow velocity U.

where c_w is the concentration at the wall, which may differ from c_x.

Similar to f, k_f must be parameterised to model solute mass decay. The parameterisation is presented in section 2.5.2. However, it suffices here to say that k_f is a function of *Re* and the molecular properties of chlorine and water. Substituting equation 2.10 into 2.9 and dividing by $\delta_L A_h$ results in:

$$\frac{dc_x}{dt} = -\dot{R} - \frac{J_w}{r_h} = -\dot{R} - \frac{k_f (c_x - c_w)}{r_h}. \tag{2.11}$$

As discussed in section 2.3, wall and bulk reactions for chlorine decay are best captured by first-order reactions:

$$J_w = k_w c_w \tag{2.12}$$

$$\dot{R} = k_b c_x \tag{2.13}$$

where k_w $[LT^{-1}]$ and k_b $[T^{-1}]$ are the wall and bulk demand coefficients, respectively. As discussed in the previous section, the former depends on the pipe wall material while the latter is a function of the concentration of bulk solute materials (such as NOMs). Tables 2.4 and 2.5 give typical values for these coefficients in a network. Metallic pipes have a higher k_w than non-metallic pipes. Furthermore, water which has not received treatment processes for removal of solute materials (section 2.2.1) has a higher k_b.

Combining equations 2.10 and 2.12 gives

$$c_w = \frac{k_f c_x}{k_w + k_f}. \tag{2.14}$$

Substituting the equation above into equation 2.11 results in

$$\frac{dc_x}{dt} = -\underbrace{\left(k_b + \frac{k_w k_f}{r_h (k_w + k_f)}\right)}_{k_t} c_x \tag{2.15}$$

with solution

$$c_x = c_0 e^{-k_t t} \tag{2.16}$$

where c_0 is the crosswise mean concentration at the pipe entrance ($x = 0$), k_t is the chlorine decay rate $[T^{-1}]$ and $e \approx 2.71$ is the Euler (also known as Napier) number. Given that the pipe segment in figure 2.8 moves at velocity U and therefore has a position $x = Ut$, we obtain

$$c_x = c_0 e^{-kx} \tag{2.17}$$

where the decay coefficient k $[L^{-1}]$ is given by (Rossman, 2000)

TABLE 2.4. Reported average values for k_w based on the (new) pipe material (Rossman, 2006).

Pipe material	Cast iron	Ductile iron	PVC	Asbestos cement
k_w (m / sec) $\times 10^5$	0.05 - 1.92	0.12-0.18	≈ 0	≈ 0

TABLE 2.5. Reported average values for k_b based on the treatment method applied (Rossman, 2006).

Solute removal process	Not applied	Ozone	Activated carbon	Reverse osmosis
k_b $(1/\text{sec}) \times 10^7$	10.11	5.58	0.52	0.81

$$k = \frac{1}{U}\left(k_b + \frac{k_w k_f}{r_h\,(k_w + k_f)}\right). \tag{2.18}$$

Equation 2.17 is an important result because it links the concentration at the pipe entrance to the concentration at the pipe exit[21]. In terms of the example (figure 2.5), if the concentration at $\mathbf{n}_0$ is known, the concentration at $\mathbf{n}_1$ can be calculated and so on.

2.5. Parameterisation of wall flux

It was discussed in the previous section that the Fanning friction factor f and the mass transfer coefficient k_f relate the wall fluxes of momentum and mass to the mean velocity and concentration. When f and k_f are known, it is then possible to solve equations 2.6 and 2.17 for all the pipes of the network and therefore, it becomes possible to determine the main network performance indicators (velocity, pressure and chlorine residual). The parameterisation of f and k_f depends on whether the pipe wall surface is hydraulically smooth or rough. The difference between these two surface types is discussed below, prior to the actual parameterisations for f and k_f.

A schematic showing for smooth and rough surfaces is presented in figure 2.9. Pipe surface roughness is a consequence of the presence of protrusions on the pipe surface. Pipe roughness can have several causes such as encrustation and tuberculation of corrosion products in metallic pipes (see e.g. Zhang *et al.* (2008); Sarin *et al.* (2004)) or the formation of biofilms in non-metallic pipes (and also in metallic pipes). Pipe

[21] Note that models such as EPANET use a Lagrangian method and, therefore, use equation 2.16, which allows for time-dependant demands. See Rossman (2000) for more information.

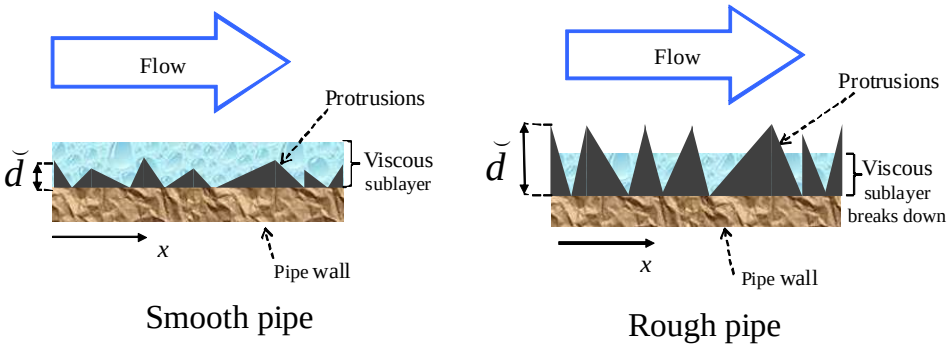

FIGURE 2.9. A Schematic of hydraulically smooth (left) and rough (right) surfaces. The former has protrusions with the averaged height $\breve{d}$ smaller than the thickness of the viscous sublayer while $\breve{d}$ in the latter is larger than this thickness. Figure is not to scale.

roughness in networks is an important (and undesirable) phenomenon since it can cause an extra pressure drop and host colonies of microorganisms (DiBona *et al.*, 1992).

Rough and smooth surfaces can be distinguished by comparing the averaged height of pipe surface protrusions (shown with $\breve{d}$ in figure 2.9) to the thickness of the viscous sublayer. This sublayer is a layer immediately adjacent to the wall in which turbulent momentum transport is negligible in comparison with viscous transport (see chapter 3 for more details). The thickness of the viscous sublayer is $5\delta_v$, where

$$\delta_v = \frac{\nu}{u_\tau} \tag{2.19}$$

is the viscous length scale $[L]$ and

$$u_\tau = \sqrt{\frac{\tau_w}{\rho}} \tag{2.20}$$

is the friction velocity $[LT^{-1}]$ (see chapter 3 for more details). In the case that $\breve{d}$ is smaller than the thickness of the viscous sublayer ($\breve{d} < 5\delta_v$), the surface is regarded as hydraulically smooth (figure 2.9 (left)). For the case of $\breve{d} > 70\delta_v$, the viscous sublayer breaks down and therefore, the surface is hydraulically rough (figure

2.9 (right)) (Kays *et al.*, 2005). A transition-state also exists between the two cases (Kays *et al.*, 2005).

Discussion in section 2.5.1 is associated with the parameterisation of f for both smooth and rough surfaces. In sections 2.5.2 and 2.5.3, parameterisations of k_f are presented for smooth and rough surfaces, respectively.

2.5.1. Parameterisation of f.

In order to determine empirical correlations for f, laboratory experiments were carried out for different flow rates passing through pipes (Bird *et al.*, 2002). In this case, f is defined by measuring the pressure drop between the two ends of the pipe and the volumetric flow rate Q, using equation 2.6. Reported parameterisations for f in smooth pipes are discussed below.

For laminar flows, the dependence of f on Re can be determined analytically (see e,g, Bird *et al.* (2002)), with the result $f = 16/Re$. For turbulent flows, several correlations exist, each valid for a specific range of Re. The first explicit correlation for f was the Blasius formula (Bird *et al.*, 2002):

$$f = \frac{0.0791}{Re^{1/4}}, \quad 2.1 \times 10^3 < Re < 10^5. \tag{2.21}$$

The correlation in equation 2.21 was then modified for higher Re by Prandtl (1932), which resulted in the following implicit correlation for f:

$$\frac{1}{\sqrt{f}} = 4\log Re\sqrt{f} - 4.0, \quad 2.3 \times 10^3 < Re < 4 \times 10^6. \tag{2.22}$$

The next advancement in the parameterisation of f was with respect to rough pipes. The pressure drop in rough pipes has been studied since the 1930s. Several experiments were carried out by Nikuradse (1950)[22] to classify the surface roughness. He introduced the concept of roughness height $\breve{d}$ $[L]$, which is the average height of the pipe surface protrusions (see figure 2.9). In his studies, different pipe materials

[22] The original study by Nikuradse was done in 1933 and reported in German. In 1950, results were also reported in English, which are widely used in the literature.

with different relative roughness ($\check{d}/2R$) were selected. By measuring the pressure drop and volumetric flow rate at the two pipe ends, it became possible to present experimental data on the relationship between the relative roughness, flow rate and pressure drop.

Colebrook & White (1937) and Colebrook (1939) combined results of the pressure drop for rough and smooth walls into one implicit interpolation formula[23]. This formula was then plotted by Moody (1944) which is shown in figure 2.10 and is known as the Moody diagram[24]. The Moody diagram illustrates the relationship between *Re*, relative roughness and the Fanning friction factor. It is seen that pipe roughness increases f, which eventually leads to a higher pressure drop in rough pipes. In addition, the friction factor becomes constant for each $\check{d}/2R$ at sufficiently high *Re*. In this case, the flow is called fully rough which indicates that the pressure drop is independent of *Re*.

Several researchers have developed empirical correlations for f in rough pipes which are not implicit and are therefore easier to calculate. Each of the correlations is tuned to specific ranges of *Re* and relative roughness. Two of these correlations are introduced here. Haaland (1983) suggested

$$\frac{1}{\sqrt{f}} = -3.6\log\left[\frac{6.9}{Re} + \left(\frac{\check{d}/2R}{3.7}\right)^{10/9}\right], \quad 4\times10^4 < Re < 10^8 \tag{2.23}$$

and Swamee & Jain (1976) proposed

$$f = \frac{0.0625}{\left[\log\left(\frac{\check{d}}{7.4R} + \frac{5.74}{Re^{0.9}}\right)\right]^2}, \quad 2.5\times10^4 < Re < 10^5. \tag{2.24}$$

Equation 2.24 is the default correlation used in EPANET.

[23] This work was carried out in the hydrodynamics laboratory at Imperial College (Department of Civil Engineering).

[24] Note that f can also represent the Darcy-Weissbach friction factor, which is defined as $8\tau_w/\rho U^2$, and is therefore a factor of four higher than the Fanning friction factor defined in equation 2.7. The two friction factors can be distinguished in the Moody diagram by the laminar behaviour, which is $16/Re$ and $64/Re$ for the Fanning and Darcy-Weissbach friction factors, respectively (Bird *et al.*, 2002; Rossman, 2000).

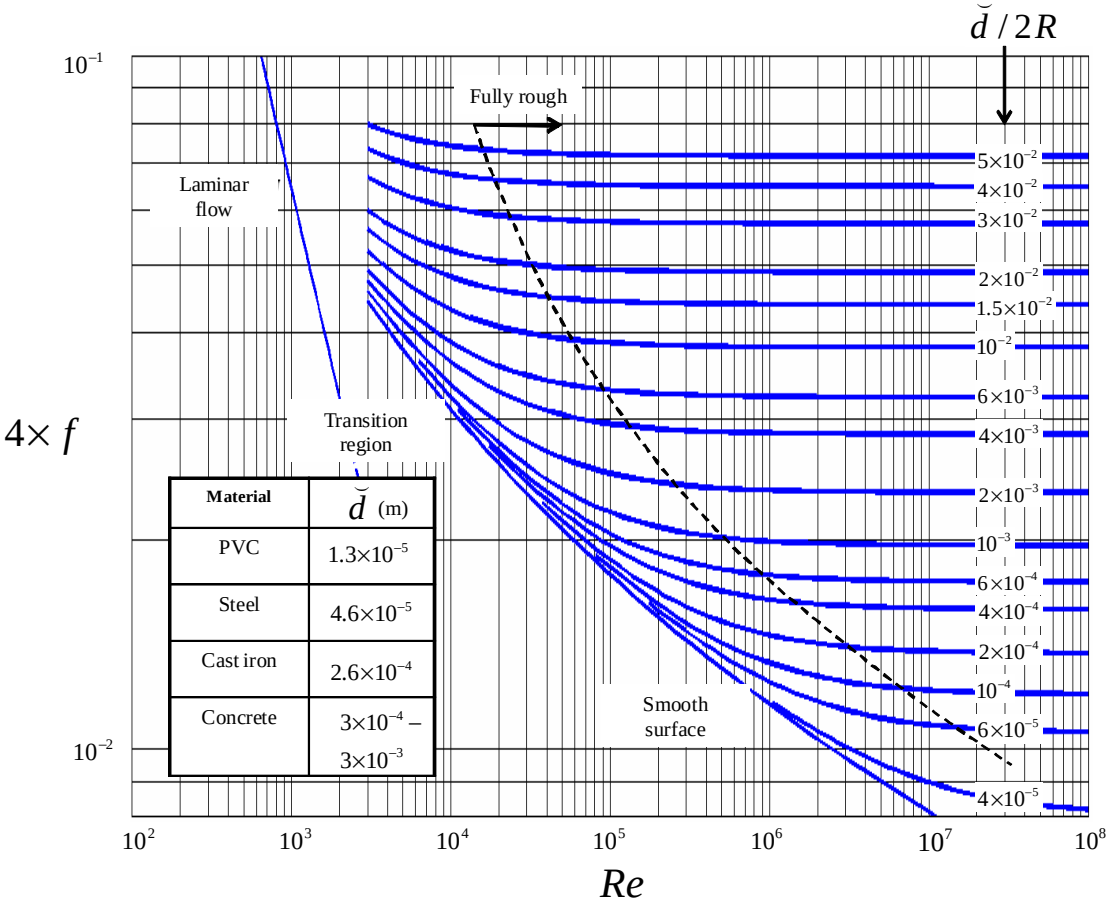

FIGURE 2.10. Moody diagram shows $4\times f$ as a function of *Re* and relative roughness ($\breve{d}/2R$) (Moody, 1944). The data for $\breve{d}$ are adopted from Huguenin & Colt (2002).

2.5.2. Parameterisation of k_f for smooth pipes.

As for the case of the friction factor, parameterisations must also be provided for k_f so that the wall demand can be modelled. This section discusses parameterisations of k_f for smooth surfaces; rough surface parameterisations will be discussed in the next section.

Correlations for k_f in smooth pipes are usually presented in terms of the dimensionless Sherwood number (*Sh*):

$$Sh = \frac{2R\mathrm{k_f}}{D} \tag{2.25}$$

in which D is the molecular diffusion. The value of D for the solution of chlorine in water as a function of temperature is shown in figure 2.11. The Sherwood number can be interpreted as the ratio of the realised wall mass flux to a purely diffusive mass flux[25]. In general, *Sh* for smooth pipes can be expected to depend on the molecular properties of the fluid and solute, the pipe diameter and velocity. In dimensionless form:

$$Sh = Sh\left(Sc, Re\right). \tag{2.26}$$

Here, the Schmidt number *Sc* represents the ratio of kinematic viscosity (of the fluid) to the molecular diffusion coefficient (Bird *et al.*, 2002):

$$Sc = \frac{\nu}{D}. \tag{2.27}$$

There are three methods for the determination of *Sh* correlations: 1) laboratory experiments; 2) analytical solutions to the mass transport equations; and 3) numerical simulations. Laboratory experiments and analytical solutions have been used extensively in the past. Numerical simulations have received much less attention and form the focus of this thesis. The three methods are discussed below.

Experimental correlations for *Sh* (and therefore $\mathrm{k_f}$) require measurements of c_w, c_x and J_w (equation 2.10). The first correlation for smooth pipes was obtained by using a method which dissolved materials in turbulent flows (Linton & Sherwood, 1950). The method used a soluble compound on the pipe wall (usually benzoic acid) and a fluid (usually glycerine water) which dissolves this compound (Harriott & Hamilton, 1965). It is assumed that very close to the pipe wall, c_w is approximately equal to the saturated concentration. In addition, c_x is determined by measuring the concentration of the soluble material in the flow. J_w can be

[25] A detailed discussion on the physical representation of *Sh* is also provided in chapter 7.

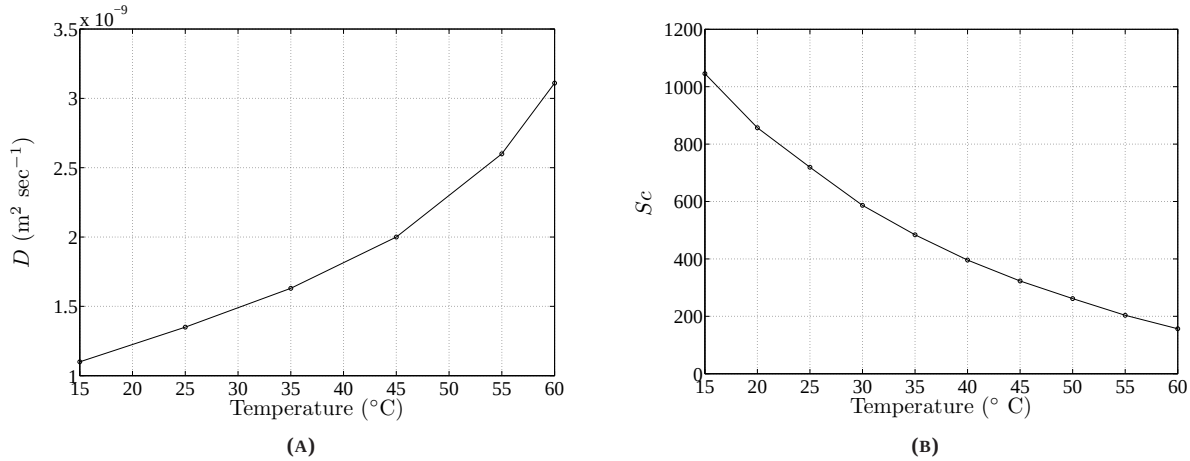

FIGURE 2.11. Molecular properties for the solution of chlorine in water as a function of temperature. (A) molecular diffusion coefficient for the solution of chlorine in water, (B) *Sc* for the solution of chlorine in water (Crittenden *et al.*, 2005).

determined by measuring the weight of the pipe before and after the experiment. The values for c_w, c_x and J_w are then used in equation 2.10 to determine a value for k_f. By determining k_f for different *Re* and *Sc* (changing the latter is done by changing the temperature), a correlation for *Sh* is then obtained. Using this method, Harriott & Hamilton (1965) obtained (see also table 2.6):

$$Sh = 0.009 Re^{0.913} Sc^{0.346}. \tag{2.28}$$

Advances in experimental methods in the late 1960s replaced the dissolving method with a more elegant and accurate electrochemical method. This method used a fluid containing positive ferric ions (Fe^{3+}) and negative cyanide ions (CN^-) (figure 2.12) (Zhao & Trass, 1997). When the (metallic) pipe surface is subjected to a positive potential, the cyanide ions start to travel to the wall and release electrons when they make contact with the wall surface. Once released, electrons create an electrical current which is measureable (via an electrometer). Using the molecular weight of cyanide and the number of electrons released per ion, it is possible to translate the measured electrical current to the mass absorption rate on the surface. If the positive

TABLE 2.6. *Sh* correlations for smooth pipes. "Dis.", "Elec." and "Analyt." represent dissolving, electrochemical and analytical method, respectively.

Study	Method	Range of *Re*	Range of *Sc*	*Sh* correlation
Harriott & Hamilton (1965)	Dis.	$10^4 - 10^6$	$430 - 10^5$	$0.009Re^{0.913}Sc^{0.346}$
Mizushina *et al.* (1971)	Elec.	$3\times10^3 - 8\times10^5$	$800 - 1.5\times10^3$	$0.019Re^{0.90}Sc^{0.33}$
Dawson & Trass (1972)	Elec.	$3\times10^3 - 1.2\times10^5$	$400 - 4600$	$0.0153Re^{0.88}Sc^{0.32}$
Berger & Hau (1977)	Elec.	$8\times10^3 - 2\times10^5$	$10^3 - 6\times10^3$	$0.0165Re^{0.86}Sc^{0.33}$
Zhao & Trass (1997)	Elec.	$4\times10^3 - 2\times10^5$	$550 - 4720$	$0.013Re^{0.88}Sc^{0.32}$
Notter & Sleicher (1971)	Analyt.	$10^4 - 10^6$	$10^2 - 10^4$	$0.0149Re^{0.88}Sc^{0.33}$
Aravinth (2000)	Analyt.	$2.1\times10^3 - 10^5$	$10^2 - 10^5$	$0.0149Re^{0.88}Sc^{0.33}$

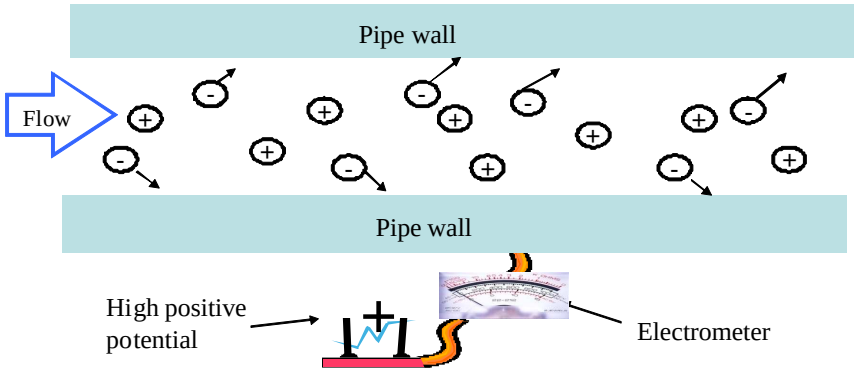

FIGURE 2.12. Schematic of the electrochemical method which comprises passing ions from an electrically charged pipe and measuring the electrical current produced at the pipe surface due to the adsorption of ions with an opposite electrical charge (Zhao & Trass, 1997). Figure is not to scale.

potential is sufficiently large[26], it can be assumed that $c_w \approx 0$ and therefore, $k_f = J_w/c_x$. Consequently, it will be possible to obtain *Sh* correlations based on the measurements (Zhao & Trass, 1997). Several experimental correlations for *Sh* by the electrochemical method are reported in table 2.6. These correlations have roughly the same exponents for *Re* and *Sc* but a prefactor nearly a factor of two larger than for the dissolving method.

Analytical methods have also been used for the determination of *Sh* correlations in turbulent pipe flows with smooth walls. A discussion of these methods requires a discussion of mass transport in turbulent flows, which is presented in chapter 3. Analytical methods are also discussed in chapters 5 and 7. It suffices here to say that these methods are based on the method of separation of variables (Kreyszig, 2006). One of the main

[26]This is easily recognized because the mass flux at the wall becomes independent of the potential (Zhao & Trass, 1997).

analytical correlations for *Sh* was proposed by Notter & Sleicher (1971). As for the experimental studies, Notter & Sleicher (1971) used the boundary condition $c_w = \text{constant}$. Based on the analytical solution, they proposed the following *Sh* correlation for $100 < Sc < 10^4$ and $10^4 < Re < 10^6$:

$$Sh = 0.0149 Re^{0.88} Sc^{0.33}. \tag{2.29}$$

As this correlation directly follows from the governing equations, it is completely reliable provided that all assumptions hold (see chapter 5 for more details). Equation 2.29 is also consistent with the most recent experimental studies (table 2.6) and is used in EPANET-based models to determine k_f in equation 2.10 in smooth pipes.

The third method to obtain parameterisations for k_f is by numerical simulation. This method is extensively used in this thesis. Simulation of turbulent flows can be pursued with different levels of complexity. The method which resolves all the turbulent fluctuations of velocity, pressure and concentration is called direct numerical simulation (DNS) and is, therefore, the most reliable numerical method to simulate fluid flow and mass transport problems (Pope, 2000). However, simulating all the temporal and spatial scales of the turbulence is a very expensive task in terms of computational calculation (see chapter 3 for more details). For the case of flow, the grid requirements are proportional to $Re^{9/4}$ and for the case of high *Sc* mass transport (as will be characterised in chapter 5), it is proportional to $Re^{9/4} Sc^{3/2}$ (Schwertfirm & Manhart, 2010). Consequently, application of DNS is still restricted to low *Re* and *Sc*.

The current state-of-the-art of the DNS for parameterisation of k_f is restricted[27] to $Re < 6000$ and $Sc < 50$ (Schwertfirm & Manhart, 2007). As an example of *Sh* correlations by the DNS approach, two correlations by Na *et al.* (1999) and Schwertfirm & Manhart (2007) are reported in table 2.7 [28].

[27] DNS data reported in table 2.7 are categorised as Eulerian DNS which is the most accurate numerical approach. However, a Lagrangian approach has also been used for parameterisation of k_f. This method includes statistical tracing of a number of solute mass markers and therefore, it provides less detailed physical insight than Eulerian DNS. However, the method is applicable for higher *Sc* (see e.g. Papavassiliou & Hanratty (1997) for Lagrangian DNS of compounds with *Sc* up to 2400). Nevertheless, data obtained by this method is less credible in a theoretical background than the Eulerian DNS (Schwertfirm & Manhart, 2007).

[28] The original DNS studies report the mass transfer coefficient in plus units (i.e. the mass transfer coefficient divided by the friction velocity). Here, the Blasius formula (equation 2.21) is used to derive *Sh* correlations based on *Re*.

TABLE 2.7. Numerical *Sh* correlations for smooth pipes.

Study	Method	*Re*	Maximum *Sc*	*Sh* correlation
Na *et al.* (1999)	DNS	5250	10	$0.0102Re^{0.875}Sc^{0.454}$
Schwertfirm & Manhart (2007)	DNS	5250	49	$0.0174Re^{0.875}Sc^{0.29}$
Hickel & Adam (2007)	LES	5250	400	$0.013Re^{0.875}Sc^{0.33}$

The highest *Sc* attainable with DNS studies is still far below $Sc \approx 1000$ for chlorine (figure 2.11) at 15^o C (the desired drinking water temperature (WHO, 2008)). In order to extend studies to higher *Sc*, other numerical schemes have also been used to determine *Sh* correlations for smooth pipes. In contrast with DNS, which resolves all the temporal fluctuations due to the turbulence conditions, other methods are mostly based on partial or total averaging of the turbulence effects in time and space and, therefore, several assumptions are involved in their simulation method (see chapter 3). In general, these methods are categorised into large eddy simulation (LES) and Reynolds averaged Navier Stokes (RANS) approaches. The latter is the focus of this thesis and will be discussed in detail in chapter 3. One of the most recent *Sh* correlations by LES is reported by Hickel & Adam (2007):

$$Sh = 0.013Re^{0.875}Sc^{0.33} \tag{2.30}$$

for compounds with $Sc < 400$. It is seen that this correlation is much closer to the correlation by Notter & Sleicher (1971) than DNS correlations for lower *Sc*. It should be emphasized that all *Sh* correlations presented in this section were obtained for boundary conditions in which the wall concentration of the solute material (c_w) remained constant. In the case of chlorine wall demand however, c_w will not remain constant (see equation 2.14).

2.5.3. Parameterisation of k_f in rough pipes.

It was stated in the previous section that parameterisation of the wall demand in turbulent flows by numerical methods is non-trivial. Application of such methods in turbulent flows over rough pipes is much harder since the effect of the surface structure must also be considered. Due to the complexity of flow and mass transport simulation over rough surfaces, DNS and LES of mass transport over such surfaces is even more restricted than for smooth surfaces. For instance, reported parameterisations include compounds with $Sc < 1$

(see e.g. Nagano *et al.* (2004)). The complexity of the surface also prohibits application of solutions for fully developed flow to derive analytical *Sh* correlations (Suga, 2007). Consequently, the effect of surface roughness on the parameterisation of wall demand is usually obtained experimentally.

The natural (and therefore irregular) roughness pattern used for parameterisation of f cannot be used for electrochemical experiments. As stated before, electrochemical experiments need a surface with high electrical conductivity. Some of the materials used in pipes with natural roughness (e.g. asbestos cement, PVC and PE pipes) are not electrically conductive. Even the rough surface in metallic pipes is not conductive enough because the corroded pipe materials (which are the source of roughness) are not highly conductive (Sarin *et al.*, 2004). Consequently, the study of mass transfer over rough surfaces by electrochemical experiments requires artificially roughened surfaces (Lolja, 2005).

The artificial roughness pattern used in electrochemical experiments is schematically shown in figure 2.13. For this pattern, the roughness elements (crests) are perpendicular to the streamwise direction. This pattern is further categorized into three major groups; d-type, intermediate and k-type. In the d-type pattern, the width of cavities (void spaces between the crests) is equal or less than the crests. For the k-type roughness, the cavities are three times wider than the crests. The intermediate roughness pattern covers the remaining cases not covered by the d-type and k-type roughness patterns (Leonardi *et al.*, 2007). In all of the cases, λ is the length of one period of the roughness pattern, d is the depth and w is the width of the cavity.

Electrochemical experiments have used d-type surfaces to obtain a better understanding of the mass transport problem over rough walls for two reasons. First, the mechanical process for the construction of such surfaces (with appropriate alloying for electrochemical studies) is easier than the k-type patterns; and second, such surfaces (especially with lower λ/d) are better representatives for natural roughness patterns (Lolja, 2005). Ranges of $\lambda/d = 3-8$, $d/R \approx 0.001-0.1$ and various crest shapes (square, groove or triangle) were studied. Measured data were then collected and presented in the form of the ratio between the rough and smooth wall *Sh*:

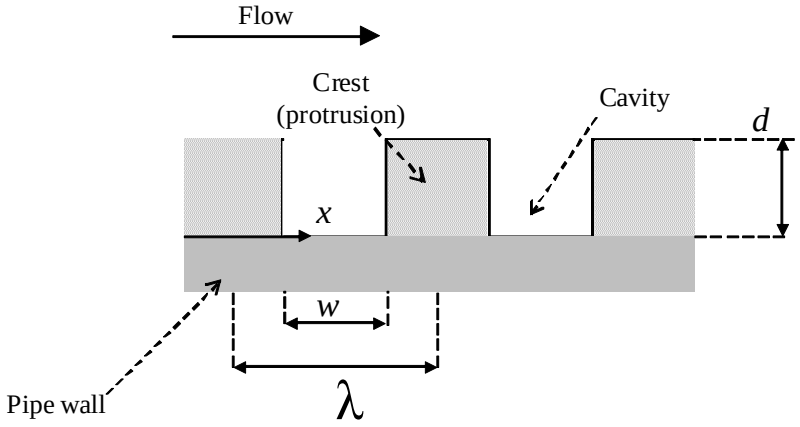

FIGURE 2.13. An artificially roughened surface includes one crest and one cavity in one periodic length of the roughness pattern (λ) (Leonardi *et al.*, 2007).

$$\frac{Sh_R}{Sh} = \mathrm{a}_1 \left(\sqrt{\frac{f}{2}} Re_\mathrm{d} \right)^{\mathrm{a}_2} Sc^{\mathrm{a}_3} \tag{2.31}$$

where the subscript R refers to rough surfaces and

$$Re_\mathrm{d} = \frac{Ud}{\nu} \tag{2.32}$$

is the roughness Reynolds number. The empirical coefficients a_1, a_2 and a_3 are reported in table 2.8. Since a_2 is negative in all of the correlations in table 2.8 and f remains almost constant for fully rough surfaces (see figure 2.10), the correlations indicate that wall demand for deep cavities is lower than for shallow cavities. In other words, the (length averaged) rough surface mass transfer coefficient $\mathrm{k}_{\mathrm{f}_R}$ can be defined as (recognizing that $Sh_R/Sh = \mathrm{k}_{\mathrm{f}_R}/\mathrm{k}_\mathrm{f}$)

$$\mathrm{k}_{\mathrm{f}_R} = \theta_{\mathrm{k}_\mathrm{f}} \mathrm{k}_\mathrm{f} \tag{2.33}$$

TABLE 2.8. Conditions and proposed empirical coefficients for equation 2.31 in different electrochemical experimental studies.

Study	*Re*	*Sc*	a_1	a_2	a_3
Dawson & Trass (1972)	$3\times10^3-1.2\times10^5$	$390-4590$	1.94	-0.1	0.09
Berger & Hau (1977)	$8\times10^3-2\times10^5$	$1000-6000$	1.79	-0.17	0.12
Grimanis & Abedian (1985)	$2\times10^3-1.5\times10^5$	$500-1500$	2.0	-0.2	0.1
Lolja (2005)	$3\times10^3-3\times10^4$	$2780,8520$	2.138	-0.182	0.00654

in which $\theta_{k_f} < 1$ for sufficiently deep cavities. Substituting equation 2.33 in equation 2.18 gives the following rough surface decay coefficient equation:

$$k_R = \frac{1}{Ur_h}\frac{k_w\theta_{k_f}k_f}{k_w+\theta_{k_f}k_f}. \tag{2.34}$$

The effect of the reduced mass transfer coefficient on reducing the decay coefficient can be determined by analysing the above equation. For very high wall demand coefficients ($k_w \gg k_f$), $\theta_{k_f}k_f$ becomes negligible in comparison with k_w. The value of k_R from the electrochemical experiments then approaches $k_R = \theta_{k_f}k_f/Ur_h$. For smooth walls, $k_w \gg k_f$ in equation 2.18 leads to $k = k_f/Ur_h$. Since $\theta_{k_f} < 1$ for very deep cavities, such analysis shows that the rough wall decay coefficient for high wall demand coefficient is decreased in comparison with the smooth pipe decay coefficient. (see also table 2.9).

The main limitation of correlations for electrochemical experiments is that they are only valid for high wall demand coefficients. Considering the asymptotic case of $k_w \ll k_f$ in equation 2.34 gives $k_R = k_w/Ur_h$, the same result as for smooth surfaces (equation 2.18). In other words, the correlations for wall demand using the electrochemical approach would suggest that there is no effect of the wall surface structure on the value of the decay coefficient for low k_w. This is indeed in contrast with several experimental studies which reported that the rough surface decay coefficient (k_R) is increased in comparison with the smooth surface decay coefficient (k) for low wall demand coefficients (see e.g. Al-Jasser (2007)).

To overcome this drawback, a method of adjusting the wall demand coefficient is used in EPANET-based models to consider the effect of wall roughness on the decay coefficient. This method is based on the assumption that surface roughness increases the available reacting surface and therefore, a higher mass

withdrawal due to the wall demand is expected. In this case, the value of the wall demand coefficient for rough surfaces is adjusted as:

$$k_{w_R} = \theta_{k_w} k_w \tag{2.35}$$

in which θ_{k_w} is an empirical coefficient which increases the wall demand coefficient based on the value of the relative roughness (Rossman, 2000):

$$\theta_{k_w} = -\frac{C_{k_w}}{\log \frac{\breve{d}}{2R}} \tag{2.36}$$

where $C_{k_w}(>0)$ is an empirical constant which should be defined for a reference condition (in terms of flow and pipe roughness) in field measurements. In general, equation 2.36 is calibrated for the reference condition by adjusting C_{k_w}. It is then assumed that $C_{k_w}(>0)$ remains constant for all the pipes of similar material. The value of k_{w_R} for pipes of the same material but different roughness is then defined by equation 2.36. Since the logarithm of the relative roughness (which is always less than 1) appears in the denominator of this equation, equation 2.36 implies that an increase in pipe roughness increases the wall demand coefficient. In other words, $\theta_{k_w} > 1$ for pipes with higher relative roughness than the reference roughness condition (Rossman, 2000) .

Substituting equation 2.35 into equation 2.18 gives the following equation for decay coefficient in rough pipes

$$k_R = \frac{1}{U r_h} \frac{\theta_{k_w} k_w k_f}{\theta_{k_w} k_w + k_f}. \tag{2.37}$$

When considering a low wall demand coefficient ($k_w \ll k_f$), the term containing $\theta_{k_w} k_w$ in the denominator of equation 2.37 can be neglected in comparison with k_f and, therefore, $k_R = \theta_{k_w} k_w / U r_h$. For smooth

TABLE 2.9. Comparison of the asymptotic behaviour of the two approaches for parameterisation of rough wall demand

	$k_w \ll k_f$	$k_w \gg k_f$
Smooth conduits	$\frac{k_w}{r_h U}$	$\frac{k_f}{r_h U}$
EPANET	$\frac{\theta_{k_w} k_w}{r_h U}$	$\frac{k_f}{r_h\, U}$
Experiments	$\frac{k_w}{r_h U}$	$\frac{\theta_{k_f} k_f}{r_h\, U}$

walls, the condition $k_w \ll k_f$ results in $k = k_w/U r_h$. This, once more, confirms that the method used in EPANET assumes that rough surfaces lead to an increase in the decay coefficient compared to smooth pipes. However, for high wall demand coefficients ($k_w \gg k_f$), the decay coefficient using the EPANET approach is $k_R = k = k_f/U r_h$. This is in contrast with the electrochemical experiments which suggest that the decay coefficient for high wall demand coefficients and deep cavities is lower than k (for smooth surfaces).

The results of the analysis are summarised in table 2.9. In general, the results in the table suggest that each parameterisation (adjusting k_w in EPANET or adjusting k_f using Sh_R correlations) works for an asymptotic case. However, an ideal wall demand parameterisation for rough walls would capture both asymptotes, physically accurately transitioning from one to the other.

2.6. Position of the current study in the literature

Parameterisations for wall friction and wall demand are powerful tools which significantly simplify the analysis of flow and mass transport in network pipes. The previous section introduced several parameterisations of f and k_f for both smooth and rough pipes, but also exposed weaknesses and gaps in the literature. This leads us to formulate four research questions which will be addressed in this thesis. The questions are discussed below and the position of the main chapters in addressing them is shown in figure 2.14.

Is the use of the *Sh* correlation by Notter & Sleicher (1971), which is valid for constant c_w (Dirichlet boundary conditions) valid for first-order wall demand (Robin boundary conditions), and under

which circumstances?

It was mentioned in the previous section that determination of k_f in EPANET-based models relies on Notter & Sleicher (1971) *Sh* correlation for smooth pipes. However, as this correlation was derived for a boundary condition in which c_w was constant (Dirichlet boundary condition), this correlation may not be appropriate for chlorine depletion due to wall reactions.

Chlorine concentration at the wall depends on details of reaction kinetics, flow and turbulence near the wall. If we assume that for very low wall demand coefficients $c_w \approx c_x$, we immediately see from equation 2.17 that the wall concentration is not constant along the pipe. Hence, the question that requires answering is whether, and under which conditions, the Notter & Sleicher (1971) *Sh* correlation is applicable to first-order wall demand? This question is addressed in chapter 5.

Do wall demand and bulk demand influence each other, and under which circumstances?

One of the assumptions in network models is that bulk and wall demands do not influence each other. This is a reasonable assumption because of the high capacity of turbulent flows to mix solute mass in the bulk (see chapter 3). However, at high k_w and k_b, the mixing capacity may become insufficient. In chapter 6, combined wall and bulk demands are studied in order to establish bounds for which this assumption is valid.

How should nonlinear wall demand be parameterised?

As was discussed in section 2.4.3, several studies have supported the idea that chlorine decay due to reactions with the pipe surface can be appropriately modelled as a first-order wall demand (Clark & Haught, 2005; Mutoti *et al.*, 2007). However, other studies (e.g. Kiéné *et al.* (1993) and Jones (2001)) observed a nonlinear relationship between the chlorine concentration and the rate of wall demand. The question which then must be addressed is how a generic wall demand should be parameterised. This question is addressed in chapter 7.

How can parameterisations of wall demand over rough surfaces be improved?

Section 2.5.3 clearly demonstrated that the two approaches for parameterisation of wall demand over

rough surfaces are mutually inconsistent, as both parameterisations have a different asymptotic behaviour for high and low wall demand coefficients. The main reason for such inconsistency is that the parameterisations insufficiently consider the complex interaction of flow, turbulence and mass transport which occur for rough surfaces.

In order to improve rough wall parameterisations for wall demand, detailed information is required about mass transport very close to the wall. Especially for the case of high *Sc* compounds, this information is extremely difficult to obtain experimentally, and the author was unable to find any relevant literature on this topic. Additionally, no literature on the numerical simulation of wall demand for rough surfaces was found. In chapters 8 and 9, RANS models will be used to provide this information, and a detailed analysis will lead to an improved physics-based parameterisation for a particular rough surface.

2.7. Summary

The current chapter started with a broad background on water supply systems. The history of water treatment, transport and distribution was presented. It was discussed that modelling the distribution networks includes determination of the main network operational indicators which are pressure, velocity and residual chlorine.

It was shown how the application of assumptions on negligible pipe entrance effects and full mixing in network junctions simplifies modelling the network into modelling flow and mass transport in single pipes. A discussion of history and state-of-the-art of flow and mass transport models was presented, which included introducing EPANET as a reference water quality model for the chlorine decay problem. The level of complexity by which EPANET models chlorine decay due to first-order wall and bulk demands in single pipes was also demonstrated.

It was mentioned that flow and mass transport modelling in EPANET-based models includes parameterisation of f and k_f. The parameterisation of these variables was discussed for both smooth and rough pipes. Four open research questions in using such parameterizations for modelling chlorine decay were identified and the position of the current study in answering these questions was determined.

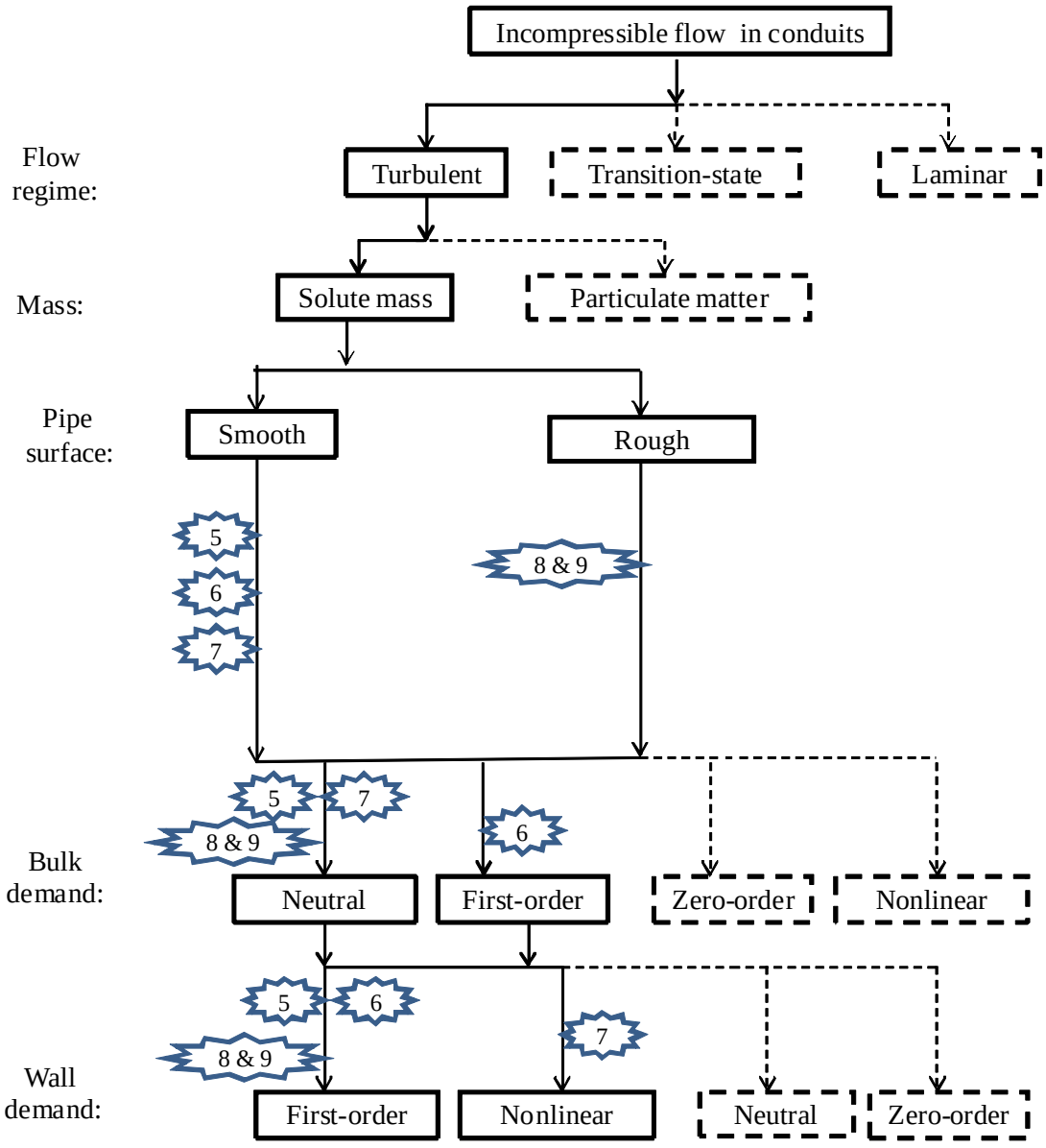

FIGURE 2.14. Structure of the studies provided in the thesis. Numbers indicate the main chapters of the thesis.

CHAPTER 3

Momentum and mass transfer in pipes

The discussions in chapter 2 motivated why the study of flow and mass transport in a single pipe is representative for a network. In this chapter, the focus moves from the network scale to a single pipe. The chapter starts by presenting the governing equations for flow and mass transport, turbulence and simulation techniques in turbulent flows (section 3.1). Reynolds averaging is introduced in section 3.2. In section 3.3, the universality of the near wall region is discussed, which is of great importance for understanding mass transport in turbulent wall bounded flows. The gradient diffusion hypothesis is introduced in section 3.4. In section 3.5, the Reynolds averaged equations for flow and mass transport in an axisymmetric pipe are introduced which form the basis for chapters 4 to 7.

3.1. Governing equations, turbulence and simulation methods

The continuity and Navier Stokes (NS) equations are believed to describe the behaviour of fluid motion in differential form, as long as the fluid can be regarded a continuum. These equations describe the conservation of mass and momentum, respectively. For incompressible fluids such as water, the continuity and NS equations are[1] (Hanjalić *et al.*, 2009; Bird *et al.*, 2002):

$$\frac{\partial \hat{u}_j}{\partial x_j} = 0 \tag{3.1}$$

$$\rho \frac{\partial \hat{u}_i}{\partial t} + \rho \hat{u}_j \frac{\partial \hat{u}_i}{\partial x_j} = \rho g_i - \frac{\partial \hat{p}}{\partial x_i} + \frac{\partial \hat{\tau}_{ij}}{\partial x_j}, \quad \hat{\tau}_{ij} = \mu \left(\frac{\partial \hat{u}_i}{\partial x_j} + \frac{\partial \hat{u}_j}{\partial x_i} \right) \tag{3.2}$$

[1] Equations are provided for Newtonian fluids like water. Categorizing fluids into Newtonian and non-Newtonian is based on the relationship between stress and strain. In Newtonian fluids this relationship is linear (Bird *et al.*, 2002).

where the hat sign ($\hat{}$) represents the instantaneous value of the variables and implicit summation over repeated indices is applied. The coordinate system is Cartesian and $\hat{u}_i$ denotes the velocity in the x_i direction. Furthermore, g_i is the gravitational acceleration [LT^{-2}], $\hat{p}$ is the pressure [$ML^{-1}T^{-2}$] and $\hat{\tau}_{ij}$ is the stress tensor [$ML^{-1}T^{-2}$].

By solving the continuity and NS equations, the pressure and velocity field can be determined. Once the velocity field is known, it is possible to study the transport of solute mass which is governed by[2] (Bird *et al.*, 2002):

$$\frac{\partial \hat{c}}{\partial t} + \hat{u}_j \frac{\partial \hat{c}}{\partial x_j} = \hat{r} + \frac{\partial}{\partial x_j}\left(D \frac{\partial \hat{c}}{\partial x_j}\right) \tag{3.3}$$

where $\hat{c}$ is the concentration [ML^{-3}] and $\hat{r}$ is the bulk reaction rate [$ML^{-3}T^{-1}$]. The continuity and NS equations (and consequently, mass transport equation) do not have analytical solutions, except in very simple cases[3] and therefore, numerical methods are often the only way to obtain solutions (Hanjalić *et al.*, 2009). However, numerical study of these equations for turbulent flows is non-trivial because of the large number of active scales in turbulent flows.

As a typical time history for the instantaneous dummy variable $\hat{X}$ in figure 3.1 shows, turbulent variables fluctuate in time without ever repeating themselves. The solution technique which resolves all fluctuations is called direct numerical simulation (DNS, as introduced in the previous chapter). This technique is usually referred to in the literature as the most accurate numerical method for the study of turbulent flows. However, considering the shortest fluctuations requires very high computational cost (Pope, 2000). Therefore, the use of DNS is usually limited to *Re* and *Sc* much smaller than those occurring in practical applications[4].

To reduce the cost of the computation, methods have been developed that use "preprocessed" NS and mass transport equations. In this case, all the variables are averaged over time[5] which is called Reynolds

[2] Here, it is assumed that the solute mass does not affect the fluid density (which is the case for passive scalars) (Bird *et al.*, 2002). Due to the dilute solution of chlorine in water, this is an appropriate assumption.

[3] Such as the Poiseuille solution for laminar flows in pipes. See e.g. Bird *et al.* (2002) for more details.

[4] As stated in the previous chapter, the resolution of the numerical mesh used for DNS is roughly proportional to $Re^{9/4}$ for the flow and $Re^{9/4}Sc^{3/2}$ for mass transport (Schwertfirm & Manhart, 2010; Hanjalić *et al.*, 2009).

[5] Ensemble averaging is used for flows which are not statistically steady-state (Hanjalić *et al.*, 2009).

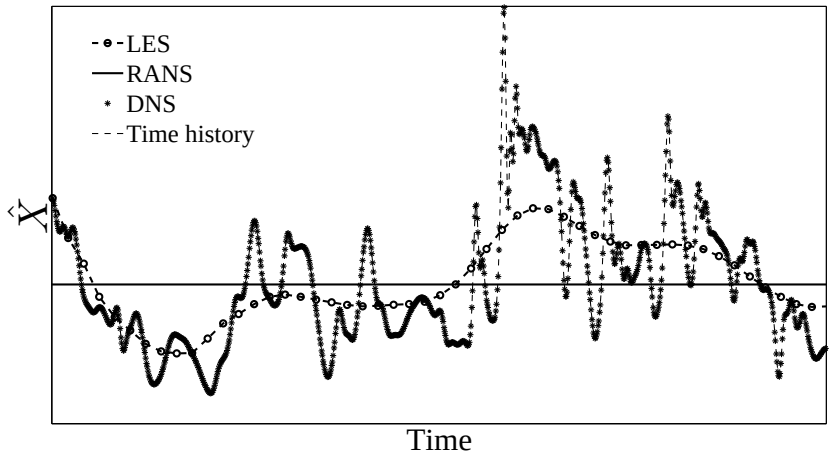

FIGURE 3.1. Schematic of different turbulent simulation approaches for a time history of $\hat{X}$ (DNS data are adopted from a time history for temperature by van Reeuwijk (2007))

averaging. The equations describing the behaviour of the mean (time averaged) variables are called the Reynolds averaged (RA) equations (Reynolds averaged NS equations are usually referred to as RANS). At the cost of having to model turbulent fluxes, RA equations are computationally much cheaper than DNS (see figure 3.1) (Pope, 2000). Since RA equations will be used in this study, they are discussed in more detail in section 3.2.

A different method of "preprocessing" the NS and mass transport equations is by filtering them spatially using low-pass filters. This method is called large eddy simulation (LES, as introduced in the previous chapter). LES resolves the larger scales in turbulence and models the smaller scales (figure 3.1). Although the computational cost of LES is less than DNS, this method still needs heavy mathematical calculations. In other words, LES is computationally closer to DNS than RANS (Hirsch, 2007).

Different methods of turbulence simulation are appropriate for different problems and purposes. Whilst DNS and LES give more accurate results than RANS simulations, their application is restricted to the available computational capabilities. The computational cost for DNS and LES studies is a function of the flow *Re*, *Sc* and complexity of the geometry being simulated. For instance, recent DNS and LES studies on flows and mass transport in smooth pipes are restricted to $Re < 10^4$ and $Sc < 400$ (see table 2.7).

The range of *Re* in a network is typically $10^4 - 10^6$ (Ho, 2008). In addition, $Sc \approx 1000$ for chlorine at 15^o C (figure 2.11). Therefore, DNS and LES are still incapable of providing results for the aforementioned conditions. Hence, RA equations will be used in the remainder of the thesis. Extended studies have shown that RANS models provide credible solutions both for smooth and rough pipes (Bergmann & Fiebig, 1999). The Reynolds averaging process and the turbulence closure problem for RANS equations are discussed in the next section.

3.2. Reynolds averaging

The concept of Reynolds averaging is schematically shown in figure 3.2. The figure shows that each instantaneous value of a variable like $\hat{X}$ in a turbulence context can be decomposed into a mean ($\overline{\hat{X}}$) and a fluctuating value X':

$$\hat{X} = \overline{\hat{X}} + X', \tag{3.4}$$

where the Reynolds averaging operator (shown with the overline) is defined as

$$\overline{\hat{X}}(x_i) = \lim_{t\to\infty} \frac{1}{t} \int_0^t \hat{X}(x_i, t')dt'. \tag{3.5}$$

Application of the Reynolds averaging operator on equations 3.1, 3.2 and 3.3 results in[6]:

$$\frac{\partial u_j}{\partial x_j} = 0, \tag{3.6}$$

$$\rho \frac{\partial u_i}{\partial t} + \rho u_j \frac{\partial u_i}{\partial x_j} = \rho g_i - \frac{\partial p}{\partial x_i} + \frac{\partial}{\partial x_j}\left(\tau_{ij} - \rho\overline{u_i' u_j'}\right), \quad \tau_{ij} = \mu\left(\frac{\partial u_i}{\partial x_j} + \frac{\partial u_j}{\partial x_i}\right), \tag{3.7}$$

[6]Detailed discussions for derivation of these equations are presented in many turbulent flows textbooks (see e.g. Pope (2000)).

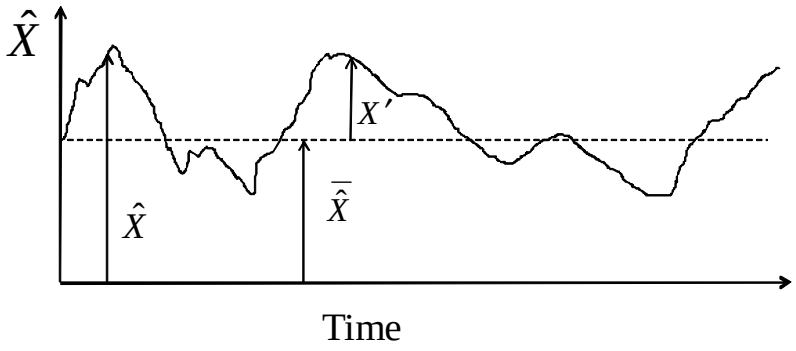

FIGURE 3.2. Instantaneous, mean and fluctuating values.

$$\frac{\partial c}{\partial t} + u_j \frac{\partial c}{\partial x_j} = \dot{r} + \frac{\partial}{\partial x_j}\left(D\frac{\partial c}{\partial x_j} - \overline{u'_j c'}\right). \tag{3.8}$$

The equations above contain new unknown correlations for fluctuation products (turbulent fluxes). In the RANS equations, the Reynolds stress $\overline{u'_j u'_i}$ represents the momentum transport due to turbulent fluctuations. In the mass transport equation, the term $\overline{u'_j c'}$ represents the turbulent mass transport. These correlations form nine new unknowns (six for momentum and three for mass); a turbulence closure (which relates the unknowns to the mean variables) is needed before equations 3.6, 3.7 and 3.8 can be solved. Turbulence closures are discussed in detail in section 3.4, chapters 4 (for smooth walls) and 8 (for rough walls).

3.3. Universality in turbulent wall bounded flows

Before discussing turbulence closures, some physical properties of the wall bounded flows require discussion[7]. For a fully developed turbulent wall bounded flow (like a pipe or channel flow), the behaviour of the inner layer, which includes the region immediately adjacent to the wall (figure 3.3) is expected to be governed by the wall shear stress τ_w, kinematic viscosity ν and the distance from the wall y. A dimensional analysis then suggests (see e.g. Pope (2000)):

[7] See e.g. Pope (2000) for complementary discussions.

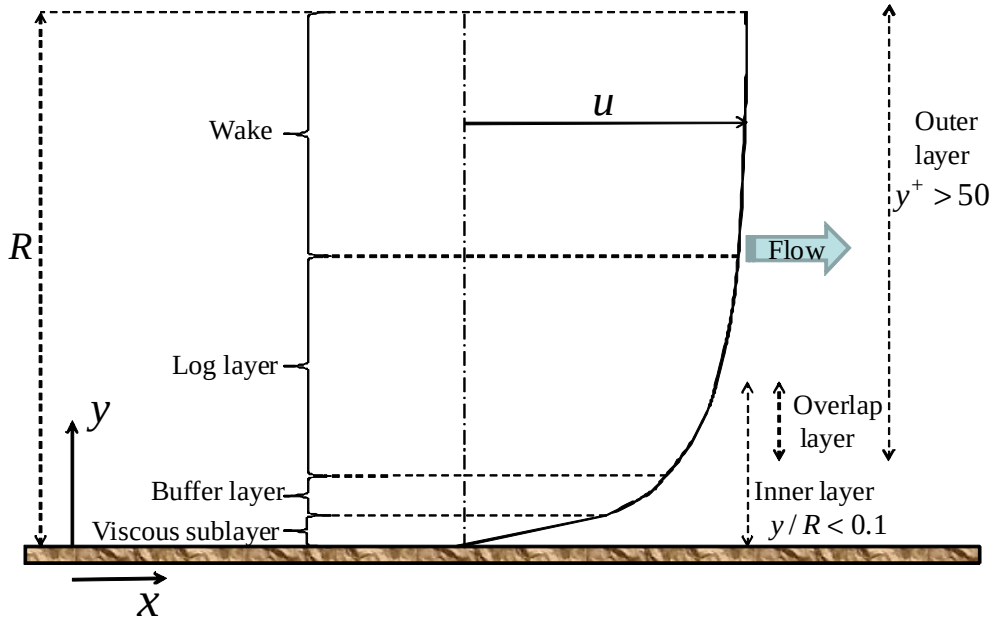

FIGURE 3.3. Schematic of different layers of a fully developed turbulent flow in a pipe as a case for wall bounded flows. Figure is not to scale.

$$\frac{u}{u_\tau} = \mathrm{F}\left(\frac{y u_\tau}{\nu}\right) \tag{3.9}$$

which is a relationship known as the "law of the wall". Here, $u_\tau = \sqrt{\tau_w/\rho}$ is the wall friction velocity $[LT^{-1}]$, which can also be recognised as a typical velocity scale for the momentum flux to the wall. The relationship in equation 3.9 is often written in plus units as $u^+ = \mathrm{F}(y^+)$, where

$$u^+ = \frac{u}{u_\tau}, \text{ and } y^+ = \frac{y}{\delta_\nu} = \frac{y u_\tau}{\nu} \tag{3.10}$$

where the quantity $\delta_\nu = \nu/u_\tau$ represents a viscous length scale. One of the features of the inner layer is that

the summation of the viscous and Reynolds stress in this layer is (approximately) constant (constant stress hypothesis), and is equal to the wall shear stress (Pope, 2000):

$$-\overline{u'v'} + \nu\frac{\partial u}{\partial y} = \frac{\tau_w}{\rho} = u_\tau^2 \tag{3.11}$$

where v' represents the fluctuating component of the instantaneous wall normal velocity $\hat{v}$. The inner layer includes distinct sublayers (figure 3.3) which are discussed below.

Viscous sublayer

This is the layer immediately adjacent to the wall in which the effect of the Reynolds stress is negligible in comparison with the viscous stress. The behaviour of the similarity function F in the viscous sublayer can be studied by performing a Taylor expansion series (around $y = 0$) for the instantaneous and fluctuating values of the streamwise and wall normal velocities:

$$\hat{u}(y,t) = \hat{a}_1(t) + \hat{a}_2(t)y + \hat{a}_3(t)y^2 + O(y^3), \tag{3.12}$$

$$\hat{v}(y,t) = \hat{b}_1(t) + \hat{b}_2(t)y + \hat{b}_3(t)y^2 + O(y^3) \tag{3.13}$$

where $\hat{a}_1$, $\hat{a}_2$ and $\hat{a}_3$ and $\hat{b}_1$, $\hat{b}_2$ and $\hat{b}_3$ are the expansion constants for the instantaneous velocity components $\hat{u}$ and $\hat{v}$, respectively. The boundary conditions at the wall are $\hat{u} = \hat{v} = 0$ and therefore, $\hat{a}_1 = \hat{b}_1 = 0$. Reynolds averaging equations 3.12 and 3.13 results in

$$u(y) = \bar{\hat{a}}_2 y + \bar{\hat{a}}_3 y^2 + O(y^3), \tag{3.14}$$

$$v(y) = \bar{\hat{a}}_2 y + \bar{\hat{b}}_3 y^2 + O(y^3). \tag{3.15}$$

In addition, equation 3.11 gives $\overline{\hat{a}_2} = u_\tau^2/\nu$ for $y \to 0$ (Since Reynolds stress is negligible in comparison with viscous stress very close to the wall). Therefore, equation 3.14 can also be written as

$$u^+ = y^+ + O(y^{+2}). \tag{3.16}$$

Hence, in the viscous sublayer, the universal function F depends linearly on y^+.

The Taylor expansions can also be used to infer the second property of the viscous sublayer, which forms one of the cornerstones of this thesis: the cubic dependence of $\overline{u'v'}$ on y. By subtracting equation 3.14 from 3.12 and 3.15 from 3.13 we obtain

$$u'(y,t) = \underbrace{\left(\hat{a}_2 - \bar{\hat{a}}_2\right)}_{a'_2} y + \underbrace{\left(\hat{a}_3 - \bar{\hat{a}}_3\right)}_{a'_3} y^2 + O(y^3) \tag{3.17}$$

$$v'(y,t) = \underbrace{\left(\hat{b}_2 - \bar{\hat{b}}_2\right)}_{b'_2} y + \underbrace{\left(\hat{b}_3 - \bar{\hat{b}}_3\right)}_{b'_3} y^2 + O(y^3). \tag{3.18}$$

The continuity equation of the fluctuating velocities ($\partial u'_j/\partial x_j = 0$) and the no slip boundary condition at the wall (i.e. $\partial/\partial x = 0$) and symmetry over the xy plane gives $\partial v'/\partial y = 0$ and therefore, $b'_2 = 0$. Multiplying equations 3.17 and 3.18 and Reynolds averaging the results gives:

$$\overline{u'v'} = \overline{a'_2 b'_3} y^3 + O(y^4). \tag{3.19}$$

Hence, $\overline{u'v'} \propto y^3$ in the viscous sublayer (Pope, 2000).

Log layer

This layer is still influenced by wall effects, but turbulence dominates over viscous effects. Therefore, the universal velocity profile is expected to be independent of the viscosity in this layer. This implies that the velocity gradient is not a function of the viscosity (Hanjalić *et al.*, 2009). Differentiating equation 3.9 (with respect to y) results in

$$\frac{du}{dy} = u_\tau \frac{dF}{dy^+}\frac{dy^+}{dy} = \frac{u_\tau^2}{\nu}\frac{dF}{dy^+}. \tag{3.20}$$

Only when $dF/dy^+ \propto y^{+-1}$ does the velocity gradient become independent of the fluid viscosity and hence, the velocity profile in the log layer is expected to be logarithmic. Figure 3.4 shows the data of some of the classical experiments for the determination of F, together with the relationship (Bird *et al.*, 2002)

$$u^+ = \frac{1}{\kappa}\ln y^+ + 5.2. \tag{3.21}$$

Here, $\kappa = 0.41$ is the von Karman constant.

Buffer layer

This layer is situated between the viscous sublayer and the log layer. Consequently, both viscous and turbulence contributions are important and none of them can be ignored. This causes difficulties in determining the similarity function in the buffer layer. Extensive numerical and experimental studies have been performed to fit empirical correlations to the velocity profile in this layer (Hanjalić *et al.*, 2009). These correlations will be introduced in the next chapter.

The wake

This layer is a part of the outer layer, which is expected to be independent of the molecular properties. The velocity profile in this layer depends on the geometry and therefore, may vary in different cases such as pipes and channels (see e.g. Pope (2000) for more details).

3.4. The gradient diffusion hypothesis

There are several ways in which the unknown turbulent fluxes can be linked to known resolved variables. Currently there are two levels of closure widely used for turbulence models: 1) first moment closure, also

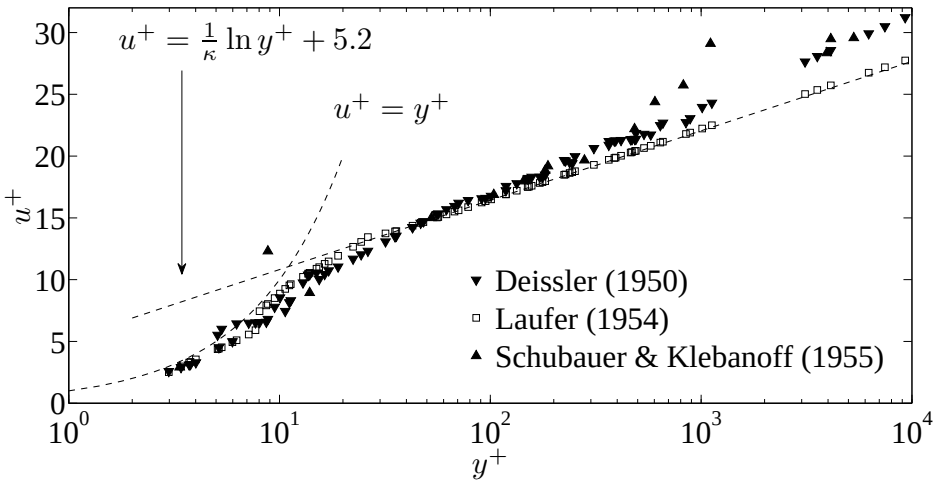

FIGURE 3.4. Experiments on wall bounded flows. Data from Laufer (1954), Deissler (1950) and Schubauer & Klebanoff (1955)

known as eddy viscosity models (EVMs) and 2) second moment closure models. The EVMs assume that the turbulent fluxes (momentum and mass) can be directly related to the mean flow fields and therefore, provide closures on the level of the first-order moments. Second moment closures, as the name suggests, solve additional explicit equations for the turbulence fluxes and provide closures on the level of the second-order moments. In this study, EVMs are used to model flow and mass transport in turbulent pipe flows.

The simplest and most commonly used closure in EVMs is the gradient diffusion hypothesis:

$$\overline{u_j' u_i'} = -\nu_T \left(\frac{\partial u_i}{\partial x_j} + \frac{\partial u_j}{\partial x_i} \right) \tag{3.22}$$

$$\overline{u_j' c'} = -D_T \frac{\partial c}{\partial x_j}. \tag{3.23}$$

Here, ν_T and D_T are the turbulent viscosity and turbulent diffusion coefficient, respectively [L^2T^{-1}] (The subscript T refers to turbulence in this thesis). In contrast with ν and D (which are the molecular properties of the fluid and solute mass, respectively), ν_T and D_T are flow properties. Analogous to Sc, $Sc_T = \nu_T / D_T$ is the turbulence Schmidt number. However, since ν_T and D_T are flow properties, $Sc_T \approx 1$

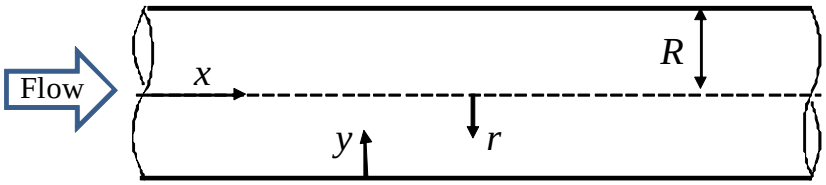

FIGURE 3.5. Schematic of the coordinate system for smooth pipes.

irrespective of the fluid[8] (Bird *et al.*, 2002).

The gradient diffusion hypothesis involves a linear relationship between turbulent fluxes and the mean variables (mean concentration and velocities) analogous to molecular diffusion. As turbulence is a fundamentally different process, this hypothesis is not always valid, which led to several proposals for nonlinear relations between the turbulent fluxes and the mean variables. One popular class for nonlinear EVMs is algebraic Reynolds stress models which are discussed in e.g. Pope (2000). In this thesis, use will be made of linear EVMs.

3.5. Specialisation on chlorine transport in pipes

The governing equations, for the problem which will be studied in chapters 4 to 7, are now discussed. The geometry for this problem is a pipe, as sketched in figure 3.5. By making the following assumptions:

(1) the pipe is axisymmetric;
(2) the pipe walls are hydraulically smooth;
(3) flow is fully developed;
(4) flow and concentration are statistically in a steady-state;
(5) transport due to streamwise diffusion is negligible in comparison with the advection;

[8] Average values from 0.6 (Flesch *et al.*, 2002) to 1 (Koeltzsch, 2000) are reported for Sc_T.

equations 3.7 and 3.8 simplify to:

$$\frac{1}{r}\frac{d}{dr}\left[r\left(\nu+\nu_T\right)\frac{du}{dr}\right]=-\frac{dp}{dx} \tag{3.24}$$

$$u\frac{\partial c}{\partial x}=\dot{r}+\frac{1}{r}\frac{\partial}{\partial r}\left[r\left(D+D_T\right)\frac{\partial c}{\partial r}\right] \tag{3.25}$$

where p is the RA kinematic pressure $[L^2T^{-2}]$. The coordinate system is shown in figure 3.5 and x, r and y represent the streamwise, radial direction and the distance to the wall (wall normal coordinate), respectively. The governing equations for rough surfaces are discussed in chapters 8 and 9.

CHAPTER 4

Flow models for turbulent pipe flow with smooth walls

Before mass transfer can be studied, the flow field in the pipe must be determined. Consequently, the aim of this chapter is to introduce linear EVMs used in chapters 5 to 7 for modelling turbulent flows in smooth pipes. The governing equation for the flow field in smooth pipes was presented in the previous chapter (equation 3.24). The EVMs which are used for solving this equation in chapters 5 to 7 are discussed here.

The models discussed in this chapter are selected based on their ability to accurately model the behaviour of ν_T close to the wall. It will be shown in chapter 5 that capturing the third-order dependence of ν_T to the wall distance is crucial for obtaining the correct exponent for *Sc* in the *Sh* correlation.

This chapter introduces two turbulence models which have this dependence: a modified van Driest mixing length (section 4.2) and k-ε model (section 4.3). Both models are compared against the standard benchmarks for turbulent pipe flow.

4.1. Turbulence models for RANS

As discussed in the previous chapter, linear EVMs are considered for the current study. Linear EVMs are usually categorized based on the method by which the turbulent viscosity is determined (Hanjalić *et al.*, 2009):

(1) Algebraic models which rely on direct relations between ν_T and u;
(2) Differential EVMs, which are further categorized in one-equation EVMs (which introduce one auxiliary differential equation for determination of ν_T) and two-equation EVMs (which introduce two auxiliary differential equations for determination of ν_T).

Detailed discussions on various models in these categories can be found in textbooks on turbulent flows (e.g. Pope (2000)). In this section, the models which are used for flow modelling in chapters 5 to 7 are discussed. From the first category, the modified van Driest mixing length model is used in the current study and introduced in section 4.2. The high Reynolds number (HRN) $k-\varepsilon$ model, which is a two-equation EVM is discussed in section 4.3. It will be explained later in chapter 8 that none of these models are suitable for flow in rough conduits and therefore, a low *Re* (LRN) EVM is used in chapter 8. The turbulence models used in each of the chapters are summarised in figure 4.1.

4.2. Modified van Driest mixing length model

The modified van Driest mixing length model is an algebraic EVM. In general, mixing length models relate the turbulent viscosity to a mixing length l_{m} $[L]$:

$$\nu_T = l_{\mathrm{m}}^2 \left| \frac{du}{dy} \right|. \tag{4.1}$$

The mixing length l_{m} is a function of the geometry and will be discussed in more detail later on. By combining the constant stress hypothesis (equation 3.11), the gradient diffusion hypothesis (equation 3.22) and equation 4.1, the velocity profile is given by (Pope, 2000):

$$u^+ = \int_0^{y^+} \frac{2dy^+}{1+\left(1+4l_{\mathrm{m}}^{+2}\right)^{1/2}}. \tag{4.2}$$

For the turbulent viscosity profile, equations 4.1 and 4.2 give:

$$\frac{\nu_T}{\nu} = l_{\mathrm{m}}^{+2}\frac{du^+}{dy^+} = \frac{2l_{\mathrm{m}}^{+2}}{1+\left(1+4l_{\mathrm{m}}^{+2}\right)^{1/2}}. \tag{4.3}$$

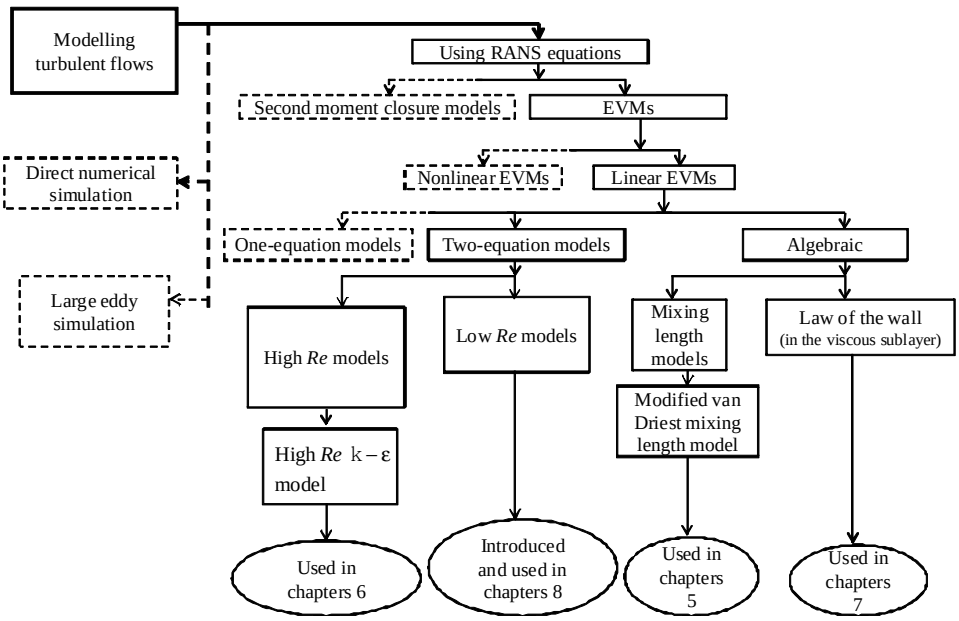

FIGURE 4.1. Position of turbulent flow models applied in different chapters of the thesis within a wider turbulent flows simulation and modelling framework.

Equations 4.2 and 4.3 are valid for all mixing length models in the inner layer (provided the stress can be assumed constant (chapter 3)).

At this point, the only remaining issue is to specify l_{m}. For the case of wall bounded flows, the mixing length must vary from zero at the wall to a constant value far away from the wall. Prandtl proposed a linear variation of the mixing length with respect to the distance from the wall (Pope, 2000):

$$l_{\mathrm{m}} = \kappa y. \tag{4.4}$$

Using equations 4.1 and 4.2, it is straightforward to demonstrate that equation 4.4 is consistent with the log law (equation 3.21). However, viscosity affects the mixing length in the viscous sublayer and buffer layer and therefore, equation 4.4 must be modified very close to the wall. van Driest (1956) proposed the following (empirical) mixing length model:

$$l_{\mathrm{m}} = \kappa y \left(1 - \exp\left(\frac{-y^+}{A^+}\right)\right), \quad A^+ = 26. \tag{4.5}$$

As can be seen, the modification comprises a damping of l_{m} close to the wall. The van Driest mixing length model faithfully reproduces the velocity profile in the viscous sublayer and the buffer layer, and produces accurate estimates for ν_T from the buffer layer onwards (Pope, 2000). However, the standard van Driest mixing length fails to model appropriately the behaviour of ν_T in the viscous sublayer. As mentioned at the beginning of the chapter, for simulation of mass transport of high *Sc* compounds, it is crucial that $\nu_T \propto y^3$ very close to the wall. This issue is discussed below.

If a Taylor expansion is performed (around $y^+ = 0$) for the standard van Driest mixing length model (equation 4.5), it is seen that this model has a second-order dependency on y^+ near the wall:

$$l_{\mathrm{m}}^+ = \frac{\kappa}{A^+} y^{+2} + O\left(y^{+3}\right). \tag{4.6}$$

Hence, using equations 4.1 and 3.16, the turbulent viscosity scales as

$$\frac{\nu_T}{\nu} = l_{\mathrm{m}}^{+2} \frac{du^+}{dy^+} \propto y^{+4}. \tag{4.7}$$

This behaviour is not correct. Indeed, it was shown in section 3.3 that $\overline{u'v'} \propto y^{+3}$ in the viscous sublayer. Using the gradient diffusion hypothesis (equation 3.22), we obtain

$$\nu_T = -\overline{u'v'} / \frac{\partial u}{\partial y} = -\frac{\overline{a_2' b_3'}}{\overline{a_2}} y^3 + O(y^4) \tag{4.8}$$

i.e. a *third-order* dependence on y. Equation 4.8 is usually denoted by (Bird *et al.*, 2002)

$$\frac{\nu_T}{\nu} = by^{+3} \tag{4.9}$$

and laboratory experiments and DNS studies have shown that $b \approx 9.5 \times 10^{-4}$ (Notter & Sleicher, 1971; Bird *et al.*, 2002).

To correct this inconsistency in the original van Driest model, the following modification was proposed (Hanna *et al.*, 1981):

$$l_m = \kappa y \frac{1 - \exp\left(\frac{-y^+}{A}\right)}{\sqrt{1 - \exp\left(\frac{-y^+}{B^+}\right)}}, \quad A^+ = 26, \; B^+ = 4. \tag{4.10}$$

Substituting equation 4.10 in equation 4.3 and using a Taylor expansion, it can be shown that the near wall behaviour of ν_T using the modified van Driest model is correct (Bird *et al.*, 2002):

$$\frac{\nu_T}{\nu} = \frac{\kappa^2 B^+}{A^{+2}} y^{+3} \approx by^{+3}. \tag{4.11}$$

The modified van Driest mixing length model faithfully reproduces velocity and turbulent viscosity profiles close to the wall (Bird *et al.*, 2002), as will be shown in figure 4.2. Equation 4.2 was solved numerically using a trapezoidal integration method (the MATLAB[1] function `cumtrapz`, see appendix B for application of the function and e.g. Atkinson (1989) for more details). The numerical domain is the half width of a pipe which was discretised with 200 segments. To check grid convergence, the calculation was repeated with double resolution. No considerable sensitivity was observed.

Figure 4.2 show the velocity and turbulent viscosity profiles predicted by the modified van Driest mixing length model, compared with DNS results for $Re_\tau = u_\tau R/\nu = 1142$, where Re_τ is the shear Reynolds number (Wu & Moin, 2008). Figure 4.2 shows that the modified van Driest mixing length model can accurately

[1] A registered trademark of MathWorks Inc.

predict the velocity and turbulent viscosity in the viscous sublayer, buffer layer and the log layer. However, this approximation deteriorates in the pipe centre (i.e. the wake). This occurs because the constant stress hypothesis (equation 3.11) is only valid in the inner layer. However, the outer layer is less important (than the inner layer) for simulation of wall demands as the concentration will be almost uniform far away from the wall. It will be shown in chapter 5, which deals with the wall demand in smooth pipes, that application of the modified van Driest mixing length model provides results for solute mass decay, which agree well with other analytical and experimental results.

The study in chapter 7 also deals with the wall demand problem but for nonlinear reactions, however, it focuses on the study of high *Sc* compounds (such as chlorine). It will be shown in chapter 5 that if *Sc* is sufficiently high, all of the changes in the crosswise concentration profile occur in the viscous sublayer and consequently, the mass transport problem is not affected by changes in the velocity and turbulent viscosity profiles in the buffer zone and log law layer. Consequently, equations 3.16 and 4.9 are used in chapter 7 to model the entire flow field.

4.3. HRN $k-\varepsilon$ model with wall functions

The $k-\varepsilon$ model is one of the most widely used turbulence models available. As the name suggests, it introduces two new variables k and ε, which represent the turbulence kinetic energy $[L^2T^{-2}]$ and the energy dissipation rate $[L^2T^{-3}]$, respectively. From a dimensional analysis, it follow that a suitable expression for ν_T is

$$\nu_T = C_\mu \frac{k^2}{\varepsilon} \tag{4.12}$$

where $C_\mu = 0.09$ is an empirical coefficient[2]. The governing equations for a fully developed flow in an axisymmetric pipe geometry, augmented with the HRN $k-\varepsilon$ turbulence model, are (Pope, 2000):

[2]Turbulence models generally contain a number of empirical coefficients such as C_μ. The value of coefficients are generally based on DNS and experimental data (Pope, 2000).

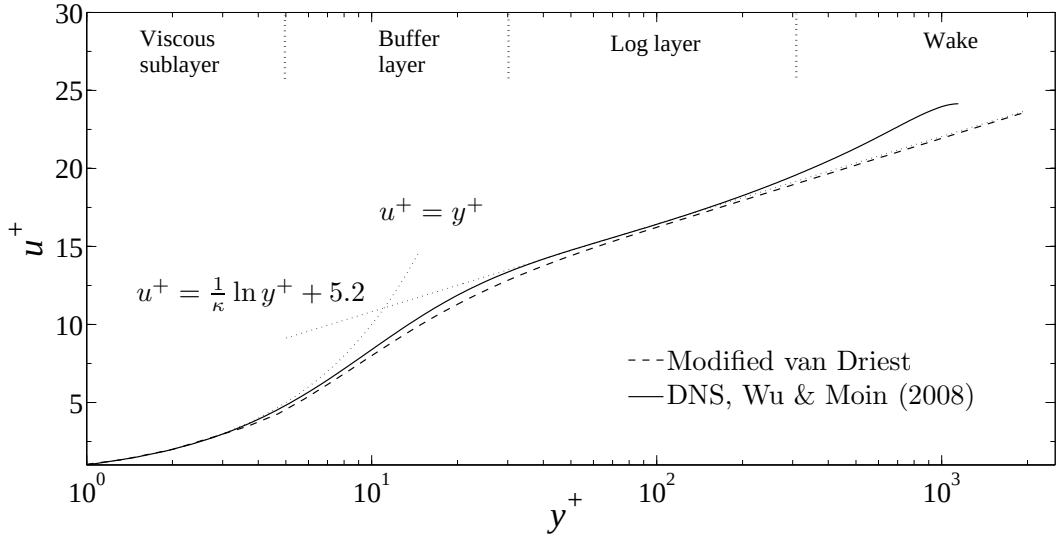

(A) u^+

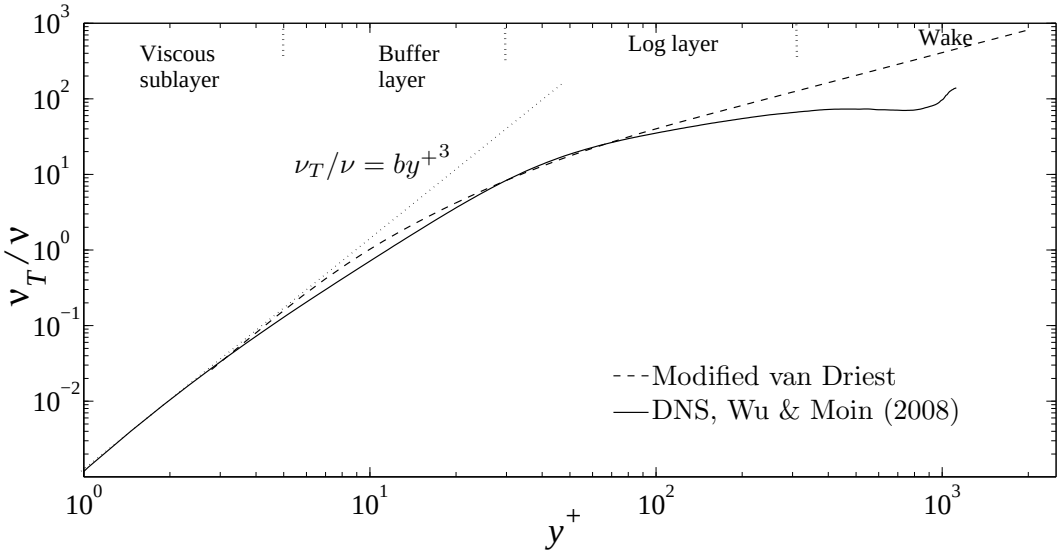

(B) ν_T/ν

FIGURE 4.2. Comparison of fully developed smooth pipe flow velocity and turbulent viscosity profiles by the modified van Driest mixing length model and DNS data by Wu & Moin (2008) for $Re_\tau = 1142$.

$$\frac{1}{r}\frac{d}{dy}\left[r\left(\nu+\nu_T\right)\frac{du}{dy}\right]=-\frac{dp}{dx} \tag{4.13}$$

$$\frac{1}{r}\frac{d}{dy}\left[r\left(\nu+\frac{\nu_T}{\sigma_k}\right)\frac{dk}{dy}\right]+\nu_T\left(\frac{du}{dy}\right)^2-\varepsilon=0 \tag{4.14}$$

$$\frac{1}{r}\frac{d}{dy}\left[r\left(\nu+\frac{\nu_T}{\sigma_\varepsilon}\right)\frac{d\varepsilon}{dy}\right]+C_1\nu_T\left(\frac{du}{dy}\right)^2\frac{\varepsilon}{k}-C_2\frac{\varepsilon^2}{k}=0 \tag{4.15}$$

where $C_1=1.44$, $C_2=1.92$, $\sigma_k=1$ and $\sigma_\varepsilon=1.3$ are (empirical) coefficients. However, the equations are only valid when molecular viscosity does not play an important role. This is the reason such models are called HRN models. Consequently, HRN models are not valid in the viscous sublayer and the buffer zone and therefore, wall functions must be used to bridge the distance from the log layer to the wall. In the current study, the modified van Driest mixing length model is used as the wall function.

Equations 4.12 to 4.15 are discretised with a conservative finite difference method[3] (Hirsch, 2007) on the grid shown in figure 4.3. The numerical code for solving the discretised equations is also presented in appendix B. Fractional indices in the figure denote a non-weighted average $X_{j+1/2}=\left(X_j+X_{j+1}\right)/2$. The variables u, k and ε are defined in the cell centres, and the cell adjacent to the wall has its cell centre at $y^+=50$.

The equations 4.12 to 4.15 are nonlinear and therefore, an iterative approach is needed to solve them. Let the superscripts (n) and $(n+1)$ denote the values of the variables in the old and new iteration, respectively, A second-order accurate discretisation of equations 4.13 to 4.15 is

$$\frac{1}{r_{j+1/2}}\frac{r_{j+1}\left(\nu+\nu_{T_{j+1/2}}^{(n)}\right)\frac{u_{j+1}^{(n+1)}-u_j^{(n+1)}}{\Delta r_{j+1/2}}-r_j\left(\nu+\nu_{T_{j-1/2}}^{(n)}\right)\frac{u_j^{(n+1)}-u_{j-1}^{(n+1)}}{\Delta r_{j-1/2}}}{\Delta r_j}=-\frac{u_\tau^2}{r_h} \tag{4.16}$$

$$\frac{1}{r_{j+1/2}}\frac{r_{j+1}\left(\nu+\nu_{T_{j+1/2}}^{(n)}\right)\frac{k_{j+1}^{(n+1)}-k_j^{(n+1)}}{\Delta r_{j+1/2}}-r_j\left(\nu+\nu_{T_{j-1/2}}^{(n)}\right)\frac{k_j^{(n+1)}-k_{j-1}^{(n+1)}}{\Delta r_{j-1/2}}}{\Delta r_j}+P_j^{(n+1)}-\varepsilon_j^{(n+1)}=0 \tag{4.17}$$

[3]The finite difference discretisation, which is extensively used throughout the thesis, is conservative since it is equivalent to a finite volume discretisation when multiplied by $r_{j+1/2}$ (Hirsch, 2007).

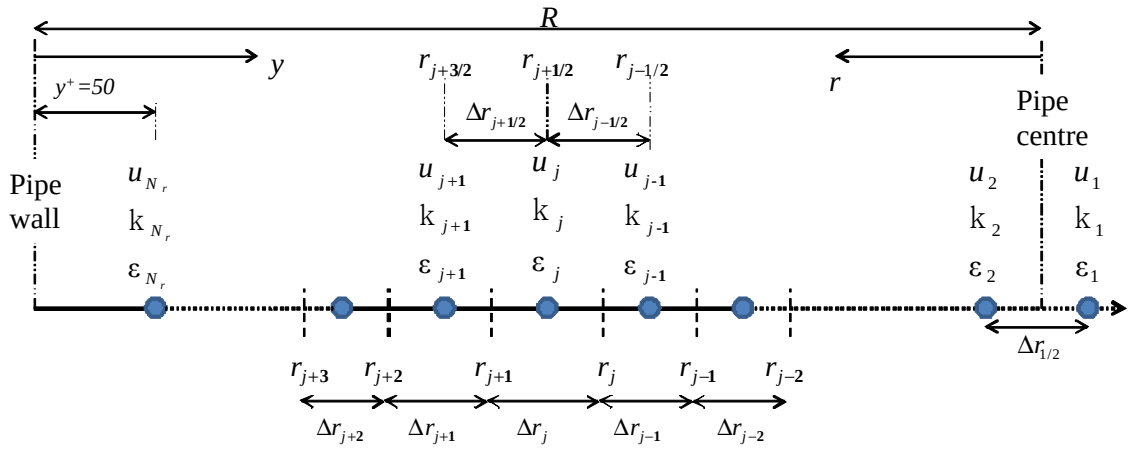

FIGURE 4.3. Domain discretisation for HRN $\mathsf{k}-\varepsilon$ model includes half width of the smooth pipe, with the first node on $y^+ = 50$.

$$\frac{1}{r_{j+1/2}}\frac{r_{j+1}\left(\nu+\nu_{T_{j+1/2}}^{(n)}\right)\frac{\varepsilon_{j+1}^{(n+1)}-\varepsilon_{j}^{(n+1)}}{\Delta r_{j+1/2}} - r_j\left(\nu+\nu_{T_{j-1/2}}^{(n)}\right)\frac{\varepsilon_{j}^{(n+1)}-\varepsilon_{j-1}^{(n+1)}}{\Delta r_{j-1/2}}}{\Delta r_j} + C_1\frac{\varepsilon_j^{(n)}}{\mathsf{k}_j^{(n)}}P_j^{(n+1)} - C_2\frac{\varepsilon_j^{(n)}}{\mathsf{k}_j^{(n)}}\varepsilon_j^{(n+1)} = 0 \tag{4.18}$$

where

$$P_j^{(n)} = \nu_{T\,j}^{(n)}\left[\frac{1}{2}\left(\frac{u_{j+1}^{(n)}-u_j^{(n)}}{\Delta r_{j+1/2}} + \frac{u_j^{(n)}-u_{j-1}^{(n)}}{\Delta r_{j-1/2}}\right)\right]^2 \tag{4.19}$$

is the discterised turbulence kinetic energy production $[L^2T^{-3}]$. In addition, it was considered in equation 4.16 that $-dp/dx = -d(\mathrm{P}/\rho)/dx = u_\tau^2/r_\mathrm{h}$ (equations 2.6 and 3.11). As equations 4.16 to 4.18 are linear, it is possible to organise these equations as

$$\mathbf{A}_\mathrm{u}\mathbf{u}^{(n+1)} = \mathbf{r}_\mathrm{u} \tag{4.20}$$

$$\mathbf{B}_\mathrm{u}\mathbf{u}^{(n+1)} + \mathbf{B}_\mathrm{k}\mathbf{k}^{(n+1)} - \boldsymbol{\varepsilon}^{(n+1)} = \mathbf{0} \tag{4.21}$$

$$\mathbf{C}_\mathrm{u}\mathbf{u}^{(n+1)} + \mathbf{C}_\varepsilon\boldsymbol{\varepsilon}^{(n+1)} = \mathbf{0} \tag{4.22}$$

where

$$\mathbf{u}^{(n+1)} = \left[u_1^{(n+1)}, u_2^{(n+1)}, u_3^{(n+1)}, ..., u_{N_r-2}^{(n+1)}, u_{N_r-1}^{(n+1)}, u_{N_r}^{(n+1)}\right]^\mathrm{T} \tag{4.23}$$

$$\mathbf{k}^{(n+1)} = \left[\mathrm{k}_1^{(n+1)}, \mathrm{k}_2^{(n+1)}, \mathrm{k}_3^{(n+1)}, ..., \mathrm{k}_{N_r-2}^{(n+1)}, \mathrm{k}_{N_r-1}^{(n+1)}, \mathrm{k}_{N_r}^{(n+1)}\right]^\mathrm{T} \tag{4.24}$$

$$\boldsymbol{\varepsilon}^{(n+1)} = \left[\varepsilon_1^{(n+1)}, \varepsilon_2^{(n+1)}, \varepsilon_3^{(n+1)}, ..., \varepsilon_{N-2}^{(n+1)}, \varepsilon_{N-1}^{(n+1)}, \varepsilon_{N_r}^{(n+1)}\right]^\mathrm{T} \tag{4.25}$$

are the vectors containing the unknowns and $\mathbf{r}_\mathrm{u}$ is a $N_r \times 1$ vector for the right hand side of equation 4.16. N_r is the number of cells in the r direction. The matrices $\mathbf{A}_\mathrm{u}$, $\mathbf{B}_\mathrm{u}$, $\mathbf{B}_\mathrm{k}$, $\mathbf{C}_\mathrm{u}$ and $\mathbf{C}_\varepsilon$ are all of size $N_r \times N_r$. The system of equations can be written as a single matrix-vector equation:

$$\begin{bmatrix} \mathbf{A}_\mathrm{u} & \mathbf{0} & \mathbf{0} \\ \mathbf{B}_\mathrm{u} & \mathbf{B}_\mathrm{k} & -\mathbf{I} \\ \mathbf{C}_\mathrm{u} & \mathbf{0} & \mathbf{C}_\varepsilon \end{bmatrix} \begin{bmatrix} \mathbf{u} \\ \mathbf{k} \\ \boldsymbol{\varepsilon} \end{bmatrix}^{(n+1)} = \begin{bmatrix} \mathbf{r}_u \\ \mathbf{0} \\ \mathbf{0} \end{bmatrix} \tag{4.26}$$

where $\mathbf{I}$ is the identity matrix. Equation 4.26 can be solved once the boundary conditions are specified. Since the first node is located in the log layer, the following boundary conditions can be derived (see e.g., Pope (2000)):

$$u_{N_r} = \frac{u_\tau}{\kappa}\ln\left(\frac{u_\tau(R - r_{N_r+1/2})}{\nu}\right) + 5.2 \tag{4.27}$$

$$\mathrm{k}_{N_r} = \frac{u_\tau^2}{\sqrt{C_\mu}} \tag{4.28}$$

$$\varepsilon_{N_r} = \frac{\nu u_\tau^2}{\kappa(R - r_{N_r+1/2})}. \tag{4.29}$$

In addition, the symmetry condition in the pipe centre gives the following boundary conditions at the first cell:

$$u(1) = u(2),\ \mathsf{k}(1) = \mathsf{k}(2),\ \varepsilon(1) = \varepsilon(2). \tag{4.30}$$

The iterative algorithm for solving this system is briefly discussed below. The following steps are taken:

(1) Specify Re_τ, ν and R;
(2) Initial guess for u, k and ε;
(3) Determine the matrices and right hand side of equation 4.16;
(4) Solve system of linear equations 4.26 to determine $u^{(n+1)}$, $\mathsf{k}^{(n+1)}$ and $\varepsilon^{(n+1)}$;
(5) Calculate the relative residual E for all three variables;

$$\mathrm{E} = \frac{\max\left(X_1^{(n+1)} - X_1^{(n)}, X_2^{(n+1)} - X_2^{(n)}, \ldots\right)}{\max(X_1^{(n+1)}, X_2^{(n+1)}, \ldots)} \tag{4.31}$$

(6) If $\mathrm{E} < 10^{-9}$ for all the variables, then terminate the calculation (the results are not sensitive to lower E). Otherwise, proceed to step 3 after updating the variables according to the under relaxation scheme

$$X^{(n+1)} \leftarrow \mathtt{urf}\, X^{(n+1)} + (1 - \mathtt{urf}) X^{(n)} \tag{4.32}$$

where $\mathtt{urf}$ is the under relaxation factor. Application of this method enhances the convergence since the changes between two iterations remain controlled. For the current study $\mathtt{urf} = 0.1$ is applied. A number of $N_r = 200$ cells was used to determine u and ν_T for $Re_\tau = 1142$. The solutions converged after 4100 iterations. Figure 4.4 shows the relative residuals (E) as a function of the number of iterations.

The converged profiles for u and ν_T are shown in figure 4.5 (note that the first node is located at $y^+ = 50$). The figures also include DNS results by Wu & Moin (2008) ($Re_\tau = 1142$). In comparison with the modified

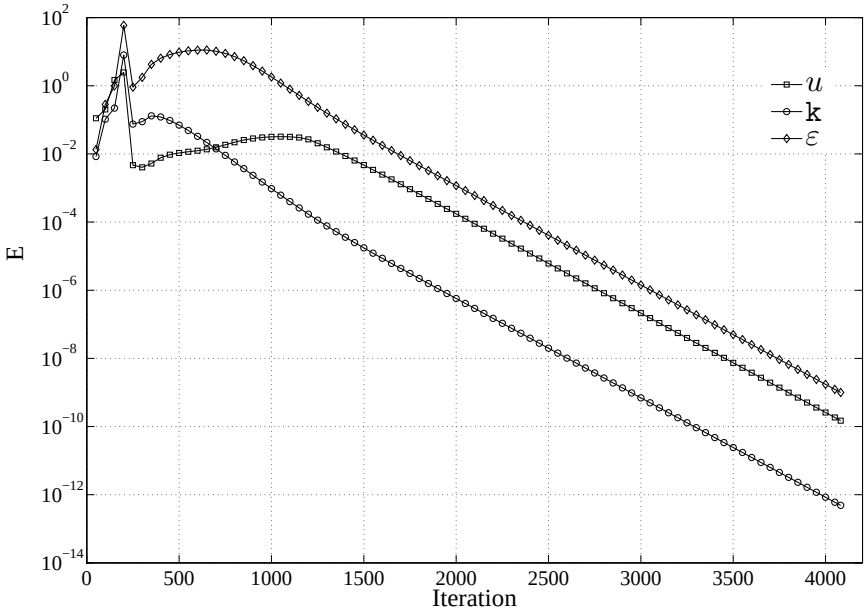

FIGURE 4.4. Convergence of the HRN $\mathsf{k}-\varepsilon$ model.

van Driest mixing length model (figure 4.2), the HRN $\mathsf{k}-\varepsilon$ model reproduces the profiles in the outer layer ($y^+ > 50$) more accurately. The HRN $\mathsf{k}-\varepsilon$ model will be used in chapter 6, where the bulk demands are studied and more accurate flow and turbulence levels in the bulk (than the modified van Driest mixing length model) are important.

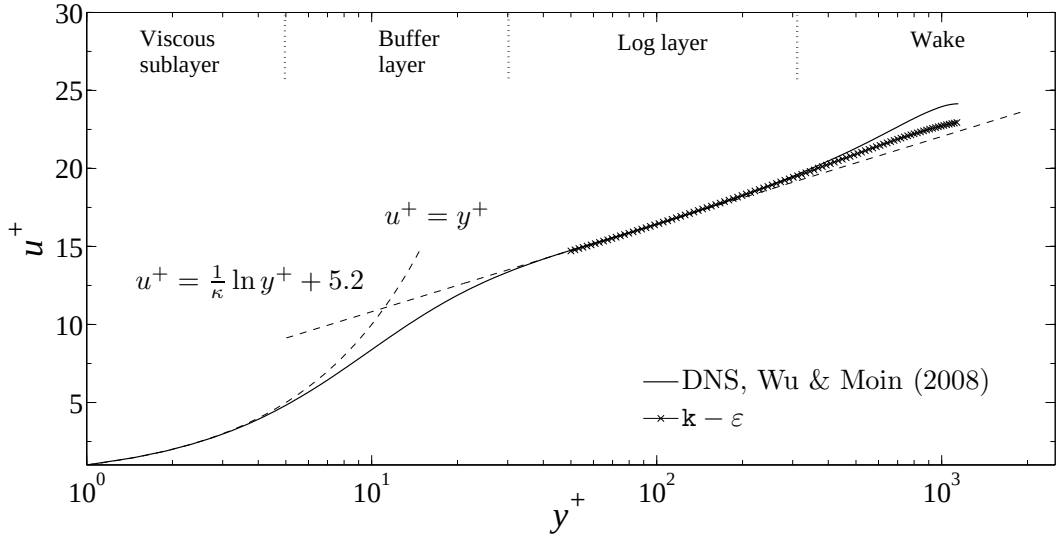

(A) u^+

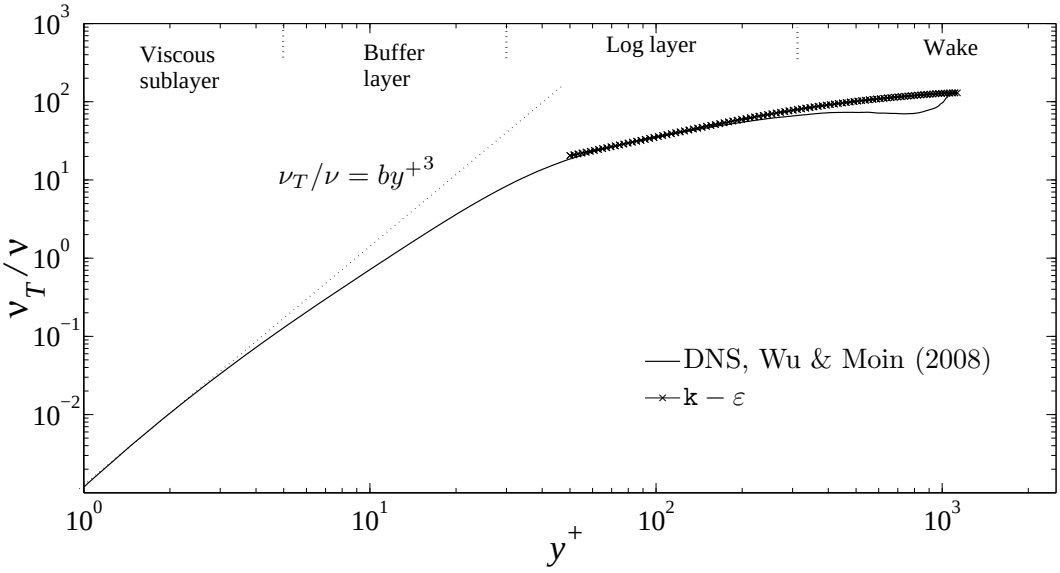

(B) ν_T/ν

FIGURE 4.5. Comparison of fully developed smooth pipe flow velocity and turbulent viscosity profiles for the HRN k – ε model and DNS data for $Re_\tau = 1142$ (Wu & Moin, 2008).

CHAPTER 5

First-order wall demand

As stated in section 2.6, the first research question in wall demand parameterisation is related to the criteria under which the *Sh* correlation by Notter & Sleicher (1971) can be applied to modelling solute mass decay due to first-order wall demand. In particular, the Notter & Sleicher (1971) correlation was determined for constant c_w. The questions which must be answered are then: is this correlation valid for the first-order wall demand and what are the bounds for which the assumption of analogy is valid?

In order to answer these questions, a wide range of k_w is considered to cover chlorine wall demand with different materials (table 2.4). In addition, $Re = 10^4 - 10^6$ is adopted as the typical *Re* range for a well-designed network (section 2.4.1). Furthermore, $Sc = 1000$ is considered as a close approximation for chlorine at 15^o C (figure 2.11), which is the recommended temperature for drinking water (WHO, 2008). The modified van Driest mixing length model is used in this chapter to model smooth pipe velocity and turbulent diffusion coefficient profiles in the mass transport equations.

In section 5.1, a separation of variables is performed to derive a one-dimensional (1D) model for the radial concentration profile from the two-dimensional (2D) axisymmetric RA mass transport equation posed in chapter 3 (equation 3.25 with no bulk reactions). A 2D model is also presented for solving the original 2D mass transport equation. The numerical methods for both models (which are applicable for arbitrary *Sc*) are introduced in section 5.2.

Results presented in section 5.3 are used to verify the 1D model by comparing the predicted concentration profile with the 2D model results. The results of the 1D model are also compared with the EPANET parameterisation for first-order wall demand.

In order to characterize high *Sc* compounds for the case of first-order wall demand, an asymptotic analytical solution for high *Sc* compounds is proposed in section 5.4. Results are then compared with the

1D model to determine the criterion for high *Sc* compounds. The chapter ends with a summary in section 5.5. The study in this chapter is extended in chapter 6 where simultaneous first-order wall and bulk demands are studied.

5.1. Governing equations

Equation 3.25 is the governing equation for an axisymmetric RA mass transport problem. The study in this chapter does not consider bulk reactions and therefore:

$$u\frac{\partial c}{\partial x} - \frac{1}{r}\frac{\partial}{\partial r}\left[r\left(D+D_T\right)\frac{\partial c}{\partial r}\right] = 0. \tag{5.1}$$

For the case of first-order wall demand, this equation is subject to a Robin boundary condition at the wall:

$$-D\frac{\partial c}{\partial r}(x,R) = \mathrm{k_w} c_w. \tag{5.2}$$

At the pipe centre, a symmetry condition is imposed:

$$\frac{\partial c}{\partial r}(x,0) = 0. \tag{5.3}$$

In addition, $c(0,r) = c_0$ is considered at the inlet (due to the assumption of full mixing in junctions, see chapter 2).

As the system of equations 5.1 to 5.3 comprises a linear partial differential equation (PDE) with variable coefficients (velocity and turbulent diffusion coefficient), two solution methods are available:

- Numerical methods;
- Analytical methods.

The first approach uses a simple and well-established numerical technique. However, it does not provide much insight into the physics of the problem. In addition, the computational cost of this approach is also higher than the second approach. A discretisation of equations 5.1 to 5.3 (the 2D model) is used in this study as a verification of other models which are proposed in this chapter. However, since the aim is to provide a deep insight into the problem, an analytical approach will be pursued. A standard analytical method to solve equations 5.1 to 5.3 is to use a separation of variables:

$$c(x,r) = \sum_{n=1}^{\infty} c_{\mathrm{x}n}(x) c_{\mathrm{r}n}(r) \tag{5.4}$$

where $c_{\mathrm{x}n}$ [ML^{-3}] and $c_{\mathrm{r}n}$ [-] are the functions describing the streamwise and wall normal concentration profiles, respectively. Substituting equation 5.4 in equation 5.1, c_{x_n} can be characterised as (see e.g. Weigand (2004))

$$c_{\mathrm{x}n} = c_0 e^{-k_n x} \tag{5.5}$$

where k_n is the nth eigenvalue of the following boundary value problem

$$k_n u c_{\mathrm{r}n} + \frac{1}{r}\frac{d}{dr}\left[r\left(D + D_T\right)\frac{dc_{\mathrm{r}n}}{dr}\right] = 0 \tag{5.6}$$

which is derived by the same substitution and governs the behaviour of c_{r_n}. The value of k_n is not specified in equation 5.6. Finding the values of k_n (via a characteristic equation) for which both equation 5.6 and the boundary conditions are satisfied is called a Sturm Liouville problem (see e.g. Kreyszig (2006)). The corresponding solutions of $c_{\mathrm{r}n}$ are the eigenfunctions of the boundary value problem.

Considering constant c_w as the boundary condition (i.e. Dirichlet boundary condition), Sleicher *et al.* (1970) determined a characteristic equation for k_n in equation 5.6 based on explicit functions for u and D_T.

By assuming that all the changes in the concentration profile occur in the viscous sublayer (which is the case for high *Sc* compounds as discussed later in this chapter), Notter & Sleicher (1971) proposed $u = u_\tau y^+$ and $D_T = b\nu {y^+}^3 / Sc_T$ as explicit functions for u and D_T in equation 5.6. They solved this characteristic equation and determined the first four eigenvalues which eventually led to the determination of $c(x,r)$ in equation 5.4. Equation 2.10 was then used to determine k_f and the Notter & Sleicher (1971) *Sh* correlation.

The study by Notter & Sleicher (1971) did not consider the effect of Robin boundary conditions (equation 5.2) on the solutions for the characteristic equation for k_n. These boundary conditions were partially addressed by Biswas *et al.* (1993) who assumed a constant velocity and turbulent diffusion coefficient in the crosswise direction. With these assumptions, equation 5.6 becomes a Bessel differential equation for which a characteristic equation for k_n was determined for first-order wall demands (i.e. equation 5.2). The first three eigenvalues in this characteristic equation were then determined and calibrated for an existing network by adjusting the effective turbulent diffusion coefficient. However, since this method needs calibrations of this diffusion coefficient for each specific flow rate, it was not incorporated in water quality models like EPANET (Clark & Haught, 2005).

As higher eigenvalues decay quicker than lower ones, they will be of influence near the pipe entrance only[1] (Bird *et al.*, 2002). Consequently, the solution far away from the entrance is determined by the lowest eigenvalue of the problem. In other words, equation 5.4 is simplified to

$$c(x,r) = c_x(x)c_r(r) \tag{5.7}$$

where $c_x(x) = \langle c(x,r) \rangle$ was previously introduced in section 2.4.3 as the crosswise mean concentration and $c_r(r)$ is a dimensionless radial scaling function [-] with the following property:

$$\langle c_r(r) \rangle = 1 \tag{5.8}$$

[1] See chapter 7 for the effect of pipe entrance on the developing concentration profile.

where

$$\langle X \rangle = \frac{\int_0^R X r dr}{\int_0^R r dr} = \frac{2}{R^2} \int_0^R X r dr \tag{5.9}$$

is the crosswise averaging operator. Substituting equation 5.7 in equation 5.1 and averaging, yields

$$\langle u c_{\mathrm{r}} \rangle \frac{dc_{\mathrm{x}}}{dx} - \frac{2}{R^2} c_{\mathrm{x}} r \left(D + D_T\right) \left[\frac{dc_{\mathrm{r}}}{dr}\right]_0^R = 0. \tag{5.10}$$

By using equations 5.2 and 5.3 we obtain

$$\frac{dc_{\mathrm{x}}}{dx} \langle u c_{\mathrm{r}} \rangle + \frac{\mathrm{k_w} c_{\mathrm{r}_w}}{r_{\mathrm{h}}} c_{\mathrm{x}} = 0 \tag{5.11}$$

where $c_{\mathrm{r}_w} = c_{\mathrm{r}}(r = R)$ is the value of the radial scaling function at the pipe wall. Equation 5.11 is a first-order ordinary differential equation (ODE) in x with the solution $c_{\mathrm{x}} = c_0 e^{-kx}$ (equation 2.17), where k (the lowest eigenvalue) takes the following form

$$k = \frac{\mathrm{k_w} c_{\mathrm{r}_w}}{r_{\mathrm{h}} \langle u c_{\mathrm{r}} \rangle}. \tag{5.12}$$

The decay coefficient k can also be deduced on more detailed physical grounds. Indeed this coefficient is the ratio of the mass withdrawal rate and the total mass flux convected by the mean flow:

$$k = \frac{\oint J_w ds}{\iint u c dA}. \tag{5.13}$$

Here ds and dA are the infinitesimal perimetric and areal elements, respectively. By substituting equations 2.17 and 5.7 into equations 5.1, 5.2 and 5.3 , the governing equation for c_{r} is obtained:

$$kuc_{\mathrm{r}} + \frac{1}{r}\frac{d}{dr}\left[r\left(D+D_T\right)\frac{dc_{\mathrm{r}}}{dr}\right] = 0 \tag{5.14}$$

which is a second-order ODE with variable coefficients $u(r)$ and $D_T(r)$. As stated in chapter 4, the van Driest mixing length model will be used to determine $u(r)$ and $D_T(r)$. The boundary conditions are:

$$\frac{dc_{\mathrm{r}}}{dr}(0) = 0 \tag{5.15}$$

$$-D\frac{dc_{\mathrm{r}}}{dr}(r=R) = \mathrm{k_w}c_{\mathrm{r}_w}. \tag{5.16}$$

As stated before, k is the lowest eigenvalue of equation 5.6 and equation 5.12 is its characteristic equation (Kreyszig, 2006). Eigenvalues may have a closed form solution for simple cases, but often can only be determined numerically in more complex situations (Weigand, 2004).

Equation 5.14 is one of these complex situations, since u and D_T are non-trivial functions of r. In addition, the Robin boundary condition (equation 5.16) couples c_{r_w} and $dc_{\mathrm{r}}/dr(r=R)$ which significantly complicates solving the characteristic equation. For such cases, numerical iteration is carried out between the characteristic equation and the ODE (i.e. equation 5.14) until the eigenvalue is converged and the boundary condition is satisfied (Weigand, 2004). At each specific x and r, the value for $c(x,r)$ is then determined by applying k in equation 5.12 and considering $c_{\mathrm{x}}(x)$ and $c_{\mathrm{r}}(r)$ in equation 5.7. This solution is called the 1D solution since it separates the 2D behaviour of c into two 1D ODEs in the x and r directions.

5.2. Numerical simulation

The numerical simulation of equations 5.1 and 5.14 form the 2D and 1D models, which are discussed in sections 5.2.1 and 5.2.2, respectively. In each section, the discretisation scheme and the method for solving

the discretised equations are discussed. The numerical codes are provided in appendix B.

5.2.1. The 2D model.

In order to perform the 2D simulation, equation 5.1 is discretised via a conservative finite difference numerical method (introduced in the previous chapter). The code for the numerical solution is briefly discussed below. Figure 5.1 shows a schematic for the domain discretisation. Using a first-order upwind and second-order central difference scheme (see e.g. Hirsch (2007)) for the advective and diffusive terms respectively[2], equation 5.1 is discretised as:

$$u_j \frac{c_{i,j} - c_{i-1,j}}{\Delta x_i} - \frac{1}{r_{j+1/2}} \frac{r_{j+1}\left(D + D_{T_{j+1/2}}\right)\frac{c_{i,j+1}-c_{i,j}}{\Delta r_{j+1/2}} - r_j\left(D + D_{T_{j-1/2}}\right)\frac{c_{i,j}-c_{i,j-1}}{\Delta r_{j-1/2}}}{\Delta r_j} = 0 \tag{5.17}$$

where indices i and j are associated with the x and r directions, respectively (figure 5.1). Application of the upwind scheme for the advective term allows for explicit marching in the x direction which significantly speeds up the simulation. As the upwind scheme is only first-order accurate and has numerical diffusion (as discussed in more detail in chapter 9), it is important to check for grid convergence (which is discussed in the next section).

The Robin boundary condition at the wall (equation 5.2), symmetry condition in the pipe centre (equation 5.3) and constant concentration at the pipe entrance are, respectively, discretised as follows:

$$D\frac{c_{i,N_r-1} - c_{i,N_r}}{\Delta r_{N_r-1/2}} = \mathrm{k_w}\frac{c_{i,N_r-1} + c_{i,N_r}}{2} \tag{5.18}$$

$$c_{i,1} = c_{i,2} \tag{5.19}$$

$$c_{1,j} = c_0. \tag{5.20}$$

The following approach is used to solve discretised equations:

[2]The terms containing the velocity are referred to as the advective term and the terms containing diffusion are referred to as diffusive terms.

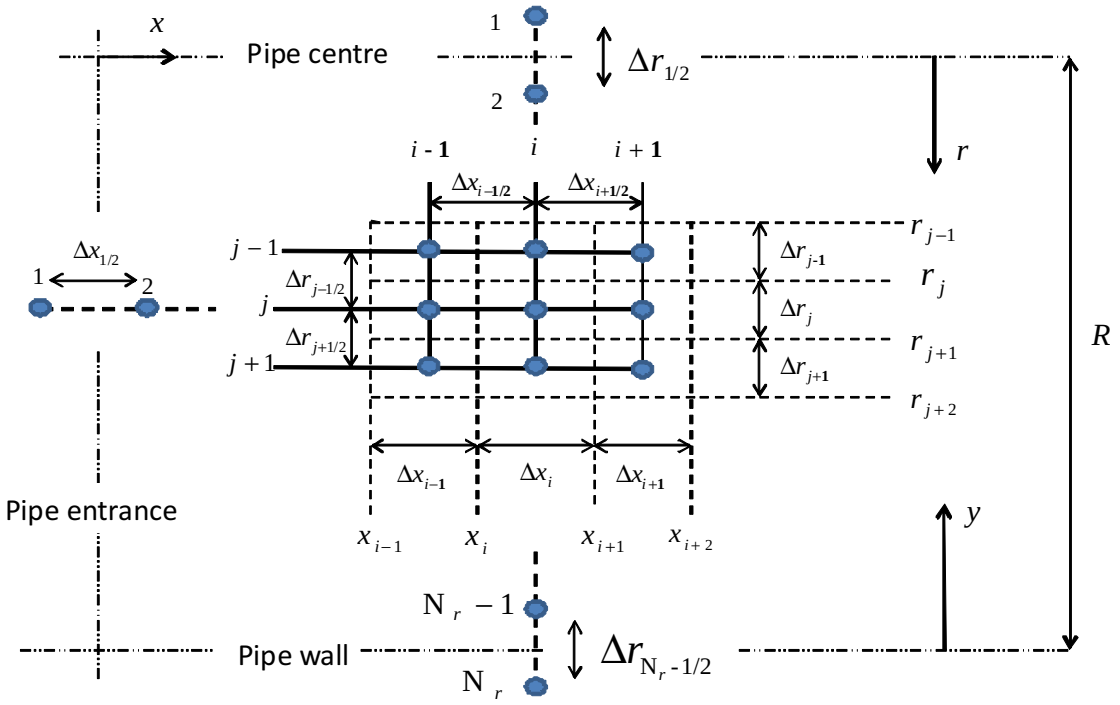

FIGURE 5.1. The 2D domain discretisation for modelling the mass transport equation.

(1) equation 5.20 is used as the boundary condition for the cells with $i = 1$;

(2) all the cells with $i = 2$ are selected;

(3) equations 5.17, 5.18 and 5.19 form a system of linear equations of the form $\mathbf{A}_c\mathbf{c} = \mathbf{r}_c$. Here, $\mathbf{A}_c$ ($N_r \times N_r$) is the matrix of coefficients, $\mathbf{c}$ ($N_r \times 1$) is the vector of unknown concentrations with the same i and $\mathbf{r}_c$ ($N_r \times 1$) is the right hand side vector for equation 5.17 (and the boundary conditions at the pipe wall and centre);

(4) the system of equations is solved;

(5) increment i and return to step 3.

5.2.2. The 1D model.

The 1D model is also discretised via the same finite difference scheme. A schematic of the grid and variables is shown in figure 5.2. On this grid, equation 5.14 is discretised as:

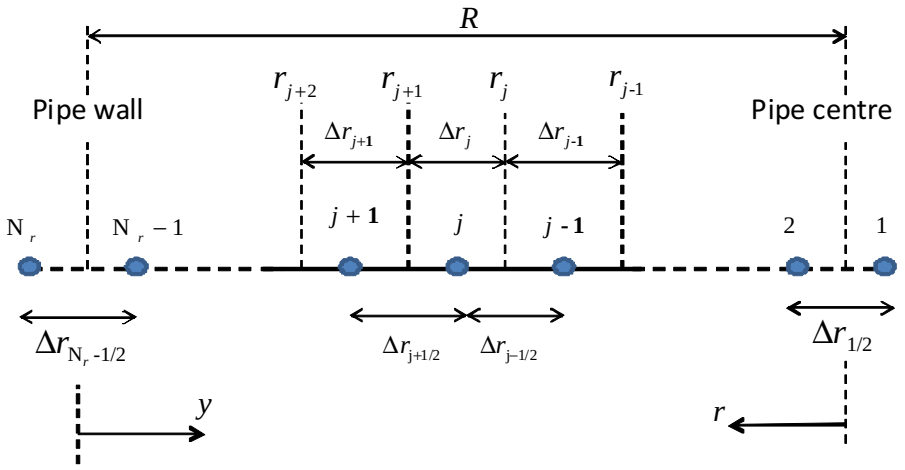

FIGURE 5.2. The 1D domain discretisation for modelling the mass transport equation.

$$ku_j c_{r_j} + \frac{1}{r_{j+1/2}} \frac{r_{j+1}\left(D + D_{T_{j+1/2}}\right)\frac{c_{r_{j+1}} - c_{r_j}}{\Delta r_{j+1/2}} - r_j\left(D + D_{T_{j-1/2}}\right)\frac{c_{r_j} - c_{r_{j-1}}}{\Delta r_{j-1/2}}}{\Delta r_j} = 0 \tag{5.21}$$

with the following boundary conditions (equations 5.15 and 5.16)

$$D\frac{c_{r_{N_r-1}} - c_{r_{N_r}}}{\Delta r_{N_r-1/2}} = k_w \frac{c_{r_{N_r-1}} + c_{r_{N_r}}}{2} \tag{5.22}$$

$$c_{r_1} = c_{r_2}. \tag{5.23}$$

Since k is not known *a priori*, the following iterative approach is carried out:

(1) an initial value for $k = k_w / r_h U$ and $c_r = 1$ is assumed (see section 5.3.1);
(2) equation 5.21 is solved numerically and the profile for c_r and the value for c_{r_w} are determined;
(3) equation 5.12 is used to update k;
(4) if the updated value of k is converged in the form of the relative residual $E < 10^{-9}$ (see chapter 4), the solution is converged;
(5) in the case that k is not converged, step 2 is repeated using the updated k.

5.3. Results

Numerical results for the 2D and 1D models in the previous section are presented here. Both models rely on $u(r)$ and $D_T(r)$ profiles by the modified van Driest mixing length model (chapter 4). A number of $N_r = 150$ and 300 cells were used in the 2D and 1D model, respectively. The cells were logarithmically distributed in the crosswise direction with more resolution near the wall. For the 2D and 1D models, such distribution resulted in 18 and 36 cells in the viscous sublayer ($y^+ < 5$), respectively. A grid convergence study for a doubled resolution was also performed, which showed no practical difference in the results. For the 2D model, the cells in the x direction were also logarithmically distributed. The simulation was performed for a length equal to $10^5 R$. A number of 10^3 cells were logarithmically distributed, which resulted in 375 cells in $x < R$ (with the first cell at $x/R = 10^{-3}$). In addition, a doubled resolution in the x direction is also used to check grid convergence.

The results include concentration profiles and the decay coefficients. The profiles of the 1D model are verified against the 2D model profiles in section 5.3.1. A comparison between the experimental results for k and the 1D model was also provided. In section 5.3.2, the 1D model results for k are compared with the EPANET parameterisation.

5.3.1. Decay coefficients and concentration profiles.

For verification of the 1D against the 2D model, a comparison was undertaken for $Re = 10^6$, $Sc = 10^3$, and $\mathrm{k_w}/U = 10^{-4}$. It will be observed in this section that the value for $\mathrm{k_w}/U$ is chosen to have a considerable concentration gradient in the viscous sublayer. The decay coefficient k in the 2D model is determined based on the e folding length L_e, defined as the streamwise distance from the origin at which $\langle c(x,r)\rangle / c_0 = e^{-1}$. Once the e folding length is determined, the 2D decay coefficient is defined as $k = 1/L_\mathrm{e}$. The decay coefficient for the 1D model is a part of the solution (equation 5.12). For the case considered here, the 1D and 2D models give $kr_\mathrm{h} = 2.01 \times 10^{-5}$ and 2×10^{-5}, respectively.

The near wall concentration profiles at $kx = 0$, 0.5 and 1 are shown in figure 5.3 for both models. The initial concentration profile at $x = 0$ for the 2D model is constant (c_0). The 1D model describes the equilibrium behaviour of c (i.e., the behaviour sufficiently far away from the pipe entrance). Therefore, at

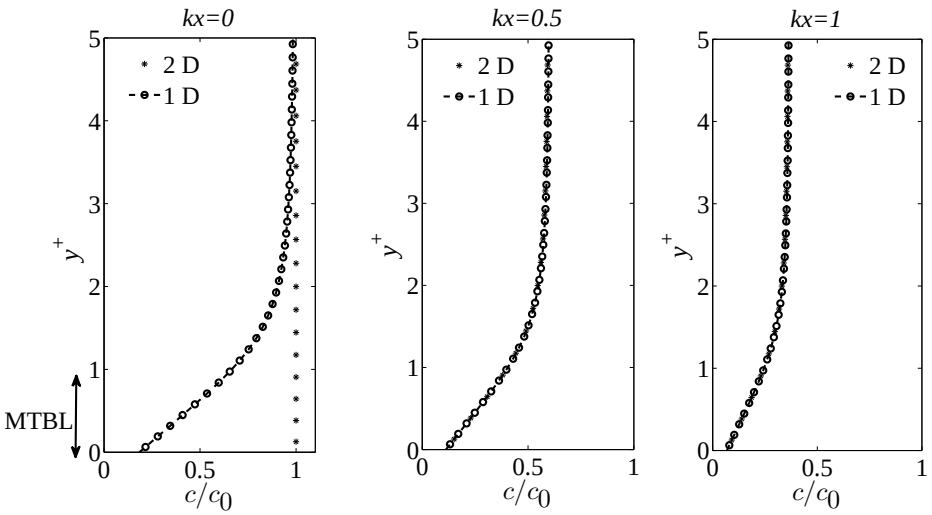

FIGURE 5.3. Comparison of the concentration profiles in the 1D (solid line) and 2D models (stars) for $Sc = 10^3$, $Re = 10^6$ and $k_w/U = 10^{-4}$.

$kx = 0$ the profiles for the 1D and 2D models are very different. However, from $kx = 0.5$ onward, the two solutions are almost identical. This implies that the assumptions made for the derivation of the 1D model are valid. Entrance effects are discussed in chapter 7.

Another observation from figure 5.3 is that the concentration profile has an approximately linear behaviour very close to the wall. Similar to the case of the viscous sublayer in which momentum transport is dominantly molecular, the mass transport in a layer very close to the wall is dominantly governed by molecular diffusion. This layer will be referred to as the mass transfer boundary layer (MTBL) and will be characterised in chapter 7.

Figure 5.4 compares the decay coefficients between the 1D model and experimental data of chlorine removal due to the wall demand (Clark & Haught, 2005; Mutoti *et al.*, 2007). The experimental data span a range of Reynolds numbers from 2000 to 8000 and were obtained using different pipe materials, such as galvanized, cast, and ductile iron. Each of the experimental points corresponds to a specific velocity, pipe diameter and k_w. The 1D model curve of the decay coefficient was obtained by fixing *Re* and varying k_w such that $Re = 5000$ (as the value close to the average of the applied *Re* range in the experimental data). Results of the 1D model show good agreement with the experimental data.

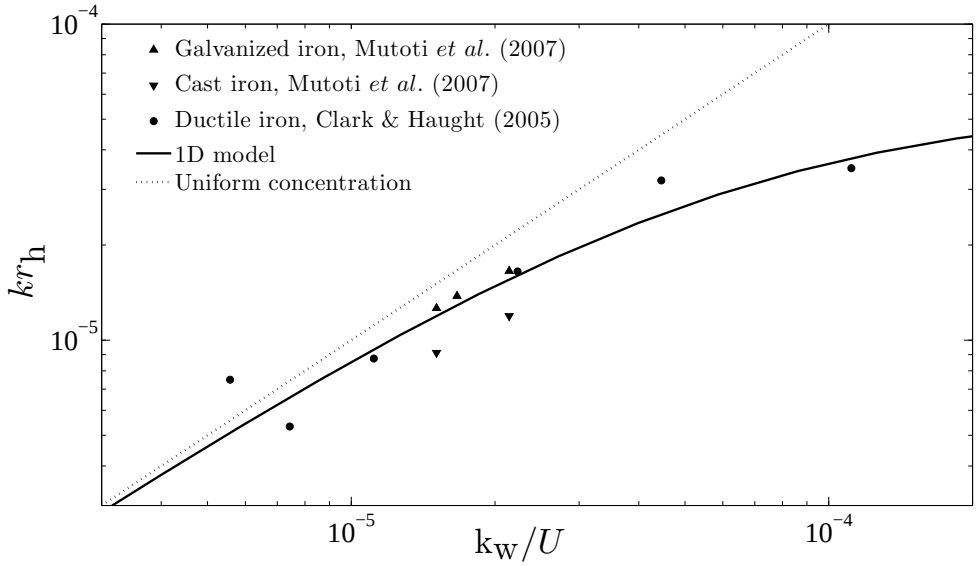

FIGURE 5.4. Comparison of the model decay coefficient and the experimental data of ductile (Clark & Haught, 2005), cast and galvanized (Mutoti *et al.*, 2007) iron pipes.

The decay coefficient varies linearly with k_w/U for small k_w/U. For high *Sc* compounds (which are characterised later on), all relevant processes take place in the viscous sublayer (figure 5.3) and so, the averaged streamwise advective mass flux $\langle uc_r \rangle$ can be approximated by $U\langle c_r \rangle \approx U$ (making use of equation 5.8). In addition, when k_w/U is very low the concentration profile is uniform (fully mixed), so $c_{r_w} \approx \langle c_r \rangle = 1$. Consequently, $k = k_w/r_h U$ which is plotted in figure 5.4 with a dashed line. For sufficiently high k_w/U, diffusion of the solute through the MTBL becomes the limiting factor, so that *k* becomes independent of k_w/U as can be observed in figures 5.4 and 5.5. The decay coefficient *k* depends weakly on *Re* (figure 5.5) with an approximate factor of two difference between $Re = 10^4$ and $Re = 10^6$ for high k_w/U. For all *Re*, the uniform concentration assumption holds for $k_w/U \leq 10^{-6}$.

The corresponding concentration profiles are shown in figure 5.6. The concentration profiles are very similar for different *Re*, and the curves shown in figure 5.6 are typical for c_r variation for $Re = 10^4$, 10^5, and 10^6 and $Sc = 10^3$. Figure 5.6 confirms that for small k_w/U, c_r is approximately constant throughout the cross-section. For $k_w/U = 10^{-6}$ the concentration is practically uniform while there is a significant difference between the wall and average concentration for $k_w/U > 10^{-6}$. Because the significant changes in

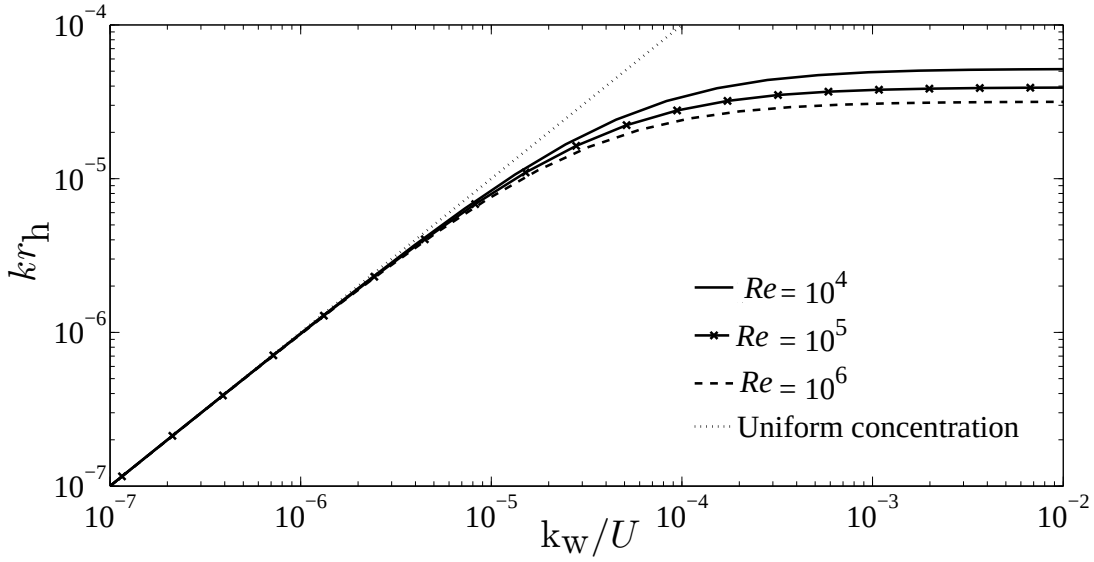

FIGURE 5.5. Decay coefficient curves for different Reynolds numbers at $Sc = 10^3$.

the concentration profile take place in the viscous sublayer, $\langle uc_r \rangle \approx U$ which means that k (equation 5.12) is solely determined by c_{r_w}. The fact that the significant changes of the concentration profile take place in the viscous sublayer will allow for a high Sc asymptotic solution to be derived in section 5.4.

5.3.2. Comparison with EPANET.

As stated in chapter 2, the Sh correlation by Notter & Sleicher (1971) is the correlation used in EPANET-based models to determine the decay coefficient due to first-order wall demand in equation 2.18. Figure 5.7 shows the results for k that follow from equation 2.18 (EPANET) and equation 5.12 (1D model) for $Re = 10^4$ and $Sc = 10^3$.

Excellent agreement is observed between the 1D numerical approach curve and EPANET. This agreement implies that the Robin boundary condition is consistent with the Dirichlet boundary condition (applied in the study by Notter & Sleicher (1971)) in terms of k when Sc is sufficiently high. Under such conditions, $kr_h \ll 1$ and therefore, the Robin and Dirichlet boundary conditions behave nearly identically. However, the agreement between the EPANET approach and the 1D model breaks down for $Sc < 100$ as will be shown in

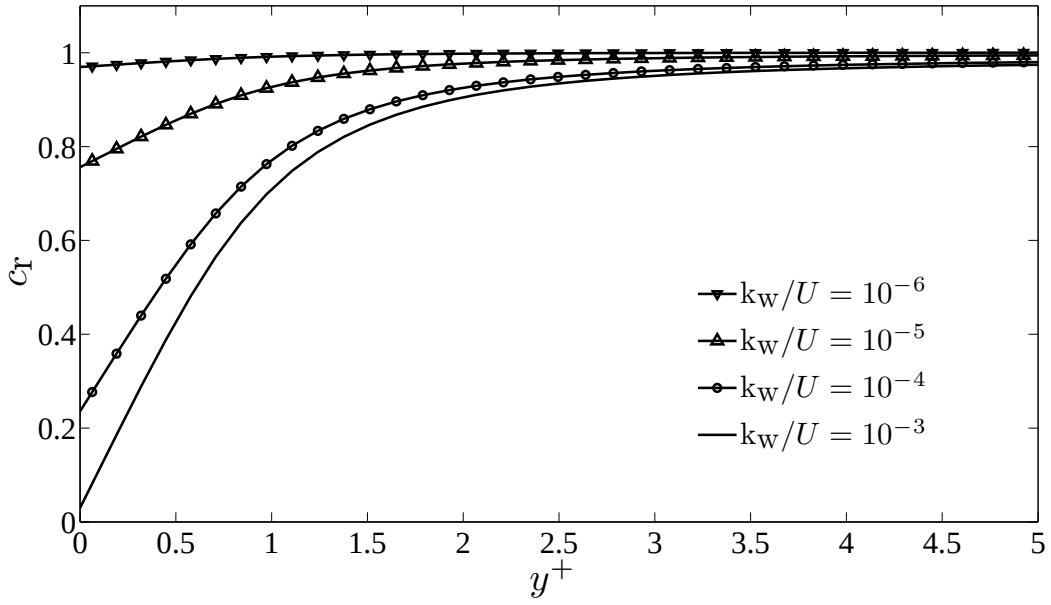

FIGURE 5.6. Radial concentration profiles at $Sc = 10^3$, $Re = 10^4 - 10^6$, and various k_w/U.

the next section. It is concluded that for high *Sc* compounds (which will be shown in the next section to be the case for chlorine), the effect of the difference in the boundary condition is small, and the wall demand parameterisation in EPANET provides accurate decay coefficients for smooth walls.

5.4. Analytical solution

Figure 5.6 indicates that for high *Sc*, the entire wall demand problem is confined to the viscous sublayer. Figure 5.8 shows the radial mass flux (obtained with the 1D model) at $Re = 10^4$ and $Sc = 10^3$. The total mass flux $J_{tot} = (D + D_T)dc/dy$ is decomposed in the molecular diffusive flux $J_D = Ddc/dy$ and turbulent diffusive flux $J_T = D_T dc/dy$. Here, the change in coordinate system from r to y is justified because the viscous sublayer (with a thickness of $5\nu/u_\tau$) is much smaller than R and therefore, $R - 5u_\tau/\nu \approx R$. In other words, the effect of wall curvature is negligible. The validity of this assumption is shown in appendix A.

It is seen that J_{tot} is practically constant and equal to the wall mass flux at the wall ($J_w = k_w c_w$), and that turbulent mass transfer is dominant for $y^+ > 1$. Therefore, there is a full analogy with the constant stress

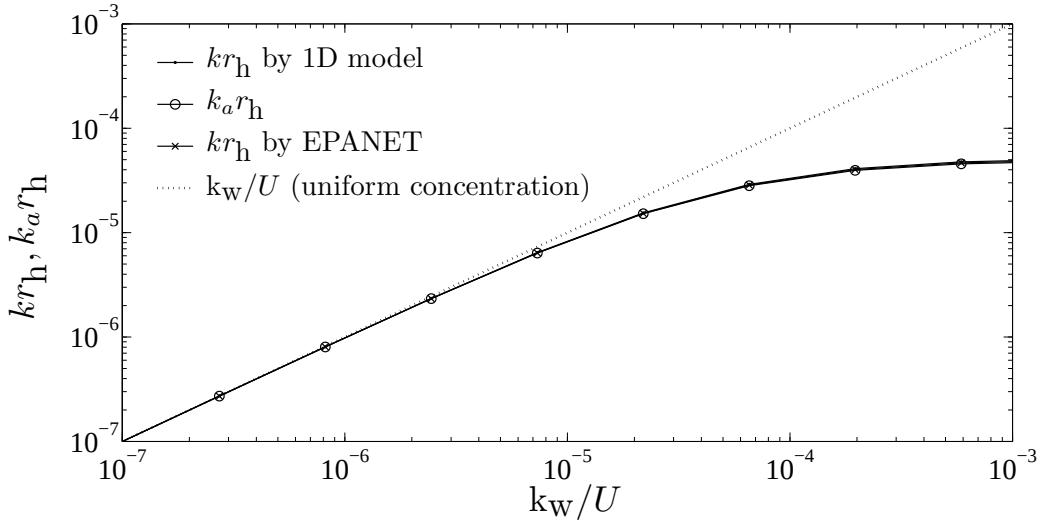

FIGURE 5.7. Comparison of the decay coefficients in EPANET, the 1D numerical model and analytical solution for $Re = 10^4$ and $Sc = 10^3$ (similar results hold for other *Re* values).

property of a turbulent inner layer, and it is possible to approximate the near wall behaviour by

$$(D + D_T)\frac{dc_\mathrm{r}}{dy} = \mathrm{k_w} c_{\mathrm{r}_w}. \tag{5.24}$$

In order to obtain an analytical solution, equation 5.24 needs to be augmented with a boundary condition. Since equation 5.16 is already used, a natural candidate is that c_r tends to one away from the wall

$$c_\mathrm{r}(y \to \infty) = 1. \tag{5.25}$$

As the entire process takes place in the viscous sublayer, it is convenient to change to plus units:

$$\frac{u_\tau}{\nu}(D + D_T)\frac{dc_\mathrm{r}}{dy^+} = \mathrm{k_w} c_{\mathrm{r}_w}. \tag{5.26}$$

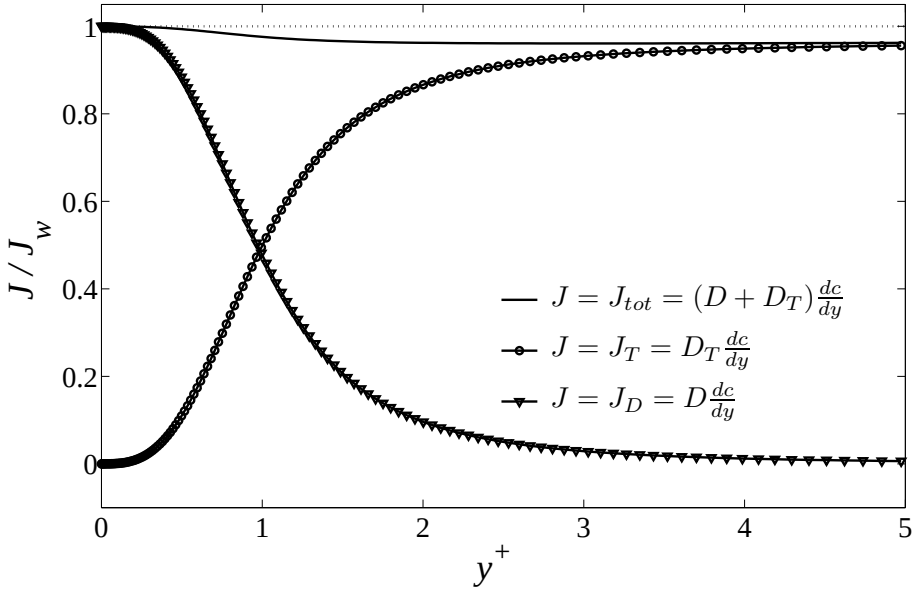

FIGURE 5.8. Normalized mass flux budget in the viscous sublayer at $Re = 10^4$ and $Sc = 10^3$; J represents the mass flux and $J_w = \mathrm{k_w} c_w$ is the mass flux at the wall.

In order to obtain an analytical solution, a simple expression for D_T in the viscous sublayer is required for which $\nu_T/\nu = by^{+3}$ (equation 4.9) is used. Using $Sc_T = \nu_T/D_T$ and assuming $Sc_T = 1$ results in:

$$\left(1 + \left(\alpha y^+\right)^3\right) \frac{dc_\mathrm{r}}{dy^+} = \beta c_{\mathrm{r}_w} \tag{5.27}$$

where

$$\alpha = \sqrt[3]{bSc}, \;\; \beta = \frac{\mathrm{k_w} Sc}{u_\tau}. \tag{5.28}$$

The exact solution to equations 5.27 and 5.25 is

$$c_{\mathrm{r}_a} = \frac{c_{\mathrm{r}_w}}{6\alpha}\left(\beta \ln \frac{(\alpha y^+ + 1)^2}{\left(\alpha^2 y^{+2} - \alpha y^+ + 1\right)} + 2\sqrt{3}\beta \arctan\left(\frac{\sqrt{3}\,(2\alpha y^+ - 1)}{3}\right) + 6\alpha + \frac{\sqrt{3}}{3}\pi\beta\right) \tag{5.29}$$

where

$$c_{\mathrm{r}_w} = c_{\mathrm{r}_a}(y^+ = 0) = \frac{1}{1 + \frac{2\pi\sqrt{3}\beta}{9\alpha}}. \tag{5.30}$$

Equations 5.29 and 5.30 describe the radial concentration profile and wall concentration for high *Sc*. It should be noted that equation 5.27 is formally only valid very close to the wall since equation 4.9 is also only valid inside the viscous sublayer (see figure 4.2). As was shown in figure 5.6, this is the region in which c_{r} changes considerably; outside the viscous sublayer, c_{r} is practically constant. Consequently, the overprediction in ν_T of equation 4.9 outside the viscous boundary layer only very marginally affects the accuracy of the solution. This is clearly demonstrated by the close agreement between the numerical and analytical solution in figure 5.9. The solution given here is consistent with another suggested approximate solution for constant c_w (Garcia-Ybarra & Pinelli, 2006).

An analytical expression for k is obtained by approximating $\langle u c_{\mathrm{r}} \rangle \approx U$ (which is applicable because c_{r} only varies in the viscous sublayer), and substituting equation 5.30 into equation 5.12 to give

$$k_a = \frac{1}{U r_{\mathrm{h}}} \frac{\mathrm{k_w}}{1 + \frac{2\pi\sqrt{3}\beta}{9\alpha}}. \tag{5.31}$$

Using equation 2.18, the *Sh* correlation for the analytical solution of the wall demand problem is given by

$$Sh = \frac{9\sqrt[3]{b}}{\pi\sqrt{3}} Re_\tau Sc^{1/3} = 0.163 Re_\tau Sc^{1/3}. \tag{5.32}$$

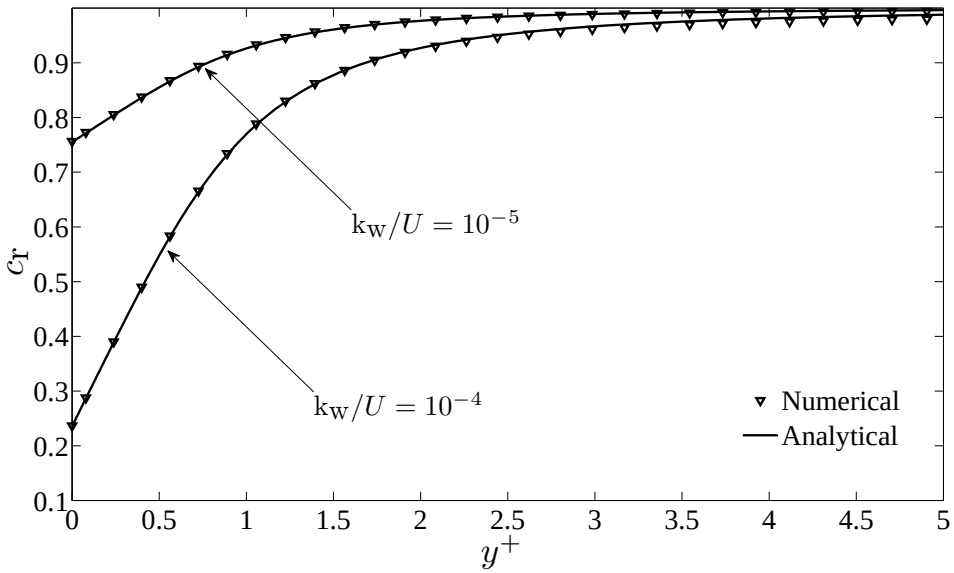

FIGURE 5.9. Comparison of concentration profiles for the numerical model and analytical solution for $Re = 10^6$ and $Sc = 10^3$.

Using equations 2.7 and 2.21, it is straightforward to show that for smooth pipes, $Re_\tau \approx 0.1Re^{0.875}$ and therefore, $Sh = 0.016Re^{0875}Sc^{1/3}$, which is in good agreement with the Notter & Sleicher (1971) *Sh* correlation (equation 2.29). This confirms once more that the EPANET approach for parameterisation of first-order wall demand is appropriate. In chapter 7, it will be shown that this is not a coincidence: *all* boundary conditions with explicit dependency to c_w have a *Sh* correlation of the form of equation 5.32 for high *Sc* compounds.

It may be questioned for which *Sc* equations 5.31 and 5.32 are valid. For this reason, the 1D numerical model results (which are valid for all *Sc*) are compared to the high *Sc* approximation, equations 5.31 and 5.32. Defining

$$\mathsf{e} = \frac{|k_a - k|}{k} \tag{5.33}$$

as the relative error (for the analytical decay coefficient), figure 5.10 shows this error as a function of *Sc* and

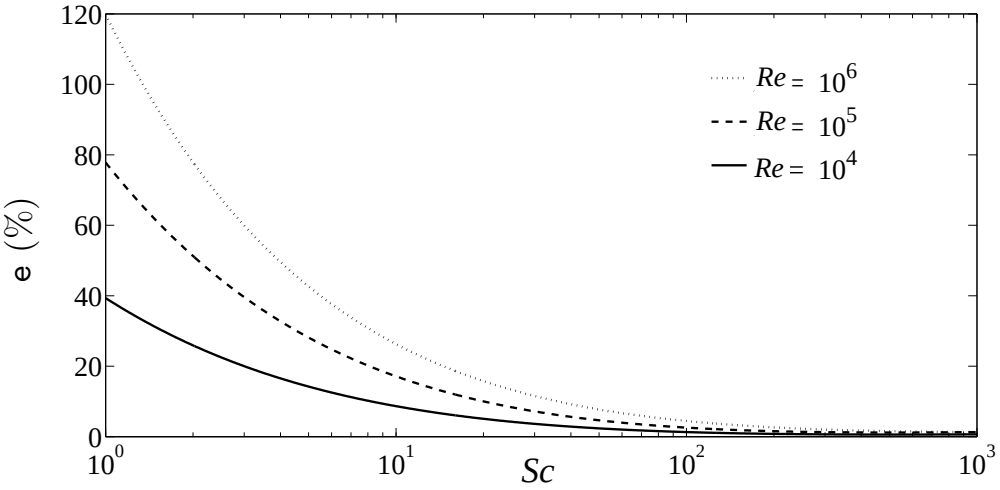

FIGURE 5.10. Deviation of the analytical decay coefficient k_a (valid for high *Sc*) from the numerical decay coefficient k (valid for all *Sc*) as a function of *Sc*.

Re. Accepting a relative error margin of 5% (which occurs for $Re = 10^6$), the high *Sc* approximation is valid for $Sc > 100$. The same relative error margin was also used by Notter & Sleicher (1971) to propose the *Sh* correlation in equation 2.29 for $Sc > 100$.

5.5. Summary

A 1D model was derived which can reliably predict the decay coefficient as well as the radial variations in the concentration profile for a fully developed pipe flow. Velocity and turbulent diffusion coefficient profiles were modelled by using a modified van Driest mixing length model. Solutions for the 1D model were obtained using a fast and robust iterative method. The comparison between the decay coefficients of the 1D numerical model and EPANET showed that for sufficiently high *Sc*, the EPANET approach for parameterisation of first-order wall demands is appropriate. In addition, it was demonstrated for $Sc = 10^3$ that regardless of the Reynolds number, the concentration profile is approximately uniform for $k_w/U < 10^{-6}$. In this case, the effect of the boundary layer on the concentration profiles can be ignored. Results of the 1D model showed that the concentration profiles are practically independent of *Re* for constant *Sc*.
With a maximum error of 5% in the asymptotic value of k and for $Sc > 100$, all relevant aspects of the wall

demand problem take place within the viscous sublayer. Based on this observation, an analytical solution for the concentration profiles in the viscous sublayer was derived. Verification of the concentration profiles and decay coefficients calculated by the analytical solution showed excellent agreement with the 1D model and EPANET.

CHAPTER 6

Combined wall and bulk demand

The study in this chapter extends the study in chapter 5 by considering combined first-order bulk and wall demands and therefore, it addresses the second research question posed in section 2.6: do wall and bulk demand influence each other, and under which circumstances?

Most of the governing equations were introduced in the previous chapter. The minor changes due to the bulk demand are discussed in section 6.1 and results are provided in section 6.2. The results include concentration profiles and decay coefficients for various combinations of wall and bulk demand coefficients, and are categorized into a case where bulk demand dominates the wall demand and a case where both of the demands are of the same order of magnitude. A summary of the chapter is also provided in section 6.3.

6.1. Governing equations

For the case where first-order bulk demand is included, the term $\dot{\mathrm{r}} = \mathrm{k_b} c$ appears in equation 3.25. With this term included, the governing equation for c_r becomes[1]:

$$kuc_\mathrm{r} + \frac{1}{r}\frac{d}{dr}\left[r\,(D+D_T)\,\frac{dc_\mathrm{r}}{dr}\right] - \mathrm{k_b} c_\mathrm{r} = 0 \tag{6.1}$$

and the decay coefficient k will be of the form:

$$k = \frac{\mathrm{k_w}}{r_h}\frac{c_{\mathrm{r}_w}}{\langle uc_\mathrm{r}\rangle} + \frac{\mathrm{k_b}}{\langle uc_\mathrm{r}\rangle}. \tag{6.2}$$

[1] See the method for derivation of equation 5.14 in chapter 5.

Note that $\langle c_\mathrm{r} \rangle = 1$ and therefore, does not appear in the numerator of the second term. In order to determine k and c_r, the iterative 1D model, introduced in chapter 5, is applied. In order to produce an accurate velocity prediction in the outer layer, the HRN $\mathsf{k}-\varepsilon$, model introduced in chapter 4, is used to provide the profiles of u and D_T.

6.2. Results

The equation for the decay coefficient k, equation 6.2, may be rearranged as:

$$k = \frac{\mathrm{k_b}}{\langle u c_\mathrm{r} \rangle}(\Lambda + 1) \tag{6.3}$$

where

$$\Lambda = \frac{\mathrm{k_w}}{\mathrm{k_b} r_\mathrm{h}} c_{\mathrm{r}_w} \tag{6.4}$$

is the ratio of wall and bulk decay coefficients. The following cases can be distinguished:

(1) $\Lambda \gg 1$, Wall demand dominated;
(2) $\Lambda \ll 1$, Bulk demand dominated;
(3) $\Lambda \approx 1$, Mixed demand.

The first case was covered in chapter 5. In this section, cases 2 and 3 are discussed. Similar to the study in chapter 5, which was performed for a wide range of $\mathrm{k_w}$, it is also desirable here to consider a wide range of $\mathrm{k_b}$. As for the dimensionless parameter $\mathrm{k_w}/U$, $\mathrm{k_b}$ is also made dimensionless:

$$Da = \frac{\mathrm{k_b} r_\mathrm{h}}{U}. \tag{6.5}$$

Here, the dimensionless group *Da* is known as the Damköhler number (Bird *et al.*, 2002). A wide range of *Da* is considered in this chapter to capture a wide range of chlorine bulk demand (see the discussion in section 6.3). It was shown in chapter 5 that the results are insensitive to *Re* as long as k_w/U is constant. Preliminary simulations in this study showed that the same argument holds for the case of *Da*. Consequently, $Re = 10^5$ is considered for all of the simulations in this chapter (which is the average *Re* in a typical distribution network (Ho, 2008)). In addition, the value of $Sc = 1000$ is considered to be a fair approximation for chlorine.

6.2.1. Bulk demand dominated ($\Lambda \ll 1$).

In the absence of wall demand (i.e. $k_w = 0$), the expression for the decay coefficient k (equation 6.2) simplifies to

$$k = \frac{k_b}{\langle u c_r \rangle}. \tag{6.6}$$

The Robin boundary condition at the wall now changes to a Neumann boundary condition $dc_r/dr = 0$. The (numerical) decay coefficient k is plotted against *Da* with a solid line (figure 6.1), revealing a practically linear relationship. Recall from chapter 5, $\langle u c_r \rangle \approx U$. Using the same approximation, equation 6.6 is simplified to

$$k = \frac{k_b}{U} \tag{6.7}$$

which is the decay coefficient for the uniform concentration condition. Equation 6.7 is plotted in figure 6.1 with a dashed line. It is observed that equations 6.6 and 6.7 are identical for small *Da*. However, a slight deviation between the two equations can be observed for large *Da*. In order to study this deviation in more detail, the ratio of the numerical decay coefficient (equation 6.6) to the uniform concentration condition (equation 6.7) is shown in the inner plot of figure 6.1. This figure shows that equations 6.6 and 6.7 start to deviate from each other when $Da > 10^{-3}$. However, even at $Da = 1$, the deviation is less than 5%. This

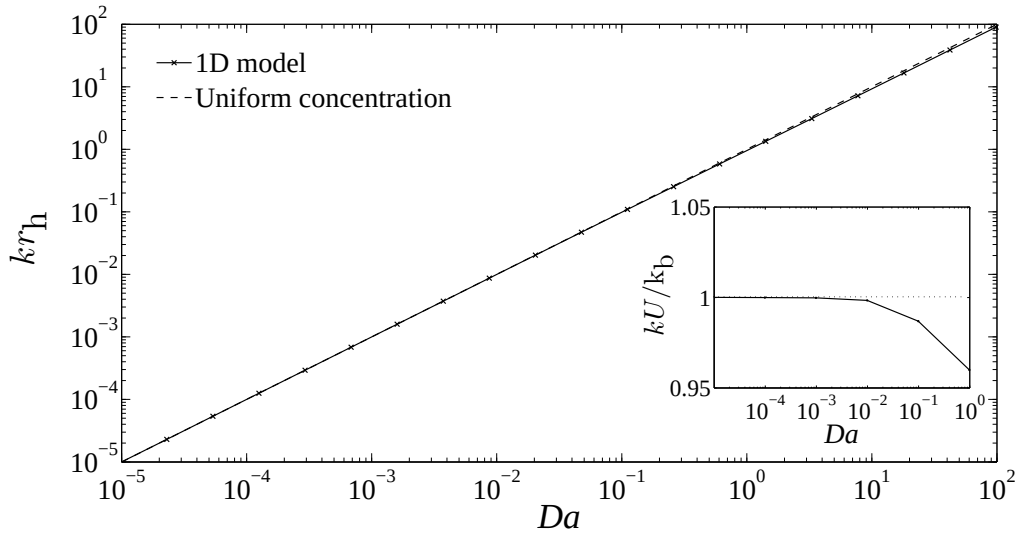

FIGURE 6.1. Bulk demand dominated decay coefficient (outer plot) and the ratio of the two bulk decay coefficients (inner plot).

implies that the assumption of $\langle uc_r \rangle \approx U$ holds for a very large range of Da.

Figure 6.2 shows the concentration profiles at different Da in the viscous sublayer (A) and bulk region (B). It is seen that the wall concentration is a function of Da. For $Da < 10^{-3}$, the wall concentration is almost equal to $\langle c_r \rangle$. However, the difference between c_{r_w} and $\langle c_r \rangle = 1$ gets larger as Da increases.

It is also seen in this figure that for $Da < 10^{-3}$, $c_r(r=0) \approx \langle c_r \rangle = 1$. For $Da > 10^{-3}$, the concentration profile is no longer uniform in the bulk region. An intriguing observation is that regardless of Da, all the concentration profiles coincided at $y^+ \approx 1700$.

The deviation of $c_r(r=0)$ and c_{r_w} from $\langle c_r \rangle$ occurs for $Da > 10^{-3}$ as is shown in figure 6.3. Due to the (molecular) limited mixing in the viscous sublayer, the deviation of c_{r_w} increases much faster than $c_r(r=0)$ (which is located in a region with a much larger turbulent diffusivity). The criterion for the concentration uniformity ($c_{r_w} = c_r(r=0) = \langle c_r \rangle$ when $Da < 10^{-3}$) in figure 6.3 is consistent with the inner plot of figure 6.1 (which shows that the assumption of $\langle uc_r \rangle \approx U$ holds for $Da < 10^{-3}$).

6.2.2. Mixed demand ($\Lambda \approx 1$).

For mixed demand, the iterative solution of equation 6.2 for a range of k_w/U and Da results in decay

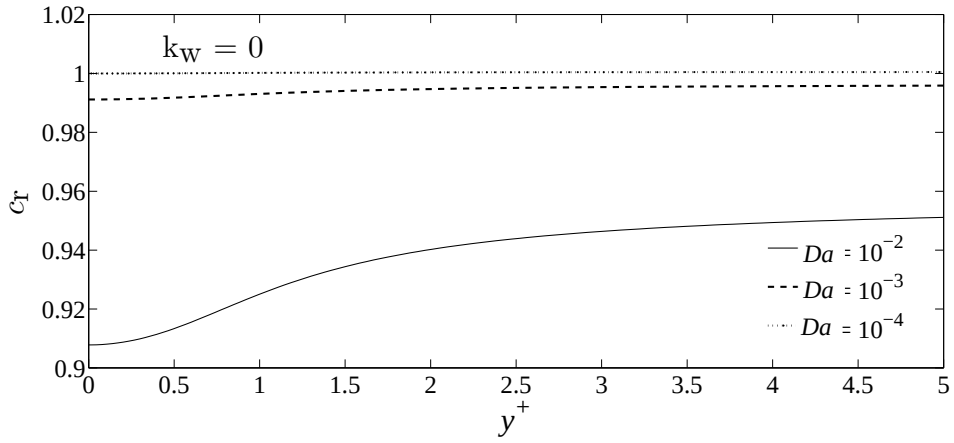

(A) Viscous sublayer

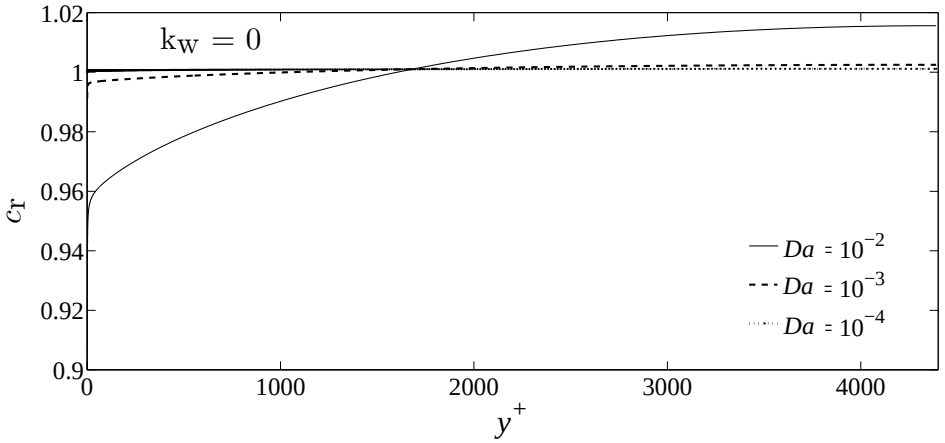

(B) Bulk flow

FIGURE 6.2. Concentration profiles for the bulk demand dominated case.

coefficients shown in figure 6.4. For $\Lambda \ll 1$, the value of the decay coefficient converges to the bulk demand dominated decay coefficient (which is shown in figure 6.1). Similarly, it is observed that the total decay approaches the wall demand dominated decay coefficient (figure 5.5) for $\Lambda \gg 1$.

To evaluate the EPANET assumption on the independency of wall and bulk demands, it is now assumed that wall and bulk demands do not influence each other because the former takes place in the viscous sublayer, whereas the latter mainly takes place in the bulk. This means that the analytical expression for c_{r_w}

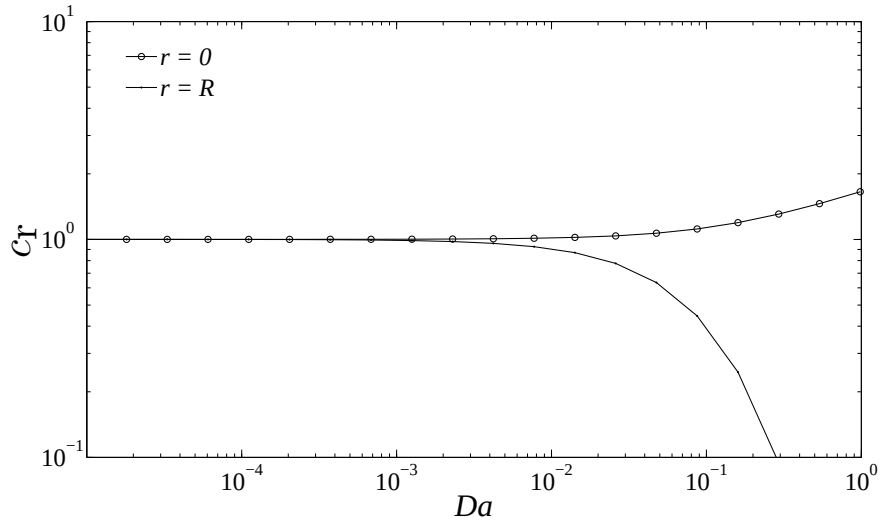

FIGURE 6.3. Variation of wall and mid-channel concentrations versus *Da*.

(equation 5.30) is applicable. If, in addition, it is assumed that $\langle uc_{\mathrm{r}} \rangle \approx U$, the following analytical decay coefficient is obtained:

$$k_a = \frac{\mathrm{k_b}}{U}(\Lambda_a + 1). \tag{6.8}$$

Here

$$\Lambda_a = \frac{\mathrm{k_w}}{r_{\mathrm{h}}\mathrm{k_b}\left(1 + \frac{2\pi\sqrt{3}\beta}{9\alpha}\right)} \tag{6.9}$$

is an analytical formulation for Λ. The parameters α and β were introduced in chapter 5 (equation 5.28). Equation 6.8 is consistent with the decay coefficient used in EPANET. In this package, the wall decay coefficient term (equivalent to $\mathrm{k_b}\Lambda_a/U$ in equation 6.8) is determined using the *Sh* correlation by Notter & Sleicher (1971), which is derived for the constant c_w (Dirichlet boundary condition), and the bulk decay coefficient is assigned as in equation 6.7 (i.e. $\mathrm{k_b}/U$) (Rossman, 2000).

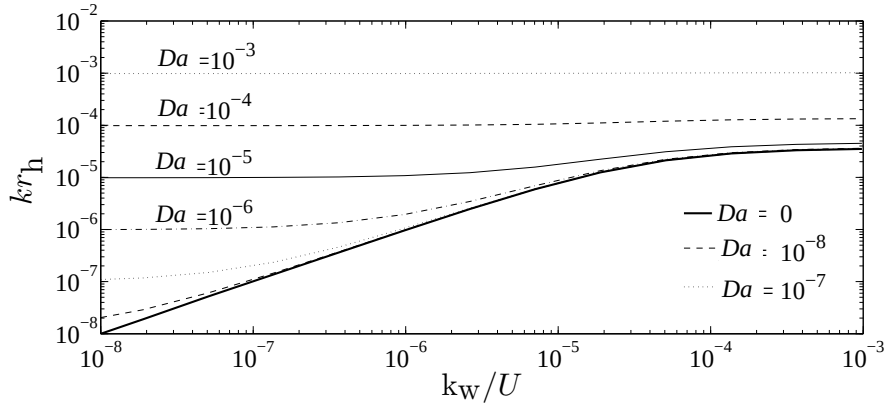

(A) 2D plot

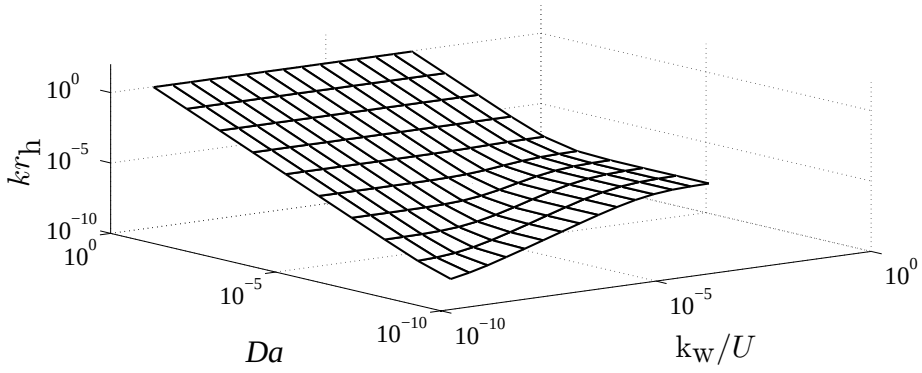

(B) 3D plot

FIGURE 6.4. Mixed demand decay coefficient.

To check the accuracy of the analytical approximation (equation 6.8), the relative error e (equation 5.33) is calculated for numerical and analytical decay coefficients. Figure 6.5 shows contours (isolines) of e. For $Da < 10^{-3}$, the error is less than 0.1%. The error slightly increases when Da is larger than 10^{-3}, the reason for which is that the assumption of $\langle uc_r \rangle = U$ no longer holds. This was discussed in detail in the previous section. Despite some small deviations (maximum $\mathsf{e} = 5\%$), equation 6.8 is a good approximation for the

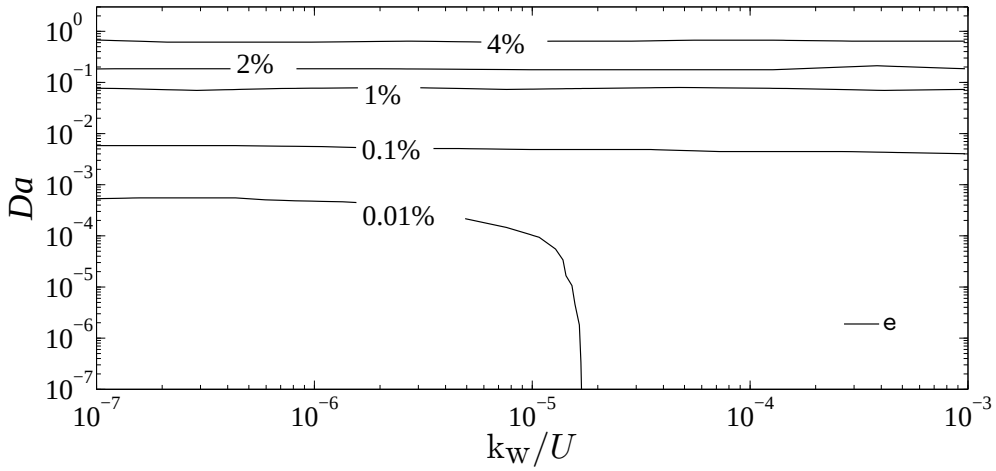

FIGURE 6.5. Contours of e

total decay coefficient for high *Sc* compounds (like chlorine) as long as $Da < 1$ (the average *Da* in a typical network is discussed in section 6.3).

The concentration profiles for the mixed demand case are shown in figure 6.6. It was found in chapter 5 that wall demand only affects the wall concentration, c_{r_w}. In addition, results of the previous section showed that the bulk demand affects the entire concentration profile. In the case of mixed demand, the entire profile is also affected.

It is seen in figure 6.6 that the value of c_{r_w} is not only a function of *Da* but also k_w/U. The bulk concentration profile is only affected by the value of *Da*. Based on observations so far, a diagram may be constructed for the validity of the assumption of uniform concentration profile. The results may be categorized with respect to k_w/U and *Da*. Figure 6.7 shows different regions for which the uniform concentration assumption is valid or violated. For $Da > 10^{-3}$ both viscous sublayer and bulk layer uniformity assumptions are violated. The viscous sublayer uniformity remains valid for $Da < 10^{-3}$ and $k_w/U < 10^{-6}$. This assumption is violated for $k_w/U > 10^{-6}$.

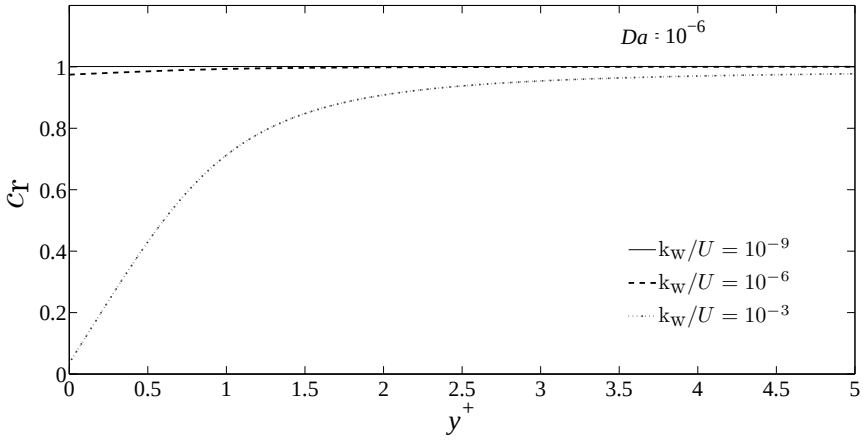

(A) Viscous sublayer close up at $Da = 10^{-6}$

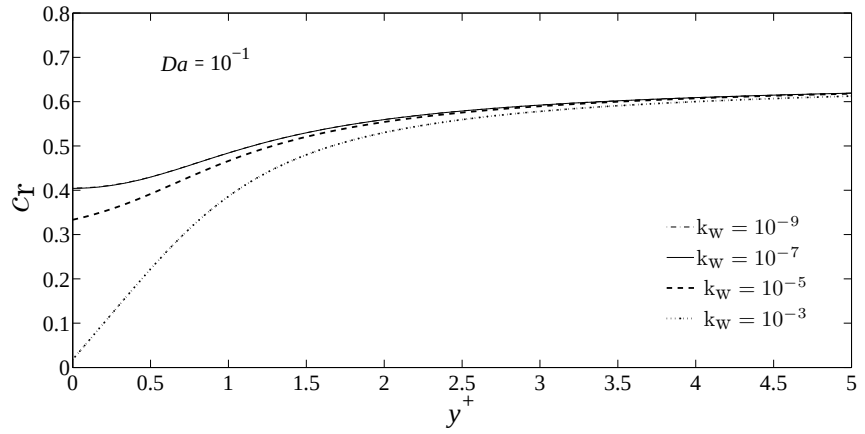

(B) Viscous sublayer close up at $Da = 10^{-1}$

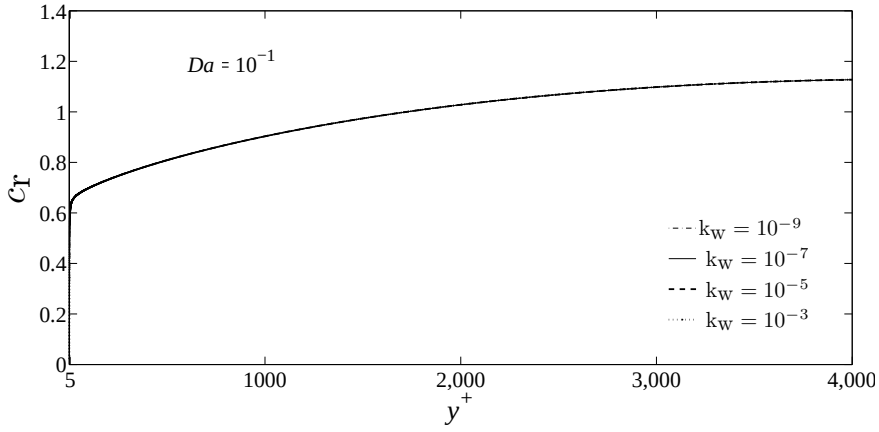

(C) Bulk layer at $Da = 10^{-1}$

FIGURE 6.6. Concentration profiles for the mixed demand case.

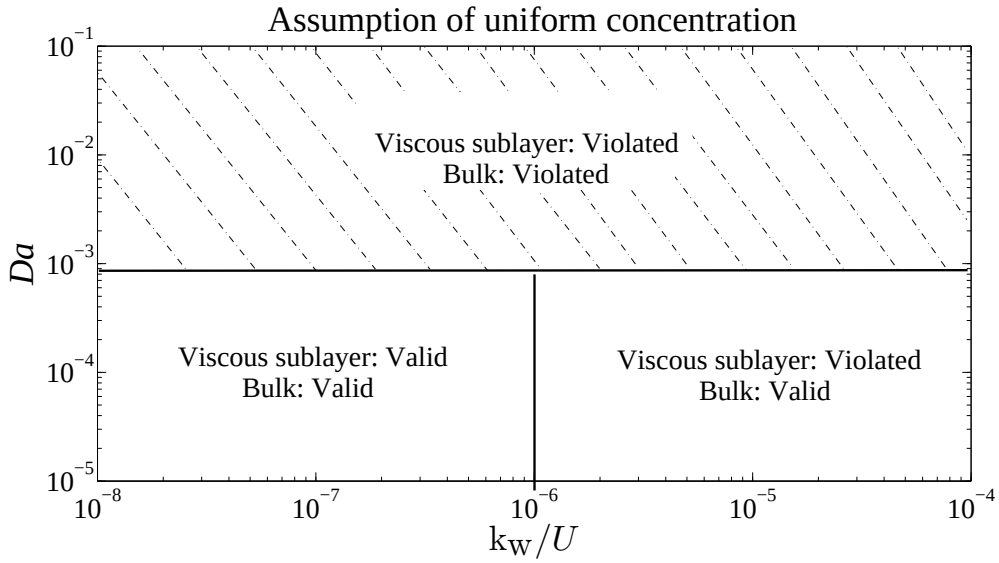

FIGURE 6.7. Concentration uniformity regions of the mixed demand case.

6.3. Summary

Combined, high *Sc*, first-order wall and bulk demands in turbulent flows were discussed in this chapter. Using the ratio of wall to bulk demand Λ, three cases could be distinguished; wall demand domination, bulk demand domination and mixed demand. The first case was discussed in the previous chapter and the other two cases were considered in the current chapter. The approximate equation of Λ (equation 6.9), which was obtained using the analytical solution to the wall demand c_{r_w} (equation 5.30), provides a good description of all these cases. The most important findings of the cases studied here are summarised below.

Bulk demand dominated $\Lambda \ll 1$:

- The decay coefficient is practically a linear function of *Da*;
- When $Da > 10^{-3}$, the concentration profile becomes non-uniform across the entire fluid layer;
- The deviation of $c_r(r = 0)$ (for $Da > 10^{-3}$) causes a maximum 5% deviation in the assumption of $\langle uc_r \rangle \approx U$ when $Da < 1$.

Mixed demand $\Lambda \approx 1$:

- Combined bulk and wall demands only very weakly influence each other;
- Because of the weak influence, an analytical approximation of the decay coefficient is accurate with maximum $\mathsf{e} = 5\%$ for $Da < 1$;
- For $Da < 10^{-3}$, the concentration profile is only affected in the viscous sublayer, while both viscous sublayer and bulk layer concentration profiles are affected for $Da > 10^{-3}$.

Considering very large pipe diameters in a network (table 2.3) and very high bulk demand coefficients (table 2.5), the value of Da in a network is of the order of 10^{-5} for $Re = 10^5$. Consequently, this study demonstrated that wall and bulk demands can indeed be treated independently for all practically conceivable values of k_w/U and Da. The design choices made in water quality models such as EPANET are therefore fully justified.

CHAPTER 7

Approximate solutions for nonlinear wall demand

The third research question with respect to wall demand parameterisation posed in section 2.6 is addressed in the current chapter. The question was how nonlinear wall demands of high *Sc* compounds can be parameterised in turbulent smooth pipe flows. The 1D model which was used in chapters 5 is applicable for linear wall demand only and therefore, cannot be used for this purpose. Instead, a generic framework for high *Sc* mass transport is developed.

The governing equations and solution methods for the framework are discussed in section 7.1. It is then shown in section 7.2 that the *Sh* equation for smooth pipes is universal for arbitrary boundary conditions. Application of the framework to linear and nonlinear wall demands is discussed in sections 7.3 and 7.4, respectively. A summary of the chapter is presented in section 7.5.

7.1. Governing equations

For the case of arbitrary wall demand, equation 3.25 (with $\dot{r} = 0$) is supplemented by a generic boundary condition at the wall:

$$\mathtt{f}\left(c_w, \frac{\partial c}{\partial r}(r = R)\right) = 0 \tag{7.1}$$

where $\mathtt{f}$ represents any function describing arbitrary wall demands. As equation 7.1 can be nonlinear, the 1D model, which is based on a separation of variables, cannot be used. Consequently, an alternative model must be developed.

The first step in developing such a model is to study the asymptotic behaviour of the concentration

profile in the crosswise direction. It was shown in chapter 5 that for high *Sc* mass transport, the crosswise concentration profile is expected to be uniform, except within the MTBL, where significant changes in c occur. The MTBL can be characterised as the layer in which $D_T < D$ (Kays *et al.*, 2005). The cubic dependence of ν_T on wall distance (equation 4.9) can be used to define the thickness of the MTBL (δ_m):

$$\delta_m = \sqrt[3]{\frac{Sc_T}{bSc}}\delta_v. \tag{7.2}$$

Equation 7.2 indicates that for high *Sc* compounds, the MTBL will be nested in the viscous sublayer (see figure 7.1). Indeed, taking chlorine as an example ($Sc \approx 1000$), equation 7.2 indicates that $\delta_m \approx \delta_v$ and the viscous sublayer has a thickness of $5\delta_v$. Figures 5.3, 5.6 and 5.9 also clearly demonstrated that the concentration profiles is almost linear for $y = \delta_m$.

A dimensional analysis of the advective and diffusive terms of equation 3.25 in the MTBL results in:

$$u\frac{\partial c}{\partial x} \propto u_\tau \frac{\delta_m}{\delta_v}\frac{C}{L} \tag{7.3}$$

$$\frac{1}{r}\frac{\partial}{\partial r}\left[r\left(D+D_T\right)\frac{\partial c}{\partial r}\right] \propto \frac{1}{R}\frac{RDC}{\delta_m^2} \tag{7.4}$$

where C is a typical concentration and L is the typical length scale for the streamwise variations. The typical velocity in the MTBL was estimated by evaluating equation 3.16 at $y = \delta_m$.

The central premise of the approximation is that streamwise variations occur on much longer length scales than changes in the wall normal direction, i.e. $L \gg R$ (Sookhak Lari *et al.*, 2010; Garcia-Ybarra & Pinelli, 2006; Notter & Sleicher, 1971). Therefore, it follows from the estimates above that advection will be negligible relative to diffusion if the ratio R/L satisfies

$$\frac{R}{L} \ll bRe_\tau, \tag{7.5}$$

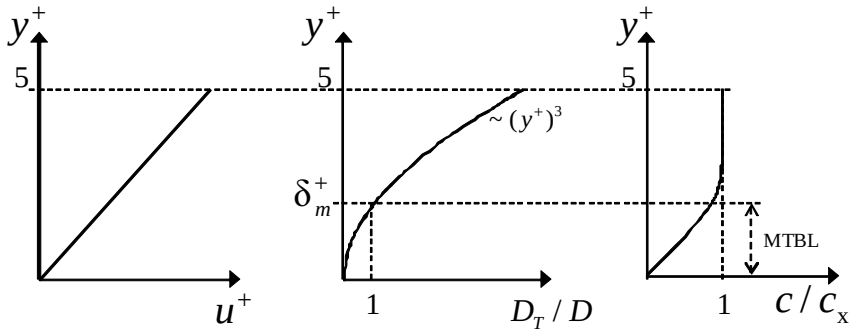

FIGURE 7.1. Schematic of the velocity profile (left), turbulent diffusion coefficient profile (middle) and the concentration profile (right) of a compound with $Sc \gg 1$ inside the viscous sublayer. Figure is not to scale.

where $Sc_T = O(1)$ and therefore not included. The validity of this assumption will be established at the end of this section.

When equation 7.5 holds, equation 3.25 will no longer depend on x. Indeed, by neglecting the advective term, changing the r coordinate to mass transfer wall units $\widetilde{y} = (R-r)/\delta_m$ and assuming that $\delta_m \ll R$, equation 3.25 simplifies to

$$\frac{\partial}{\partial \widetilde{y}}\left[\left(1+\frac{D_T}{D}\right)\frac{\partial c}{\partial \widetilde{y}}\right] = 0. \tag{7.6}$$

Using the cubic for ν_T (and therefore D_T) given in equation 4.9, the following linear ODE with variable coefficients is then obtained:

$$\frac{\partial^2 \widetilde{c}}{\partial \widetilde{y}^2} + \frac{\partial}{\partial \widetilde{y}}\left[\widetilde{y}^3 \frac{\partial \widetilde{c}}{\partial \widetilde{y}}\right] = 0 \tag{7.7}$$

where $\widetilde{c} = c/c_0$. At this point, only one boundary condition will be specified: $\widetilde{c}(x,\widetilde{y}\to\infty) = \widetilde{c}_x(x) = \langle \widetilde{c}(x) \rangle$, which states that c tends to the bulk concentration $c_x = \langle c \rangle$ far away from the MTBL. With this boundary condition, equation 7.7 is of the same form as equation 5.27 and therefore, results in the following analytical

solution (see also Garcia-Ybarra & Pinelli (2006); Sookhak Lari *et al.* (2010)):

$$\widetilde{c} = \widetilde{c}_{\mathrm{x}} + \widetilde{A}\left(\ln\frac{\widetilde{y}+1}{\sqrt{\widetilde{y}^2-\widetilde{y}+1}} - \sqrt{3}\left(\frac{\pi}{2} - \arctan\frac{2\widetilde{y}-1}{\sqrt{3}}\right)\right) \tag{7.8}$$

where $\widetilde{A}$ is an integration coefficient, which can be determined by specifying the wall boundary condition in equation 7.1. The x dependence of the approximate solution of equation 3.25 will be brought out by $\widetilde{c}_{\mathrm{x}}(x)$ and $\widetilde{A}(x)$.

To complete the approximation, an equation is required which governs the behaviour of c_{x}. Such an equation can be obtained by averaging equation 3.25 over the cross-section:

$$\frac{d}{dx}\langle uc\rangle - \frac{D}{r_{\mathrm{h}}}\frac{\partial c}{\partial r}(r=R) = 0. \tag{7.9}$$

Because c is constant throughout the cross-section except in the MTBL, we can approximate $\langle uc\rangle \approx U c_{\mathrm{x}}$. This results in

$$U\frac{dc_{\mathrm{x}}}{dx} + \frac{J_w}{r_{\mathrm{h}}} = 0 \tag{7.10}$$

where

$$J_w = -D\frac{\partial c}{\partial r}(r=R) = \frac{Dc_0}{\delta_{\mathrm{m}}}\frac{\partial \widetilde{c}}{\partial \widetilde{y}}(\widetilde{y}=0). \tag{7.11}$$

Substituting equation 7.11 into equation 7.10 results in

$$\frac{d\widetilde{c}_{\mathrm{x}}}{d\widetilde{x}} + \frac{\partial \widetilde{c}}{\partial \widetilde{y}}(\widetilde{y}=0) = 0 \tag{7.12}$$

where $\widetilde{x} = x/\mathsf{L}$, and L is given by

$$\mathsf{L} = r_{\mathrm{h}} \frac{U\delta_{\mathrm{m}}}{D} = \frac{r_{\mathrm{h}}}{2} \frac{ReSc^{2/3}Sc_T^{1/3}}{Re_\tau b^{1/3}}. \tag{7.13}$$

The typical length scale L can be interpreted as the distance for which the solute mass in the entire cross-section is depleted by the flux through the wall. Equation 7.13 can be used to check the validity condition in equation 7.5, which now takes the form of

$$ReSc^{2/3}b^{2/3} \gg 1. \tag{7.14}$$

In deriving the approximation above, $Sc_T = O(1)$ and $r_{\mathrm{h}}/R = O(1)$ were used. Even for very low values of $Re = 2000$ and $Sc = 100$, $ReSc^{2/3}b^{2/3} \approx 466$ and therefore, the condition in equation 7.5 is satisfied for high Sc compounds in turbulent flows.

Equations 7.8 and 7.12, when augmented with the boundary condition in equation 7.1, comprise a set of coupled equations which can be used to construct approximate analytical solutions for the concentration profile and the mass transfer through the wall. Because the derivation does not rely on linear techniques such as a separation of variables, this includes nonlinear boundary conditions. Examples will be discussed in the next sections.

7.2. A universal Sherwood number equation

Consider a boundary condition given by

$$\frac{\partial \widetilde{c}}{\partial \widetilde{y}}(\widetilde{y}=0) = \mathfrak{g}(\widetilde{c}_w) \tag{7.15}$$

where $\mathfrak{g}(\widetilde{c}_w)$ is a generic function which depends on the wall concentration. Most boundary conditions can be captured by equation 7.15, including the standard (linear) Dirichlet, Neumann and Robin boundary conditions, but also higher order demands and other boundary conditions for which the wall flux depends nonlinearly on the wall concentration. It will be shown here that for boundary conditions which satisfy equation 7.15, the *Sh* correlation is universal, and is consistent with the classical correlation by Notter & Sleicher (1971).

Using equation 7.15, the integration coefficient $\widetilde{A}$ in equation 7.8 is given by $\widetilde{A} = \mathfrak{g}(\widetilde{c}_w)/3$. Hence, the concentration at the wall is

$$\widetilde{c}_w = \widetilde{c}_\mathrm{x} - \frac{2\pi\sqrt{3}}{9}\mathfrak{g}(\widetilde{c}_w). \tag{7.16}$$

For dissolved solutes (like chlorine) in the flow reacting with the pipe wall, the equation above implies that there is a maximum attainable mass flux which occurs when $\widetilde{c}_w = 0$. Indeed, the mass flux is bounded by:

$$\mathfrak{g}(\widetilde{c}_w) < \frac{9}{2\pi\sqrt{3}}\widetilde{c}_\mathrm{x} \approx 0.83\widetilde{c}_\mathrm{x}. \tag{7.17}$$

The physical reason is that the mass flux at the wall is limited by the rate at which material is transported through the MTBL. Indeed, the MTBL behaves like a thin film in a stagnant fluid, i.e. the wall flux J_w can be approximated by $J_w \approx \mathfrak{u}D(c_\mathrm{x} - c_w)/\delta_\mathrm{m}$, where $\mathfrak{u}$ is a prefactor to accommodate the effects of turbulence in the near wall region. This expression has a structure exactly identical to equation 7.16. By setting $c_w = 0$ and noting that $\mathfrak{g}(\widetilde{c}_w) = J_w\delta_\mathrm{m}/(Dc_0)$, equation 7.17 is obtained when $\mathfrak{u} = 0.83$.

A universal correlation for the *Sh* can be derived for boundary conditions satisfying equation 7.15.

Substituting equation 7.16 into $J_w = \mathrm{k_f}(c_\mathrm{x} - c_w)$, and using $J_w = \mathfrak{g}(\widetilde{c}_w)Dc_0/\delta_\mathrm{m}$ results in

$$\mathrm{k_f} = \frac{9}{2\pi\sqrt{3}}\frac{D}{\delta_\mathrm{m}}. \tag{7.18}$$

In other words, $\mathrm{k_f}$ is *independent* of the type of boundary condition. Using equation 7.18, the *Sh* correlation for high *Sc* compounds is:

$$Sh = \frac{9b^{1/3}}{\pi\sqrt{3}Sc_T^{1/3}}Re_\tau Sc^{1/3} \tag{7.19}$$

which is identical to equation 5.32, proposed for first-order wall demands. The universality is a direct consequence of the linear dependence of the wall concentration gradient and the concentration difference between wall and bulk, as is evident from equation 7.16. The underlying reason is the invariance of the ODE to scaling because of its linearity.

As stated in chapter 5, the universality of equation 7.19 compares favourably with experimental data. The Fanning friction factor f was defined as $f = 2\tau_w/(\rho U^2) = 8Re_\tau^2/Re^2$ (section 2.4.2) (Bird *et al.*, 2002). Substitution into equation 7.19 results in

$$Sh = \frac{9b^{1/3}}{\pi\sqrt{3}Sc_T^{1/3}}\sqrt{\frac{f}{8}}ReSc^{1/3} \tag{7.20}$$

which corresponds well to the established correlation $Sh = 0.0566\sqrt{f}ReSc^{1/3}$ (Bird *et al.*, 2002, equation 14.2-5). By applying the Blasius formula $f = 0.0791\,Re^{-0.25}$ (Bird *et al.*, 2002, equation 6.2-12), we obtain

$$Sh = 0.016Re^{0.875}Sc^{1/3}$$

which is in good agreement with the *Sh* correlation by Notter & Sleicher (1971) for the Dirichlet boundary condition: $Sh = 0.0149 Re^{0.88} Sc^{1/3}$.

7.3. Linear boundary conditions

Analytical solutions for Dirichlet, Neumann, and Robin boundary conditions are provided in this section. Consider a general linear boundary condition of the form:

$$\widetilde{\beta}\frac{\partial \widetilde{c}}{\partial \widetilde{y}}(\widetilde{y}=0) = (1-\widetilde{\beta})\widetilde{\sigma}\widetilde{c}_w + \widetilde{\gamma}. \tag{7.21}$$

Here $\widetilde{\beta} = 0$, 1 and $1/2$ imply Dirichlet, Neumann and Robin boundary conditions, respectively, and $\widetilde{\gamma}$ and $\widetilde{\sigma}$ are constants. In terms of the template in equation 7.15, equation 7.21 becomes:

$$\mathfrak{g}(\widetilde{c}_w) = \frac{(1-\widetilde{\beta})\widetilde{\sigma}\widetilde{c}_w + \widetilde{\gamma}}{\widetilde{\beta}}. \tag{7.22}$$

Using equation 7.16, the wall concentration is given by

$$\widetilde{c}_w = \frac{\widetilde{\beta}\widetilde{c}_{\mathrm{x}} - \frac{2\pi\sqrt{3}}{9}\widetilde{\gamma}}{\widetilde{\beta} + \frac{2\pi\sqrt{3}}{9}(1-\widetilde{\beta})\widetilde{\sigma}} \tag{7.23}$$

and the wall gradient by

$$\frac{\partial \widetilde{c}}{\partial \widetilde{y}}(\widetilde{y}=0) = \widetilde{E}(\widetilde{c}_{\mathrm{x}} + \widetilde{F}) \tag{7.24}$$

where

$$\widetilde{E} = \frac{(1-\widetilde{\beta})\widetilde{\sigma}}{\widetilde{\beta} + \frac{2\pi\sqrt{3}}{9}(1-\widetilde{\beta})\widetilde{\sigma}}, \qquad \widetilde{F} = \frac{\widetilde{\gamma}}{(1-\widetilde{\beta})\widetilde{\sigma}}. \tag{7.25}$$

Substituting equation 7.24 into equation 7.12 and solving for $\widetilde{c}_\mathrm{x}$ results in:

$$\widetilde{c}_\mathrm{x} = -\widetilde{F} + (\widetilde{F}+1)\exp(-\widetilde{E}\widetilde{x}). \tag{7.26}$$

Equations 7.23, 7.24 and 7.26 are a general solution for linear mass transfer boundary conditions. The specific solutions for Dirichlet, Neumann and Robin boundary conditions are discussed below.

Dirichlet boundary conditions: $\widetilde{\beta} = 0$ **and** $\widetilde{\sigma} = -1$

Equations 7.23, 7.24 and 7.26 are now given by:

$$\widetilde{c}_w = \widetilde{\gamma} \tag{7.27}$$

$$\frac{\partial\widetilde{c}}{\partial\widetilde{y}}(\widetilde{y}=0) = \frac{9}{2\pi\sqrt{3}}(\widetilde{c}_\mathrm{x} - \widetilde{\gamma}) \tag{7.28}$$

$$\widetilde{c}_\mathrm{x} = \widetilde{\gamma} + (1-\widetilde{\gamma})\frac{9}{2\pi\sqrt{3}}\exp(-\widetilde{x}). \tag{7.29}$$

This solution is in correspondence with the lowest eigenvalue solution of Weigand (2004, equations 3.23 and 3.26).

Neumann boundary conditions: $\widetilde{\beta} = 1$

Equations 7.23, 7.24 and 7.26 become:

$$\widetilde{c}_w = \widetilde{c}_\mathrm{x} - \frac{2\pi\sqrt{3}}{9}\widetilde{\gamma} \tag{7.30}$$

$$\frac{\partial \widetilde{c}}{\partial \widetilde{y}}(\widetilde{y}=0) = \widetilde{\gamma} \tag{7.31}$$

$$\widetilde{c}_{\mathrm{x}} = 1 - \widetilde{\gamma}\widetilde{x}. \tag{7.32}$$

Here, a Taylor expansion series around $\widetilde{x}=0$, taking the limit of $\widetilde{\beta} \to 1$, was used to obtain $\widetilde{c}_{\mathrm{x}}$. These solutions are consistent with Bird *et al.* (2002, equation 10.8-32).

Robin boundary conditions: $\widetilde{\beta} = 1/2$ **and** $\widetilde{\gamma} = 0$

Equations 7.23, 7.24 and 7.26 now simplify to

$$\widetilde{c}_w = \frac{1}{1+\frac{2\pi\sqrt{3}}{9}\widetilde{\sigma}}\widetilde{c}_{\mathrm{x}} \tag{7.33}$$

$$\frac{\partial \widetilde{c}}{\partial \widetilde{y}}(\widetilde{y}=0) = \widetilde{\sigma}\widetilde{c}_w \tag{7.34}$$

$$\widetilde{c}_{\mathrm{x}} = \exp(-\widetilde{k}\widetilde{x}), \quad \widetilde{k} = \frac{\widetilde{\sigma}}{1+\frac{2\pi\sqrt{3}}{9}\widetilde{\sigma}} \tag{7.35}$$

where $\widetilde{k}$ is the non dimensional decay coefficient. The equations above correspond identically to the solutions presented in chapter 5 (equation 5.31). Note that the maximum decay coefficient for this boundary condition is

$$\lim_{\widetilde{\sigma}\to\infty} \widetilde{k} = \frac{9}{2\pi\sqrt{3}} \approx 0.83 \tag{7.36}$$

which is consistent with equation 7.17.

7.4. Nonlinear boundary conditions

Using the method presented in this chapter, approximate analytical solutions can be constructed for nonlinear boundary conditions. Since some of the studies on chlorine depletion due to wall demand propose

second-order demand of this compound (Kiéné *et al.*, 1993; Jones, 2001; Rossman, 2006), the same type of demand is also considered here as a demonstration for nonlinear wall demands:

$$\frac{\partial \widetilde{c}}{\partial \widetilde{y}}(\widetilde{y}=0) = \widetilde{\alpha}\widetilde{c}_w^2 \tag{7.37}$$

where $\widetilde{\alpha}$ is the non dimensional second-order wall demand coefficient. Substituting equation 7.37 in equation 7.16 gives

$$\widetilde{c}_w = \widetilde{\eta}^{-1}\left(\sqrt{1+2\widetilde{\eta}\widetilde{c}_x}-1\right) \tag{7.38}$$

where $\widetilde{\eta} = 4\pi\sqrt{3}\widetilde{\alpha}/9$. Substitution into equation 7.37 results in

$$\frac{\partial \widetilde{c}}{\partial \widetilde{y}}(\widetilde{y}=0) = \widetilde{\alpha}\widetilde{\eta}^{-2}\left(\sqrt{1+2\widetilde{\eta}\widetilde{c}_x}-1\right)^2 \tag{7.39}$$

and equation 7.12 is therefore given by

$$\frac{d\widetilde{c}_x}{d\widetilde{x}} + \widetilde{\alpha}\widetilde{\eta}^{-2}\left(\sqrt{1+2\widetilde{\eta}\widetilde{c}_x}-1\right)^2 = 0. \tag{7.40}$$

The following change of variables

$$\widetilde{\lambda} = \frac{1}{\sqrt{1+2\widetilde{\eta}\widetilde{c}_x}-1} \tag{7.41}$$

simplifies equation 7.40 to

$$\frac{\widetilde{\lambda}+1}{\widetilde{\lambda}}\frac{d\widetilde{\lambda}}{d\widetilde{x}}+\frac{9}{4\pi\sqrt{3}}=0 \tag{7.42}$$

which has a solution

$$\widetilde{\lambda}+\ln\widetilde{\lambda}=\frac{9}{4\pi\sqrt{3}}\widetilde{x}+\widetilde{B}. \tag{7.43}$$

Here, $\widetilde{B}=\widetilde{\lambda}_0+\ln\widetilde{\lambda}_0$ with $\widetilde{\lambda}_0=\left(-1+\sqrt{1+2\widetilde{\eta}}\right)^{-1}$. The solution can be compactly written as

$$\widetilde{\lambda}=W_0\left(\exp\left(\frac{9}{4\pi\sqrt{3}}\widetilde{x}+\widetilde{B}\right)\right) \tag{7.44}$$

where W_0 is the Lambert W function (Corless *et al.*, 1996). To verify the asymptotic solution in equation 7.44, results were compared to the 2D mass transport model introduced in chapter 5 (the code for the model is presented in appendix B). The only difference is that the boundary condition at the wall is second-order. The boundary condition 7.37 is incorporated by using a simple iterative method similar to the linearization approach described for solution of the HRN $\mathsf{k}-\varepsilon$ model equations in chapter 4.

The values 10^{-1}, 10^{0} and 10^{1} were chosen for $\widetilde{\alpha}$ and the problem was solved for $Re=10^5$ and $Sc=10^3$. Grids include $N=600$ and $N=300$ nodes in the x and r directions, respectively. Logarithmic spacing was required because of strong variations very close to the wall and near the entrance ($\widetilde{x}=0$). The first grid points were located at $\widetilde{x}=10^{-5}$ and $y^+=10^{-3}$, which results in cell sizes varying up to eight orders of magnitude[1]. A grid convergence study with double resolution was also performed and showed no practical difference in the results. A constant concentration profile $c(0,r)=c_0$ was used at the entrance.

The analytical solution and the 2D numerical model are in excellent agreement (figure 7.2). In the far field where $\widetilde{x}\gg 1$, $\ln\widetilde{\lambda}\ll\widetilde{\lambda}$ and therefore, equation 7.43 simplifies to

[1] A conservative method such as the applied finite difference discretisation method is crucial for such extreme stretching (Mathias & van Reeuwijk, 2009).

$$\widetilde{\lambda}_{far} = \frac{9}{4\pi\sqrt{3}}\widetilde{x}. \tag{7.45}$$

Moreover, equation 7.41 simplifies to $\widetilde{\lambda}_{far} \approx 1/(\widetilde{\eta}\widetilde{c}_{x_{far}})$, and therefore

$$\widetilde{c}_{x_{far}} = \frac{1}{\widetilde{\alpha}\widetilde{x}}. \tag{7.46}$$

The far field solution in equation 7.46 is shown in figure 7.2 together with the numerical results. Note that the vertical axis is scaled by $\widetilde{\alpha}$ in order to collapse the far field behaviour. This figure indicates that the far field solution is valid for $\widetilde{x} > 100$.

The approximate solutions do not account for entrance effects, so it is useful to study the local Sherwood number in the x direction (Sh_x). In figure 7.3, $Sh_x = 2J_w(x)R/(D(c_x(x) - c_w(x))$ is normalised by the analytical value from equation 7.19 for all three values of $\widetilde{\alpha}$. Two observations can be made; 1) The entrance length scale L_E is much shorter than L, and 2) the steady-state value for Sh_x is about 3.5 percent larger than the analytical Sh.

The difference between Sh_x and the Sh can be traced back to the differences in the D_T profile. The wall damping employed in the modified van Driest mixing length model is purely empirical and only satisfies cubic behaviour very close to the wall. Between $1 < y^+ < 5$, D_T is up to thirty percent higher than a pure cubic. This will make the MTBL a bit thinner in the simulations, and the maximum wall flux higher. Indeed, whilst the maximum achievable flux according to equation 7.18 is $k_f\delta_m/D = 9/(2\pi\sqrt{3}) \approx 0.83$, the maximum achievable flux using a numerical solution of equation 7.6 with the modified van Driest wall function results in $k_f\delta_m/D \approx 0.85$. This is 2.4 percent higher, and accounts for a significant part of the observed deviations. The rest of the deviation is likely to be caused by the effect of approximations.

The reason the entrance length scale L_E is much shorter than L can be understood by realising that L_E is related to the time it takes for the mass in the MTBL to deplete:

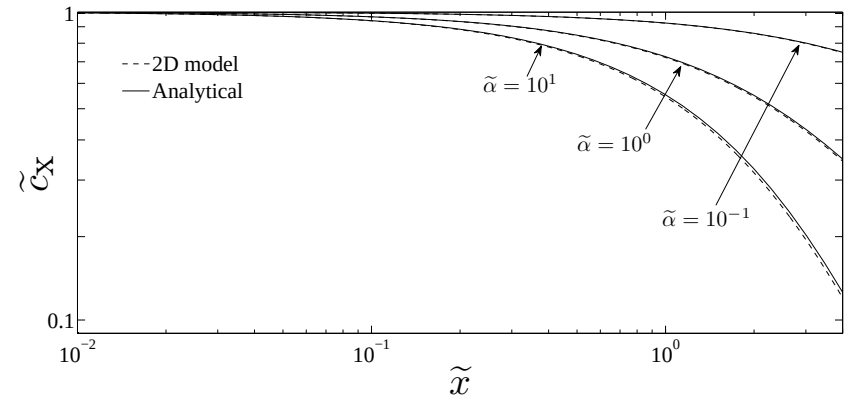

(A) Comparison with equation 7.44

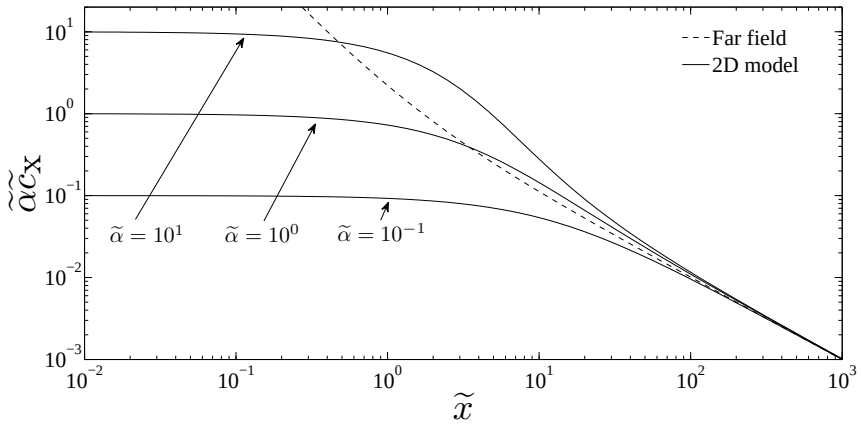

(B) Comparison with equation 7.46

FIGURE 7.2. Comparison of the approximate analytical solution with the 2D model for $\widetilde{\alpha} = 10^{-1}$, 10^0 and 10^1.

$$T_m \propto \frac{C\delta_m}{J_w} \approx \frac{C\delta_m}{DC/\delta_m} = \frac{\delta_m^2}{D}. \tag{7.47}$$

Using the velocity scale at the edge of the MTBL ($\delta_m/\delta_\nu u_\tau$), the entrance length scale L_E can be estimated by

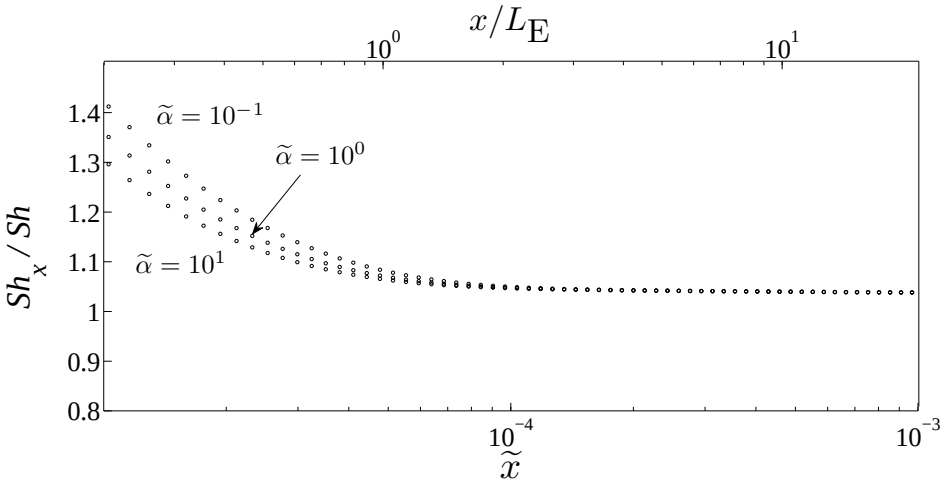

FIGURE 7.3. Local Sh_x normalised by Sh in equation 7.19.

$$L_{\mathrm{E}} \propto \frac{\delta_{\mathrm{m}}}{\delta_{\mathrm{v}}} u_\tau \frac{\delta_{\mathrm{m}}^2}{D} = \frac{\delta_{\mathrm{v}}}{b} = \frac{Sc_T}{bRe_\tau} R. \tag{7.48}$$

The normalisation x/L_{E} is shown on a secondary horizontal axis in figure 7.3. Clearly, equation 7.48 much better represents the entrance length scale than L. A number of simulations at different Re_τ and Sh (not shown) indicate that the estimate equation 7.48 is robust. It is interesting to note that equation 7.48 does not contain any dependence on Sc. For practical purposes, equation 7.48 indicates that entrance effects will not be important beyond the first few pipe diameters. For the case of developing turbulent flows, the same issue was indicated for the developing velocity profile in figure 2.4.

7.5. Summary

The intention in this chapter was to provide parameterisations for nonlinear wall demands in smooth pipes. A method was developed to construct asymptotic solutions for high Sc compounds for both linear and nonlinear boundary conditions. An advantage of this method is that it provides relatively simple closed form solutions which predict accurately the concentration profile and mass transfer. In addition, the analysis provided useful estimates for 1) the length scale L, which represents the length it takes for all the material

originally in the pipe to deplete (equation 7.13), and 2) the typical length scale L_E for which entry effects are important (equation 7.48). Substitution of typical values for *Re* and *Sc* showed that $L \gg R$, and $L_E/R = O(1)$. The developed solutions are therefore widely applicable for high *Sc* turbulent mass transport in pipes whose length is much larger than its diameter (which is the case for chlorine transport in networks).

It was shown in this study that the analytical solution for *Sh* in flows subjected to arbitrary wall demands is consistent with experimental *Sh* equations derived for various types of wall demand. It was described that *Sh* is a universal number, independent of the type of wall demand. Consequently, the *Sh* correlation by Notter & Sleicher (1971) which is used in EPANET-based models for parameterisation of first-order wall demands in smooth pipe turbulent flows can also be applied for nonlinear wall demands.

The linear boundary conditions, Dirichlet, Neumann and Robin, were studied as a subcategory of arbitrary mass transfer boundary conditions. Analytical solutions for streamwise and cross-sectional concentration profiles were derived and compared with the literature.

For the case of nonlinear boundary conditions, the second-order mass transfer boundary condition was studied. This condition was chosen as a similar case is also reported in studies on chlorine wall demand (Kiéné *et al.*, 1998; Jones, 2001; Rossman, 2006). Results of the concentration variation were compared to the 2D numerical model and found to be in excellent agreement.

CHAPTER 8

Flow models for turbulent plane channel flow with d-type rough walls

The current and next chapter will focus on flow and mass transport over rough surfaces. As for the chapters on smooth surfaces, the flow field simulations will be presented in this chapter, prior to discussions on mass transport in chapter 9.

In the chapters on rough walls, a plane channel geometry is adopted. Governing equations for flow (momentum) in a such geometry are discussed in section 8.1. Since the near wall treatments used in chapters 5 - 7 (law of the wall and modified van Driest mixing length) are not applicable for rough walls, the Launder Sharma (LS) LRN[1] $k-\varepsilon$ model is used to model the turbulence. As the cubic dependence of ν_T is of crucial importance to the appropriate simulation of high *Sc* wall demand, a detailed verification of the model for a smooth wall is carried out in section 8.2. Section 8.3 introduces the rough wall geometry under consideration, and contains a comparison of flow field results with existing DNS and LES results for rough channel flows. The important properties of the flow field (with respect to the mass transport problem) are also emphasized in this section. A summary of the chapter is presented in section 8.4.

8.1. Governing equations

In contrast with the studies in chapters 4 to 7, the study on rough surfaces is performed for a plane channel geometry. The reason for choosing such a geometry is the availability of DNS and LES studies, which can be used to verify the flow model. Moreover, a plane channel geometry is interchangeable with a pipe geometry for sufficiently high *Re*, as wall curvature will be negligible (see appendix A).

Due to the presence of roughness elements, the flow is no longer uniform in the *x* direction and therefore, the wall normal velocity $v \neq 0$. Consequently, the turbulence in the inner layer is no longer equilibrium, and

[1] Low *Re*, as introduced in chapter 4.

wall functions no longer appropriately describe its behaviour.

Several studies were done to modify HRN $k-\varepsilon$ equations to enable them to deal with the near wall effects, such as the dominating molecular viscosity, wall blocking and pressure reflection (Rodi & Mansour, 1993). The main idea of a LRN $\mathsf{k}-\varepsilon$ model is that by introducing empirical functions, the governing equations for the HRN $\mathsf{k}-\varepsilon$ model are adjusted in a way that there will be no need for further near wall treatment. Consequently, the equations can be integrated up to the wall and no more wall functions are needed. These models are a good choice when dealing with complex geometries like corners or regularly ribbed walls (Bergmann & Fiebig, 1999).

The continuity and RANS equations for a planar geometry are (Pope, 2000):

$$\frac{\partial u}{\partial x}+\frac{\partial v}{\partial y}=0 \tag{8.1}$$

$$u\frac{\partial u}{\partial x}+v\frac{\partial u}{\partial y}=\frac{\partial}{\partial x}\left[(\nu+\nu_T)\frac{\partial u}{\partial x}\right]+\frac{\partial}{\partial y}\left[(\nu+\nu_T)\frac{\partial u}{\partial y}\right]+\frac{\partial p}{\partial x} \tag{8.2}$$

$$u\frac{\partial v}{\partial x}+v\frac{\partial v}{\partial y}=\frac{\partial}{\partial x}\left[(\nu+\nu_T)\frac{\partial v}{\partial x}\right]+\frac{\partial}{\partial y}\left[(\nu+\nu_T)\frac{\partial v}{\partial y}\right]+\frac{\partial p}{\partial y}. \tag{8.3}$$

In this coordinate system, a general LRN $\mathsf{k}-\varepsilon$ closure is (Bergmann & Fiebig, 1999):

$$u\frac{\partial \mathsf{k}}{\partial x}+v\frac{\partial \mathsf{k}}{\partial y}=P-\varepsilon+\frac{\partial}{\partial x}\left(\left[\nu+\frac{\nu_T}{\sigma_\mathsf{k}}\right]\frac{\partial \mathsf{k}}{\partial x}\right)+\frac{\partial}{\partial y}\left(\left[\nu+\frac{\nu_T}{\sigma_\mathsf{k}}\right]\frac{\partial \mathsf{k}}{\partial y}\right) \tag{8.4}$$

$$u\frac{\partial \widetilde{\varepsilon}}{\partial x}+v\frac{\partial \widetilde{\varepsilon}}{\partial y}=(C_1 f_1 P-C_2 f_2\widetilde{\varepsilon})\frac{\widetilde{\varepsilon}}{k}+\frac{\partial}{\partial x}\left(\left[\nu+\frac{\nu_T}{\sigma_\varepsilon}\right]\frac{\partial \widetilde{\varepsilon}}{\partial x}\right)+\frac{\partial}{\partial y}\left(\left[\nu+\frac{\nu_T}{\sigma_\varepsilon}\right]\frac{\partial \widetilde{\varepsilon}}{\partial y}\right)+E \tag{8.5}$$

where the turbulent kinetic energy production P is given by

$$P=\nu_T\left(\frac{\partial u}{\partial y}+\frac{\partial v}{\partial x}\right)^2 \tag{8.6}$$

and

$$\widetilde{\varepsilon} = \varepsilon - \varepsilon_w, \quad \varepsilon_w = 2\nu \left[\frac{\partial\sqrt{k}}{\partial y}\right]_w^2. \tag{8.7}$$

In the equations above, $\widetilde{\varepsilon}$ is the modified turbulent kinetic energy dissipation rate $[L^2T^{-3}]$ and ε_w is the value of ε at the wall[2]. In addition, E, f_1 and f_2 are empirical functions. The turbulent viscosity for the LRN models is defined as (Rodi & Mansour, 1993):

$$\nu_T = C_\mu f_\mu \frac{k^2}{\widetilde{\varepsilon}} \tag{8.8}$$

where f_μ is the empirical damping function. Comparing equation 8.8 with equation 4.12, it is obvious that f_μ should tend to 1 far from the wall (since ε_w becomes negligible in comparison with ε), and 0 at the wall.

A large number of LRN $k-\varepsilon$ models have been developed over the years, each with slightly different empirical and damping functions, and optimised for specific criteria (such as a specific geometry). A comprehensive list is presented in Rodi & Mansour (1993). Here, the focus is on the Launder Sharma (LS) model.

The LS model is a classic LRN $k-\varepsilon$ model, showing a good performance for modelling flow over walls with regularly spaced ribs (Bergmann & Fiebig, 1999). In the LS model,

$$E = 2\nu\nu_T \left(\frac{\partial^2 u}{\partial y^2}\right)^2 \tag{8.9}$$

and

$$f_\mu = \exp\left[\frac{-3.4}{(1+Re_t/50)^2}\right], \quad f_1 = 1, \quad f_2 = 1 - 0.3\exp(-Re_t^2) \tag{8.10}$$

[2]By using $\widetilde{\varepsilon}$ instead of ε, the wall boundary condition is simplified significantly. Using the Taylor expansion series presented in chapter 3, it can be shown that $\varepsilon_w = 2\nu\left(\frac{\partial\sqrt{k}}{\partial y}\right)_w^2$ and therefore, $\widetilde{\varepsilon}_w = 0$. See Rodi & Mansour (1993) and Pope (2000) for more details.

where

$$Re_t = \frac{k^2}{\nu\varepsilon} \tag{8.11}$$

is the local Reynolds number (Rodi & Mansour, 1993). The LS LRN $k-\varepsilon$ model is used in this chapter to model the flow field.

8.2. Smooth surface results

For the flow simulations in this chapter, the simulation and modelling package OpenFOAM is used. OpenFOAM is a widely used open source code for the simulation of transport phenomena (OpenCFD, 2008). OpenFOAM contains generic finite volume discretisations of mathematical operators on unstructured meshes, which can be combined into solution methods for transport equations. The LS $k-\varepsilon$ model is one of the available turbulence closures in OpenFOAM.

Since simulation in OpenFOAM requires a 3D geometry, the domain sketched in figure 8.1 is considered. OpenFOAM supports several cell shapes. The domain of size $\delta \times \lambda$, where δ is the channel half width and λ is the domain size in the streamwise direction, is discretised with hexahedron cells. The simulation is performed on a unit of width in the Front-Back direction. As for rough wall simulation (see the next section), $\lambda/\delta = 2 \times 10^{-2}$ is used. The following boundary conditions are applied:

(1) Gradient of the variables u, v, p, k and $\widetilde{\varepsilon}$ in the y direction is zero in the mid-channel (symmetric condition at channel centre);
(2) Gradient of the aforementioned variables in the y direction is zero at the wall;
(3) No slip condition for the velocity is considered at the wall;
(4) Periodic boundary conditions are applied for the left and right faces of the domain (where the flow enters and leaves the domain). In other words, the left and right faces are assumed to be physically connected and therefore, all the parameters in the LS model governing equation are equal for the left and right faces (i.e. fully developed flows);

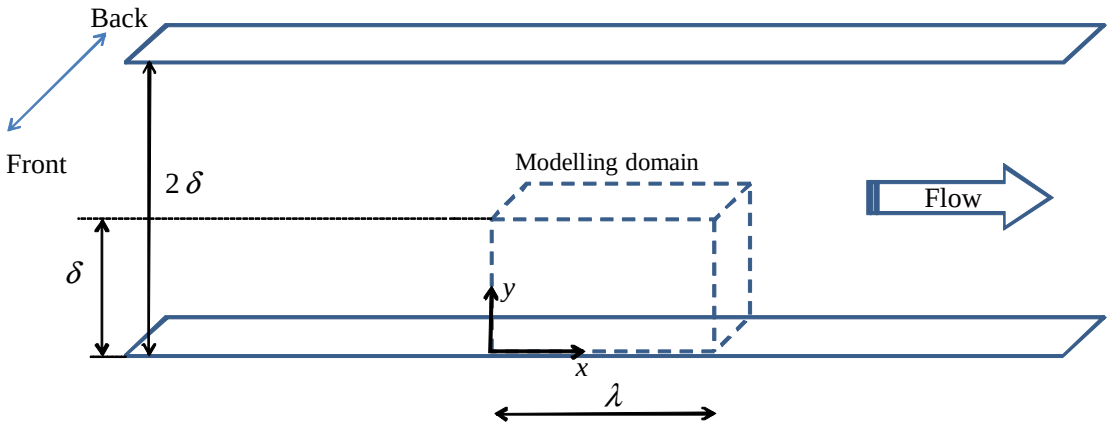

FIGURE 8.1. Smooth plane channel geometry.

(5) Gradient in the Front-Back direction is zero.

A total number of 400 cells were used in the y direction, and logarithmic grid clustering was used to increase the resolution near the wall. The first cell next to the wall is located at $y^+ = 0.7$. The x coordinate was discretised with 60 evenly distributed cells. The velocity u in the mid-channel was chosen such that $Re_\tau = 2003$, which allows for comparison with DNS results of Hoyas & Jiménez (2006). The conditions for convergence of u, v, p, k and $\widetilde{\varepsilon}$ in OpenFOAM were defined as the relative residual $\mathrm{E} < 10^{-9}$ since the results were insensitive to lower residuals. The streamwise velocity (u) is compared with DNS data of Hoyas & Jiménez (2006) in figure 8.2. Clearly, the LS model faithfully predicts the velocity field for a smooth wall.

It can be shown that f_μ should have a first-order behaviour with respect to y very close to the wall in order to reproduce $\nu_T = by^{+3}$ (see e.g. Rodi & Mansour (1993) for more details). Various LRN k-ε models then use different empirical correlations for f_μ to produce the first-order behaviour. However, since the exact value of f_μ very close to the wall does not affect the flow field, it is not obvious that the LS model will reproduce an appropriate prefactor b.

As an example, figure 8.3 shows f_μ for the LS model compared to f_μ calculated from DNS data[3] by Hoyas & Jiménez (2006). Although f_μ from the LS model shows a satisfactory power law close to the wall,

[3]The DNS data includes $\overline{u'v'}$. Using the gradient diffusion hypothesis (equation 3.22), it is possible to determine ν_T. In addition, k and ε are parts of the DNS data. Consequently, f_μ can be determined from DNS data using equation 8.8. The data on f_μ by Jiménez (2004) were derived by the author and are in agreement with results reported by Rodi & Mansour (1993).

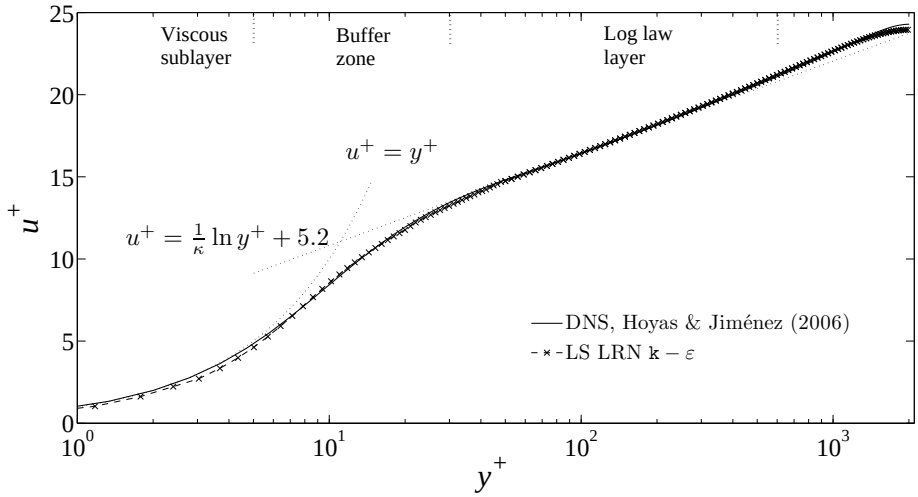

FIGURE 8.2. Comparison of the fully developed smooth plane channel flow velocity profile in LS LRN $k-\varepsilon$ model versus DNS data by Jiménez (2004) for $Re_\tau = 2003$.

the prefactor *b* is incorrect. This will lead to inaccurate values for ν_T close to the wall, as shown in figure 8.3.

The LS turbulent viscosity indeed has a third-order dependence on the wall distance in the viscous sublayer and converges to the correct value of ν_T from $y^+ = 20$ onwards. However, the near wall values of ν_T in the LS model are about a factor of 10 smaller than what they should be[4]. In other words, the LS model reproduces equation 4.9 but with a prefactor b_{LS} (the LS *b* prefactor) which is 10 times lower than the real *b*. Consequently, using the LS model to study high *Sc* mass transport will require extra consideration, which are discussed in detail in chapter 9.

8.3. Rough surface results

A schematic of the geometry of the problem is shown in figure 8.4. The geometry consists of regularly spaced ribs (which will be called crests) on the surface of a plane channel. The space between the ribs will be called the cavity. One periodic length of the domain (λ) is the centre to centre measurement of two

[4]The primary aim of the classic LRN models was to reproduce the velocity fields. Since the near wall behaviour of f_μ does not affect the velocity profile, the inaccuracy of this function in reproducing ν_T close to the wall was not thoroughly modified in the literature. Consequently, all the classic LRN models suffer from such an inaccuracy in f_μ. See e.g. Rodi & Mansour (1993) for more details.

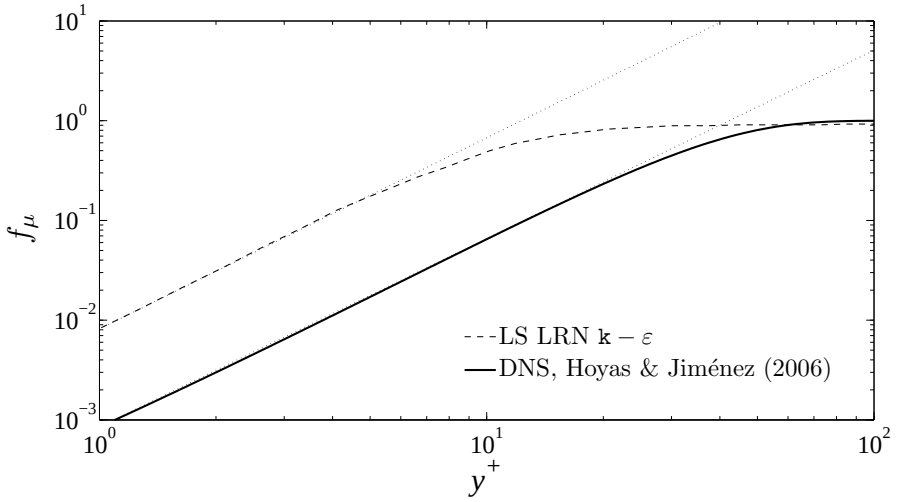

(A) $f_\mu(\widetilde{\varepsilon})$

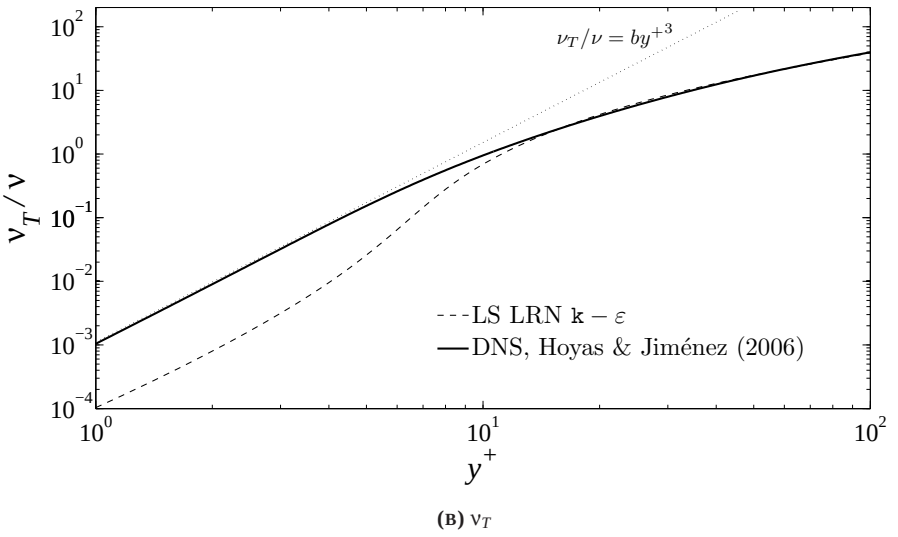

(B) ν_T

FIGURE 8.3. f_μ and ν_T in the LS LRN $\mathtt{k}-\varepsilon$ model versus DNS results by Hoyas & Jiménez (2006).

sequential crests. As stated in chapter 2, the ratio of the cavity width to depth, w/d, is used to characterize the roughness type. Rough walls with $w/d \approx 1$ represents a d-type roughness (Leonardi *et al.*, 2007; Djenidi *et al.*, 1999), and when $w/d \gg 1$, the geometry has a k-type roughness. The value of $w/d = 1$ is adopted in this study (i.e. d-type roughness) since it is a better representative for a natural roughness in distribution

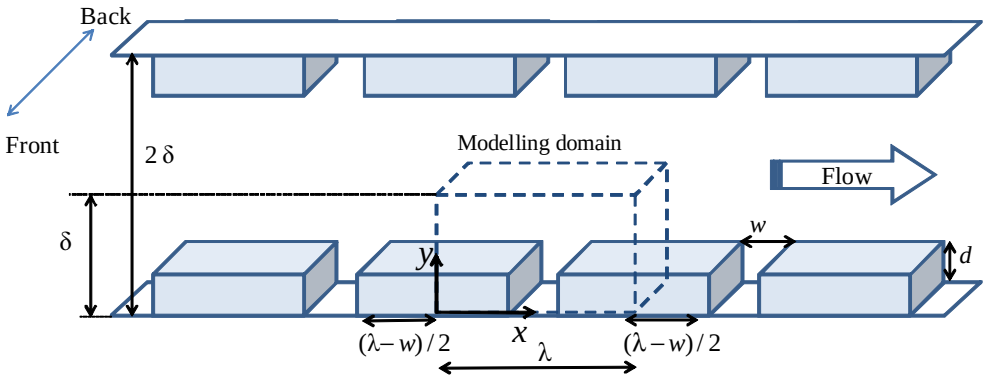

FIGURE 8.4. The modelling domain studied in chapters 8 and 9 comprises one periodic length of a half channel with d-type roughness. Figure is not to scale.

network pipes (Lolja, 2005). This choice of w/d allows for comparison of the flow field with DNS results by Leonardi *et al.* (2003) and Leonardi *et al.* (2007), LES results by Cui *et al.* (2003) and the mass transport with electrochemical experiments (in chapter 9).

Another important ratio of regular roughness patterns is λ/d. Most DNS and LES studies on d-type rough surfaces have used $\lambda/d = 2$ (Cui *et al.*, 2003; Leonardi *et al.*, 2007; Djenidi *et al.*, 1999; Orlandi & Leonardi, 2006). However, experimental data for mass transport over such surfaces are reported only for $\lambda/d > 3$ (Dawson & Trass, 1972; Zhao & Trass, 1997; Lolja, 2005). Consequently, two cases with $\lambda/d = 2$ and 4 are simulated in this study. The first case is used to verify the flow field against DNS and LES studies. The second case is then used to generate conditions similar to the electrochemical experiments. Both of the rough surfaces used in this study have $d/\delta = 10^{-2}$, in close correspondence with the experimental studies on mass transfer (see chapter 9).

Figure 8.5 shows important locations on the domain highlighted with numbers and capital letters for further citation. The figure also shows the applied coordinates. Coordinates x and y have their origins on the intersection of lines G and 1, or simply the point G1. The tangential coordinate s starts from the point C3 and follows the surface inside the cavity (i.e., it passes C3, F3, F7, C7 and C9). The normal coordinate n is perpendicular to s and points into the fluid.

Simulations were performed on a coarse, intermediate and fine mesh. The resolution of the meshes for

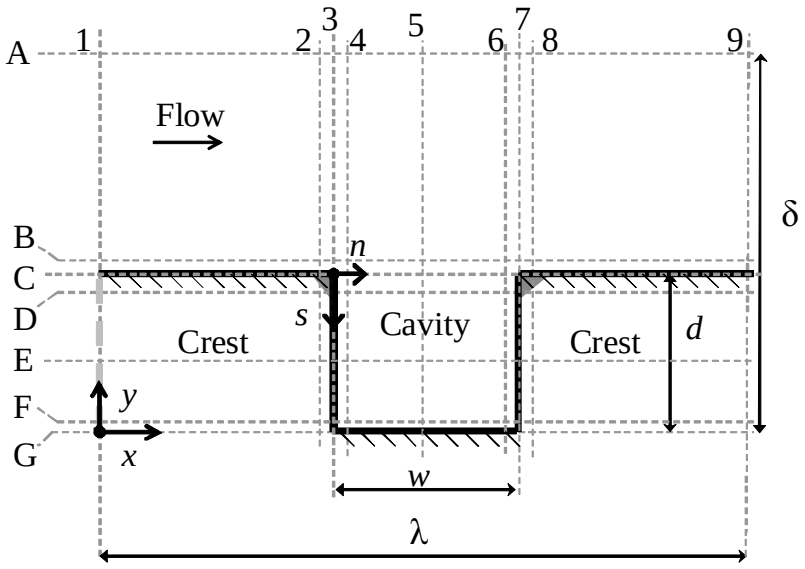

FIGURE 8.5. Schematic of the modelling domain geometry plus the applied coordinates. Lines which are nominated by letters or numbers will be used to cite specific locations in the geometry. Figure is not to scale.

the rough surface with $\lambda/d = 4$ is presented in table 8.1. The reason for the application of three meshes is to monitor the effect of numerical diffusion, as will be discussed later in this section. Meshes for the rough surface with $\lambda/d = 2$ are similar to those with $\lambda/d = 4$, except that the A1-C3 and A7-C9 blocks have $1/3$ of the resolution in the x direction. Figure 8.6 also shows the fine mesh of the rough surface (with $\lambda/d = 4$) inside and over the cavity. It shows that extra resolution is provided near the crest, as well as on the interface of the bulk flow and the cavity.

TABLE 8.1. Numerical meshes for $\lambda/d = 4$.

	C3-G7	A1-C3	A3-C7	A7-C9	Total number of cells
Coarse	40×70	60×250	40×250	60×250	42800
Intermediate	60×70	90×250	60×250	90×250	64200
Fine	80×70	120×250	80×250	120×250	85600

The simulations use the following boundary conditions:

(1) As in the case of the smooth surface, the gradient of all the variables in the wall normal direction n is zero;
(2) Periodic boundary conditions are applied to left and right domain faces;
(3) Gradient in y is zero at the upper domain face (symmetry condition at the channel centre);
(4) Gradient in the Front-Back direction is zero.

The simulations are performed for $Re = 2.5 \times 10^5$. Before discussing the results, a grid convergence study is carried out to ensure that the results are independent of the grid resolution. This is particularly importance because the default OpenFOAM discretisation scheme for advection is first-order upwind, which has numerical diffusion (see chapter 9 for more discussion).

Figure 8.7 shows the turbulent viscosity profile of the rough surface with $\lambda/d = 4$ for $(y-d)^+ = (y-d)u_\tau/\nu = 1$ (line B1-B9) for three meshes introduced in table 8.1. The method for the determination of u_τ and interpretation of the results in the figure are discussed later in this section. However, it is sufficient here

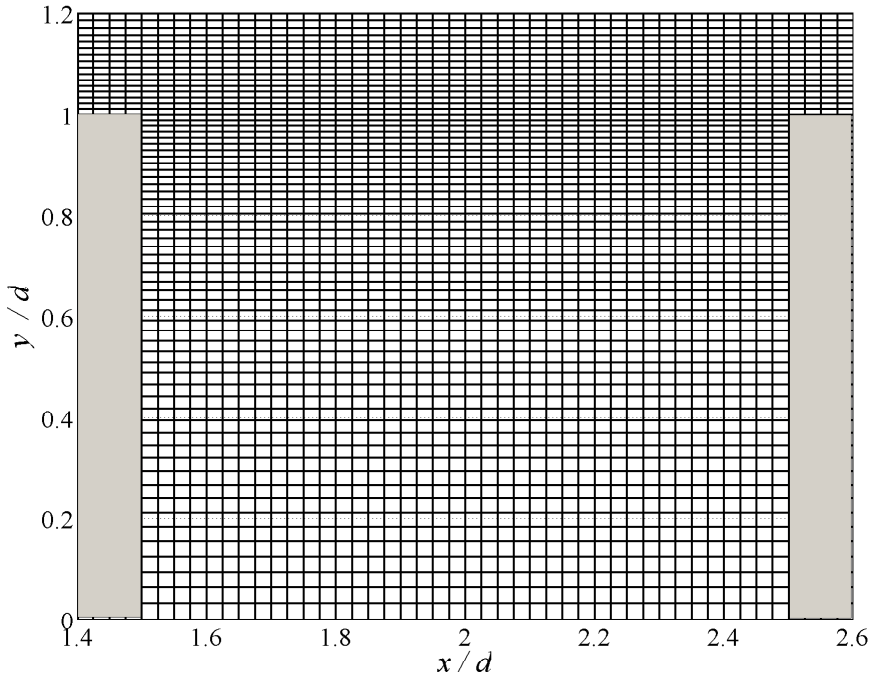

FIGURE 8.6. Domain discretisation of the fine mesh inside and around the cavity.

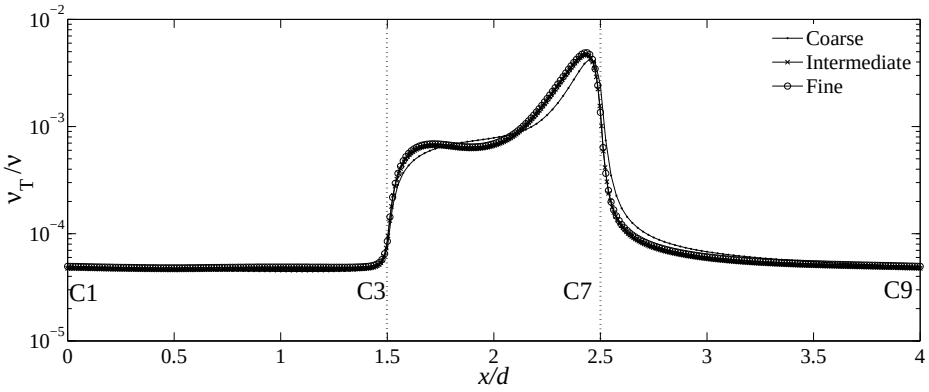

FIGURE 8.7. Turbulent viscosity profile (across line B) for $(y-d)u_\tau/\nu = (y-d)^+ = 1$. Results are provided for three meshes introduced in table 8.1. Figure shows that the solution is converged for the intermediate mesh.

to note that the results in the figure are provided for a location where the numerical diffusion is expected to be most visible since both ν_T and D_T decrease near the wall.

Figure 8.7 shows that numerical diffusion has a considerable effect on the results for the coarse mesh (smoother curve). However, grid convergence is observed for the intermediate and the fine mesh. To stay on the safe side, the fine mesh was used in this study.

Figure 8.8 compares streamlines for the LS model with DNS results by Leonardi *et al.* (2007) for a $\lambda/d = 2$ geometry. The streamlines for the LS model were determined by calculating the stream function Ψ for the flow field, which is related to the velocity components as (Bird *et al.*, 2002):

$$u = \frac{\partial \Psi}{\partial y} \tag{8.12}$$

$$v = -\frac{\partial \Psi}{\partial x}. \tag{8.13}$$

Equations 8.12 or 8.13 can be integrated (with respect to x and y) to determine the stream function. Equation 8.12 was used to determine values of Ψ in figure 8.8 (left). The values for Ψ are shown on the

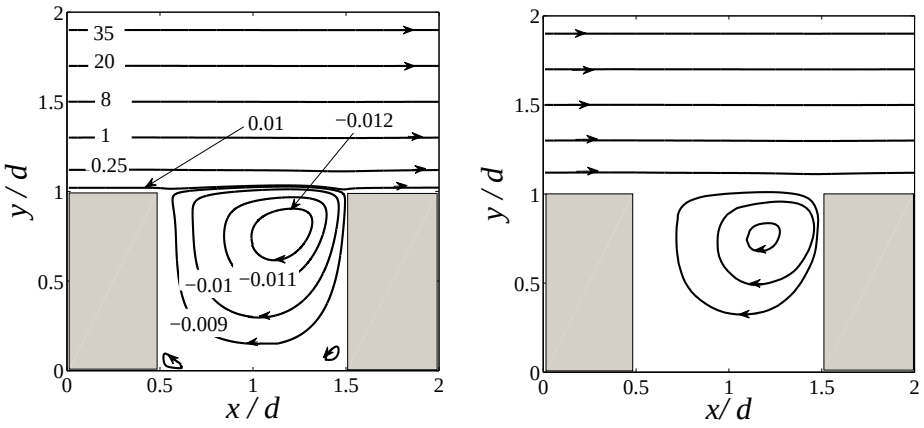

FIGURE 8.8. Flow streamlines for $\lambda/d = 2$ by the LS model (left) and Leonardi *et al.* (2007) DNS results (right). The values on the LS model streamlines represent the value of the stream function (Ψ).

streamlines. Application of equation 8.13 also gave identical values, which is another confirmation for the convergence of the velocity results[5]. Since Ψ is determined from equation 8.12 by integration, a constant value for Ψ should be considered at specific locations for determination of the integration constant. Here, Ψ is set to zero on the wall, as is standard practice for no slip boundary conditions (Bird *et al.*, 2002).

The streamlines in figure 8.8 (right) are adopted from a DNS study by Leonardi *et al.* (2007) for $Re = 2.4 \times 10^4$. This study (as well as other relevant studies such as Cui *et al.* (2003), Leonardi *et al.* (2003), Smalley *et al.* (2001), Orlandi & Leonardi (2006) and Orlandi & Leonardi (2008)) does not report values of Ψ for streamlines. However, the qualitative agreement between the LS and DNS results is good, and the centre of the recirculation zone (inside the cavity) is practically at the same location (approximately $0.7d$ from the wall).

The difference between values of Ψ between adjacent streamlines provides a measure for the flow rate between them. Figure 8.8 (left) clearly shows the rapid increase in the flow rate (and therefore the velocity) when moving away from the crest of the wall. Furthermore, analysis of the values of Ψ indicates that the circulating flow rate in the cavity is almost negligible in comparison with the flow rate in the bulk.

[5]Due to the continuity equation, application of each of the aforementioned equations must give identical results for converged solutions (Bird *et al.*, 2002).

The drag force over a smooth surface is caused by the shear force at the surface, referred to as frictional drag. For the case of rough walls, pressure causes an extra drag force referred to as pressure drag and consequently, the total drag increases[6]. This increases the wall shear velocity u_τ for rough walls. The length averaged wall shear stress is defined as (Leonardi *et al.*, 2007):

$$\tau_w = \frac{\rho U^2}{\lambda} \int_0^{\lambda+2d} (C_f \vec{s} \cdot \vec{x} + C_p \vec{n} \cdot \vec{x}) ds \tag{8.14}$$

where

$$C_f = \frac{\nu}{U^2} \frac{\partial \vec{v} \cdot \vec{s}}{\partial n} \tag{8.15}$$

$$C_p = \frac{p - p_0}{U^2} \tag{8.16}$$

are the normalized local friction and pressure drags, respectively (Cui *et al.*, 2003; Leonardi *et al.*, 2007). In the equations above, $\vec{x}$, $\vec{s}$ and $\vec{n}$ (pointing into the fluid) are the unit vectors in the x, s and n directions, respectively. In addition, $\vec{v} = (u, v)$ is the velocity vector and p_0(=0) is the reference pressure (which is considered as the pressure at point B1 with $x = 0$ and $(y - d)^+ = 1$).

Figure 8.9 shows C_f and C_p of the current study (for $\lambda/d = 2$ and 4), together with DNS results by Leonardi *et al.* (2007) for $\lambda/d = 2$. The figure shows that the LS model adequately reproduces DNS results for λ/d = 2. In general, both friction and pressure drag increase at the point C7. This is due to the presence of a sharp corner. The high turbulence levels at this corner, as evident from figure 8.7, cause vigorous mixing which results in thin shear layers and therefore, a high C_f. Furthermore, the corner is a stagnation point which indicates high pressure and therefore, a high C_p.

Using equation 8.14 and the results of figure 8.9, the friction velocity is $u_\tau = 9.1 \times 10^{-3}$ and 8.9×10^{-3} for λ/d = 2 and 4, respectively. The friction velocity contains simultaneous effects of pressure and friction drag. For the geometry under consideration, the main contributor to u_τ is friction drag, which is

[6]Although, under special circumstances, a rough surface can have less drag than a smooth surface (Pujals *et al.*, 2010; Choi, 2006).

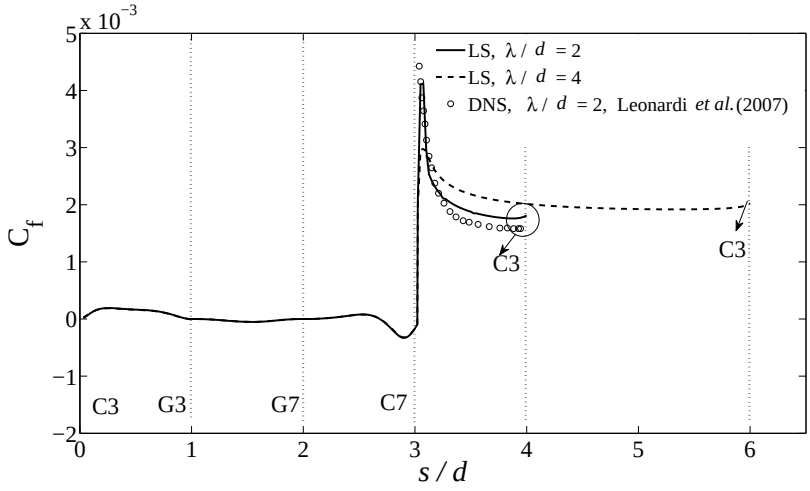

(A) Friction drag

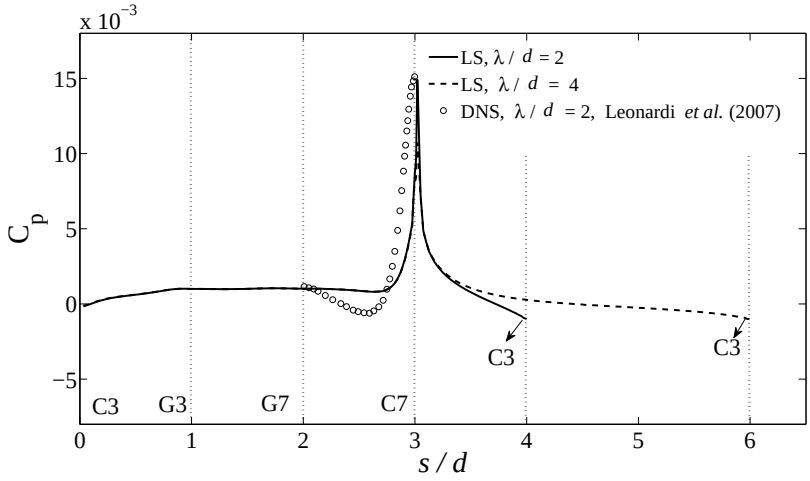

(B) Pressure drag

FIGURE 8.9. Local friction and pressure drags for $\lambda/d = 2$ and 4 by the LS model plus Leonardi *et al.* (2007) DNS results for $\lambda/d = 2$. Locations for different points in figure 8.5 are also determined.

in accordance with the findings of Leonardi *et al.* (2007). The Moody diagram (figure 2.10) can be used to determine if the surface is in a fully rough state or not. Using equation 2.7, the Fanning friction factor $f = 1.06 \times 10^{-2}$ and $f = 1.01 \times 10^{-2}$ is determined for $\lambda/d = 2$ and 4, respectively. Consequently, the surfaces can be considered fully rough for $Re = 2.5 \times 10^5$.

The rough surface (which increases the friction velocity) affects the velocity profile in the log layer. This effect can be incorporated in the log law by (e.g. Jiménez (2004)):

$$u^+ = \frac{1}{\kappa}\ln(y-d)^+ + 5.2 - S \tag{8.17}$$

where S is the shift in the law of the wall. For the case of a d-type fully rough surface, various experimental and numerical studies have shown that S is almost constant as a function of Re. Reported values for this parameter are between 2 and 3 for the case of d-type roughness with $\lambda/d = 2$ (Leonardi *et al.*, 2007; Cui *et al.*, 2003) . The velocity profile by the LS model along the line C1-A1 is shown in figure 8.10 for both λ/d=2 and 4. This figure also shows DNS data by Leonardi *et al.* (2003) ($\lambda/d = 2$). The value of S for the DNS data is 2.6. For the LS model results, this value is 2.2, which is in agreement with the DNS results. For the $\lambda/d = 4$ case, $S = 2.2$ is determined. The decrease in S is expected as $S \to 0$ as $\lambda/d \to \infty$ (i.e. the geometry becomes smooth).

Once the velocity and turbulent viscosity fields are determined by the LS model, it is possible to calculate $\overline{u'v'}$ from the gradient diffusion hypothesis (Hanjalić *et al.*, 2009):

$$\overline{u'v'} = -\nu_T\left(\frac{\partial u}{\partial y} + \frac{\partial v}{\partial x}\right). \tag{8.18}$$

Results of the LS model for $\overline{u'v'}$ are shown in figure 8.11 (left) for $\lambda/d = 2$. Figure 8.11 (right) also shows LES results for the same λ/d (Cui *et al.*, 2003). Results of both figures are normalized by U^2. It can be seen that results of the LS model are very similar to the LES results. This is further evidence that the LS model is appropriate for the prediction of the flow field and Reynolds stresses for the geometry under consideration.

8.3.1. Critical flow properties for $\lambda/d = 4$.

A comparison of the LS model with DNS and LES data for $\lambda/d = 2$ has demonstrated that the LS model is suitable for flow and turbulence predictions. In this section, critical flow properties for the case of $\lambda/d = 4$,

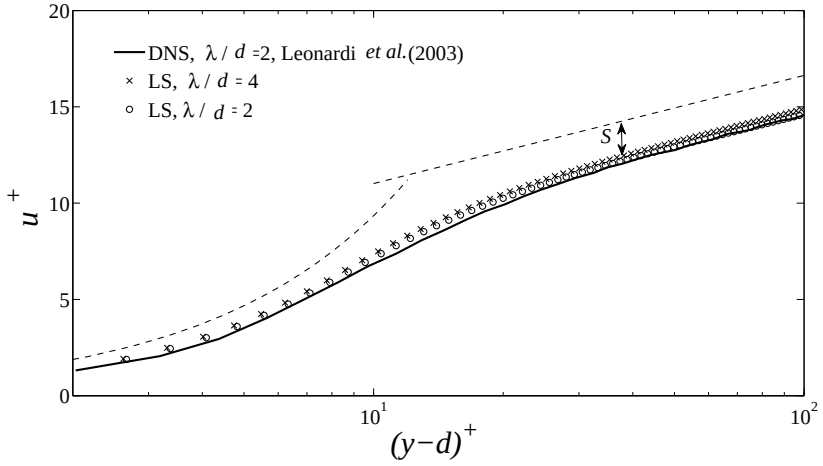

FIGURE 8.10. Streamwise velocity profile by the LS model over the crest (line C1-A1) for $\lambda/d = 2$ and 4 together with Leonardi *et al.* (2003) DNS results for λ/d=2.

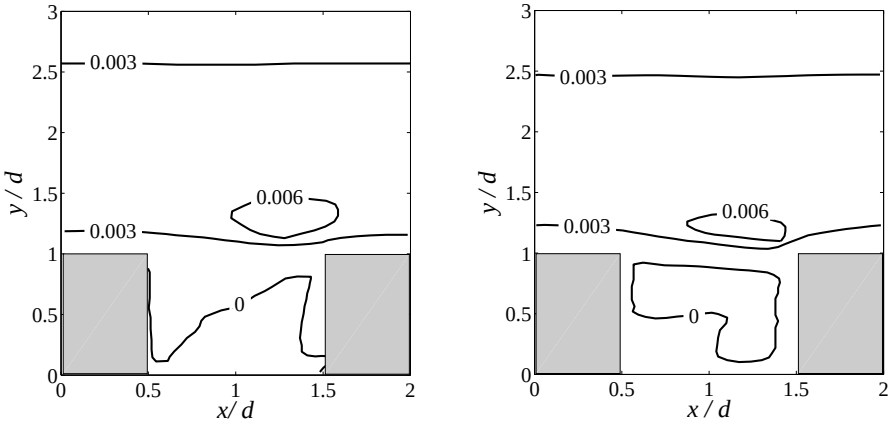

FIGURE 8.11. Reynolds stress ($\overline{u'v'}$) by the LS model (left) and Cui *et al.* (2003) LES results (right) for $\lambda/d = 2$.

which will be used in the next chapter for the simulation of solute mass transport, are reported.

Figure 8.12 shows LS results of streamlines for $\lambda/d = 4$. As in the $\lambda/d = 2$ case, a recirculation zone forms inside the cavity and the mean flow does not enter the cavity. This implies that the average flow does not transport the solute into the cavity and therefore, the only mass transport mechanisms between the bulk

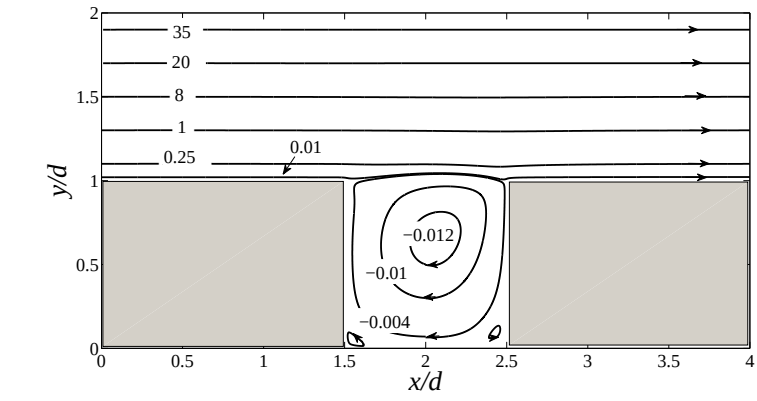

(A) Ψ

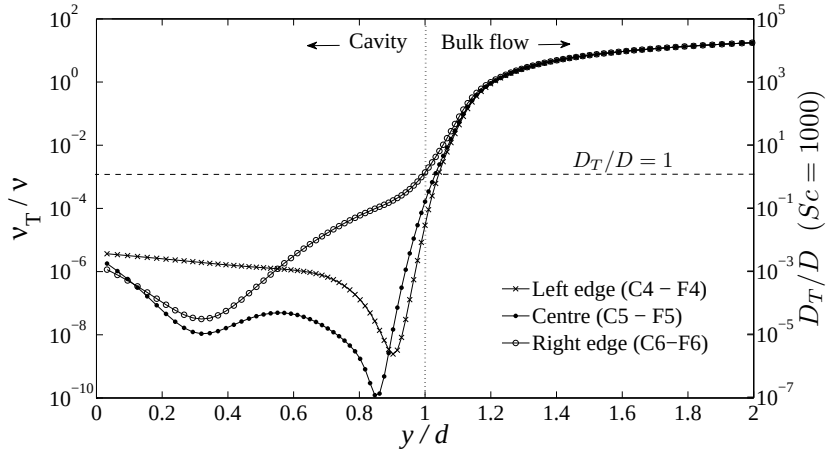

(B) ν_T

FIGURE 8.12. (A) Flow streamlines and values of the stream function Ψ for λ/d = 4, (B) turbulent viscosity inside and above the cavity for λ/d = 4.

and the cavity are molecular and turbulent diffusion.

Figure 8.12 shows the normalized turbulent viscosity profile ν_T/ν for three vertical sections C4-F4, C5-F5 and C6-F6. The figure also shows D_T/D for $Sc = 1000$ and $Sc_T = 1$ on the secondary vertical axis. Outside the cavity (for $y/d > 1$), turbulent diffusion dominates over molecular diffusion ($D_T/D > 1$). However, inside the cavity molecular diffusion dominates ($D_T < D$). It is then concluded that for the high *Sc* case under consideration, the mass transport inside the cavity is governed by molecular diffusion.

8.4. Summary

The study in this chapter was focused on the simulation of the flow field for rough surfaces. The LS LRN $k-\varepsilon$ model was introduced, implemented and verified for two cases; a smooth channel flow and a d-type rough surface with λ/d = 2. For the case of smooth channels, it was shown that the LS model faithfully reproduces the velocity profile. However, the near wall value of ν_T was lower than the DNS data. It was discussed that although such inconsistency does not affect the velocity, special consideration will be required for the simulation of high *Sc* solute mass transport.

For the case of a rough surface with $\lambda/d = 2$, a comparison was made with DNS and LES results. Good agreement was found with the results from the LS model. Results for a rough wall simulation for λ/d = 4 were also presented. The results will be used in the next chapter to simulate mass transport over a rough surface. The key properties of the flow are:

(1) The mean flow does not enter the cavity;
(2) $D_T/D < 1$ inside the cavity for a compound with $Sc \geq 10^3$. This implies that the mass transport inside this area is governed by molecular diffusion for such *Sc*.

The aforementioned observations are used in the next chapter for interpretation of the mass transport results. In addition, they are used to present an analytical solution for determination of the concentration decay coefficient for the rough surface being studied.

CHAPTER 9

Geometry limited mass transfer in turbulent plane channel flow with d-type rough walls

Following the description and verification of the LS model in the previous chapter, the current chapter studies the physics of high *Sc* mass transport over a d-type rough surface with λ/d = 4 at $Re = 2.5 \times 10^5$. The aim of this chapter is to develop simple parameterisations of wall demand for rough surfaces (the fourth research question posed in section 2.6). Similar to the study in chapter 5, the physics of mass transport is revealed by imposing a wide range of wall demand coefficients and analysing the mechanism of mass transport.

As this is, to the author's knowledge, the first time wall demand has been studied using a LRN $k-\varepsilon$ model, smooth wall demand must be analysed first. The smooth wall verification in section 8.2 showed that the prefactor *b* was a factor of 10 too low, and a simple method to compensate for the difference is presented in section 9.1.

The governing equations for mass transport and their discretisation for the rough surface being studied are presented in section 9.2. The rough wall simulations are discussed in section 9.3, which makes use of the flow calculations for the $\lambda/d = 4$ case described in the previous chapter. The dominant physics of the mass transport mechanism are identified and used in section 9.4 to develop a simple parameterisation for the decay coefficient. In section 9.5, the performance of this approach is compared with the two existing parameterisations that were discussed in section 2.5.3. A summary of the chapter is presented in section 9.6.

9.1. Compensating for the inaccuracy in the prefactor *b*

In section 8.2, it was established that the LS model correctly reproduces the cubic dependence of ν_T on the wall distance, but the prefactor b_{LS} (the prefactor *b* for the LS model) is a factor of 10 too low (figure

8.3). Given the strong influence of b_{LS} on k (equation 5.31), this difference must be compensated for. A simple solution will be outlined below, after the influence of b_{LS} on k is explored.

The LS flow field results for a smooth channel (as presented in section 8.2) are used to model the first-order wall reactions. The approach presented in chapter 5 is used to determine k via the 1D model. The only difference is that the equations are now in a Cartesian coordinate system. These equations are presented in appendix A. The results are then compared with the analytical solution presented in equation 5.31 (with $r_h = \delta$ for channel flows, see appendix A):

$$k_a = \frac{1}{U\,\delta}\frac{\mathrm{k_w}}{1+\frac{2\pi\sqrt{3}\mathrm{k_w}}{9u_\tau}\sqrt[3]{\frac{Sc^2}{b}}}. \tag{9.1}$$

The analytical decay coefficient for $Sc = 3162$ is shown as a function of $\mathrm{k_w}/U$ in figure 9.1. The reason for selection of this specific value of Sc will be clarified later in this section. It was shown in chapter 5 that for small values of $\mathrm{k_w}$, equation 9.1 simplifies to $k_a = \mathrm{k_w}/U\delta$. This region is known as the uniform concentration region for which the wall concentration is approximately equal to the bulk concentration. For very high values of $\mathrm{k_w}$, equation 9.1 reaches an asymptotic value given by $k_a = (9u_\tau\sqrt[3]{b})/(2\pi\sqrt{3}\sqrt[3]{Sc^2})$. In this region, $c_w \approx 0$. The asymptotic value of k_a in this region is then a linear function of $\sqrt[3]{b/Sc^2}$.

Figure 9.1 also shows the decay coefficient determined by using the numerical 1D model in chapter 5 with the LS flow results for $Sc = 3162$. It can be seen in this figure that the asymptotic value of the LS decay coefficient is too low. This is a direct consequence of the incorrect prefactor b for ν_T in the LS model (figure 8.3). Since b_{LS} is 10 times lower than the real b ($= 9.5 \times 10^{-4}$), we do indeed expect that the ratio between the decay coefficient of the LS model and equation 9.1 is $\sqrt[3]{b/b_{LS}} = 0.46$. This difference is naturally unacceptably large, but a straightforward correction can be applied to circumvent it.

The correction is simply to simulate with a different Sc_{LS} (the corrected LS Sc). Indeed, defining $Sc_{LS} = \sqrt[3]{b_{LS}/b}Sc$, the offset in the LS model decay coefficient can be compensated for and a physically realistic decay coefficient is obtained. This is shown in figure 9.1 for $Sc_{LS} = 1000$. As can be seen, the results of the LS model decay coefficient using the modified Sc_{LS} are in agreement with the real decay coefficient

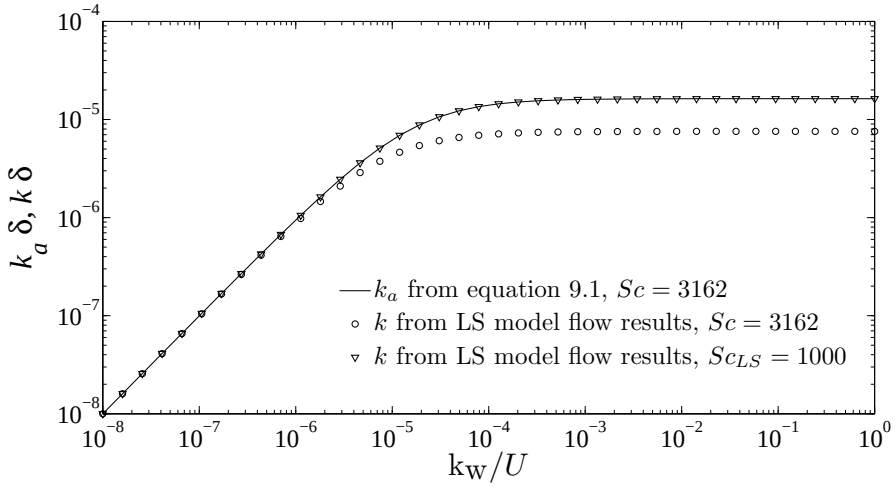

FIGURE 9.1. Decay coefficients of the smooth surface using the LS model results and high *Sc* approximation analytical solution in equation 9.1.

k_a. In this study, $Sc_{LS} = 1000$ is used, which corresponds to $Sc = 3162$. Although this value of *Sc* does not match the properties of chlorine in water (see figure 2.11), it is close to the conditions of experimental electrochemical studies in which an average $Sc \approx 3000$ is used to determine a Sh_R correlation (Zhao & Trass, 1997).

9.2. Governing equations and numerical method

With the assurance that wall demand can be sufficiently simulated using u and D_T from the LS model, the next step is to move to a rough surface. The governing equation for mass transport in a plane channel geometry is (Bird *et al.*, 2002):

$$u\frac{\partial c}{\partial x} + v\frac{\partial c}{\partial y} = \frac{\partial}{\partial x}\left[(D + D_T)\frac{\partial c}{\partial x}\right] + \frac{\partial}{\partial y}\left[(D + D_T)\frac{\partial c}{\partial y}\right] \tag{9.2}$$

where bulk demand has been neglected. The wall demand is modelled by a Robin boundary condition at the wall (figure 8.4):

$$D\frac{\partial c}{\partial n} = \mathrm{k_w} c_w. \tag{9.3}$$

In the centre of the channel, a constant concentration boundary condition is used, and periodic boundary conditions are used on the left and right faces of the domain. This subtle change in boundary conditions is justified because $\mathrm{L} \gg \lambda$, where L is the typical length scale for changes in c in the x direction[1] (chapter 7).

As OpenFOAM does not support Robin boundary conditions, a custom mass transport solver was developed, the code of which is presented in appendix B. Equations 9.2 and 9.3 are discretised on a rectangular structured grid, shown in figure 9.2. The domain includes the crests. However, all the cells located inside the crests are rendered inactive by setting $c = 0$. The concentration c, velocities u and v and the turbulent diffusion coefficient D_T are all located in the cell centres. The flow data (u, v and D_T) was imported and interpolated to the grid. Resolutions were similar to the fine mesh introduced in the previous chapter (table 8.1).

A central difference scheme (as introduced in chapter 5) is used to model the diffusive terms in equation 9.2. However, application of a central scheme for the advective terms can result in numerical instability in the convergence of the solution, because the scheme is not monotonic and can cause over and under shoots[2] (Hanjalić *et al.*, 2009). Consequently, a first-order upwind scheme is used to approximate advective terms. The advective term $u\partial c/\partial x$ in equation 9.2 is then discretised as:

$$\begin{cases} u_{i,j}\frac{c_{i,j}-c_{i-1,j}}{\Delta x_i} & \text{if } u_{i,j} > 0 \\ \\ u_{i,j}\frac{c_{i+1,j}-c_{i,j}}{\Delta x_i} & \text{if } u_{i,j} < 0. \end{cases}$$

[1] To check the validity of these assumptions, the results were also compared with appropriate boundary conditions for the developing concentration field. A loop of 50 periodic lengths was simulated. In this case, one periodic length was simulated at each step. A symmetric boundary condition was considered at the channel centre and a uniform concentration profile was assumed at the inlet of the first simulated periodic length. The concentration profile at the outlet of each simulation was then used as the inlet boundary condition of the next simulation. Results using this approach of simulation did not show considerable differences.

[2] Elements in the coefficient matrix are positive definite. However, application of the central difference scheme for the advective terms can cause negative elements in the coefficient matrix, if the advection dominates the molecular transport (Hanjalić *et al.*, 2009).

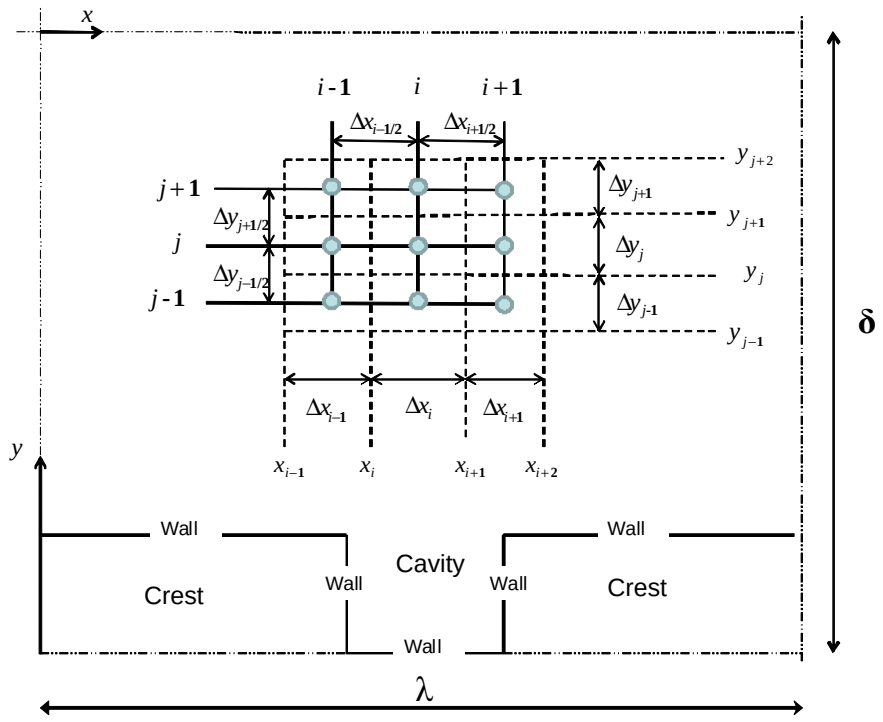

FIGURE 9.2. Schematic of the domain discretisation. Figure is not to scale.

In addition, the advective term $v\partial c/\partial y$ in equation 9.2 is discretised as:

$$\begin{cases} v_{i,j}\frac{c_{i,j}-c_{i,j-1}}{\Delta y_j} & \text{if } v_{i,j} > 0 \\ \\ v_{i,j}\frac{c_{i,j+1}-c_{i,j}}{\Delta y_j} & \text{if } v_{i,j} < 0. \end{cases}$$

However, the upwind scheme is known to have numerical diffusion (Hirsch, 2007). This numerical diffusion is in addition to the molecular viscosity (for flow) and diffusion (for mass transport) and therefore, causes numerical errors. The numerical diffusion in the x and y directions (assuming flow purely in the x and y directions[3], respectively) is:

[3]This is the case for maximum numerical diffusion.

$$\Gamma_x = \frac{u_{i,j}\Delta x_i}{2}, \quad \text{and} \quad \Gamma_y = \frac{v_{i,j}\Delta y_j}{2}. \tag{9.4}$$

The method for controlling this numerical diffusion is to use a grid sufficiently fine so that the value of the numerical diffusion is negligible in comparison with the molecular viscosity (for flow) and molecular diffusion (for mass transport). The criterion applied for controlling numerical diffusion in chapters 8 and 9 is $\max(\Gamma_x, \Gamma_y) < 10^{-2}(D + D_T)$ which is achieved for the intermediate mesh. The fine mesh is used to be on the safe side.

9.3. Results

As in the study in chapter 5, a wide range of $\mathrm{k_w}/U$ is considered. In accordance with the results of section 9.1, $Sc_{LS} = 1000$ is considered which corresponds physically to $Sc = 3160$. Figure 9.3 shows the concentration contours for different $\mathrm{k_w}/U$. It is seen that for lower $\mathrm{k_w}/U$, the concentration in the cavity is only slightly lower than in the bulk. However, for high $\mathrm{k_w}/U$, concentration levels inside the cavity drop significantly. Therefore, wall mass flux in the cavity will become small in comparison with the crest. This phenomenon becomes clearer when the decay coefficient is studied.

The decay coefficient is defined as the ratio of the mass withdrawal from the system to the mass being convected by the bulk flow (chapter 5). Since $\lambda \ll \delta$, λ can be considered as an infinitesimal element of length (in comparison with δ) and therefore, the decay coefficient for (unit of width of) the rough surface shown in figure 8.5 is:

$$k_R = \frac{1}{\lambda}\frac{\int_{C1}^{C9} \mathrm{k_w} c_w \, ds}{\int_{C1}^{A1} uc \, dy}. \tag{9.5}$$

Figure 9.4 shows decay coefficients for the rough and smooth surfaces. The ratio of the rough and smooth surface decay coefficients is also shown in this figure. It can be seen that for small $\mathrm{k_w}/U$, the rough wall decay coefficient k_R is 1.5 times higher than the smooth wall decay coefficient (k). This is due to the

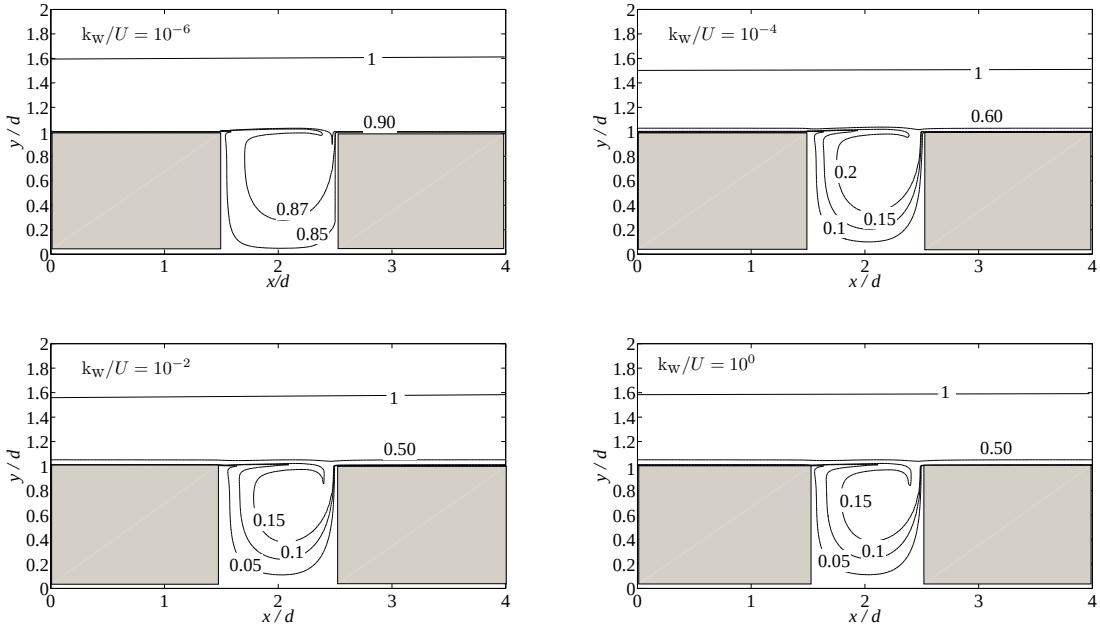

FIGURE 9.3. Concentration contours for different k_w/U.

fact that when k_w is small, molecular diffusion is not a limiting factor and therefore, $c_w \approx c_x$ everywhere on the surface (figure 9.3). In addition, the reaction length for one periodic length of the surface with λ/d = 4 is $(\lambda + 2d)/\lambda = 1.5$ times higher than the counterpart length for the smooth surface. However, for $k_w/U \approx 2 \times 10^{-6}$, k_R and k are equal and for even higher k_w/U, $k_R < k$. Hence, despite the extra surface area, the decay coefficient is *lower* for a rough surface than for a smooth surface at high k_w/U. This phenomenon will be referred to as geometry limited mass transfer, because the (diffusive) transport through the cavity becomes the limiting factor.

To further clarify the behaviour of the decay coefficient for rough wall geometries, its value is decomposed in the contribution of the crest and the cavity, i.e. $k_R = k_{cr} + k_{ca}$. Approximating $\int_{C1}^{A1} uc\,dy$ in equation 9.5 as $Uc_x\delta$, we obtain

$$k_{cr} = \frac{J_{cr}}{\lambda U \delta c_x} \quad \text{and} \quad k_{ca} = \frac{J_{ca}}{\lambda U \delta c_x} \tag{9.6}$$

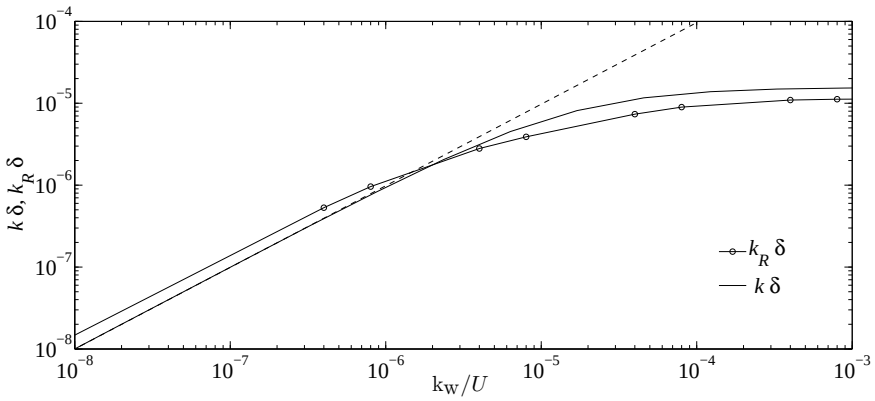

(A) Decay coefficients

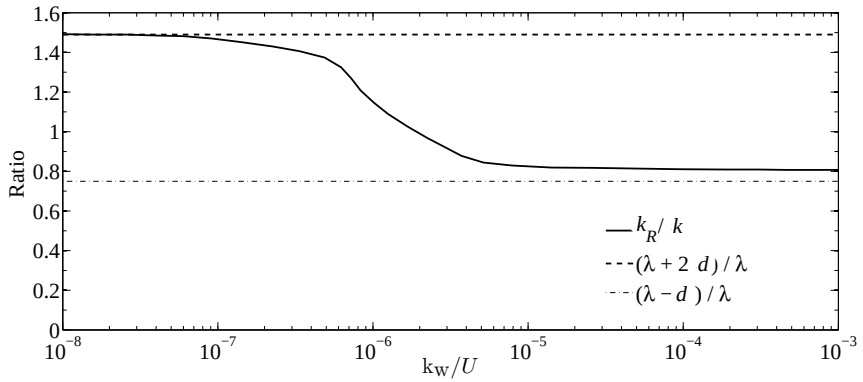

(B) Ratio

FIGURE 9.4. (A) Decay coefficients of the rough surface (k_R) and smooth surface (k) as functions of k_w/U, (B) The ratio of k_R/k.

where

$$J_{cr} = \int_{C1}^{C3} k_w c_w ds + \int_{C7}^{C9} k_w c_w ds, \quad \text{and} \quad J_{ca} = \int_{C3}^{C7} k_w c_w ds \tag{9.7}$$

are the integral wall mass flux of the crest and the cavity, respectively. For the case of $\lambda/d = 4$, the area of the crest and the cavity are equal ($\lambda - d = 3d$) and therefore, it is expected that for small k_w (when $c_w \approx c_x$),

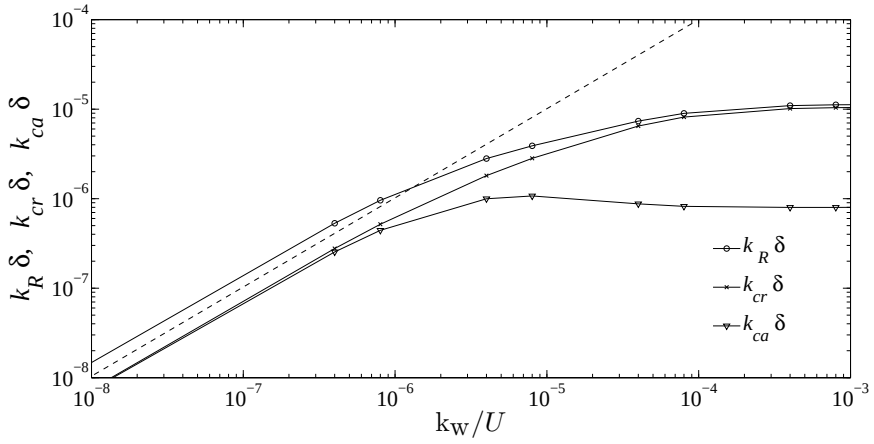

FIGURE 9.5. The rough wall decay coefficient (k_R) plus decomposed cavity and crest decay coefficients (k_{ca} and k_{cr}) as functions of k_w.

both regions contribute equally to k_R. This expectation is confirmed in figure 9.5, where k_{ca} and k_{cr} are plotted. When increasing k_w, k_{ca} asymptotes to a much lower value than k_{cr}. This is a direct consequence of the geometry limited mass transport inside the cavity.

Figure 8.12 showed that the cavity is governed by molecular diffusion and therefore, behaves like a MTBL, which is much thicker than the MTBL over the crest. Therefore, the maximum possible diffusive mass flux in the cavity is much lower than over the crest and consequently, the mass transfer through the cavity becomes negligible (compared to the crest) for high k_w/U. For one periodic length λ, the ratio of crest and smooth surface is $(\lambda - d)/4d = 3/4$ (note that $\lambda/d = 4$). Figure 9.4 confirms that for high k_w/U, the ratio of rough to smooth surface decay coefficients is close to $3/4$, although is slightly higher (since the contribution of the cavity in the decay coefficient is not zero).

9.4. Parameterisation of the rough wall demand

Results of figures 8.12 and 9.5 suggest that the wall demand for the cavity and the crest have different behaviours. For the case of the crest, the results suggest that the thickness of the MTBL is approximately the same as for a smooth surface. For the cavity, this thickness is from the order of the depth of the cavity d. These two observations are used in this section to develop a parameterisation for the rough surface decay

coefficient k_R.

The starting point for the parameterisation is to decompose the analytical rough wall decay coefficient into the analytical coefficients for describing the contribution of the crest and the cavity,

$$k_{R_a} = k_{ca_a} + k_{cr_a}. \tag{9.8}$$

Using the definition for k_{ca} in equation 9.6, and defining $J_{ca_a} = 3d\mathrm{k_w}c_{w_{ca}}$, where c_{w_a} is the average wall concentration in the cavity

$$c_{w_{ca}} = \frac{1}{3d}\int_{\mathrm{C3}}^{\mathrm{C7}} c_w ds \tag{9.9}$$

we obtain

$$k_{ca_a} = \frac{3\ d\ \mathrm{k_w}c_{w_{ca}}}{\lambda\delta U c_{\mathrm{x}}}. \tag{9.10}$$

The study in chapter 8 demonstrated that the cavity is dominated by diffusion (figure 8.12). Additionally, figure 8.7 showed that the turbulent viscosity increases rapidly at the interface of the bulk flow and cavity. Consequently, it is assumed that $c \approx c_{\mathrm{x}}$ on the line C3-C7 and that the mass transport from the bulk flow to the cavity (and its further consumption by cavity walls) is molecular diffusion dominant. This mass transport is then described by thin film theory (Bird *et al.*, 2002):

$$J_{ca_a} = D\frac{c_{\mathrm{x}} - c_{w_{ca}}}{\alpha_{\mathrm{d}} d} \tag{9.11}$$

where α_{d} is an empirical coefficient between 0 and 1 ($\alpha_{\mathrm{d}}d$ is the effective thickness of the MTBL inside the cavity). Together with the Robin boundary condition $J_{ca_a} = \mathrm{k_w}c_{w_a}$, equation 9.11 can be rearranged to

$$c_{w_{ca}} = \frac{c_{\mathrm{x}}}{1 + \frac{\alpha_{\mathrm{d}} \mathrm{k_w} d}{D}} \tag{9.12}$$

and therefore,

$$k_{ca_a} = \frac{3d}{\lambda\delta} \frac{\mathrm{k_w}/U}{1 + \alpha_{\mathrm{d}} Re_{\mathrm{d}} Sc \frac{\mathrm{k_w}}{U}}. \tag{9.13}$$

Results of section 9.3 agree well with $\alpha_{\mathrm{d}} = 0.7$ for $Sc = 3162$. The analytical decay coefficient for the crest k_{cr_a} will be approximated using the smooth wall solution (equation 9.1), taking into account the ratio of the length of the crest ($\lambda - d = 3d$) to the periodic length λ:

$$k_{cr_a} = \frac{\lambda - d}{\lambda} k_a = \frac{\lambda - d}{\lambda} \frac{1}{U\delta} \frac{\mathrm{k_w}}{1 + \frac{2\pi\sqrt{3}\mathrm{k_w}}{9u_\tau} \sqrt[3]{\frac{Sc^2}{b}}}. \tag{9.14}$$

This completes the formulation of the parameterisation. The parameterisation and the individual contributions of k_{ca_a} and k_{cr_a} are compared to the simulation results in figure 9.6. The agreement is good, especially at low and high $\mathrm{k_w}/U$. At intermediate $\mathrm{k_w}/U$, k_{cr_a} seems to slightly underpredict the mass transfer. This demonstrates the separable nature of the mass transport of high *Sc* compounds over d-type rough walls. In other words, the crest can be considered as a smooth surface and the molecular diffusion can be considered as the dominant transport mechanism inside the cavity. More research is however necessary to see how widely applicable the parameterisation is.

9.5. Comparison of different parameterisations of wall demand in rough pipes

The two major methods for parameterisation of wall demand of high *Sc* compounds in rough pipes were introduced in chapter 2. The electrochemical experiments showed that the effect of rough walls involved a modification of the form $\mathrm{k_{f_R}} = \theta_{\mathrm{k_f}} \mathrm{k_f}$, where $\theta_{\mathrm{k_f}} < 1$ for sufficiently large Re_d (equation 2.31). Water quality

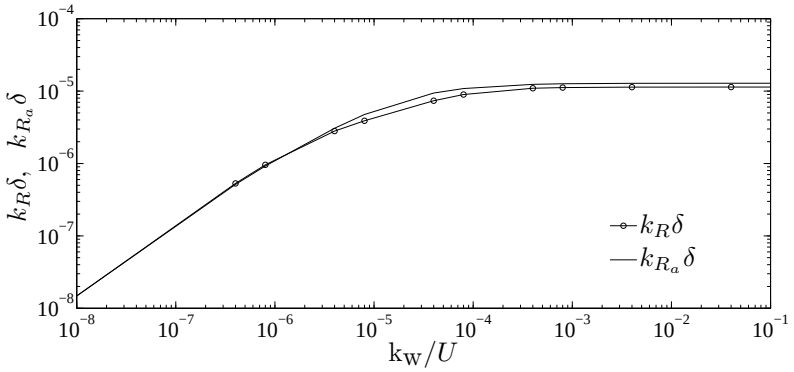

(A) k_R and k_{R_a}

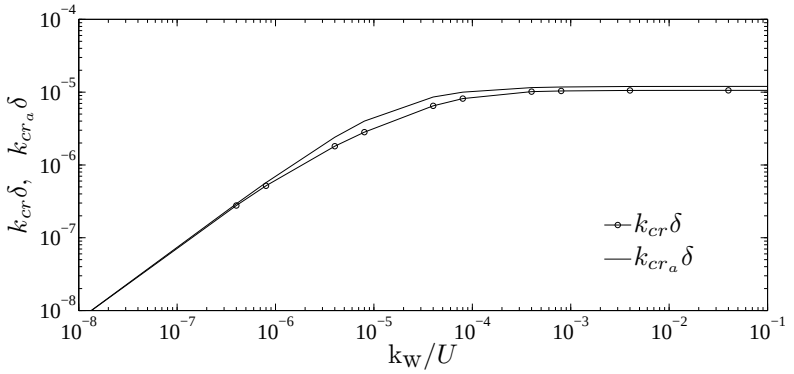

(B) k_{cr} and k_{cr_a}

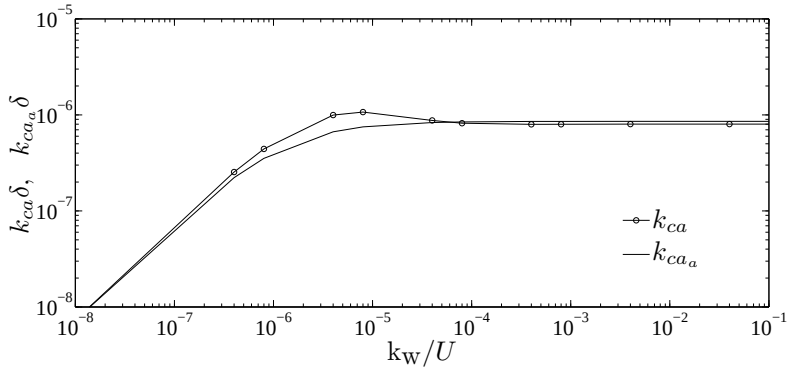

(C) k_{ca} and k_{ca_a}

FIGURE 9.6. Analytical versus numerical decay coefficients for the d-type rough surface as functions of $\mathrm{k_w}$.

TABLE 9.1. Conceptual comparison of the existing parameterisation methods for rough wall demand with the parameterisation proposed in this study.

Parameterisation	$k_w \ll k_f$	$k_w \gg k_f$
Smooth conduits	$\frac{k_w}{r_h U}$	$\frac{k_f}{r_h U}$
EPANET	$\frac{\theta_{k_w} k_w}{r_h U}$	$\frac{k_f}{r_h U}$
Experimental	$\frac{k_w}{r_h U}$	$\frac{\theta_{k_f} k_f}{r_h U}$
Equation 9.8	$\frac{\theta_{k_w} k_w}{r_h U}$	$\frac{\theta_{k_f} k_f}{r_h U}$

models such as EPANET take into account the added surface area and use a parameterisation of the form $k_{w_R} = \theta_{k_w} k_w$, where $\theta_{k_w} > 1$, i.e. an increase in the wall demand coefficient. Table 2.9, which showed the behaviour of the parameterisations for low and high wall demand, can now be augmented with the behaviour of the new parameterisation (table 9.1).

Let us consider a sufficiently deep cavity and assume that the new parameterisation fully describes the wall demand as a function of k_w/U. Furthermore, it is assumed that the experimental and EPANET parameterisations match as well as possible. For the EPANET parameterisations, this will be at small k_w/U, and for the experimental parameterisation, this will be at high k_w/U.

All parameterisations are schematically shown in figure 9.7. The two classical parameterisations each capture a limit behaviour, but provide incorrect predictions at the other limit. The EPANET parameterisation overpredicts k_R at high k_w/U. From a practical perspective, this is good because it provides a conservative estimate, although chlorine levels may be much higher than strictly necessary as a result. The experimental parameterisation will underpredict k_R for low k_w/U.

In fact, for the simple geometry studied in this chapter, the new parameterisation is essentially a blend of the two existing parameterisations. This once more illustrates (within the limitations of the new parameterisation) that the modifications of the wall demand coefficient or the mass transfer coefficient are driven by the geometry. For small k_w/U, the extra surface area will enhance the mass withdrawal but the geometry becomes the limiting factor of the mass withdrawal for higher k_w/U.

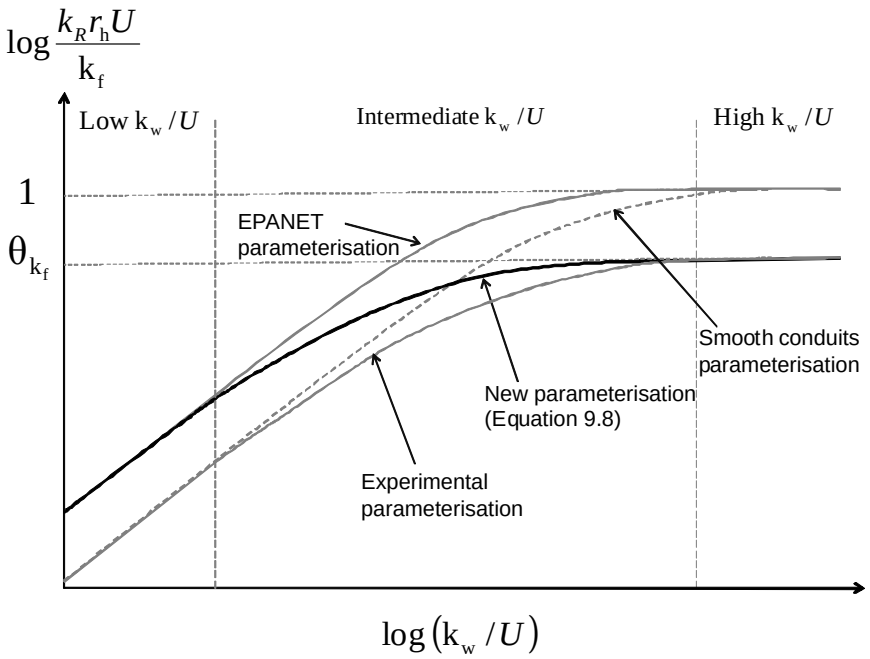

FIGURE 9.7. A conceptual schematic of k_R using three methods of wall demand parameterisation.

9.6. Summary

A comparison between mass transfer in turbulent flows over a smooth and a d-type rough surface was performed in this chapter. The study was restricted to $\lambda/d = 4$ and $Re = 2.5 \times 10^5$. A wide range of first-order wall demand coefficients was studied. Results of the mass transport simulation showed that for relatively low k_w, the rough wall decay coefficient is 1.5 times higher than the smooth wall. On the other hand, the ratio of the rough to smooth surface decay coefficient became 0.8 for very high k_w/U.

It was discussed that these values were dictated by the geometry. For low k_w/U, the additional surface area of the rough surface causes an increased mass decay coefficient, compared with smooth walls. For high k_w/U, the mass transfer through the MTBL was shown to become diffusion limited. Consequently, the rate of wall mass flux in the cavity becomes negligible in comparison with the crest wall mass flux. This effectively "switched off" the cavity. For the $\lambda/d = 4$ case, the surface area with and without the cavity is 1.5λ and $3\lambda/4$ respectively. The latter is close to the calculated ratio of k_R/k for high wall demands (0.8, see figure 9.4).

A parameterisation of wall demand was presented, based on decomposition of the decay coefficient into the coefficients describing separate contributions of the cavity and the crest. Results using this model were verified by the numerical results. In general, presenting such a simple analytical model supports the feasibility of parameterisation of wall demand over rough surfaces on a physical basis. This parameterisation was also conceptually compared with the two existing parameterisation approaches for rough wall demand introduced in section 2.5.3. It was shown that the new parameterisation, for this particular geometry, correctly captures both high and low k_w limits, in contrast with existing parameterisations.

CHAPTER 10

Conclusions

The work presented in this thesis was motivated by the need for accurate water quality models for water distribution networks, and aimed to improve understanding about the influence of flow and turbulence on wall demand. A combined numerical and analytical approach was pursued. The main findings and conclusions will be discussed in sections 10.1 to 10.3 and are summarised in table 10.1. A discussion on the contribution of the findings to water quality modelling and further extensions are also presented in sections 10.4 and 10.5, respectively.

10.1. First-order wall and bulk demand in smooth pipes

Chapters 4 to 6 laid the foundations for the thesis. First, turbulence models were carefully selected based on their ability to reproduce the cubic dependence of turbulent viscosity on the distance to the wall in the viscous sublayer. The cubic dependence is crucial for appropriate simulation of wall demand for high *Sc* compounds such as chlorine. In chapter 5, two solution methods for the wall demand were developed:

(1) a 1D model valid for arbitrary *Sc* which predicts the decay coefficient and concentration profiles. The model is based on a separation of variables;
(2) an analytical solution valid for $Sc \gg 1$. The solution is based on the observation that all transport occurs in the viscous sublayer and that the total flux in the MTBL is approximately constant.

The methods were extended in chapter 6 to include first-order bulk demand, and were used to answer two research questions (posed in section 2.6), which will be discussed below.

Is the use of the Sh correlation by Notter & Sleicher (1971) which is valid for constant c_w (Dirichlet boundary conditions) valid for first-order wall demand (Robin boundary conditions), and under which circumstances?

The analysis in chapter 5 shows that the Notter & Sleicher (1971) correlation (equation 2.29) is in very good agreement with the *Sh* correlation derived for first-order wall demand (equation 5.32). The reason the correlations are identical, even though the boundary conditions are different, is that changes in concentration in the streamwise direction occur on much larger scales than in the wall normal direction. This observation was exploited in chapter 7, which facilitated the development of several new asymptotic solutions for linear and nonlinear wall demands.

It was shown that the decay coefficient exhibits different behaviour for very low and very high wall demand coefficients k_w. For $\mathrm{k_w}/U < 10^{-6}$ the concentration profile is uniform and therefore $c_w \approx c_x$. Consequently, the decay coefficient is independent of *Sc* and represented by $k = \mathrm{k_w}/r_h U$. For high wall demand coefficients, the diffusive transport through the MTBL becomes the limiting factor and therefore, $c_w \approx 0$. For this situation, the analytical asymptotic solution for high *Sc* compounds predicts $k = (9u_\tau \sqrt[3]{b})/(2\pi U r_h \sqrt{3}\sqrt[3]{Sc^2})$, i.e. k is *independent* of k_w and depends on flow and molecular properties only.

Bounds were established for the validity of the *Sh* correlation by comparing the differences between the decay coefficient predicted by the analytical method (valid for $Sc \gg 1$) and the 1D model. Accepting a maximum 5% relative error (e) in the value of k, the *Sh* correlation is valid for $Sc > 100$, once more in agreement with Notter & Sleicher (1971). Since, for the case of chlorine, $Sc \approx 1000$ for the desired water temperature (15^oC (WHO, 2008)), the correlation is applicable for modelling chlorine first-order wall demands.

Do wall demand and bulk demand influence each other, and under which circumstances?

It is common to assume that wall demand and bulk demand do not influence each other. Whilst this is a reasonable assumption it is important to establish the parameter range for which this assumption is valid. This was the topic of chapter 6.

As expected, the interaction between wall and bulk demand was indeed very weak. The only nonlinear effect of combined wall and bulk demands on the decay coefficient k is the attenuation of the average mass flux $\langle uc \rangle$. For large *Da*, the concentration profile in the bulk is no longer constant, and therefore the approximation $\langle uc \rangle \approx U c_\mathrm{x}$ is no longer valid. It was shown that with a maximum 5% relative error (e) in the value of k for high *Sc* compounds, the assumption of uniformity in the bulk concentration profile holds for

$Da < 1$. As typical values for Da in distribution networks are $Da \approx 10^{-5}$ (see tables 2.3 and 2.5 and note that the average Re in a typical network is 10^5 (Ho, 2008)), it can be concluded that wall and bulk demand can be safely assumed to be independent of each other.

10.2. Parameterisation of nonlinear wall demands

As an answer to the third research question posed in section 2.6, parameterisation of nonlinear wall demands was addressed in chapter 7. The chapter was inspired by the insights developed in chapter 5. Using a dimensional analysis, it was argued that the contribution of streamwise advection was negligible compared to the wall normal mass transport. This resulted in a PDE which depended on the wall normal direction only, the solution of which had the same form as the asymptotic solution derived in chapter 5. The streamwise concentration profile took the form of an ODE. Because this method did not rely on a separation of variables, it could be used to obtain solutions for mass transfer problems with nonlinear boundary conditions. Several closed form solutions were presented, notably those for Dirichlet, Neumann and Robin boundary conditions, and one example of a nonlinear boundary condition was provided.

One of the most remarkable findings was that all boundary conditions of the class $\partial c/\partial r(r = R) = \mathtt{f}(c_w)$ have a universal Sh correlation:

$$Sh = \frac{2\mathrm{k_f}R}{D} = \frac{9\sqrt[3]{b}}{\pi\sqrt{3}} Re_\tau Sc^{1/3}. \tag{10.1}$$

This offered a direct explanation for the close correspondence between the Notter & Sleicher (1971) correlation for Dirichlet boundary conditions and first-order wall demand (Robin boundary conditions) as studied in chapter 5: both are part of the class $\partial c/\partial r(r = R) = \mathtt{f}(c_w)$ and therefore have the same Sh correlation. The asymptotic solutions also provided an upper bound to mass flux due to wall demand, J_w, given by

$$J_w < \frac{Dc_\mathrm{x}}{1.21\delta_\mathrm{m}} \tag{10.2}$$

TABLE 10.1. Summary of the findings of the study.

Study	Approach of study	Findings and results
First-order wall and bulk demand in smooth pipes (studied in chapters 5 and 6)	1D mass transport model (by separation of variables)	(1) The *Sh* correlation for the Dirichlet boundary condition is applicable for first-order wall demand for $Sc > 100$. For the case of chlorine at 15^o C, $Sc \approx 10^3$ and therefore, the correlation is applicable for modelling first-order chlorine wall demands; (2) The bulk concentration profile is uniform as long as $Da < 1$. For chlorine bulk reactions in distribution networks, $Da \approx 10^{-5}$ and therefore, the concentration profile uniformity assumption holds; (3) For the case of high *Sc* compounds and pure wall demand, the concentration profile is not uniform in the viscous sublayer for $k_w/U > 10^{-6}$; (4) For the case of high *Sc* compounds and bulk demand, the concentration profile is not uniform in the bulk for $Da > 10^{-3}$.
Parameterisation of nonlinear wall demands (studied in chapter 7)	An analytical framework for approximate solutions	(1) *Sh* is universal; (2) Maximum attainable wall flux due to wall demand is set by the thickness of the MTBL; (3) The pipe entrance effect is negligible for solute mass since the solute mass entrance length $L_E = \delta_v/b$; (4) Solutions for the case of linear and second-order wall demands were presented.
Wall demand for rough surfaces (studied in chapters 8 and 9)	2D flow and mass transport model for d-type rough channels	(1) The LRN LS model is able to faithfully model the velocity field; (2) An adjustment in *Sc* is needed to modify the natural inaccuracy of the LS model in determination of ν_T close to the wall; (3) Molecular diffusion dominates over turbulence inside the cavity; (4) For small k_w/U, the extra surface area causes an increase in k_R compared to k (for smooth walls); (5) For high k_w/U, the diffusion transport through the cavity becomes the limiting factor, and causes a decrease in k_R compared to k (for smooth walls); (6) Based on this insight, a new parameterisation was developed which correctly reproduced the behaviour of k_R for low and high k_w/U.

which implies that the maximum wall flux is controlled by flow and molecular properties, not the reaction type and rate.

The solutions are only valid sufficiently far away from the pipe entrance, i.e. entrance effects are not taken into account. In order to obtain an estimate for the length L_E over which entrance effects are important, a dimensional analysis was carried out, which resulted in $L_E = \delta_v/b$. In the range of *Re* and *Sc* applicable to distribution networks, L_E is of the order of a few pipe diameters, and the solutions derived in chapter 7 are therefore suitable for these situations.

10.3. Wall demand for rough surfaces

The main uncertainty regarding parameterisation of wall demand pertains to rough surfaces. The two existing parameterisations are mutually inconsistent, predicting different asymptotic values of decay coefficient for low and high wall demand. These differences led to the fourth research question posed in section 2.6.

To address this question in chapters 8 and 9, a numerical study was conducted to obtain insight into the complex interaction between flow, turbulence and wall demands. The first advantage of using a numerical method for studying wall demand on rough surfaces was the availability of the full flow and concentration fields. This made it possible to extract the dominant mass transport mechanism and use it to construct a physics-based parameterisation, as opposed to fitting a power law through measurements as is the norm in the experiments. A second important advantage of using a numerical method was that it became possible to perform the first systematic study for the dependence of the rough wall decay coefficient k_R on the wall demand coefficient $\mathrm{k_w}$.

The study was conducted with fixed *Re* and *Sc*, and a d-type rough channel geometry was used. The LRN LS model was used for the turbulence closure. Although the model faithfully reproduced velocity profiles and turbulence levels, analysis of the near wall behaviour of ν_T showed that the prefactor b for the cubic dependence of ν_T on the wall distance was a factor 10 too small. As the mass transport depends sensitively on b, this problem needed to be solved. A simple solution was to simulate with a different *Sc*, which was justified because the cubic dependence was correctly reproduced.

For the case of low wall demand coefficients ($\mathrm{k_w}/U < 10^{-7}$), it was shown that the decay coefficient k_R for the d-type rough wall increased in comparison with a smooth wall. For these low wall demand coefficients, the concentration was uniform through the fluid, and the increase in wall demand could be attributed to the increase in surface contact area.

However, for high wall demand coefficients ($\mathrm{k_w}/U > 10^{-5}$), k became *lower* than for a smooth wall. At first sight, this seemed counterintuitive, given that the rough wall case had higher turbulence levels and surface contact area than the smooth wall case. The reason can be traced back to the turbulence levels

inside the cavities, which were very low. Indeed, the cavities were dominated by molecular diffusion and consequently, the fluid in the cavity acted like a thick MTBL. Analogous to the smooth wall case, the transport through this layer became the limiting factor for k_w/U sufficiently high. As this happened for much lower k_w/U because the layer was thicker, this effectively "switched off" the contribution of the cavities. The mass transfer became limited by the geometry.

A detailed analysis of the flow field suggested that the crest and the cavity could be modelled as two independent regions each with their own behaviour. The crest behaved like a regular smooth surface, and the cavity like a stagnant layer of fluid governed by molecular diffusion. Consequently, the analytical solution of chapter 5 was used for the behaviour of the crest, and the cavity was modelled using thin film theory.

Although the agreement between the analytical model and the numerical simulations was not entirely perfect, especially at intermediate k_w/U, it captured both small and large k_w/U adequately. In particular, the model was able to successfully reproduce the observed geometry limited mass transfer to the cavity. Both the parameterisations used in EPANET and the electrochemical approach were unable to reproduce this behaviour.

10.4. Implications for water quality modelling

From a practical perspective, the overriding conclusion is that the design decisions that were made for EPANET with respect to wall demand for smooth pipes are very good. The results from chapters 5 and 6 clearly show that both wall demand and bulk demand are appropriately modelled for the range of parameters occurring in water distribution networks. The main model uncertainties are with respect to the reaction kinetics, which are best unravelled with laboratory experiments and were outside of the scope of this thesis. However, the findings of this thesis, in particular those in chapter 7, may guide subsequent incorporation of improved reaction kinetics in water quality models.

It was shown in chapter 7 that nonlinear wall reactions behave identically to first-order wall reactions, and consequently, they can be incorporated into water quality models like EPANET without complications. Nonlinear wall reactions are of particular importance for various types of water quality deteriorating phenomena. For instance, chlorine decay kinetics have been suggested in some studies to better correspond to

a second-order wall demand than the commonly used first-order wall demand (Kiéné *et al.*, 1998; Rossman, 2006). Another example is the wall demand of solute compounds essential for the growth of biofilms, which is usually modelled by a Monod equation:

$$J_w = \frac{K_1 c_w}{K_2 + K_3 c_w} \tag{10.3}$$

where K_1 $[LT^{-1}]$, K_2 [-] and K_3 $[M^{-1}L^3]$ are the growth parameters (Tchobanoglous *et al.*, 2003).

Rough walls, however, are the norm in water distribution networks. The results of this thesis show that neither the EPANET parameterisation nor those stemming from electrochemical experiments are able to capture the effects of wall geometry on wall demand, even for a simple rough wall geometry as considered in chapters 8 and 9. As stated in chapters 2 and 9, EPANET captures the rough wall behaviour for small k_w/U by attributing the increase in surface area to a higher wall demand coefficient k_w, but fails to capture the high k_w/U asymptote. The rough wall parameterisations in electrochemical approaches adjust k_f and therefore, do capture the high k_w/U asymptote, but fail to reproduce the effects of higher surface area for low k_w/U.

The wall demand characteristics for a pipe with natural roughness will be much more complex. Roughness elements are neither square nor spaced equidistantly, having different sizes and shapes. Consequently, the effects of geometry limited wall demand will occur over the entire range of k_w/U, the deepest cavities becoming "inactive" first, and the shallower ones following for larger k_w/U. Therefore, the linear behaviour observed for the d-type rough walls at low k_w/U might not occur at all or have a different slope (as in figure 10.1). For natural rough surfaces, the EPANET parameter θ_{k_w} is therefore likely to be dependent on k_w/U, and not generic.

10.5. Further research

The work on rough walls in this thesis comprised an exploratory study of the effect of k_w/U on the rough wall decay coefficient k_R for one pipe geometry at fixed *Sc* and *Re*. Whilst the study provided valuable

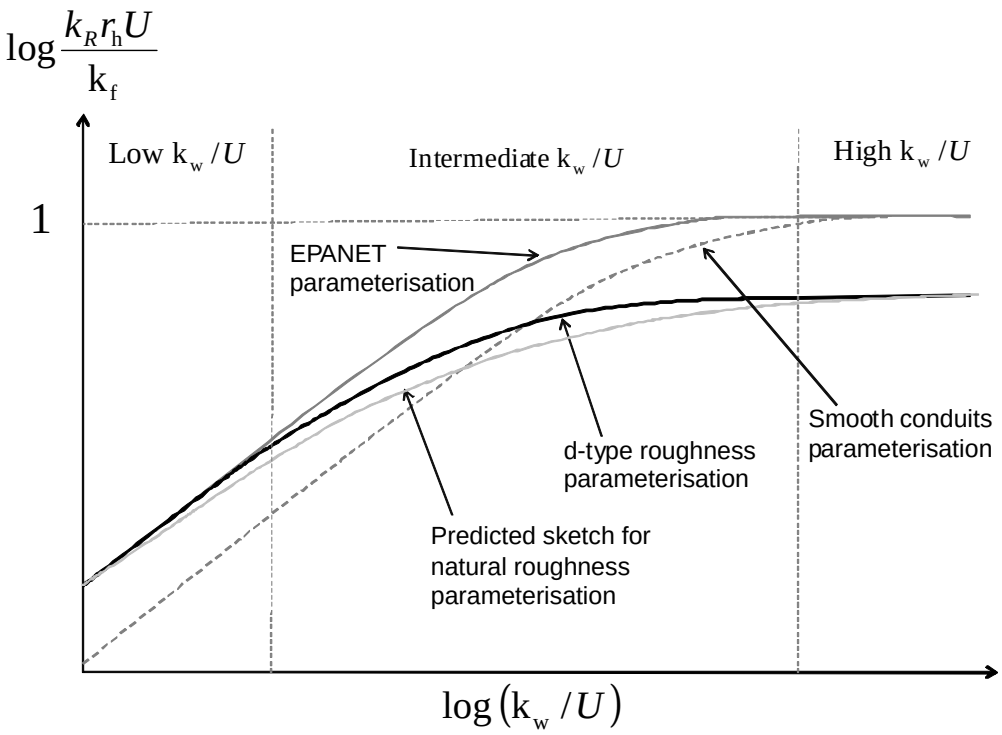

FIGURE 10.1. Schematic of k_R for the EPANET approach, d-type and natural roughness.

insights and led to the development of a simple parameterisation of wall demand for that particular geometry, much more work needs to be undertaken before the coveted robust parameterisations for wall demand for rough walls become reality.

The current results should be interpreted qualitatively rather than quantitatively, mainly because of uncertainties in the turbulent viscosity levels very close to the wall. These uncertainties are inherent when using RANS models, as any turbulence model is partly empirical. The most accurate simulation method available is DNS, which does not rely on turbulence modelling at all. However, the computations become exorbitantly expensive as *Re* increases, especially for high *Sc* mass transfer problems (see e.g. Schwertfirm & Manhart (2007)). Here, a hybrid approach might be most effective: to perform rough wall simulations with DNS, and to feed the time averaged flow field results (velocity and turbulent viscosity) to a RA mass transport equation.

With an accurate flow model in place, a detailed programme could be conducted in which roughness

was systematically studied:

(1) Analyse regular roughness patterns. Vary the spacing, the cavity height and width and determine the appropriate dimensionless parameterisation for d- and k-type rough walls;
(2) Study the influence of the element shape;
(3) Consider regular roughness patterns with increasing complexity;
(4) Analyse synthetically generated roughness patterns which approximate natural rough walls.

The programme above should be accompanied by laboratory experiments in order to verify the robustness of the parameterisations.

There are several other avenues for further research. The occurrence of dead zones in distribution networks, which are places where the flow is stagnant or laminar[1], will cause inaccuracies in water quality predictions.

Furthermore, the study performed in this thesis was restricted to consumption of a single solute compound. However, recent awareness of the serious health effect of DBPs has also urged parameterisation of solute mass formation. Similar to the case of chlorine decay, which is modelled by sink terms, source terms can also be considered for the case of solute mass formation. The methodologies presented in this thesis are equally valid for source terms, and an extension to multiple species is a natural progression[2].

[1] Existence of such zones is a result of poor hydraulic design or less water demand in the early years of the network's operational life, when the population is usually less than the design population (Skipworth, 2002).

[2] As stated in chapter 2, extensions to EPANET are in progress to add a multi species simulation ability to the model which can also consider formation of solute compounds (Shang *et al.*, 2008).

Bibliography

ABDERRAHMAN, W. A. 2000 Urban water management in developing arid countries. *International Journal of Water Resources Development* **16**, 7–20.

AGARD, L., ALEXANDER, C., GREEN, S., JACKSON, M., PATEL, S. & ADESIYUN, A. 2002 Microbial quality of water supply to an urban community in Trinidad. *Journal of Food Protection* **65**, 1297–1303.

AL-JASSER, A. O. 2007 Chlorine decay in drinking-water transmission and distribution systems: Pipe service age effect. *Water Research* **41**, 387–396.

ARAVINTH, S. 2000 Prediction of heat and mass transfer for fully developed turbulent fluid flow through tubes. *International Journal of Heat and Mass Transfer* **43**, 1399–1408.

ASHBOLT, N. J. 2004 Microbial contamination of drinking water and disease outcomes in developing regions. *Toxicology* **198**, 229–238.

ATKINSON, K. E. 1989 *An Introduction to Numerical Analysis (second edition)*. John Wiley & Sons, Inc.

AWWA 1996 *Characterization and Modeling of Chlorine Decay in Distribution Systems*. American Water Works Association Research Foundation.

AWWA & US EPA 1991 *Water Quality Modeling in Distribution Systems: Conference Proceedings*. The Foundation.

BABOVIC, V., DRÉCOURT, J. P., KEIJZER, M. & HANSEN, P. F. 2002 A data mining approach to modelling of water supply assets. *Urban Water* **4**, 401–414.

BAILEY, I. W. & THOMPSON, P. 1995 Monitoring water quality after disinfection. *Water Supply* **13**, 35–48.

BEDIENT, P. B., RIFAI, H. S. & NEWELL, C. J. 1999 *Ground Water Contamination: Transport and Remediation*. Prentice Hall PTR.

BERGER, F. P. & HAU, K. F. 1977 Mass transfer in turbulent pipe flow measured by the electrochemical method. *International Journal of Heat and Mass Transfer* **20**, 1185–1194.

BERGMANN, J. & FIEBIG, M. 1999 Comparison of experimental and numerical investigation on local and

global heat transfer in turbulent square channel flow with roughness elements in the form of V-shaped broken ribs. *Flow, Turbulence and Combustion* **62**, 163–181.

BIRD, R. B., STEWART, W. E. & LIGHTFOOT, E. N. 2002 *Transport Phenomena (second edition)*. John Wiley & Sons, Inc.

BISWAS, P., LU, C. & CLARK, R. M. 1993 A model for chlorine concentration decay in pipes. *Water Research* **27**, 1715–1724.

VAN BLOEMEN WAANDERS, B., HAMMOND, G., SHADID, J., COLLIS, S. & MURRAY, R. 2005 A comparison of Navier Stokes and network models to predict chemical transport in municipal water distribution systems. In *World Water and Environmental Resources Congress*. Anchorage, Alaska, USA.

BRIÈRE, F. G. 2007 *Drinking-Water Distribution, Sewage, and Rainfall Collection (second edition)*. Presses internationales Polytechnique.

CHOI, K. S. 2006 The rough with the smooth. *Nature* **440**, 754.

CLARK, R. M., GRAYMAN, W. M., MALES, R. M. & COYLE, J. A. 1986 Predicting water quality in distribution systems. In *AWWA Distribution System Symposium*. Minneapolis, MN, USA.

CLARK, R. M. & HAUGHT, R. C. 2005 Characterizing pipe wall demand: implications for water quality modeling. *Journal of Water Resources Planning and Management* **131**, 208–217.

COATES-STEPHENS, R. 1998 The walls and aqueducts of Rome in the early middle ages, A.D. 500-1000. *Journal of Roman Studies* **88**, 166–178.

COLEBROOK, C. F. 1939 Turbulent flow in pipes, with particular reference to the transition region between the smooth and rough pipe laws. *American Institute of Chemical Engineers Journal* **11**, 133–156.

COLEBROOK, C. F. & WHITE, C. M. 1937 Experiments with fluid friction in roughened pipes. *Proceedings of the Royal Society A* **161**, 367–381.

CORLESS, R. M., GONNET, G. H., HARE, D. E. G., JEFFREY, D. J. & KNUTH, D. E. 1996 On the Lambert W function. *Advances in Computational Mathematics* **5**, 329–359.

CRITTENDEN, J. C., TRUSSELL, R. R., HAND, D. W., HOWE, K. J. & TCHOBANOGLOUS, G. 2005 *Water Treatment Principles and Design (second edition)*. John Wiley & Sons, Inc.

CROSS, H. 1936 Analysis of Flow in Networks of Conduits or Conductors. *Technical report*. University of Illinois.

CUI, J., PATEL, V. C. & LIN, C. L. 2003 Large-eddy simulation of turbulent flow in a channel with rib

roughness. *International Journal of Heat and Fluid Flow* **24**, 372–388.

DAWSON, D. A. & TRASS, O. 1972 Mass transfer at rough surfaces. *International Journal of Heat and Mass Transfer* **15**, 1317–1336.

DEISSLER, R. G. 1950 Analytical and Experimental Investigation of Adiabatic Turbulent Flow in Smooth Tubes. *Technical report*. National Advisory Committee for Aeronautics.

DIBONA, P., HELMICK, J. & SMITH, J. E., editors 1992 *Control of Biofilm Growth in Drinking Water Distribution Systems*. Diane Publishing Co.

DICKINSON, H. W. 2010 *A Short History of the Steam Engine*. Cambridge University Press.

DJENIDI, L., ELAVARASAN, R. & ANTONIA, R. A. 1999 The turbulent boundary layer over transverse square cavities. *Journal of Fluid Mechanics* **395**, 271–294.

VAN DRIEST, E. R. 1956 On turbulent flow near a wall. *Journal of Aeronautical Sciences* **23**, 1007–1011.

EGOROV, A., FORD, T., TERESCHENKO, A., DRIZHD, N., SEGEDEVICH, I. & FOURMAN, V. 2002 Deterioration of drinking water quality in the distribution system and gastrointestinal morbidity in a Russian city. *International Journal of Environmental Health Research* **12**, 221–233.

EU 1998 Council Directive 98/83/EC of 3 November 1998 on the Quality of Water Intended for Human Consumption. *Technical report*. Council of European Union.

FLESCH, T. K., PRUEGER, J. H. & HATFIELD, J. L. 2002 Turbulent Schmidt number from a tracer experiment. *Agricultural and Forest Meteorology* **111**, 299–307.

FRATEUR, I., DESLOUIS, C., KIENE, L., LEVI, Y. & TRIBOLLET, B. 1999 Free chlorine consumption induced by cast iron corrosion in drinking water distribution systems. *Water Research* **33**, 1781–1790.

GARCIA-YBARRA, P. L. & PINELLI, A. 2006 Turbulent channel flow concentration profile and wall deposition of a large Schmidt number passive scalar. *Comptes Rendus Mécanique* **334**, 531–538.

GRAYMAN, W. M., CLARK, R. M. & MALES, R. M. 1988 Modeling distribution-system water quality dynamic approach. *Journal of Water Resources Planning and Management* **114**, 295–312.

GRIMANIS, M. & ABEDIAN, B. 1985 Turbulent mass transfer in rough tubes at high Schmidt numbers. *Physicochemical Hydrodynamics* **6**, 775–787.

HAALAND, S. E. 1983 Simple and explicit formulas for the friction factor in turbulent pipe flow. *Journal of Fluids Engineering* **105**, 89–90.

HALLAM, N. B., WEST, J. R., FORSTER, C. F., POWELL, J. C. & SPENCER, I. 2002 The decay of

chlorine associated with the pipe wall in water distribution systems. *Water Research* **36**, 3479–3488.

HANJALIĆ, K., KENJEREŠ, S., TUMMERS, M. J. & JONKER, H. J. J. 2009 *Analysis and Modelling of Physical Transport Phenomena*. VSSD, Netherlands.

HANNA, O. T., SANDALL, O. C. & MAZET, P. R. 1981 Heat and mass transfer in turbulent flow under conditions of drag reduction. *AIChE Journal* **27**, 693–697.

HARDY, A. 1984 Water and the search for public health in London in the eighteenth and nineteenth centuries. *Medical History* **28**, 250–282.

HARRIOTT, P. & HAMILTON, R. M. 1965 Solid-liquid mass transfer in turbulent pipe flow. *Chemical Engineering Science* **20**, 1073–1078.

HEALTH CANADA 2010 Guidelines for Canadian Drinking Water Quality-Summary Table. *Technical report*. Federal Provincial Territorial Committee on Drinking Water.

HICKEL, S. & ADAM, N. A. 2007 Implicit subgrid-scale modeling for large-eddy simulation of passive-scalar mixing. *Physics of Fluids* **19**, 095102.

HIRSCH, C. 2007 *Numerical Computation of Internal and External Flows*. Elsevier.

HO, C. K. 2008 Solute mixing models for water-distribution pipe networks. *Journal of Hydraulic Engineering* **134**, 1236–1244.

HOYAS, S. & JIMÉNEZ, J. 2006 Scaling of velocity fluctuations in turbulent channels up to $Re_\tau = 2003$. *Physics of Fluids* **18**, 011702.

HRUDEY, S. E., PAYMENT, P., HUCK, P. M., GILLHAM, R. W. & HRUDEY, E. J. 2003 A fatal waterborne disease epidemic in Walkerton, Ontario: comparison with other waterborne outbreaks in the developed world. *Water Science and Technology* **47**, 7–14.

HUGUENIN, J. E. & COLT, J. 2002 *Design and Operating Guide for Aquaculture Seawater Systems (second edition)*. Elsevier.

JIMÉNEZ, J. 2004 Turbulent flows over rough walls. *Annual Review of Fluid Mechanics* **36**, 173–196.

JONES, J. B. 2001 Mass transfer reactions and decay sinks for disinfectants in water distribution systems. PhD thesis, Old Dominion University, Norfolk, VA, USA.

KAYS, W. M., CRAWFORD, M. E. & WEIGAND, B. 2005 *Convective Heat and Mass Transfer*. McGraw-Hill Higher Education.

KIÉNÉ, L., LU, W. & LEVI, Y. 1993 Parameters governing the rate of chlorine decay throughout distribution system. In *Proceedings of the AWWA Annual Conference*, pp. 503–511. Denver, CO, USA.

KIÉNÉ, L., LU, W. & LEVI, Y. 1998 Relative importance of the phenomena responsible for chlorine decay in drinking water distribution systems. *Water Science and Technology* **38**, 219–227.

KOELTZSCH, K. 2000 The height dependence of the turbulent Schmidt number within the boundary layer. *Atmospheric Environment* **34**, 1147–1151.

KREYSZIG, E. 2006 *Advanced Engineering Mathematics (ninth edition)*. John Wiley & Sons, Inc.

LAUFER, J. 1954 The Structure of Turbulence in a Fully Developed Pipe. *Technical report*. National Advisory Committee for Aeronautics.

LECHEVALLIER, M. W., WELCH, N. J. & SMITH, D. B. 1996 Full-scale studies of factors related to coliform regrowth in drinking water. *Applied and Environmental Microbiology* **62**, 2201–2211.

LEE, E. J. & SCHWAB, K. J. 2005 Deficiencies in drinking water distribution systems in developing countries. *Journal of Water and Health* **3**, 109–127.

LEONARDI, S., ORLANDI, P. & ANTONIA, R. A. 2007 Properties of d- and k-type roughness in turbulent channel flow. *Physics of Fluids* **19**, 125101.

LEONARDI, S., ORLANDI, P., SMALLEY, R. J., DJENIDI, L. & ANTONIA, R. A. 2003 Direct numerical simulations of turbulent channel flow with transverse square bars on one wall. *Journal of Fluid Mechanics* **491**, 229–238.

LINTON, W. H. & SHERWOOD, T. K. 1950 Mass transfer from solid shapes to water in streamline and turbulent flow. *Chemical Engineering Progress* **46**, 258–264.

LIU, K. T. 1969 The numerical analysis of water supply networks by digital computers. In *Proceedings of thirteenth Congress of International Association for Hydraulic Research*, pp. 36–43.

LOLJA, S. A. 2005 Momentum and mass transfer on sandpaper-roughened surfaces in pipe flow. *International Journal of Heat and Mass Transfer* **48**, 2209–2218.

LU, W., KIÉNÉ, L. & LÉVI, Y. 1999 Chlorine demand of biofilms in water distribution systems. *Water Research* **33**, 827–835.

MATHIAS, S. A. & VAN REEUWIJK, M. 2009 Hydraulic fracture propagation with 3-D leak-off. *Transport in Porous Media* **80**, 499–518.

MAYS, L. W. 2008 A very brief history of hydraulic technology during antiquity. *Environmental Fluid*

Mechanics **8**, 471–484.

MERNA, T. & NJIRU, C. 2002 *Financing Infrastructure Projects*. Thomas Telford Limited.

MIZUSHINA, T., OGINO, F., OKA, Y. & FUKUDA, H. 1971 Turbulent heat and mass transfer between wall and fluid streams of large Prandtl and Schmidt numbers. *International Journal of Heat and Mass Transfer* **14**, 1705–1716.

MOODY, L. F. 1944 Friction factors for pipe flow. *Transactions of the ASME* **66**, 671–684.

MOTIEE, H., MCBEAN, E., SEMSAR, A., GHARABAGHI, B. & GHOMASHCHI, V. 2006 Assessment of the contributions of traditional qanats in sustainable water resources management. *International Journal of Water Resources Development* **22**, 575–588.

MULHOLLAND, C. 2002 *William Mulholland and the Rise of Los Angeles*. University of California Press.

MUTOTI, G., DIETZ, J. D., AREVALO, J. & TAYLOR, J. S. 2007 Combined chlorine dissipation: pipe material, water quality and hydraulic effects. *Journal of American Water Works Association* **99**, 96–106.

NA, Y., PAPAVASSILIOU, D. V. & HANRATTY, T. J. 1999 Use of direct numerical simulation to study the effect of Prandtl number on temperature fields . *International Journal of Heat and Fluid Flow* **20**, 187–195.

NAGANO, Y., HATTORI, H. & HOURA, T. 2004 DNS of velocity and thermal fields in turbulent channel flow with transverse-rib roughness. *International Journal of Heat and Fluid Flow* **25**, 393–403.

NEEDHAM, J. 1985 *Science and Civilization in China*. Cambridge University Press.

NIKURADSE, J. 1950 Laws of Flow in Rough Pipes (translation from VDI-Forschungsheft 361, 1933). *Technical report*. National Advisory Committee for Aeronautics, NACA TM 1292.

NOGUERA, D. R. & MORGENROTH, E. 2004 Introduction to the IWA task group on biofilm modeling. *Water Science and Technology* **49**, 131–136.

NOTTER, R. H. & SLEICHER, C. A. 1971 The eddy diffusivity in the turbulent boundary layer near a wall. *Chemical Engineering Science* **26**, 161–171.

O'BRIEN, S. J. & GOEDERT, J. J. 1996 HIV causes AIDS: Koch's postulates fulfilled. *Current Opinion in Immunology* **8**, 613–618.

OPENCFD 2008 *OpenFOAM User Guide*. OpenCFD Limited.

ORLANDI, P. & LEONARDI, S. 2006 DNS of turbulent channel flows with two- and three-dimensional roughness. *Journal of Turbulence* **7**, 1–22.

ORLANDI, P. & LEONARDI, S. 2008 Direct numerical simulation of three-dimensional turbulent rough channels: parameterization and flow physics. *Journal of Fluid Mechanics* **606**, 339–415.

PANGULURI, S., GRAYMAN, W. M. & CLARK, R. M. 2005 Water Distribution System Analysis: Field Studies, Modeling, and Management. *Technical report*. US EPA.

PAPAVASSILIOU, D. V. & HANRATTY, T. J. 1997 Transport of a passive scalar in a turbulent channel flow. *International Journal of Heat and Mass Transfer* **40**, 1303–1311.

PETERSEN, J. F., SACK, D. & GABLER, R. E. 2010 *Fundamentals of Physical Geography*. Thomson Brooks.

POPE, S. B. 2000 *Turbulent Flows*. Cambridge University Press.

PORTER, C. K., PUTNAM, S. D., HUNTING, K. L. & RIDDLE, M. R. 2005 The effect of trihalomethane and haloacetic acid exposure on fetal growth in a Maryland county. *American Journal of Epidemiology* **162**, 334–344.

PRANDTL, L. 1932 Zur turbulenten Strömung in Rohren und längs Platten. *Technical report*. Ergebnisse der Aerodynamischen Versuchsanstalt zu Gottingen.

PUJALS, G., DEPARDON, S. & COSSU, C. 2010 Drag reduction of a 3D bluff body using coherent streamwise streaks. *Experiments in Fluids* **49**, 1085–1094.

RATNAYAKA, D. D., BRANDT, M. J. & JOHNSON, K. M. 2009 *Twort's Water Supply (sixth edition)*. Elsevier.

VAN REEUWIJK, M. 2007 Direct Simulation and Regularization Modeling of Turbulent Thermal Convection. PhD thesis, Delft University of Technology.

RODI, W. & MANSOUR, N. N. 1993 Low Reynolds number k-ε modelling with the aid of direct simulation data. *Journal of Fluid Mechanics* **250**, 509–529.

ROMERO-GOMEZ, P., CHOI, C. Y., VAN BLOEMEN WAANDERS, B. & MCKENNA, S. A. 2006 Transport phenomena at intersections of pressurized pipe systems. In *Eighth Annual Water Distribution System Analysis Symposium*. Cincinnati, Ohio, USA.

ROSSMAN, L. A. 2000 *EPANET2 USER MANUAL*. US EPA.

ROSSMAN, L. A. 2006 The effect of advanced treatment on chlorine decay in metallic pipes. *Water Research* **40**, 2493–2502.

ROSSMAN, L. A., CLARK, R. M. & GRAYMAN, W. M. 1994 Modeling chlorine residuals in drinking-water distribution systems. *Journal of Environmental Engineering* **120**, 803–820.

SARIN, P., SNOEYINK, V. L., LYTLE, D. A. & KRIVEN, W. M. 2004 Iron corrosion scales; model for scale growth, iron release and colored water formation. *Journal of Environmental Engineering* **130**, 364–373.

SCHETZ, J. A. & FUHS, A. E. 1999 *Fundamentals of Fluid Mechanics*. John Wiley & Sons, Inc.

SCHMITTINGER, P. 2000 *Chlorine: Principles and Industrial Practice*. Wiley-VCH.

SCHUBAUER, G. & KLEBANOFF, P. 1955 Contributions on the Mechanics of Boundary Layer Transition. *Technical report*. National Advisory Committee for Aeronautics.

SCHWERTFIRM, F. & MANHART, M. 2007 DNS of passive scalar transport in turbulent channel flow at high Schmidt numbers. *International Journal of Heat and Fluid Flow* **28**, 1204–1214.

SCHWERTFIRM, F. & MANHART, M. 2010 *Direct and Large Eddy Simulation*, chap. 8, pp. 149–155. ERCOFTAC Series.

SEMENZA, J. C., ROBERTS, L., HENDERSON, A., BOGAN, J. & RUBIN, C. H. 1998 Water distribution system and diarrheal disease transmission: a case study in Uzbekistan. *American Journal of Tropical Medicine and Hygiene* **59**, 941–946.

SHANG, F., UBER, J. G. & ROSSMAN, L. A. 2008 Modeling reaction and transport of multiple species in water distribution systems. *Environmental Science and Technology* **42**, 808–814.

SKIPWORTH, P. 2002 *Whole Life Costing for Water Distribution Network Management*. Thomas Telford.

SLEICHER, C. A., NOTTER, R. H. & CRIPPEN, M. D. 1970 A solution to the turbulent Graetz problem by matched asymptotic expansions-I The case of uniform wall temperature. *Chemical Engineering Science* **25**, 845–857.

SMALLEY, R. J., ANTONIA, R. A. & DJENIDI, L. 2001 Self-preservation of rough-wall turbulent boundary layers. *European Journal of Mechanics. B-Fluids* **20**, 591–602.

SOOKHAK LARI, K., VAN REEUWIJK, M. & MAKSIMOVIĆ, C. 2010 Simplified numerical and analytical approach for solutes in turbulent flow reacting with smooth pipe walls. *Journal of Hydraulic Engineering* **136**, 626–632.

SUGA, K. 2007 Computation of high Prandtl number turbulent thermal fields by analytical wall-function. *International Journal of Heat and Mass Transfer* **50**, 4967–4974.

SWAMEE, P. K. & JAIN, A. K. 1976 Explicit equations for pipe-flow problems. *Journal of the Hydraulics*

Division **102**, 657–664.

SWAMEE, P. K. & SHARMA, A. K. 2008 *Design of Water Supply Pipe Networks*. John Wiley & Sons, Inc.

TCHOBANOGLOUS, G., BURTON, F. L. & STENSEL, H. D. 2003 *Wastewater Engineering; Treatment and Reuse (forth edition)*. McGraw-Hill.

TWORT, A. C., RATNAYAKA, D. D. & BRANDT, M. J. 2000 *Water Supply*. Butterworth-Heinemann.

UN ENVIRONMENT PROGRAMME 2008 Vital Water Graphics: An Overview of the State of the World's Fresh and Marine Waters (second edition). *Technical report*. UN Environment Programme, Nairobi, Kenya.

UN MILLENNIUM PROJECT 2005 Investing in Development: A Practical Plan to Achieve the Millennium Development Goals. *Technical report*. UN Development Programme.

UNICEF AND WHO 2009 Diarrhoea: Why Children Are Still Dying and What Can Be Done. *Technical report*. WHO Library Cataloging-in-Publication Data.

US EPA 2009 National Primary Drinking Water Regulations. *Technical report*. US EPA.

VOLOKH, K. Y. 2002 On foundation of the Hardy Cross method. *International Journal of Solids and Structures* **39**, 4197– 4200.

WALSKI, T. M., CHASE, D. E., SAVIC, D. A., GRAYMAN, W., BECKWITH, S. & KOELLE, E. 2003 *Advanced Water Distribution Moldeling and Management*. Bentley Institute Press.

WEIGAND, B. 2004 *Analytical Methods for Heat Transfer and Fluid Flow Problems*. Springer.

WHO 2008 Guidelines for Drinking-Water Quality: Third Edition Incorporating the First and Second Addenda. *Technical report*. WHO Library Cataloguing-in-Publication Data.

WHO 2010 World Health Statistics. *Technical report*. WHO Library Cataloguing-in-Publication Data.

WOOD, D. J. 1980 Slurry flow in pipe networks. *Journal of the Hydraulics Division* **106**, 57–70.

WOOD, D. J. & RAYES, A. G. 1981 Reliability of algorithms for pipe network analysis. *Journal of the Hydraulics Division* **107**, 1145–1161.

WU, X. & MOIN, P. 2008 A direct numerical simulation study on the mean velocity characteristics in turbulent pipe flow. *Journal of Fluid Mechanics* **608**, 81–112.

ZHANG, Z., STOUT, J. E., YU, V. L. & VIDIC, R. 2008 Effect of pipe corrosion scales on chlorine dioxide consumption in drinking water distribution systems. *Water Research* **42**, 129–136.

ZHAO, W. & TRASS, O. 1997 Electrochemical mass transfer measurements in rough surface pipe flow:

geometrically similar V-shaped grooves. *International Journal of Heat and Mass Transfer* **40**, 2785–2797.

APPENDIX A

First-order wall demand in turbulent smooth channel flows

In order to determine the effect of wall curvature on the rate of the concentration decay coefficient, a study on a smooth channel geometry (figure A.1) is performed here. The 1D model introduced in chapter 5 is applied for the RA mass transport governing equation in a smooth channel geometry (Bird *et al.*, 2002):

$$u\frac{\partial c}{\partial x} - \frac{\partial}{\partial y}\left[(D+D_T)\frac{\partial c}{\partial y}\right] = 0 \tag{A.1}$$

subjected to first-order wall reactions at the wall:

$$D\frac{\partial c}{\partial y} = \mathrm{k_w} c_w. \tag{A.2}$$

Application of the method introduced in chapter 5 results in

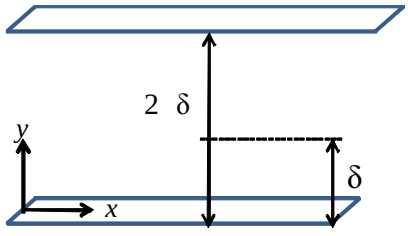

FIGURE A.1. Smooth channel geometry.

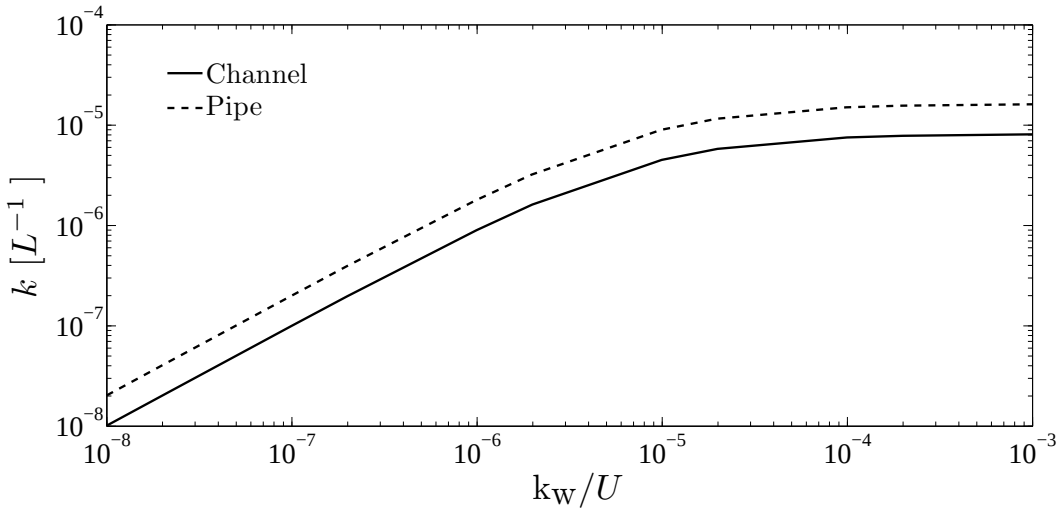

FIGURE A.2. Decay coefficient as a function of k_w for a smooth channel and pipe geometry at $Re = 10^6$.

$$kuc_y + \frac{d}{dy}\left[(D+D_T)\frac{dc_y}{dy}\right] = 0 \tag{A.3}$$

where k was introduced in equation 5.12 (replacing c_r with c_y). In addition, c_y is the crosswise scaling function. In this case, $c = c_x c_y$, where c_x was previously defined in chapter 3. The 1D numerical code was applied (with minor modifications to account for the differences in geometry. Details can be found in the code in appendix B) for $Re = 10^4$, 10^5 and 10^6, and $Sc = 1000$. The results for k were then compared with the counterpart results for pipe geometry presented in chapter 5. Figure A.2 shows the comparison for the case of $Re = 10^6$.

It is seen in this figure that although Re (and therefore, Re_τ) is identical for both geometries, the decay coefficient k for the pipe is two times larger than k for the smooth channel. The same phenomenon was also observed for $Re = 10^4$ and 10^5. This phenomenon is a direct consequence of the difference in the hydraulic perimeter. It was discussed in chapter 5 that in the case of pure wall demand (where $k_b = 0$), a physical representation of the decay coefficient is

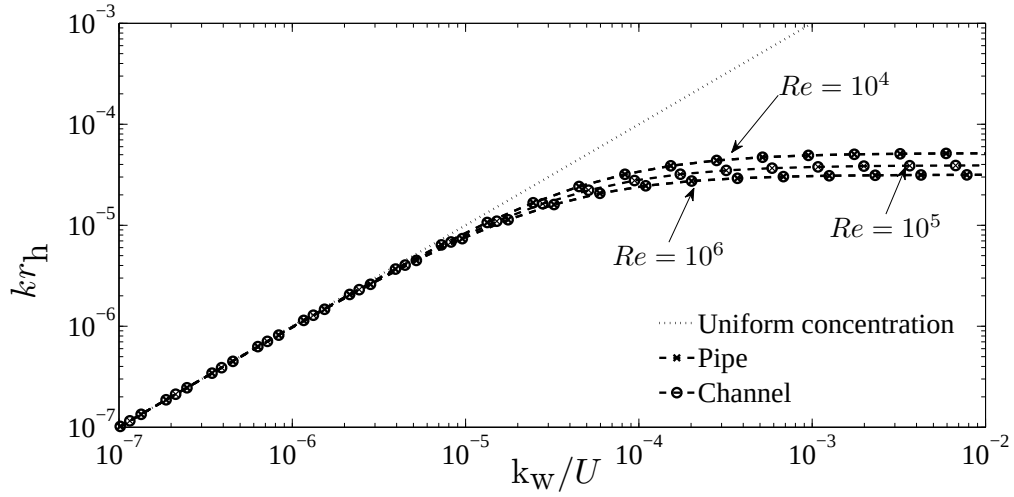

FIGURE A.3. Geometry independent representation for the decay coefficient.

$$k = \frac{\mathrm{k_w}}{r_\mathrm{h}} \frac{c_w}{\langle uc \rangle}. \tag{A.4}$$

The reason for the difference between the decay coefficients of the two geometries is now clear. Since the hydraulic radius r_h of a pipe is two times smaller than a smooth channel, the decay coefficient will be two times larger under the same conditions. This is in agreement with the results presented in figure A.2.

Equation A.4 indicates how the two separate curves in figure A.2 can be made to collapse, namely by plotting kr_h against $\mathrm{k_w}/U$. The result is shown in figure A.3 for both geometries and all the three *Re* values. As can be seen, the two curves collapse entirely, and geometry independence is confirmed. Hence, for wall demand problems at high *Re* and *Sc*, results are geometry independent, as long as one takes into account the hydraulic radius.

APPENDIX B

Numerical codes

The numerical codes written for flow and mass transport modelling are presented in this appendix. The codes are written in MATLAB and presented in an order based on their first application in each of the chapters. In section B.1, the flow modelling codes including the modified van Driest mixing length model and the HRN $k-\varepsilon$ model are presented. In section B.2, the 1D model mass transport code for first-order wall and bulk reactions (used in chapters 5 and 6) is presented. In section B.3, the 2D mass transport code is presented. This code is used in chapter 5 (with first-order wall reactions) and 7 (for second-order wall reactions). The last code presented in this appendix is the subroutine for calculation of the unknown matrix coefficients for the mass transport problem in chapter 9.

B.1. Code introduced in chapter 4

Two codes are presented here. The codes include the modified van Driest mixing length model and the HRN $k-\varepsilon$ model for the 1D flow fields.

B.1.1. Modified van Driest mixing length model.

The velocity and turbulent viscosity profiles are determined by the modified van Driest mixing length model. For the implicit function of u^+ using mixing length models, the cumulative trapezoid integration (line 10) is used. Here is the code:

```
1  %************************************************************************
2  %*      Modified van Driest mixing length model (Bird [2001], p. 164)
3  %************************************************************************
4  close all; clear all; clc;
5  Retau = 1142; nu = 1e-6; kappa = 0.41; Aplus = 26; Bplus = 4; b=9.5e-4; N=200;
6  y = linspace(1e-5, 1 , 2000);
7  yplus = y*Retau; dyplus = yplus(2) - yplus(1);
8  lmplus =  kappa * yplus .* ...
9      (1- exp(-yplus./Aplus))./sqrt((1- exp(-yplus/Bplus)));
```

```
10  uplus = cumtrapz( 2 * dyplus./ (1+ sqrt(1+ 4 * lmplus.^2)));
11
12  nuT=zeros(size(uplus));
13  nuT(2:end-1) = 2* nu * lmplus(2:end-1).^2 ./ ...
14      (1+ sqrt(1+4*lmplus(2:end-1).^2 )) ;
15  nuT(end)=nuT(end-1);
```

B.1.2. HRN $k-\varepsilon$ model.

The code for the HRN $k-\varepsilon$ model introduced in chapter 4 is presented here. The code comprises the following main sections:

(1) Introducing input parameters and constants (lines 7-21);

(2) Mesh generation (line 31 and internal function *initgrid* in line 146);

(3) Iterative solution including initiating variables (lines 39-41), assembly of the coefficients matrix (line 51-66 and internal function *calc matrices* in line 167), setting boundary conditions (lines 68-80), solving the system of equations (lines 83-85) and checking the convergence (lines 96-123).

Here is the code:

```
1   function [yc, yb, u1, e1, eps1, nuT, ...
2             ueqn, eeqn, epseqn, epseqnmod, resplot ] = channel_kepsilonHRN(...
3             delta, Retau, nu, N, a)
4
5   % ------------------------------------------------------------------------ %
6   % k-epsilon parameters
7   K            = 0.41; % Von Karman constant [-]
8   B            = 5.2;  % intercept log-law [-]
9   Cmu          = 0.09; % coefficient for turbulent viscosity [-]
10  Ce1          = 1.44; % coefficient for P_eps [-]
11  Ce2          = 1.92; % coefficient for eps_eps [-]
12  se           = 1.0;  % Prandtl number for e [-]
13  seps         = 1.3;  % Prandtl number for epsilon [-]
14
15  % iteration parameters
16  urf_u        = 1e-1; % under-relaxation factor for u [-]
17  urf_e        = 1e-1; % under-relaxation factor for e [-]
18  urf_eps      = 1e-2; % under-relaxation factor for epsilon [-]
19  rres_u_max   = 1e-10; % relative residual criterium for u [-]
20  rres_e_max   = 1e-10; % relative residual criterium for e [-]
21  rres_eps_max = 1e-10; % relative residual criterium for epsilon [-]
22  % ------------------------------------------------------------------------ %
23
24  % calculate friction velocity and forcing term
25  utau = Retau * nu / delta;  % friction velocity [m/s]
26
```

```
f    = 2*utau^2/delta;        % forcing parameter [m/s2]

% initialize grid
[ jm, j0, j1, jp, ...
  yb, yc, dyb, dyc, ycwall] = initgrid(N, a, delta, utau, nu);

% calculate desired velocity at first internal point
unom0 = utau * (log(ycwall(j0) * utau / nu) / K + B);
unom1 = utau * (log(ycwall(j1) * utau / nu) / K + B);

% iterate until a solution is obtained
u0   = ones(size(yc));
e0   = ones(size(yc));
eps0 = ones(size(yc));


it = 1;itres=0;
isconverged = false;
while ~isconverged
  % calculate eddy viscosity
  nuT = Cmu * e0.^2 ./ eps0;

  % assemble matrix, apply boundary conditions and solve the u eqn
  [Au, Ae, Aeps, Bu, Be, Beps, ...
                 Cu, Ce, Ceps]  = calc_matrices(nuT, u0, e0, eps0);

  % set rhs of u, e, and epsilon equations ...
  ru   = -f * ones(size(u0));
  re   = zeros(size(e0));
  reps = zeros(size(eps0));

  % set Robin BC's for u (see Pope, p. 443)
  Au(jm, jm) = -0.5 * (nuT(jm) + nuT(j0)) / dyb(j0);
  Au(jm, j0) =  0.5 * (nuT(jm) + nuT(j0)) / dyb(j0) - utau^2 / unom0;
  ru(jm) = 0;

  Au(jp, j1) = -0.5 * (nuT(j1) + nuT(jp)) / dyb(jp) + utau^2 / unom1;
  Au(jp, jp) =  0.5 * (nuT(j1) + nuT(jp)) / dyb(jp);
  ru(jp) = 0;

  % set Dirichlet BC for e on first internal cell
  Be(jm, j0) = 1;
  re(jm) = utau^2 / sqrt(Cmu);

  Be(jp, j1) = 1;
  re(jp) = utau^2 / sqrt(Cmu);

  % set Dirichlet BC for epsilon on first internal cell
  Ceps(jm, j0) = 1;
  reps(jm) = utau^3 / (K*ycwall(j0));

  Ceps(jp, j1) = 1;
  reps(jp) = utau^3 / (K*ycwall(j1));

  % assemble matrix and solve system
  A = [Au, Ae, Aeps; Bu, Be, Beps; Cu, Ce, Ceps];
```

```
  r = [ru; re; reps];
  x = A \ r;

  us   = x(1+0*(N+2):1*(N+2));
  es   = x(1+1*(N+2):2*(N+2));
  epss = x(1+2*(N+2):3*(N+2));

  u1   = u0   + urf_u   * (us - u0);
  e1   = e0   + urf_e   * (es - e0);
  eps1 = eps0 + urf_eps * (epss - eps0);

  % calculate the residuals to check on convergence
  res_u   = max(abs(u1 - u0));     rres_u = res_u / max(u1);
  res_e   = max(abs(e1 - e0));     rres_e = res_e / max(e1);
  res_eps = max(abs(eps1 - eps0)); rres_eps = res_eps / max(eps1);

  isconverged = (rres_u   <= rres_u_max) && ...
                (rres_e   <= rres_e_max) && ...
                (rres_eps <= rres_eps_max);

  if (mod(it, 50) == 0) || isconverged
    disp('=========================================');
    disp(['iteration ', num2str(it)]);
    disp(['residual u:   ',   num2str(res_u,    '%10.2d'), ...
          '; relative: ', num2str(rres_u,   '%10.2d')]);
    disp(['residual e:   ',   num2str(res_e,    '%10.2d'), ...
          '; relative: ', num2str(rres_e,   '%10.2d')]);
    disp(['residual eps: ', num2str(res_eps,  '%10.2d'), ...
          '; relative: ',   num2str(rres_eps, '%10.2d')]);

    subplot(3, 1, 1); plot(yc, u1, '.-k')
    subplot(3, 1, 2); plot(yc, e1, '.-k')
    subplot(3, 1, 3); plot(yc, eps1, '.-k')
    drawnow    itres=itres+1;
    resplot(1, itres)=it;  resplot(5, itres)=rres_e;
    resplot(2, itres)=res_u;  resplot(6, itres)=res_eps;
    resplot(3, itres)=rres_u; resplot(7, itres)=rres_eps;
    resplot(4, itres)=res_e;
    % verifyODEs(u0, us, e0, es, eps0, epss);
  end

  % prepare for the next timestep
  it = it + 1;
  u0 = u1; e0 = e1; eps0 = eps1;
end

disp('=========================================');
disp(['>> solution converged in ', num2str(it - 1), ' iterations <<']);
disp('=========================================');

verifyODEs(u0, u1, e0, e1, eps0, eps1);

[ueqn, eeqn, epseqn, epseqnmod] = diagnostics(u1, e1, eps1, nuT);

yb = yb(j0:jp);     yc = yc(j0:j1);
u1 = u1(j0:j1);     e1 = e1(j0:j1);
```

```
eps1 = eps1(j0:j1); nuT = nuT(j0:j1);

% ------------------------------------------------------------------------ %
% Internal functions
% ------------------------------------------------------------------------ %

function [jm, j0, j1, jp, ...
          yb, yc, dyb, dyc, ycwall] = initgrid(N, a, delta, utau, nu)
  jm    = 1;         % virtual point on bottom
  j0    = jm+1;      % first interior point at bottom
  j1    = j0+N-jm;   % last interior point at top
  jp    = j1+1;      % virtual point at top

  sc = linspace(-1, 1, N)';
  yw = 50 * nu / utau; % first internal point at y+=50
  yc = (delta - yw) * tanh(a * sc) / tanh(a);
  yc = [-2 * delta - yc(1); yc; 2 * delta - yc(end)];
  yb = 0.5 * (yc(1:end-1)+yc(2:end));
  yb = [-2 * delta - yb(2); yb];
  dyc = [diff(yb); NaN];
  dyb = [NaN; diff(yc)];

  ycwall = delta - abs(yc);
end

% ------------------------------------------------------------------------ %

function [Au, Ae, Aeps, ...
          Bu, Be, Beps, ...
          Cu, Ce, Ceps ]  = calc_matrices(nuT, u0, e0, eps0)

  % Set up matrix system as
  %  [ Au   Ae   Aeps ] [  u  ]     [  ru  ]
  %  [                ] [     ]     [      ]
  %  [ Bu   Be   Beps ] [  e  ]     [  re  ]
  %  [                ] [     ]  =  [      ]
  %  [ Cu   Ce   Ceps ] [ eps ]     [ reps ]

  nuTb = zeros(size(u0));
  rc=yc;
  %rc=ones(size(yc)) For plain channel
  nuTb(j0:jp) = 0.5 * (nuT(jm:j1) + nuT(j0:jp));
  rb(j0:jp) = 0.5 * (rc(jm:j1) + rc(j0:jp));
  % matrix for turbulent diffusion operator
  T = sparse([], [], [], N+2, N+2, 3*(N+2));
  for j = j0:j1
    T(j, j+1) =   rb(j+1)*nuTb(j+1) / dyb(j+1) / (dyc(j)*rc(j));
    T(j, j)   = - rb(j+1)*nuTb(j+1) / dyb(j+1) / (dyc(j)*rc(j)) ...
                - rb(j)*nuTb(j) / dyb(j) / (dyc(j)*rc(j));
    T(j, j-1) =   rb(j)*nuTb(j) / dyb(j) / (dyc(j)*rc(j));
  end

  % create matrix for production of TKE
  tflx = zeros(size(u0));
  for j = j0:j1+1
    dudy      = (u0(j) - u0(j-1)) / dyb(j);
```

```
    tflx(j)   = - 0.5 * (nuT(j-1) + nuT(j)) * dudy;
  end

  P = sparse([], [], [], N+2, N+2, 3*(N+2));
  for j = j0:j1
    P(j, j-1) =  0.5 * tflx(j) / dyb(j);
    P(j, j)   =  0.5 * (tflx(j+1) / dyb(j+1) - tflx(j) / dyb(j));
    P(j, j+1) = -0.5 * tflx(j+1) / dyb(j+1);
  end

  % zeros matrix
  Z = sparse([], [], [], N+2, N+2); % all zeros

  % Construct matrices for u-equation
  Au   = T;
  Ae   = Z;
  Aeps = Z;

  % Construct matrices for e-equation
  Bu   = P;
  Be   = T/se;
  Beps = - spdiags([0; ones(N,1); 0], 0, N+2, N+2);

  % Construct matrices for epsilon-equation
  Om = spdiags([0; eps0(j0:j1) ./ e0(j0:j1); 0], 0, N+2, N+2);

  Cu = Ce1 * Om * P;
  Ce = Z;
  Ceps = T / seps - Ce2 * Om;
end

% ------------------------------------------------------------------------- %

function [ueqn, eeqn, epseqn, epseqnmod] = diagnostics(u, e, eps, nuT)
  % u-equation
  ueqn.r_turb  = Au(j0:j1, :) * u;
  ueqn.r_force = f * ones(N,1);
  ueqn.r_disp= Aeps(j0:j1, :)*eps;
  % e-equation
  eeqn.r_turb = Be(j0:j1, :) * e;
  eeqn.r_disp = Beps(j0:j1, :) * eps;
  eeqn.r_prod = Bu(j0:j1, :) * u;

  % epsilon-equation
  Om = spdiags([0; eps(j0:j1) ./ e(j0:j1); 0], 0, N+2, N+2);
  CepsT = Au / seps;
  CepsE = - Ce2 * Om;

  epseqnmod.r_prod =Cu(j0:j1, :) * u;
  epseqnmod.r_turb=Ce(j0:j1, :) * e;
  epseqnmod.r_disp=Ceps(j0:j1, :) * eps;


  epseqn.r_turb = CepsT(j0:j1, :) * eps;
  epseqn.r_disp = CepsE(j0:j1, :) * eps;
  epseqn.r_prod = Cu(j0:j1, :) * u;
```

```
251
252   % calculate the fluxes on the interfaces
253   ueqn.tflx   = zeros(N+1,1);
254   eeqn.tflx   = zeros(N+1,1);
255   epseqn.tflx = zeros(N+1,1);
256   for j = j0:j1+1
257     dudy   = (u(j) - u(j-1)) / dyb(j);
258     dedy   = (e(j) - e(j-1)) / dyb(j);
259     depsdy = (eps(j) - eps(j-1)) / dyb(j);
260     ueqn.tflx(j-j0+1)   = - 0.5 * (nuT(j-1) + nuT(j)) * dudy;
261     eeqn.tflx(j-j0+1)   = - 0.5 * (nuT(j-1) + nuT(j)) * dedy;
262     epseqn.tflx(j-j0+1) = - 0.5 * (nuT(j-1) + nuT(j)) * depsdy;
263   end
264 end
265
266 % ------------------------------------------------------------------------ %
267
268 function verifyODEs(u0, u1, e0, e1, eps0, eps1)
269   utau = sqrt(sqrt(Cmu) * e0(j0));
270   nuT = Cmu * e0.^2 ./ eps0;
271   nuTb = zeros(size(u0));
272   nuTb(j0:jp) = 0.5 * (nuT(jm:j1) + nuT(j0:jp));
273
274   % check u-equation
275   ruT = zeros(size(u0));
276   ruF = zeros(size(u0));
277   for j = j0:j1
278     ruT(j) = ( nuTb(j+1) * (u1(j+1)-u1(j)) / dyb(j+1) ...
279              - nuTb(j)   * (u1(j)-u1(j-1)) / dyb(j) ...
280              ) / dyc(j);
281     ruF(j)  = f;
282   end
283
284   ru = ruT + ruF;
285   ru(jm) = nuTb(j0) * (u1(j0)-u1(jm)) / dyb(j0) - utau^2 * u1(j0) / unom0;
286   ru(jp) = nuTb(jp) * (u1(jp)-u1(j1)) / dyb(jp) + utau^2 * u1(j1) / unom1;
287
288   % check e-equation
289   Pb = zeros(size(u0));
290   for j = j0:j1+1
291     dudy0 = (u0(j) - u0(j-1)) / dyb(j);
292     dudy1 = (u1(j) - u1(j-1)) / dyb(j);
293     tflx  = - nuTb(j) * dudy0;
294     Pb(j) = - tflx * dudy1;
295   end
296
297   reT = zeros(size(u0));
298   reP = zeros(size(u0));
299   reE = zeros(size(u0));
300   for j = j0:j1
301     reT(j) = ( nuTb(j+1) * (e1(j+1)-e1(j)) / dyb(j+1) ...
302              - nuTb(j)   * (e1(j)-e1(j-1)) / dyb(j) ...
303              ) / dyc(j) / se;
304     reP(j) = 0.5 * (Pb(j) + Pb(j+1));
305     reE(j) = -eps1(j);
306   end
```

```
307
308   re = reT + reP + reE;
309   re(jm) = utau^2 / sqrt(Cmu) - e1(j0);
310   re(jp) = utau^2 / sqrt(Cmu) - e1(j1);
311
312   % check epsilon-equation
313   repsT = zeros(size(u0));
314   repsP = zeros(size(u0));
315   repsE = zeros(size(u0));
316   for j = j0:j1
317     repsT(j) = ( nuTb(j+1) * (eps1(j+1)-eps1(j)) / dyb(j+1) ...
318                - nuTb(j)   * (eps1(j)-eps1(j-1)) / dyb(j) ...
319                ) / dyc(j) / seps;
320     repsP(j) = 0.5 * (Pb(j) + Pb(j+1)) * Ce1 * eps0(j)/e0(j);
321     repsE(j) = - Ce2 * eps1(j)*eps0(j)/e0(j);
322   end
323
324   reps     = repsT + repsP + repsE;
325   reps(jm) = utau^3 / (K*ycwall(j0)) - eps1(j0);
326   reps(jp) = utau^3 / (K*ycwall(j1)) - eps1(j1);
327
328   disp('***** VERIFYING IMPLEMENTATION OF ODES *****')
329   disp(['residual   u-eqn: ', num2str(max(abs(ru)), '%12.4e')])
330   disp(['residual   e-eqn: ', num2str(max(abs(re)), '%12.4e')])
331   disp(['residual eps-eqn: ', num2str(max(abs(reps)), '%12.4e')])
332   disp('*******************************************')
333 end
334
335 end
```

B.2. Code introduced in chapters 5 and 6

The 1D mass transport code for the determination of k and c_r is presented here. The code comprises the following main sections:

(1) Mesh generation (line 15) and internal function *scndgrid* (line 61);

(2) Determination of velocity and turbulent viscosity profiles by the modified van Driest mixing length model (lines 18-25);

(3) Iterative solution for the determination of k and c_r including initial guess for k (line 36), calculating the coefficients matrix (line 41 and the internal function *calc A* in line 74), solving the system of equations (line 44) and checking the convergence of the results (lines 40 and 48).

Here is the code:

```
function []=Algebraic()
%_____________________________________________________________________
%    1D mass transport model used for linear wall and bulk reactions
%_____________________________________________________________________

close all;clear all;
Ny=1000;                        %Number of gridpoints in X direction
  jm    = 1;                    %Virtual point on bottom
  j0    = jm+1;                 %First interior point at bottom
  j1    = j0+Ny-jm;             %Last interior point at bottom
  jp    = j1+1;                 %Virtual point at bottom
  delta=1;
  ut=0.037;nu=1e-6;
  Sc=1000;
[yb, yc, dyb, dyc]=scndgrid(delta, Ny, ut, nu);
%_____________________________________________________________________

ycplus = (delta - abs(yc)) * ut / nu;
lmplus=0.41*ycplus.*(1-exp(-ycplus/(26))./sqrt(1-exp(-0.26*ycplus));
u = ut * cumtrapz(ycplus, 2./(1+(1+(4*lmplus.^2)).^0.5));
Dt = lmplus .^2 .* ...
[0; (u(3:end) - u(1:end-2)) ./ (ycplus(3:end) - ycplus(1:end-2)); ...
0] * nu / ut;
Dt(end) = Dt(end-1);
Uav=trapz(yc, u);
%_____________________________________________________________________

for q=1:10
kb=  logspace(-10,-1,10); kbb=kb(q);
kw=logspace(-10,-4,7);

for p=1:7
D=1e-6/Sc;
kww=kw(p);
isconverged = false;
k=kww \ Uav;                     %Decay rate L^-1
abstol = 1e-8;
reltol = 1e-8;

while ~ isconverged
A=calc_A(jp, D, k, u, Dt, j0, dyb, dyc,  kbb, kww);
r=zeros(jp,1);
r(jp)=1;
cr=inv(A)*r;
cw = 0.5 * (cr(1) + cr(2));
ucav = sum(u(2:jp-1) .* cr(2:end-1) .* dyc(2:jp-1)) / delta;
k1 = ( kbb+(kww * cw / delta ) )/ ucav ;
isconverged = abs(abs(k) - abs(k1)) < abstol && ...
(abs(k)-abs(k1))/k < reltol;
abs(k - k1);
k = k1;

end
      disp(['====================']);
```

```
      disp(['kw =   ',num2str(kww)]);
      disp(['kb =   ',num2str(kbb)]);
end

end
%_____________________________________________________________________
function [ yb, yc, dyb, dyc]=scndgrid(delta, Ny, ut, nu)

    ybplus = (logspace(-3, 0, Ny+1)-1e-3)*ut./nu;% / (Retau-1e-1);
    ybplus = [-ybplus(2), ybplus]';
    ycplus = 0.5 * (ybplus(1:end-1) + ybplus(2:end));
    ycplus = [ycplus; 2*ybplus(end)-ycplus(end)];
    yb = ybplus*nu./ut-delta;
    yc = ycplus*nu./ut-delta;
    dyb=[NaN; yc(2:end)-yc(1:end-1)];
    dyc=[yb(2:end)-yb(1:end-1); NaN];

 end
%_____________________________________________________________________
 function  [A]=calc_A(jp, D, k, u, Dt, j0, dyb, dyc, kbb, kww);

  Ad = (sparse(jp,jp));
  for j = j0:jp-1
    Ad(j, j+1) =   double(D / dyb(j+1) / dyc(j));
    Ad(j, j)   =   double(- D / dyb(j+1) / dyc(j) - D / dyb(j) / dyc(j));
    Ad(j, j-1) =  double( D / dyb(j) / dyc(j));
  end

  At = (sparse(jp,jp));
  for j = j0:jp-1
    At(j, j+1) =  double( 0.5 * (Dt(j)+Dt(j+1)) / dyb(j+1) / dyc(j));
    At(j, j)   = u(j)*(k)- kbb +double( - 0.5 * (Dt(j)+Dt(j+1)) / dyb(j+1) / dyc(j) ...
             - 0.5 * (Dt(j-1)+Dt(j)) / dyb(j) / dyc(j));
    At(j, j-1) =  double( 0.5 * (Dt(j-1)+Dt(j)) / dyb(j) / dyc(j));
  end

A=Ad+At;
A(1,1)=-D/dyb(2)-0.5*kww;
A(1,2)=D/dyb(2)-0.5*kww;
A((jp) , 2:jp-1)=dyc(2:jp-1);

 end

end
```

B.3. Code introduced in chapter 7

The code presented here is used in chapter 7 and comprises two parts. The first part includes the 2D mass transport code for second-order wall demands. The code also includes the analytical model for determination

of the far field solutions for such reactions. The first part of the code was also applied in chapter 5 as the 2D mass transport model. However, the first-order wall demands were considered in that chapter.

The first part of the code comprises the following main sections

(1) Global function in lines 1-36;
(2) Grid generation (lines 61 and 75) and associated internal functions (*creategrid x* in line 128 and *creategrid r* in line 142);
(3) Determination of velocity and turbulent viscosity profiles by the modified van Driest mixing length model (line 66 and internal function *hydrodynamics* in line 166);
(4) Initiating the variables and defining the entrance boundary conditions (lines 82-93, except line 90);
(5) Iterative solution including determination of the coefficients matrix (line 90 and internal function *creatematrix* in line 186), check the convergence (lines 96 and 106) and calculation of Sh_x (lines 117-119).

The far field solution for second-order wall reactions is also presented in lines 211-241.

Here is the code:

```
1  function approximate_secondorder
2  clc
3  close all;
4
5  Retau  = 2350;
6  Sc     = 1000;
7  Nx     = 600;
8  Nr     = 300;
9  xend   = 1e3;
10
11 % do the 2D calculations ...
12 alphas = [0.1, 1, 10];
13  for i = 1:length(alphas)
14    alpha = alphas(i);
15    disp(['----- alpha=', num2str(alpha)]);
16    [x r c Sh{i}] =TwoD_2nd(Retau, Sc, alpha, Nx, Nr, xend);
17    cb{i} = c(:,1);
18    cw{i} = 0.5 * (c(:,end-1)+c(:,end));
19  end
20  save(['TwoD_Sc', num2str(Sc), '_Retau', num2str(Retau)])
21
22 load(['TwoD_Sc', num2str(Sc), '_Retau', num2str(Retau)])
23
24 % this routine establishes that the Van Driest diffusivity profile generate
```

```
% 2.4 percent higher mass fluxes than the analytical mass flux of
% 9/(2 pi sqrt(3))

L = x(end) / xend;
for i = 1:length(alphas)
  alpha = alphas(i);
  cb_an{i} = ansol_nearfield(x/L, alpha);
end
cb_anf = ansol_farfield(x/L, alpha);
b = 9.5e-4; % note: can be inferred from b=kappa^2 Bplus / (ScT Aplus^2)

Sh_an = 9 * b^(1/3) / (pi * sqrt(3)) * Retau * Sc^(1/3);

% ------------------------------------------------------------------------ %
%                         2D   model                                       %
% ------------------------------------------------------------------------ %

function [x rc c Sh dcdyw] = TwoD_2nd(Retau, Sc, alpha, Nx, Nr, xend)

% convert to a dimensional form
R=1;
nu=1e-6;
ut=Retau * nu / R;
D=nu/Sc;
c0 = 1;
ScT=1.0;

b      = 9.5e-4;   % nuT = b yplus^3
deltas = (b*Sc)^(-1/3) * nu/ut;

%changing the non-d alpha to the dimensional form
alpha=-alpha/(c0*deltas);

reltol = 1e-10;

% create and unpack grid variables
grid = creategrid_r(Nr, R, ut, nu);
vnam = fieldnames(grid);
for i=1:length(vnam); eval([vnam{i},'=grid.',vnam{i}, ';']); end

% calculate hydrodynamics
[u nuT] = hydrodynamics(ycplus, ut, nu);
DT = nuT / ScT;
U = trapz(rc, rc .* u) ./ trapz(rc, rc); % average velocity

% calculate the physical lengthscale L
rh = R/2;
L  = rh * U * deltas / D;

% now L is known, the x-grid can be initialised
grid = creategrid_x(grid, Nx, xend, L);
vnam = fieldnames(grid);
for i=1:length(vnam); eval([vnam{i},'=grid.',vnam{i}, ';']); end

% ---- end initialisation

```

```
% set west boundary condition for forward marching
c = zeros(Nx, Nr+2);
c(1,:) = c0;

r   = zeros(Nr+2, 1);
Sh = zeros(size(x));
for i=2:Nx
  dx=x(i)-x(i-1);

  A = creatematrix(grid, u, D,  DT, dx);
  r(j0:j1) = u(j0:j1) .* c(i-1, j0:j1)' / dx;

  cw = 0.5 * (c(i-1, j1) + c(i-1, jp));
  its = 0;
  isconverged = false;
  while ~ isconverged
    % set matrix-coefficients for non-linear BC
    A(jp, j1) = -1 - 0.5 * alpha * drb(jp) * cw;
    A(jp, jp) =  1 - 0.5 * alpha * drb(jp) * cw;

    c(i, :)   = A \ r;

    cw = 0.5 * (c(i, j1) + c(i, jp));
    BCres = (c(i, jp)-c(i, j1))/drb(jp) - alpha * cw^2;

    isconverged = abs(BCres/(alpha*cw^2)) < reltol;
    its = its + 1;
  end

  if (mod(i, 50)==0)
    disp(['x-location=', num2str(i), '/', num2str(Nx), ...
          '; iterations: ', num2str(its)])
  end

  % calculate local (x) Sherwood number
  % Jw = - D * (c(i, jp)-c(i, j1))/drb(jp); % ... exactly identical
  Jw(i) = - D * alpha * cw^2;
  kf = Jw(i) / (c(i, j0)-cw);
  Sh(i)=kf*2*R/D;
end

% nondimensionalize variables before outputting
c = c/c0;
dcdyw = Jw * deltas / (D * c0);

% ------------------------------------------------------------------------ %

function grid = creategrid_x(grid, Nx, xend, L)
vnam = fieldnames(grid);
for i=1:length(vnam); eval([vnam{i},'=grid.',vnam{i}, ';']); end

xi = logspace(-5, log10(xend), Nx)';
xi = (xi - xi(1))/(xi(end) - xi(1))*xi(end);

x  = xi * L;

```

```
grid.Nx = Nx;
grid.x = x;

% ------------------------------------------------------------------------ %

function grid = creategrid_r(Nr, R, ut, nu)

jm     = 1;                  % Virtual point on bottom
j0     = jm+1;               % First interior point at bottom
j1     = j0+Nr-jm;           % Last interior point at bottom
jp     = j1+1;               % Virtual point at bottom

Retau = ut * R / nu;
ybplus = (logspace(-3, 0, Nr+1)-1e-3)*Retau;
ybplus = [-ybplus(2), ybplus]';
ycplus = 0.5 * (ybplus(1:end-1) + ybplus(2:end));
ycplus = [ycplus; 2*ybplus(end)-ycplus(end)];
rb     = flipud(1 - ybplus/Retau)*R;
rc     = flipud(1 - ycplus/Retau)*R;
drb    = [NaN; rc(2:end)-rc(1:end-1)];
drc    = [rb(2:end)-rb(1:end-1); NaN];

grid.Nr = Nr;
grid.jm = jm; grid.j0 = j0; grid.j1 = j1; grid.jp = jp;
grid.rb = rb; grid.rc = rc; grid.drb = drb; grid.drc = drc;
grid.ycplus = flipud(ycplus); grid.ybplus = flipud(ybplus);

% ------------------------------------------------------------------------ %

function [u nuT] = hydrodynamics(ycplus, ut, nu)

% Van Driest modified mixing length model
kappa  = 0.41;
Aplus  = 26;
Bplus  = 1/0.26;
lmplus = kappa*ycplus.*(1-exp(-ycplus/Aplus))./sqrt(1-exp(-ycplus/Bplus));

u = ut * cumtrapz(ycplus, 2./(1+(1+(4*lmplus.^2)).^0.5));
u = u - u(end);
nuT = lmplus .^2 .* ...
  [ 0; ...
   (u(3:end) - u(1:end-2)) ./ (ycplus(3:end) - ycplus(1:end-2)); ...
    0 ] * nu / ut;
nuT(1)   = nuT(2);
nuT(end) = -nuT(end-1);


% ------------------------------------------------------------------------ %

function A = creatematrix(grid, u, D, DT, dx)
% unpack grid variables
vnam = fieldnames(grid);
for i=1:length(vnam); eval([vnam{i},'=grid.',vnam{i}, ';']); end

A = sparse(Nr+2, Nr+2);
for j = j0:j1
```

```
  DeffT = D + 0.5 * (DT(j) + DT(j+1));
  DeffB = D + 0.5 * (DT(j-1) + DT(j));
  A(j, j-1) = - rb(j) * DeffB / (rc(j) * drc(j) * drb(j));
  A(j, j)   =   u(j)/dx ...
              + rb(j) * DeffB / (rc(j) * drc(j) * drb(j)) ...
              + rb(j+1) * DeffT / (rc(j) * drc(j) * drb(j+1));
  A(j, j+1) = - rb(j+1) * DeffT / (rc(j) * drc(j) * drb(j+1));
end

% Neumann BC at r=0
A(jm , jm)= -1;
A(jm , j0)=  1;


% ------------------------------------------------------------------------ %
%                1D analytical model   (far field)                         %
% ------------------------------------------------------------------------ %

function [cb cw dcdsw] = ansol_nearfield(x, alpha)
eta     = 4*pi*sqrt(3)*alpha/9;
lambda0 = 1/(sqrt(1+2*eta)-1);
B       = lambda0+log(lambda0);

% ... too slow when dealing with large x ...
% lambda  = lambertw(exp(9/(4*pi*sqrt(3))*x+B));

% construct Wright omega function instead and use interpolation
Wrom = logspace(-3, 5, 5000);
xWrom = Wrom + log(Wrom);
lambda = interp1(xWrom, Wrom, 9/(4*pi*sqrt(3)) * x + B, 'spline');

cb      = (2*lambda+1) ./ (2*eta*lambda.^2);
cw      = (sqrt(1+2*eta*cb)-1)/eta;

dcdsw = alpha / eta^2 * (sqrt(1+2*eta*cb)-1).^2;
% ------------------------------------------------------------------------ %

function [cb cw] = ansol_farfield(x, alpha)
eta    = 4*pi*sqrt(3)*alpha/9;

% Btilde = 0;
% lambda = Btilde + 9/(4*pi*sqrt(3))*x;
% cb     = (2*lambda+1) ./ (2*eta*lambda.^2);

cb = 1 ./ (alpha * x);
cw      = (sqrt(1+2*eta*cb)-1)/eta;

cb(cb > 1) = NaN;
cw(cb > 1) = NaN;
```

B.4. Code introduced in chapter 9

The internal function for the determination of the unknown matrix coefficients for the 2D mass transport code introduced in chapter 9 is presented here. The difference between this internal function and the 2D mass transport code presented for chapter 7 is that $v \neq 0$ here. The function includes application of the first-order upwind scheme for the advective term. Here is the function:

```
function [A] = TwoDmassMatrixRoughWalls(...
    jp, ip, dxb, dxc, dyc, dyb, u, v, D, Dt)
%************************************************************************
%This function determines the unknown matrix [A] coefficients (except the
%boundary nodes) for the 2 D mass transport problem over rough walls, which
%include application of first-order upwind scheme.
%************************************************************************

A=sparse(ip*jp,ip*jp);

for w=2:jp-1
    f=1;
 for t=(w-1)*ip+2:w*ip-1
     f=f+1;
     i=f;
     j=w;
     % ***************************************************************
     if v(i,j)>0 && u(i,j)>0
         DDT=D+Dt(i,j);
         alpha=0.5*(Dt(i+1,j)-Dt(i-1,j))/dxc(i,j);
         beta=0.5*(Dt(i,j+1)-Dt(i,j-1))/dyc(i,j);

         A(t,t)=u(i,j)/dxb(i,j)+v(i,j)/dyb(i,j)+DDT*(1/(dxc(i,j)*...
             dxb(i+1,j))+ 1/(dxc(i,j)*dxb(i,j))...
             +1/(dyc(i,j)*dyb(i,j+1))+1/(dyc(i,j)*dyb(i,j)));
         A(t,t-1)=-u(i,j)/dxb(i,j) +0.5*alpha/dxc(i,j)-...
             DDT/(dxb(i,j)*dxc(i,j));
         A(t,t+1)=-0.5*alpha/dxc(i,j)-...
             DDT/(dxb(i+1,j)*dxc(i,j));
         A(t,t-ip)=-v(i,j)/dyb(i,j) +0.5*beta/dyc(i,j)-...
             DDT/(dyb(i,j)*dyc(i,j));
         A(t,t+ip)= -0.5*beta/dyc(i,j)-...
             DDT/(dyb(i,j+1)*dyc(i,j));

     elseif u(i,j)>0 && v(i,j)<0
         DDT=D+Dt(i,j);
         alpha=0.5*(Dt(i+1,j)-Dt(i-1,j))/dxc(i,j);
         beta=0.5*(Dt(i,j+1)-Dt(i,j-1))/dyc(i,j);

         A(t,t)=u(i,j)/dxb(i,j)-v(i,j)/dyb(i,j)+DDT*(1/(dxc(i,j)*...
             dxb(i+1,j))+ 1/(dxc(i,j)*dxb(i,j))...
             +1/(dyc(i,j)*dyb(i,j+1))+1/(dyc(i,j)*dyb(i,j)));
```

```
43          A(t,t-1)=-u(i,j)/dxb(i,j) +0.5*alpha/dxc(i,j)-...
44              DDT/(dxb(i,j)*dxc(i,j));
45          A(t,t+1)=-0.5*alpha/dxc(i,j)-...
46              DDT/(dxb(i+1,j)*dxc(i,j));
47          A(t,t-ip)= 0.5*beta/dyc(i,j)-...
48              DDT/(dyb(i,j)*dyc(i,j));
49          A(t,t+ip)= v(i,j)/dyb(i,j)-0.5*beta/dyc(i,j)-...
50              DDT/(dyb(i,j+1)*dyc(i,j));
51
52      elseif u(i,j)<0 && v(i,j)<0
53
54          DDT=D+Dt(i,j);
55          alpha=0.5*(Dt(i+1,j)-Dt(i-1,j))/dxc(i,j);
56          beta=0.5*(Dt(i,j+1)-Dt(i,j-1))/dyc(i,j);
57
58          A(t,t)=-u(i,j)/dxb(i,j)-v(i,j)/dyb(i,j)+DDT*(1/(dxc(i,j)*...
59              dxb(i+1,j))+ 1/(dxc(i,j)*dxb(i,j))...
60              +1/(dyc(i,j)*dyb(i,j+1))+1/(dyc(i,j)*dyb(i,j)));
61          A(t,t-1)=0.5*alpha/dxc(i,j)-...
62              DDT/(dxb(i,j)*dxc(i,j));
63          A(t,t+1)=u(i,j)/dxb(i,j) -0.5*alpha/dxc(i,j)-...
64              DDT/(dxb(i+1,j)*dxc(i,j));
65          A(t,t-ip)= 0.5*beta/dyc(i,j)-...
66              DDT/(dyb(i,j)*dyc(i,j));
67          A(t,t+ip)= v(i,j)/dyb(i,j)-0.5*beta/dyc(i,j)-...
68              DDT/(dyb(i,j+1)*dyc(i,j));
69
70      elseif u(i,j)<0 && v(i,j)>0
71
72          DDT=D+Dt(i,j);
73          alpha=0.5*(Dt(i+1,j)-Dt(i-1,j))/dxc(i,j);
74          beta=0.5*(Dt(i,j+1)-Dt(i,j-1))/dyc(i,j);
75
76          A(t,t)=-u(i,j)/dxb(i,j)+v(i,j)/dyb(i,j)+DDT*(1/(dxc(i,j)*...
77              dxb(i+1,j))+ 1/(dxc(i,j)*dxb(i,j))...
78              +1/(dyc(i,j)*dyb(i,j+1))+1/(dyc(i,j)*dyb(i,j)));
79          A(t,t-1)=0.5*alpha/dxc(i,j)-...
80              DDT/(dxb(i,j)*dxc(i,j));
81          A(t,t+1)=u(i,j)/dxb(i,j) -0.5*alpha/dxc(i,j)-...
82              DDT/(dxb(i+1,j)*dxc(i,j));
83          A(t,t-ip)=-v(i,j)/dyb(i,j) +0.5*beta/dyc(i,j)-...
84              DDT/(dyb(i,j)*dyc(i,j));
85          A(t,t+ip)= -0.5*beta/dyc(i,j)-...
86              DDT/(dyb(i,j+1)*dyc(i,j));
87      else
88          DDT=D+Dt(i,j);
89          alpha=0.5*(Dt(i+1,j)-Dt(i-1,j))/dxc(i,j);
90          beta=0.5*(Dt(i,j+1)-Dt(i,j-1))/dyc(i,j);
91
92          A(t,t)=u(i,j)/dxb(i,j)+v(i,j)/dyb(i,j)+DDT*(1/(dxc(i,j)*...
93              dxb(i+1,j))+ 1/(dxc(i,j)*dxb(i,j))...
94              +1/(dyc(i,j)*dyb(i,j+1))+1/(dyc(i,j)*dyb(i,j)));
95          A(t,t-1)=-u(i,j)/dxb(i,j) +0.5*alpha/dxc(i,j)-...
96              DDT/(dxb(i,j)*dxc(i,j));
97          A(t,t+1)=-0.5*alpha/dxc(i,j)-...
98              DDT/(dxb(i+1,j)*dxc(i,j));
```

```
99            A(t,t-ip)=-v(i,j)/dyb(i,j) +0.5*beta/dyc(i,j)-...
100               DDT/(dyb(i,j)*dyc(i,j));
101           A(t,t+ip)= -0.5*beta/dyc(i,j)-...
102               DDT/(dyb(i,j+1)*dyc(i,j));
103     end
104   end
105 end
```

APPENDIX C

List of publications

Peer reviewed journal papers:

- SOOKHAK LARI, K., VAN REEUWIJK, M., MAKSIMOVIĆ, Č. & SHARIFAN, S. 2011 Combined bulk and wall reactions in turbulent pipe flow: decay coefficients and concentration profiles. *Journal of Hydroinformatics,* **34**, 324-333. doi: 10.2166/hydro.2010.013.
- SOOKHAK LARI, K., VAN REEUWIJK, M. & MAKSIMOVIĆ, Č. 2010 Simplified numerical and analytical approach for solutes in turbulent flow reacting with smooth pipe walls. *Journal of Hydraulic Engineering,* **136**, 626-632. doi: 10.1061/(ASCE)HY.1943-7900.0000229.

Conference papers:

- SOOKHAK LARI, K., VAN REEUWIJK, M. & MAKSIMOVIĆ, Č. 2009 A study of wall demand in turbulent pipe flows. In *Proceedings of Computing and Control in the Water Industry (CCWI)*, University of Sheffield, UK.
- SOOKHAK LARI, K., VAN REEUWIJK, M. & MAKSIMOVIĆ, Č. 2009 Is using a plane-channel geometry to model wall-demand in turbulent pipe flow justified? In *Proceedings of Computing and Control in the Water Industry (CCWI)*, University of Sheffield, UK.